Beam Alignment and Image Metrology for Scanning Beam Interference Lithography—Fabricating Gratings with Nanometer Phase Accuracy

by

Carl Gang Chen

B.A., Swarthmore College (1995)
S.M., Massachusetts Institute of Technology (2000)

Submitted to the Department of Electrical Engineering and Computer Science
in partial fulfillment of the requirements for the degree of

Doctor of Philosophy

at the

MASSACHUSETTS INSTITUTE OF TECHNOLOGY

June 2003

Author .....
Department of Electrical Engineering and Computer Science
May 23, 2003

Certified by .....
Mark L. Schattenburg
Principal Research Scientist, MIT Center for Space Research
Thesis Supervisor

Accepted by .....
Arthur C. Smith
Chairman, Department Committee on Graduate Students

Beam Alignment and Image Metrology for Scanning Beam Interference Lithography—Fabricating Gratings with Nanometer Phase Accuracy

by

Carl Gang Chen

Submitted to the Department of Electrical Engineering and Computer Science
on May 23, 2003, in partial fulfillment of the
requirements for the degree of
Doctor of Philosophy

Abstract

We are developing a scanning beam interference lithography (SBIL) system. SBIL is capable of producing large-area linear diffraction gratings that are phase-accurate to the nanometer level. Such gratings may enable new paradigms in fields such as semiconductor pattern placement metrology and grating-based displacement measuring interferometry. With our prototype tool nicknamed "Nanoruler", I have successfully patterned, for the first time, a 400 nm period grating over a 300 mm-diam. wafer, the largest that the tool can currently accommodate.

By interfering two small diameter Gaussian laser beams to produce a low-distortion grating image, SBIL produces large gratings by step-and-scanning the photoresist-covered substrate underneath the image. To implement SBIL, two main questions need to be answered: First, how does one lock the interference image to a fast-moving substrate with nanometer accuracy? Secondly, how does one produce an interference image with minimum phase nonlinearities while setting and holding its period to the part-per-million (ppm) level? My thesis work solves the latter problem, which can be further categorized into two parts: period control and wavefront metrology.

Period control concerns SBIL's ability to set, stabilize and measure the image grating period. Our goal is to achieve control at the ppm level in order to reduce any related phase nonlinearity in the exposed grating to subnanometers. A grating beamsplitter is used to stabilize the period. I demonstrate experimental results where the period stabilization is at the 1 ppm level. An automated beam alignment system is built. The system can overlap the beam centroids to around 10 μm and equalize the mean beam angles to better than 2 μrad (0.4 arcsec), which translates into a period adjustability of 4 ppm at 400 nm. Image period is measured *in-situ* via an interferometric technique. The measurement repeatability is demonstrated at 2.8 ppm, three-sigma. Modeling shows that such small period measurement error does not accumulate as growing phase nonlinearities in the patterned resist grating; rather, the resist grating has an averaged period that equals the measured period. Any phase nonlinearity is periodic and subnanometer in magnitude.

SBIL wavefront metrology refers to the process of mapping the phase of the grating image and adjusting the collimating optics so that minimum image phase nonlinearity

can be achieved. The current SBIL wavefront metrology system employs phase shifting interferometry and determines the image nonlinearity through a moiré technique. The system has an established measurement repeatability of 3.2 nm, three-sigma. I am able to minimize the nonlinearity to 12 nm across a 2 mm-diam. image. Modeling shows that despite an image phase nonlinearity at the dozen nanometer level, printed phase error in the resist can be reduced to subnanometers by overlapping scans appropriately.

From the point of view of period control and wavefront metrology, I conclude that SBIL is capable of producing gratings with subnanometer phase nonlinearities.

Thesis Supervisor: Mark L. Schattenburg
Title: Principal Research Scientist, MIT Center for Space Research

To dad, mom and Xiaohui

Acknowledgments

More than half of this dissertation was written in Beijing, China, at my parents' place over the course of six months, from September 2002 to February 2003. Little did I anticipate that the anti-terrorism campaign would have such a profound impact on my own life, and on the lives of so many other foreign students. Fortunately, given the circumstances, I was stuck at the right place: home. In hindsight, the forced exile might have been one of the best things that happened to me. I am stronger because of it.

During those six agonizing months, I had the love and support of my family and friends to count on. To them, I am forever grateful. Special thanks go to Paul Konkola, Ralf Heilmann, Chulmin Joo, Raymond Scuzzarella, Craig Forest, Yanxia Sun, Juan Montoya, Ed Murphy, Bob Fleming and Mark Schattenburg. They managed to ship a hundred kilograms of notebooks, data and references to me, without which, there would not have been any thesis. Another special thank-you to Fred Gevalt, the person who braved the bureaucracy and managed to get me back in time so that I can put an appropriate end to my MIT career.

I have the honor to be the first student who did both his Master's and PhD under the guidance of Dr. Schattenburg. Mark is an effective yet easy-going advisor. I can express and argue my ideas freely in front of him. I am very grateful to his continuing financial support during my time in China. His questions and suggestions have significantly enhanced the quality of my work.

Paul's skill in controls and mechanical design is enviable. As the only people working full time on SBIL (until I was held up in China), he and I have collaborated closely over the years. I am honored to call him a dear colleague and a loyal friend. One could only hope that the camaraderie will last a lifetime.

Ralf contributed considerably towards SBIL research by designing and implementing the phase measurement optics used for heterodyne fringe locking. I also deeply appreciate his help in taking some new period measurement data so that I could analyze them in Beijing and report the findings at a conference.

With every passing day, Chulmin is a step closer to realizing his dream of becoming a MIT PhD. I wish him the best of luck, and may I remind the man that he still owes me a dinner in Seoul. I am proud to have Craig as a friend. His enthusiasm and warmth are refreshing. Yanxia has been working extremely hard since she joined the team. I wish her some joyful downtime in the coming year. Over the past couple of months, Juan has become a good colleague and friend. He is starting to put his

own signature on the SBIL project. Bob's caring for the lab made it not-too-painful a place to spend 24 hours in. His good sense of humor is most memorable. Captain Ed's mastery of fab-processes makes him invaluable to my work. He is easily one of the nicest follows that I know. I wish him the best. Not enough thank-you's can express my gratitude towards Ray, whose help during my time of need can most certainly be counted on. As new members, Chih-Hao Chang and Mireille Akilian have demonstrated their skills convincingly. The future of SNL looks bright because of them.

I thank Professors Henry Smith and Cardinal Warde for serving as my thesis readers. I benefitted from their questions.

The work documented in this dissertation is done at the MIT Space Nanotechnology Laboratory, and is supported by grants from NASA and DARPA.

Contents

List of Figures

List of Tables

Chapter 1

Introduction

> *"No single tool has contributed more to the progress of modern physics than the diffraction grating."*
>
> *George R. Harrison, 1949*

I am a part of an ongoing effort here at the MIT Space Nanotechnology Laboratory to ground and develop a novel diffraction-grating patterning technique called *scanning beam interference lithography* (SBIL). Similar to "traditional" interference lithography (IL), SBIL uses the interference of two coherent laser beams to pattern a photoresist-covered substrate. Unlike IL however, the SBIL beams, only a couple of millimeters in diameter, are much smaller than the total desired patterning area. The SBIL prototype, nicknamed "Nanoruler", can pattern substrates up to 300 mm in diameter. The interference image must therefore be step-and-scanned across the substrate in order to produce a large grating.

The goal of SBIL is to pattern large-area linear gratings while controlling any nonlinear phase errors, both short range and long, to the nanometer-level, and ultimately, subnanometer-level. For an ideal linear grating with a period p, the spatial phase of the grating is given, up to some constant, by

$$\phi_{\text{lin}}(x) = 2\pi \frac{x}{p} \quad , \tag{1.1}$$

where x is the direction of the grating vector, i.e., the in-plane direction perpendicular to the grating lines. For a nonideal grating with a varying period $p'(x)$, the spatial phase is defined in the form of an integral,

$$\phi_{\text{nonlin}}(x) = 2\pi \int_0^x \frac{x'}{p'(x)}\, dx' \quad . \tag{1.2}$$

Restated, the goal of SBIL is to pattern gratings such that the difference between $\phi_{\text{nonlin}}(x)$ and $\phi_{\text{lin}}(x)$ is at the nanometer level for very large x, which is on the order of hundreds of millimeters.

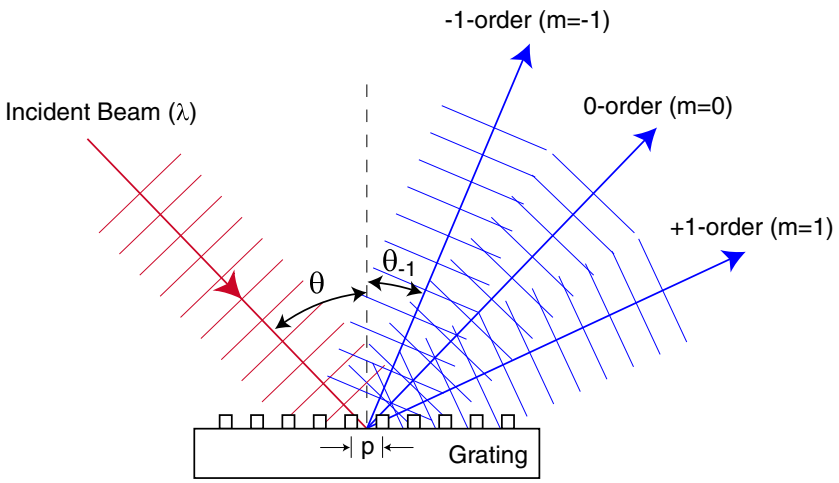

Figure 1-1: A reflection grating. Schematic only.

Although the project's original motivation is to develop fiducials for use in semiconductor metrology [1], these ultra-phase-coherent structures may have important applications in fields as diverse as displacement measuring grating interferometry, integrated optics, telecommunications, magnetic storage, field emitter array displays, distributed feedback lasers, and of course, high-resolution spectroscopy.

1.1 Mechanically-ruled gratings

Due to its early popularity, particularly with astronomers and spectroscopists, volumes have been dedicated to the study of diffraction gratings [2, 3, 4, 5]. One can not write a thesis on the subject without quoting the famous grating equation,

$$\sin\theta_m - \sin\theta = \frac{m\lambda}{p} \quad , \tag{1.3}$$

where θ is the incident beam angle, θ_m is the angle for the mth-order diffracted beam, λ is the wavelength of light and p is the spatial period of the grating. Figure 1-1 illustrates the definitions graphically using a reflection grating.

The principle of the diffraction grating was discovered by Rittenhouse back in 1785 [6]. The idea attracted little attention at the time. It was not until 1819 that Fraunhofer rediscovered the principle [7]. He ruled rudimentary gratings of sufficient quality and with them, was able to measure accurately the wavelengths of the sodium absorption lines from the Sun. From the grating equation, it can be shown that the theoretical limit of the so-called resolving power—defined as $\lambda/\Delta\lambda$ where $\Delta\lambda$ is a small change in the wavelength—for a grating of overall width w, is

$$\left.\frac{\lambda}{\Delta\lambda}\right|_{\max} = \frac{2\,w}{\lambda} \quad . \tag{1.4}$$

The push to attain ever finer spectroscopic resolution drove pioneers such as Row-

land [8] and Michelson [9], in the late 1800s, to develop the first ruling engines, and to make ever larger and better quality gratings. Reference [10] gives a detailed account on the history of mechanically-ruled gratings. Reference [11] has a good review on the design of the ruling engine. During a ruling process, each groove of the grating is formed individually by burnishing with a diamond tip. The modern era of ruling dawned when Harrison and his team here at MIT equipped their engine with interferometric position feedback control [12]. Nowadays, gratings many centimeters in dimension and with periods as fine as 100 nm can be ruled in a variety of materials[1].

Even though a modern ruling engine stands at the pinnacle of precision machine design, the ruling process suffers some major drawbacks. Due to its serial nature, ruling is painstakingly slow, some large gratings can take weeks or even months to complete. The accumulated travel by the diamond tool is measured in many tens of kilometers, which imposes significant tool wear. Reference [13] gives an estimate of the tool life: Under an ideal scenario where the best diamond crystal is used to rule the purest aluminum, the diamond can only last about 15 km. Special procedures, such as overcoating the aluminum with silver, must be adopted if longer travel is desired, but even then the tool life puts a limit on how fine a period and/or how large a grating one can make. Good environmental control and vibration isolation, both critical to a successful ruling run [5, 14], are extremely difficult to maintain over the lengthy time of operation. Although much improved on the newer interferometrically controlled engines, periodic groove positioning errors do still exist. They arise from the imperfections in the gears and linkages of the ruling engine, and can be observed as the so-called "ghosts"—spurious lines in the spectrum [3, 15]. In addition, random errors exist as well. Reference [16], for example, measures the ruling error of a typical ruled grating that is 150 mm long and with 600 grooves/mm. The maximum error is around 200 nm.

Because of the cost and the time involved in ruling gratings, it is economically inviable to apply them in any commercial sense. Grating replication is therefore required [17, 18] and the process introduces additional errors.

1.2 Interference gratings

As the name suggests, interference gratings (also known as holographic gratings) are patterned by interfering two coherent beams of light. Since the interference fringes are first captured by photoresist, the process is also known as interference lithography (IL). Michelson suggested the idea in 1927 [19], yet the first spectroscopic-quality

[1] Usually optically flat glass substrates (BK-7, fused silica, Zerodur, etc.) coated with a layer of soft metal such as aluminum or gold.

interference gratings are not made until the late 1960s [20, 21]. MIT is at the forefront of interference lithography research, with a patented IL system operating at the Space Nanotechnology Lab [22]. Reference [23] describes the system setup in detail and lists a thorough bibliography that covers its development. For the purpose of comparing it to the SBIL system, I will also briefly introduce the IL setup in Section 1.4.1.

Hutley provides a good review of the many advantages of interference gratings over ruled ones [24]. The IL process is extremely fast compared to ruling since all of the grooves are formed simultaneously. For example, the resist exposure time on the MIT IL system is typically between 10 and 60 seconds. This significantly relaxes the requirements on environmental control and vibration isolation. The process is static and the coherence length of the lithography laser determines the spatial coherence of the grating. As a result, spectral defects such as ghosts, which are prominent in ruled gratings are absent in interference gratings. The size and/or the period of a mechanically ruled grating is governed by diamond wear. Theoretically at least, IL is capable of making meter-sized gratings with very fine pitch, the real-world limitations being the laser's wavelength, coherence length and power. The early interference gratings did not have the same high diffraction efficiency as their ruled cousins, because of an apparent lack of control in shaping the groove profile. However, with the maturing of the fabrication technology, a large number of techniques can now be leveraged to properly manipulate the grating profile in order to yield the desired efficiency. Reference [25], for instance, reports the production of metallic reflection gratings through IL that has a diffraction efficiency exceeding 95% for the -1-order. The same reference gives a rich bibliography that documents the various techniques used in shaping interference gratings.

1.3 Gratings for new paradigms

Figure 1-2 is a chart adapted from the 2002 Update of the International Technology Roadmap for Semiconductors (ITRS) [26]. Within a year, integrated circuit (IC) manufacturing will officially enter the sub-100 nm technology node. In addition to the challenges of patterning and inspecting the ever-shrinking features, there lies the critical issue of pattern placement metrology.

Presently, in order to measure the pattern placement distortion, be it process induced, mastering or replication distortion, coordinate measuring tools such as Leica's LMS IPRO is used to detect alignment marks pre-written on the substrate and/or the reticle, while monitoring the XY position of the sample with heterodyne laser interferometry [27, 28], and in the end producing a so-called "market plot" [29, 30, 31, 32]. Leica specified a 5 nm repeatability and a 10 nm nominal accuracy for the IPRO [33].

Year of Production	2003	2004	2007	2010	2013	2016
Critical Dimension (CD) (nm)	100	90	65	45	32	22
CD Control (3σ) (nm)	12.2	11	8	5.5	3.9	2.7
Overlay Control (nm)	35	32	23	18	13	9
Metrology Tool Accuracy (3σ) (nm)	3.9	3.6	2.6	2	1.4	1

Manufacturable Solutions are Known

No Known Solutions

Figure 1-2: Chart adapted from the 2002 Update of the International Technology Roadmap for Semiconductors (ITRS). The first row gives the year of the device generation and the second indicates the target minimum feature size—as is customary DRAM half-pitch is used. The third row indicates the allowed CD variation. The fourth gives the wafer overlay tolerance, and the fifth is an estimate of the necessary metrology tool accuracy, taken to be one-ninth of the overlay error.

Recently, the company also announced an upgrade called IRO2, though it is unclear if the system is ready for sale. Based on preliminary test data posted on Leica's website [34], the new tool has a repeatability of 3 nm and a nominal accuracy of 5 nm over a measurement area of 120 mm × 120 mm. The market-plot approach is very slow due to its serial nature, its accuracy downgraded in practice by difficulties in detecting the alignment marks with a microscope, and it can only sample a limited number of surface locations. Whether the method can continue to satisfy the ever more demanding needs of semiconductor metrology (Fig. 1-2) is questionable.

Schattenburg et al. [1] proposed the use of highly accurate fiducial gratings to complement and perhaps eventually replace the current paradigm of market-plot pattern placement metrology. If large nanometer-accurate gratings are available, a slew of new techniques can be employed to improve both the speed and accuracy of the metrology. For example, Figure 1-3 shows a scheme to map the replication distortion of a wafer stepper. Many pattern mastering lithography systems, such as the electron beam (e-beam) lithography tool commonly used for mask making, have the ability to both write and read a substrate. Accurate gratings read by an e-beam tool will allow the mapping of the tool's mastering distortion. By referencing the e-beam position in real-time to a grating fiducial pre-patterned on the substrate, Smith et al. invented the so-called spatial-phase-locked electron beam lithography (SPLEBL) to correct for inter-field errors on the fly [35].

Almost all state-of-the-art pattern generating systems (e.g., e-beam tools, steppers, laser writers [36], etc.) and placement metrology tools utilize heterodyne laser

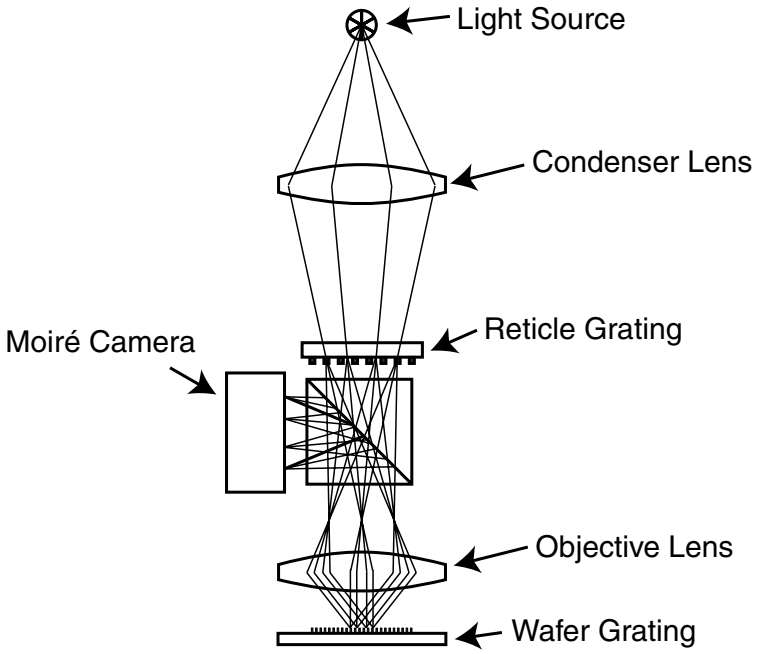

Figure 1-3: Two accurate gratings enable *in-situ* measurement of the objective-lens distortion in a stepper via a moiré technique. Schematic only.

interferometry for stage position measurement. If accurate large-dimension gratings can be made, they will permit the replacement of laser interferometers with grating-based interferometers of high accuracy. The idea of using gratings to measure displacement is not new. In 1967, Gerasimov implemented a grating interferometer to control the position of the carriage on a ruling engine [37]. He employed a pair of gratings, one transmission and one reflection, and used an achromatic setup depicted schematically in Figure 1-4[2]. Reference [38] points out the many advantages of grating-based interferometry. Besides the cost and weight savings, the small optical paths involved in a grating interferometer make the scheme essentially immune to environmental disturbances, which have plagued laser interferometry from the beginning. Patterning the grating onto a thermally stable substrate like Zerodur can substantially enhance the repeatability of the interferometer. Today, displacement measuring grating interferometers, also known as linear encoders, are commercially available and have a variety of interesting designs [39]. They offer very good resolution, but in terms of measurement accuracy, they are still far behind the top-of-the-line laser interferometers[3]. The lack of accuracy is largely due to the present lack of technology to pattern nanometer-accurate gratings over large dimensions.

[2]Figure adopted from Reference [37] and modified for better illustration.

[3]For instance, the LIP 382 Exposed Linear Encoder by Heidenhain has a resolution specification of 1 nm, but the accuracy is only ±500 nm over a measurement range of 270 mm [40].

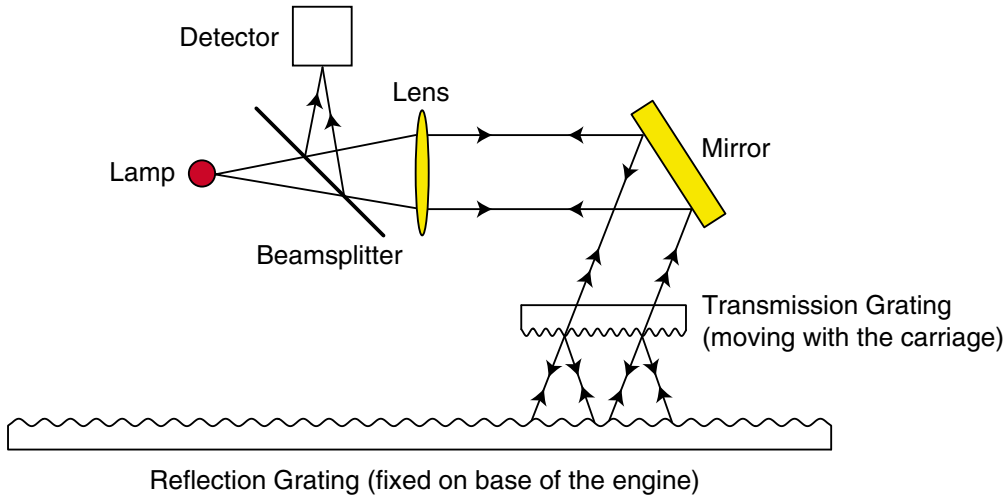

Figure 1-4: A displacement measuring grating interferometer used to control a ruling engine. The reflection grating has half the spatial frequency of the transmission grating. The reflection grating is used at ±2-orders whereas the transmission grating at zero and first order. One fringe cycle observed at the detector corresponds to a relative displacement of one-quarter the period of the reflection grating.

1.4 Scanning beam interference lithography

By interfering two small diameter Gaussian laser beams [41] and step-and-scanning the resulting interference image, SBIL can pattern large-area linear gratings with nanometer overall phase accuracy. Given the insight from the previous section, SBIL is a technology that may enable paradigm shifts in both pattern placement metrology and displacement measuring interferometry [1, 42].

In this section, I introduce the SBIL concept, but first, I briefly describe the traditional interference lithography (IL) system at MIT.

1.4.1 Interference lithography at MIT

From elementary electromagnetism, one can easily deduce the period p of the interference fringes at a substrate when two plane waves interfere,

$$p = \frac{\lambda}{\sin\theta_1 + \sin\theta_2} \quad , \tag{1.5}$$

where λ is the wavelength, θ_1 and θ_2 are the incident angles for the left and the right arm, respectively (Fig. 1-5). When $\theta_1 = \theta_2 \equiv \theta$, Eq. (1.5) reduces to

$$p = \frac{\lambda}{2\,\sin\theta} \quad . \tag{1.6}$$

Reference [23] provides a good description of IL and its history. Figure 1-6 illustrates the MIT system setup. As drawn, the two incident angles are assumed equal. The split beams from an argon-ion laser ($\lambda = 351.1$ nm) are conditioned before in-

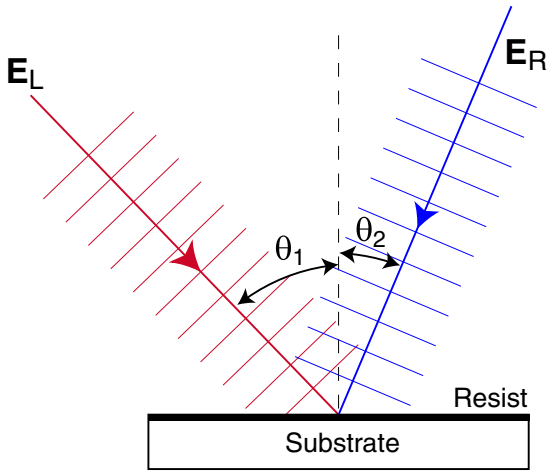

Figure 1-5: During interference lithography, the nominal fringe period p at the substrate is determined by the beam incident angles θ_1 and θ_2, and the laser's wavelength λ.

terfering at the substrate. The variable attenuator equalizes the power of the beams to maximize the fringe contrast. Polarizers in each arm ensure s-polarized[4] light exposing the substrate. Spatial filters rid wavefront distortions by blocking undesired spatial frequencies. The focal length of the lens in the spatial filter is chosen to set the divergence of the beams, thereby defining the size of the interference region. The beams have a Gaussian intensity distribution. For good dose uniformity, the spot size on the substrate should be much larger than the desired patterning area. A phase error sensor located near the plane of the substrate measures fringe drift, which is mainly due to air index change, vibration, and thermal drift of the optical setup. A differential signal from two photodiodes yields the error signal that drives the analog controller for a phase displacement actuator (a Pockel's cell), which actuates to stabilize the fringes at the substrate.

The distance from the spatial-filter pinhole to the substrate defines the radius of the expanding spherical wavefront. It is desirable for this distance to be large for reduced hyperbolic grating phase nonlinearities [23, 43, 44, 45]. In practice however, turbulence, vibration, and thermal drift limit how large the propagation distance can be. In the MIT setup, this distance is nominally 1 m. Even with such large wavefront radii and the assumption of perfectly aligned beams, Figure 1-7 shows that the image diameter with subnanometer phase nonlinearity is only 2.8 mm. This assumes a 400 nm nominal grating period. Furthermore, if one considers a 20 mm $\times$ 20 mm square area, the discrepancy worsens to over 600 nm at the four corners of the square[5].

[4] Also known as the transverse-electric (TE) polarization.
[5] See Figure 4.5(b) in Reference [23].

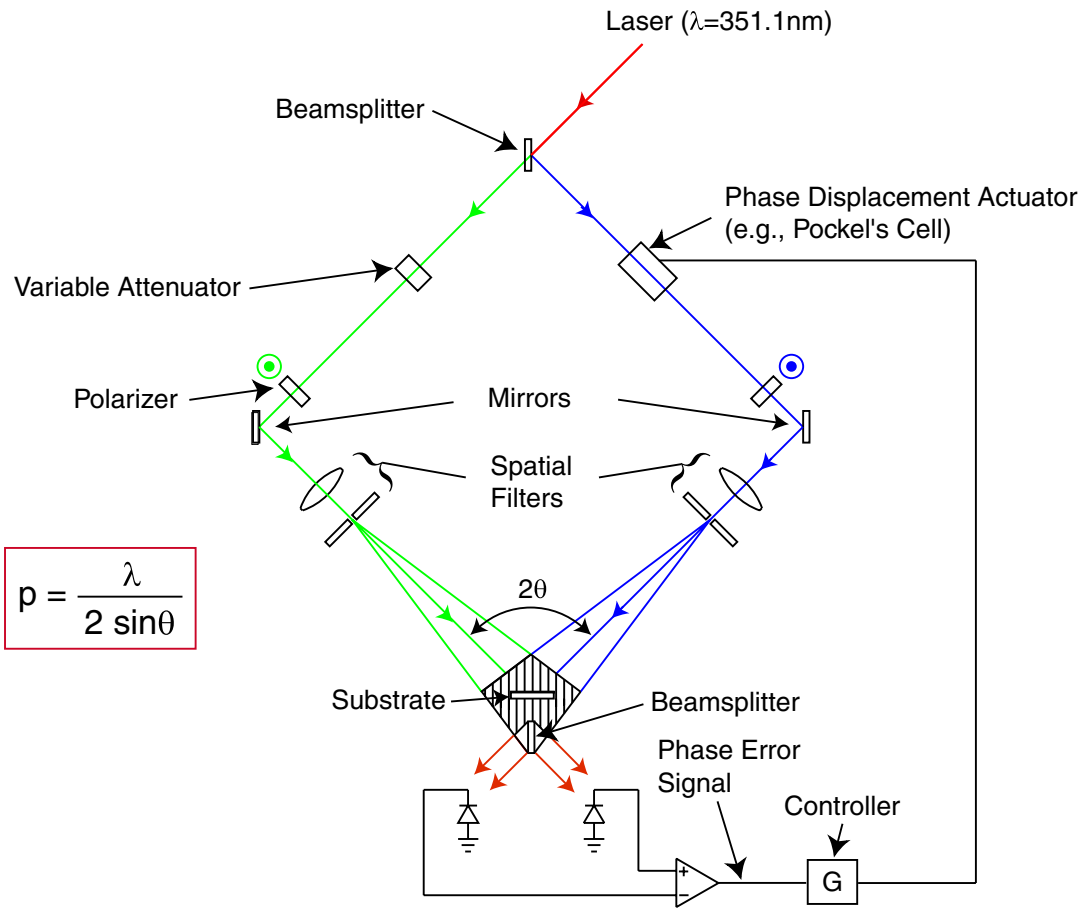

Figure 1-6: A schematic diagram of the traditional interference lithography system at MIT.

Theoretically, lenses may be used to collimate the beams after the spatial filter and thus eliminate the hyperbolic phase nonlinearity. However, it is questionable whether it is practical to fabricate, align and keep clean large optics capable of producing meter-sized gratings with nanometer phase nonlinearity.

For the purpose of conducting pattern placement metrology or displacement measuring interferometry, it is most ideal to have linear gratings, but the requirement is not absolute. If the nonlinear phase in the IL-produced gratings is highly repeatable and well characterized, one can still use them and compensate for the nonlinearity via a look-up table. However, Ferrera showed conclusively that nanometer repeatability for traditional IL is improbable if not impossible to attain because of severe beam and substrate alignment requirements [23]. For example, he showed that in order to attain a repeatability of 3 nm over an area of 25 mm $\times$ 25 mm, the two interferometer arms d_L and d_R in Figure 1-7(a) must be matched to 150 nm. With much technical prowess, he was only able to demonstrate an experimental repeatability of 50 nm for

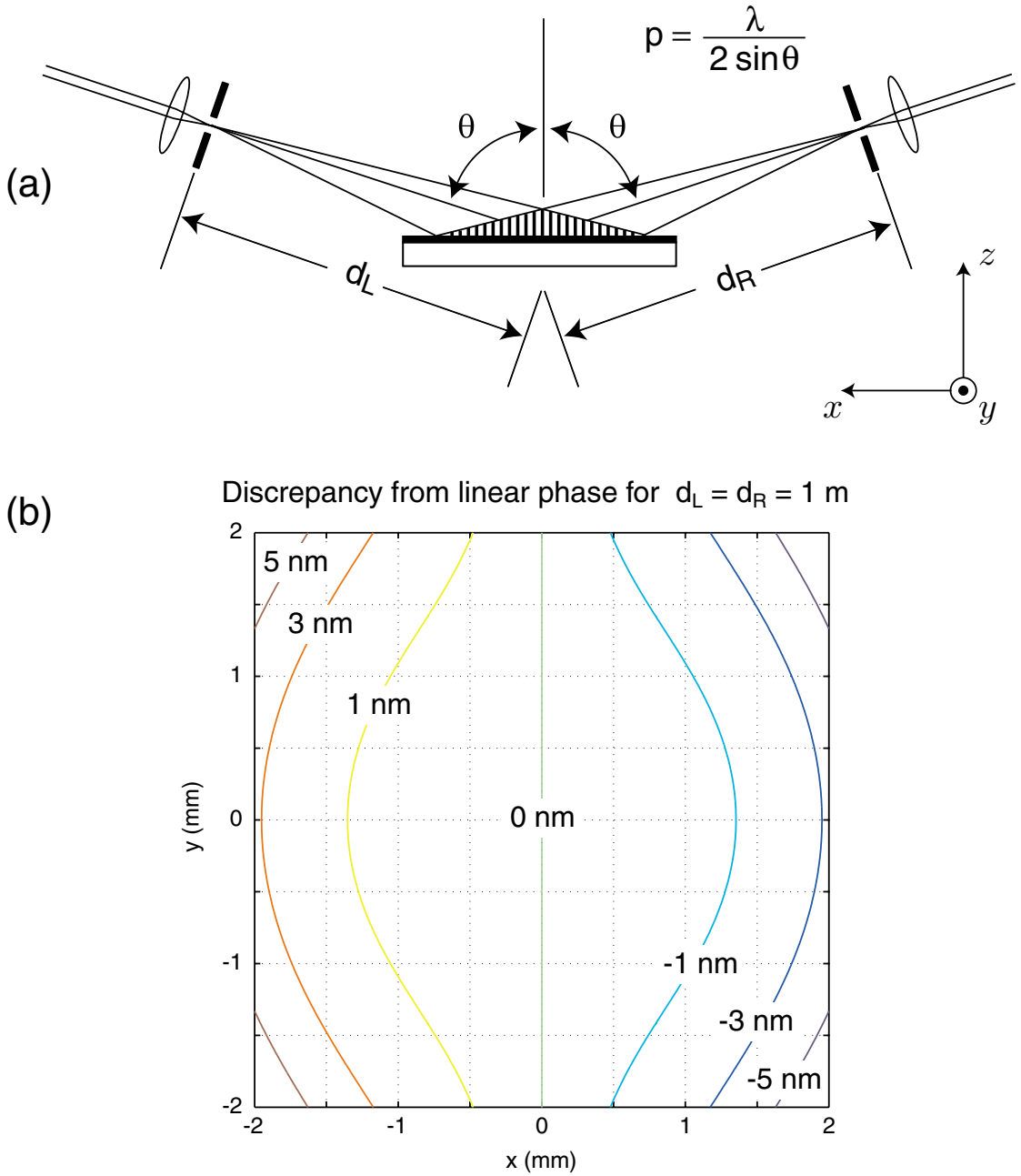

Figure 1-7: Nonlinear phase distortions due to the interference of two spherical waves with 1 m wavefront radii, assuming that the system is in perfect alignment and is set up for a nominal grating period of 400 nm. (a) The interference coordinates. (b) Phase discrepancy from an ideal linear grating. The region with subnanometer nonlinear phase is less than 2.8 mm in diameter.

400 nm period gratings over an area of 30 mm × 30 mm.

Because of phase nonlinearity and repeatability issues, conventional IL is incapable of producing large-area linear gratings.

1.4.2 SBIL concept

Figure 1-8 depicts the SBIL system concept. A grating beamsplitter splits the laser in two. The lithography interferometer optics closely resembles that of traditional IL but the grating image is much smaller than the total desired patterning area. The beams are Gaussian in nature. The $1/e^2$ intensity diameter at the substrate is typically 2 mm, but can be enlarged or reduced by adjusting the optical layout. The collimating lenses after the spatial filters ensure that the Gaussian beams interfere with each other at their waists, where the wavefronts are the most planar[6]. For a lithography laser wavelength of $\lambda = 351.1$ nm, the system is intended for writing gratings with a period in the range of 200 nm to 2 μm. The substrate is mounted on a laser interferometer controlled air-bearing XY stage. Large gratings are fabricated by scanning the substrate at a constant velocity underneath the grating image.

Figure 1-9 illustrates how SBIL achieves a uniform exposure dose by overlapping scans. Figure 1-9(a) shows the grating image being scanned along the substrate. In order to stitch scans together, one must measure the fringe period with high accuracy. SBIL period measurement goal is 1 nm uncertainty over 1 mm-radius spot, which translates into an allowed percentage measurement error of only one-part-per-million (1 ppm). At the end of the scan the stage steps over by an integer number of fringe periods and reverses direction for a new scan. SBIL has the significant added complexity over IL of accurately synchronizing the interference image to a moving substrate. The scanning grating image is illustrated in Figure 1-9(b). The interference pattern has a Gaussian intensity envelope. The effective number of fringes in the grating image may be many thousands (i.e., 5,000 fringes in a grating image with a 2 mm $1/e^2$-diameter and a 400 nm period). Figure 1-9(c) shows the individual scan intensity envelopes in dashed lines and the sum of the envelopes in a solid line. A maximum step size is constrained by the desired dose uniformity. As plotted, a step size of 0.9 times the $1/e^2$-radius produces dose uniformity of better than 1%.

Similar to IL, SBIL employs a fringe-locking controller to stabilize the fringes while writing. Unlike IL's homodyne approach, which stabilizes the fringes by sensing the differential intensity variations between two photodiodes, SBIL uses a heterodyne fringe-locking scheme. Since phase drifts are detected in the frequency domain, the

[6]Reference [45] shows that uncollimated Gaussian beams can also be used to generate a proper-sized grating image. However, the topology is not currently used due to optics packaging reasons. See Section 5.2.11 for details.

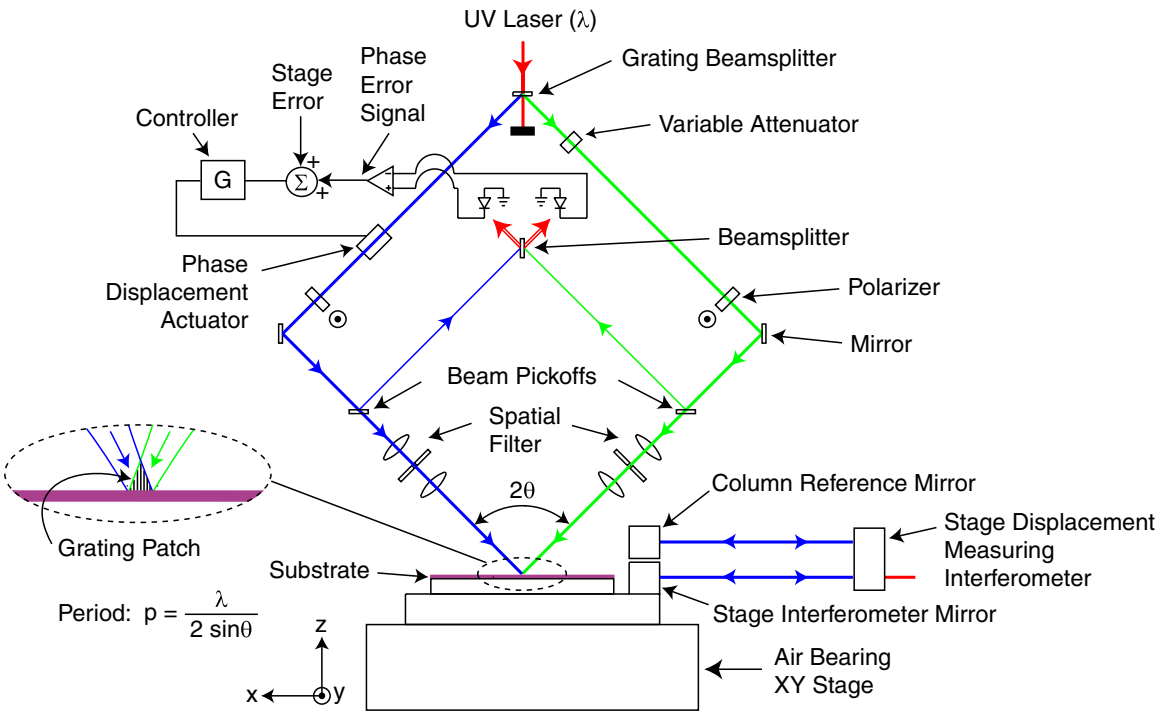

Figure 1-8: Scanning beam interference lithography system concept.

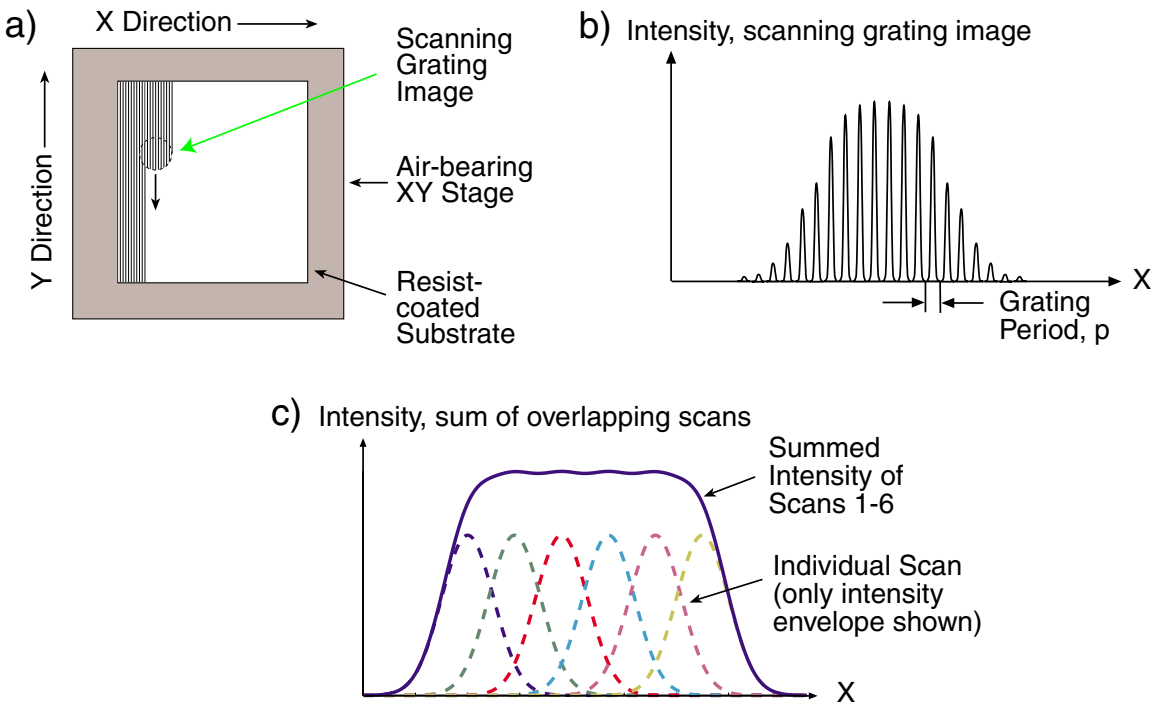

Figure 1-9: SBIL step-and-scan scheme. (a) Top view. The step and scan directions are x and y, respectively, which are also defined in Figure 1-8. To ensure good stitching between adjacent scans, the stage must step over by an integer number of fringe periods. (b) Gaussian intensity envelope of one scan. Period exaggerated. (c) Beam overlapping to create a uniform exposure dose.

heterodyne scheme is immune to laser intensity fluctuations, which can be quite significant over an hour time required to pattern a 300 mm grating. It should be noted that besides fringe motions due to the changing air index, the nonideal motion of the stage, if uncorrected, introduces additional errors in the written grating as well. For that reason, stage positioning error, especially along the sensitive x axis which is perpendicular to the fringe direction, is also compensated by fringe locking.

1.4.3 System advantages

SBIL offers significant advantages over IL. The small beams used in SBIL provide a major benefit in ease of obtaining small wavefront distortions and thereby a highly linear grating image within the interference spot [45]. Nowadays, commercial optics with figure errors, typically one-tenth of a wave (i.e., $\lambda/10$) across a one-inch (25.4 mm) clear aperture, is readily available at modest prices. Because SBIL employs small beams a couple of millimeters in diameter, they sample only a tiny fraction of the overall aperture. Therefore, the effective figure error is much smaller than $\lambda/10$.

By scanning the grating image, nonlinear distortions along the scan direction can be averaged out, so can phase jitters due to imperfect fringe locking and stage motion. Overlapping adjacent scans leads to further and more significant averaging of the phase nonlinearity; it also allows flexibility in controlling the resist grating period at the picometer level—both are subjects that I will examine in great detail in this thesis. Also, critical alignments such as lens positioning and angle of interference are much relaxed for small beams.

SBIL really is a fusion of IL and mechanical ruling. Taking the best from both worlds, our prototype tool is appropriately nicknamed "Nanoruler". Instead of a single diamond tip, SBIL in a sense writes with thousands of "tips" in parallel, which dramatically improves the system throughout. For example, to create a grating 300 mm $\times$ 300 mm in size with a period of 400 nm, the current state-of-the-art ruling engine, under a most ideal scenario, has to run continuously for 52 days, whereas Nanoruler can finish the job around an hour. By permitting adjustments of the stage scan speed, overlapping step size, and beam power, SBIL also allows good exposure dose control.

1.4.4 System overview

Figures 1-10 and 1-11 show the front and the back of the SBIL prototype, respectively. The system employs an XY air-bearing stage[7], column referencing heterodyne interferometry, refractometry, a grating length-scale reference, beam steering system, beam alignment system, *in-situ* fringe period measurement, wavefront metrology, acousto-

[7]The stage together with the servo control hardwares are purchased from Anorad Corporation.

optic fringe locking, and active vibration isolation. Figure 1-12 shows a custom-built Class 10 environmental enclosure [8] that provides acoustic attenuation, particle and ambient-light protection, as well as controls over temperature (± 0.005 °K), relative humidity ($< \pm 0.8\%$), and pressure gradient (< 15.5 Pa/m).

Displacement measuring interferometer

The most salient difference between traditional IL and SBIL is the step-and-scan feature provided by an XY air-bearing stage. The stage is controlled via displacement measuring interferometry (DMI)[9]. Large gratings are fabricated by scanning the substrate at a constant velocity underneath a small grating image. By design, the interference fringes are oriented along the stage y axis, which I will also refer to as the scan direction. The stage x axis is perpendicular to the fringes, and it defines what-I-will-call the step direction.

Presently, two two-pass column-referencing heterodyne interferometers, each with 0.31 nm resolution, measure the critical x-axis displacement and yaw (Fig. 1-17). The hardwares for doing column referencing along the y axis are in place but not yet implemented. Error terms [27, 28, 46], such as the electronics error, polarization mixing error and mirror alignment error, all impact the accuracy of the DMI measurements, thence stage performance. Their effects combine into the so-called stage error, which must be minimized during SBIL writing via real-time fringe locking. Furthermore, changes in the index of air and the vacuum wavelength of the DMI laser require an accurate way to scale the phase readings from the heterodyne electronics. A grating length-scale reference has been proposed [47], which will be incorporated on the vacuum chuck to calibrate the wavelength of the stage interferometer (Fig. 1-17). The system is designed to read the phase of a grating that has nominally the same period as the one that it is set up to write [48]. Once calibrated, the system employs a refractometer, essentially a stationary interferometer, to continuously monitor the air index-change induced wavelength change, thus allows real-time correction of the interferometer readout. To reject stage motion induced disturbances, an active vibration isolation system[10] with feed-forward control is used.

Lithography interferometer

To reduce a major source of thermal and mechanical disturbance, and to allow multiple lithography tools to share a common laser, the UV lithography laser ($\lambda =$ 351.1 nm) is located far (~ 10 m) from the SBIL system. A beam steering system [49] is used to stabilize the position and angle of the beam as it reaches the SBIL tool

[8] Built by Control Solutions LLC, Inc.

[9] DMI hardwares are manufactured by Zygo Corporation.

[10] Isolation system hardwares are manufactured by Integrated Dynamics Engineering GmbH.

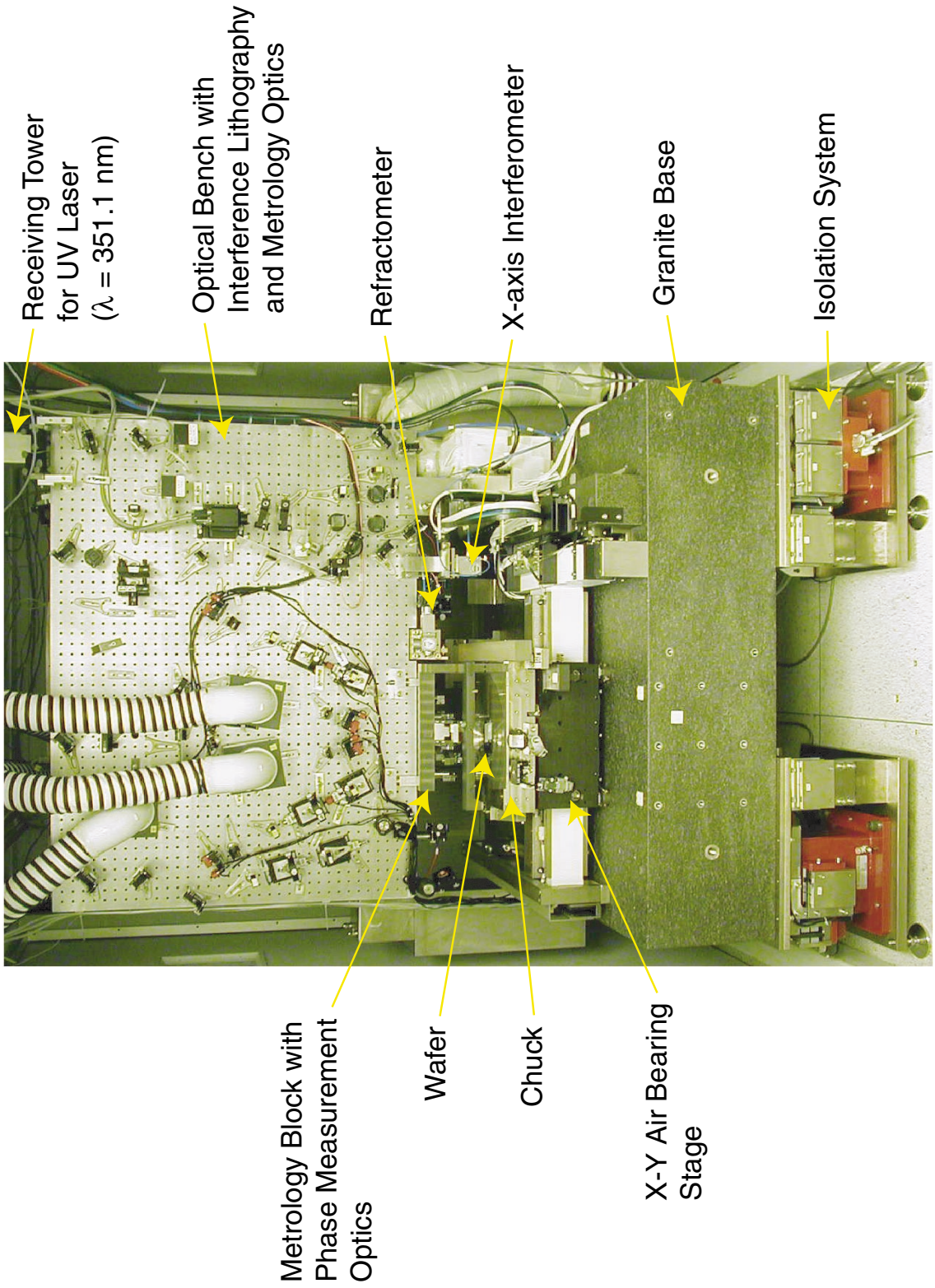

Figure 1-10: SBIL system, front view. Currently configured to write 400 nm period gratings. The whole system is housed inside a Class 10 environmental chamber.

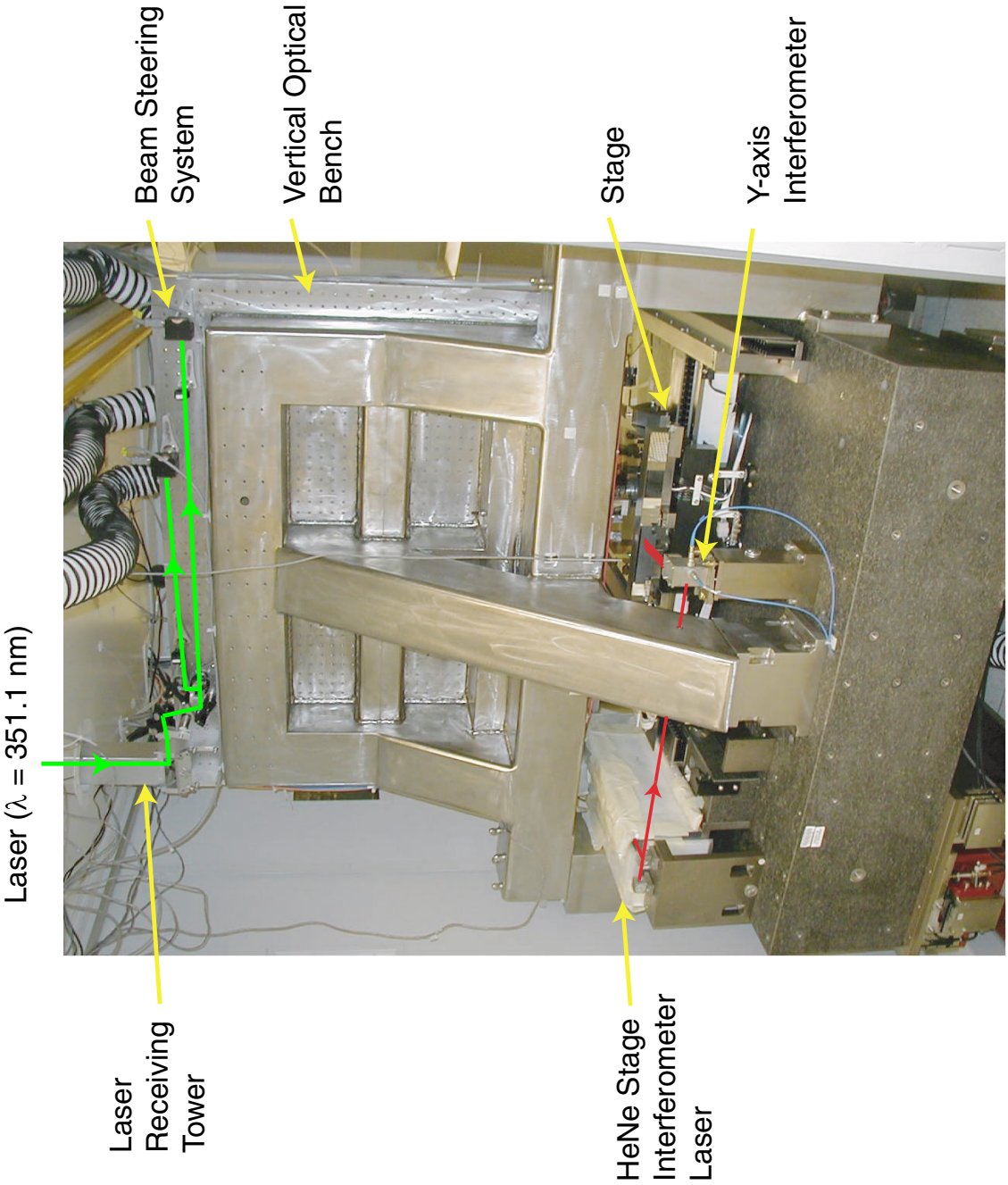

Figure 1-11: SBIL system, back view. Continued from Figure 1-10.

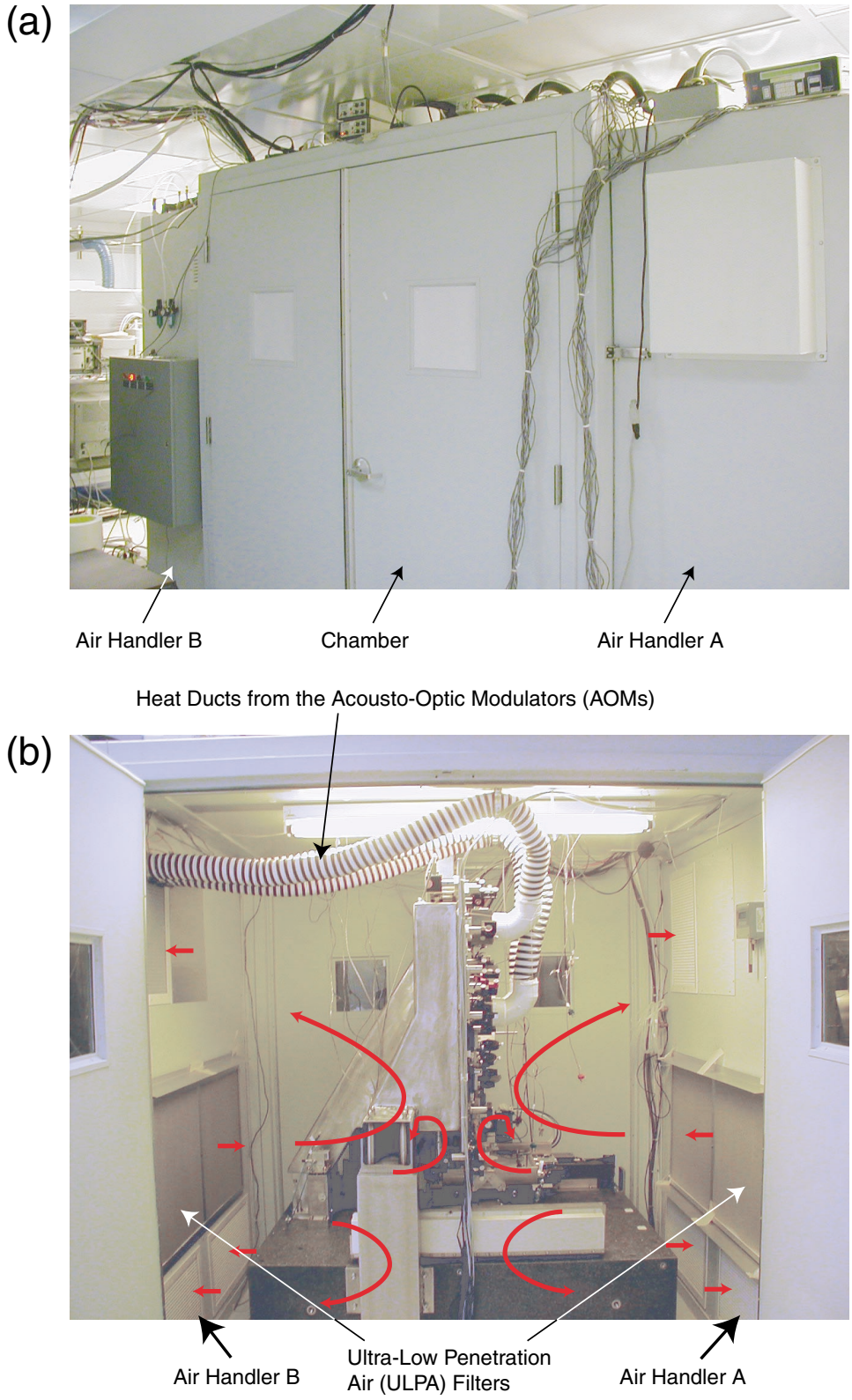

Figure 1-12: SBIL environmental enclosure. (a) External view. (b) Internal view with air flow paths outlined. All major thermal sources, which include the HeNe stage interferometer laser and all three acousto-optic modulators (AOMs), have been enclosed. Heat is actively pumped away from the optical bench via ducts.

and forms the lithography interferometer.

The optical design and layout of the interferometer, which will be discussed in detail in Chapter 2, incorporates means for spatial filtering and adjustment of laser intensity, polarization, and wavefront curvature (Fig. 1-13). A $\pm$1-order grating beamsplitter is used to separate the incoming laser into two beams that form the two arms of the interferometer. The use of the grating provides a greater tolerance on the beam angular instability [49]. In turn, this leads to superior fringe period stabilization. Appendix B discusses the physics. The grating also yields an achromatic configuration where the period of the interference fringes is insensitive to air index changes and vacuum wavelength variations of the UV laser [50, 51, 52].

Currently, the system is set up to write gratings with a nominal period of around 400 nm. While the system is capable of writing periods as small as 200 nm and as large as 2 μm, once the interference optics have been laid down for a particular period, switching to another period is impossible unless all the optics are relocated. The present goal of SBIL is to demonstrate writing with nanometer phase accuracy at a fixed period, e.g., 400 nm. Variable period writing is an interesting and practical research topic for the future.

During SBIL writing, lithography interferometer's phase error and the stage error are fed back to a high bandwidth heterodyne acousto-optic fringe locking system, which in real-time, locks the interference fringes to the moving substrate [53]. Figure 1-14(a) shows a schematic of the system in the so-called writing or lithography mode. An acousto-optic modulator is a device that can both diffract and shift the frequency of the diffracted beam [54]. In the case of SBIL, all three AOMs are tuned to diffract strongly in the first order. By setting the frequencies with a master frequency synthesizer[11] and combining the diffracted beams appropriately, two 20 MHz heterodyne signals at phase meters (PM) 1 and 2 are produced. A digital signal processor (DSP) then compares the signals and drives AOM2 to keep the phase difference between the two arms constant. The performance of the fringe locking system is limited by the controller's bandwidth and inaccuracy in the fringe locking sensor signal due to air index variations and electronic inaccuracy. It is important to note that the stage error is also fed to the fringe locking system and compensated in real-time. SBIL tool's repeatability is established by reading the phase of a previously exposed grating. Figure 1-14(b) is a schematic of the so-called grating reading mode. A SBIL-written grating is used in the Littrow condition, where the 0-order reflected beam from one arm coincides with the -1-order back-diffracted beam from the other arm. Two 20 MHz

[11] The synthesizer and the AOMs are built by IntraAction Corporation.

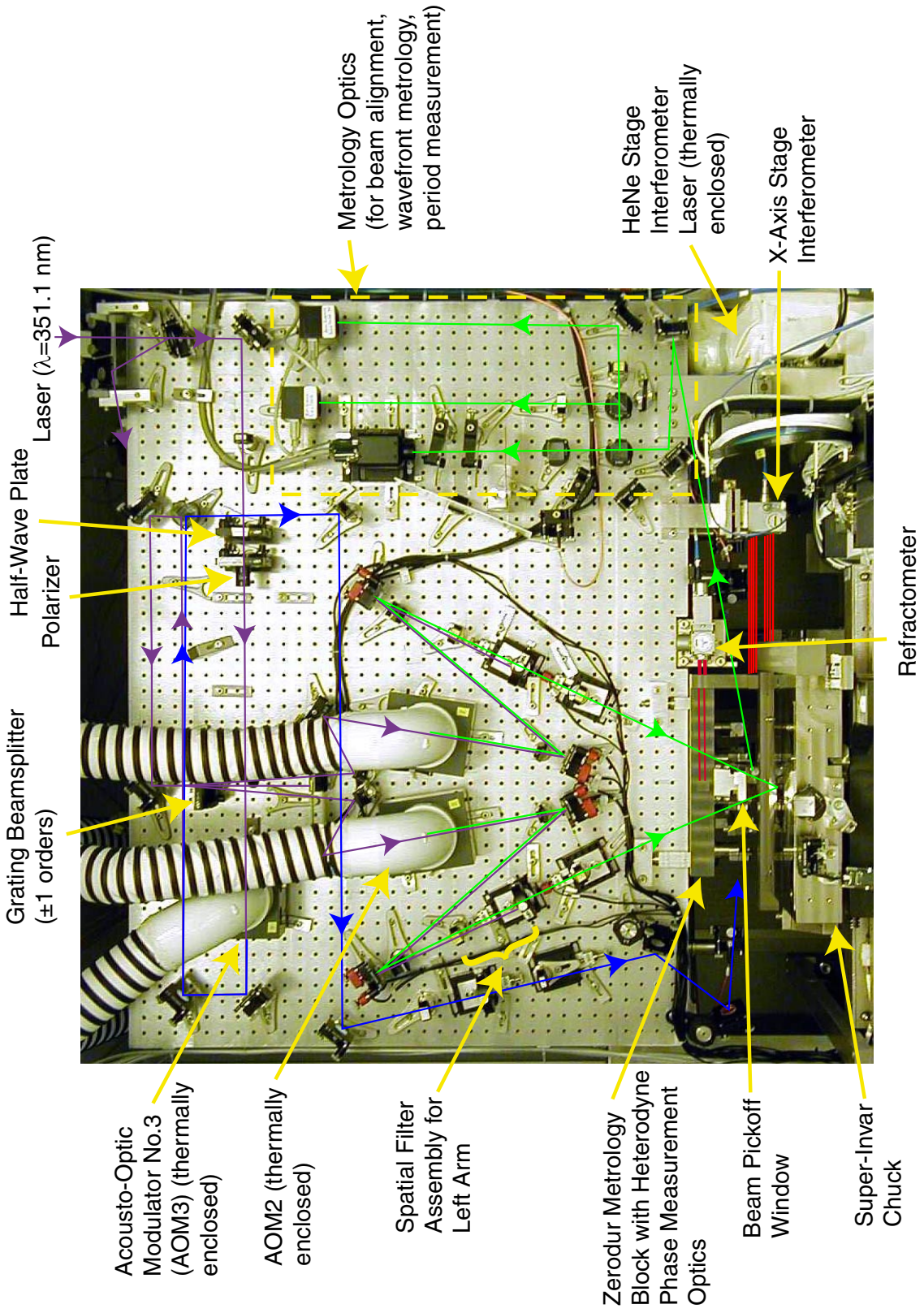

Figure 1-13: SBIL lithography and metrology optics.

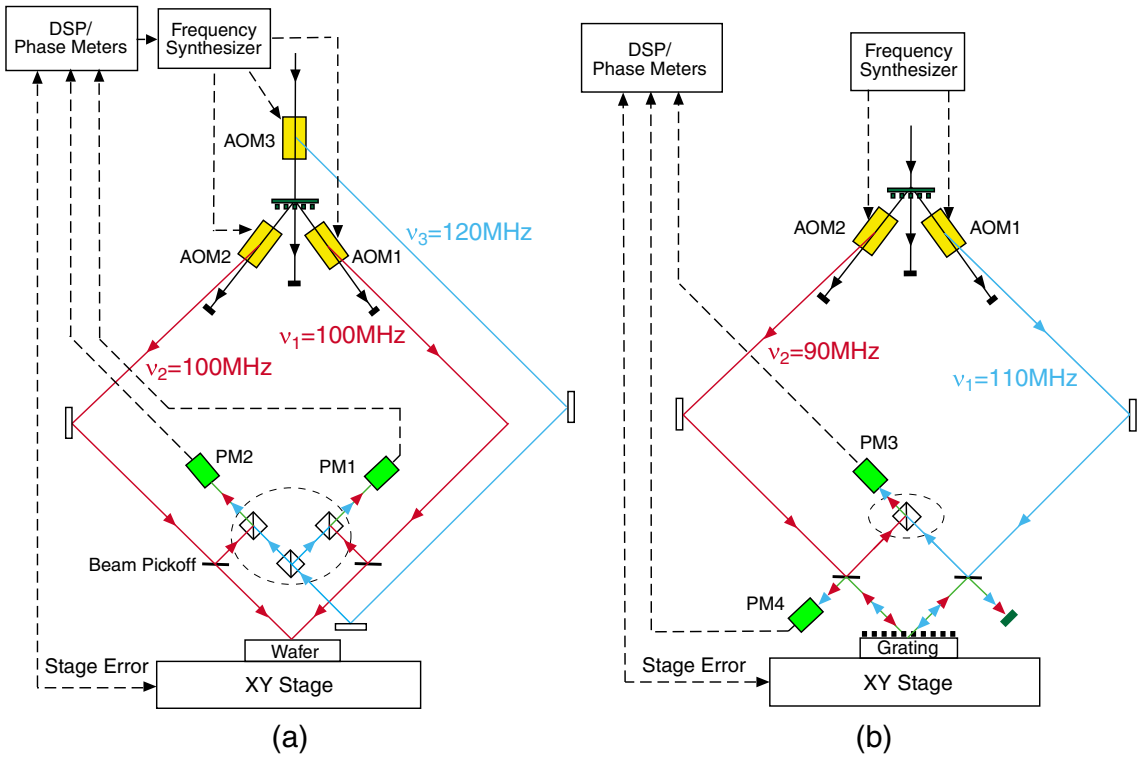

Figure 1-14: SBIL lithography and grating reading modes. Schematic only. (a) Lithography mode. By setting the frequencies to the acousto-optic modulators (AOM) and combining the appropriate diffracted beams, one generates two heterodyne signals at phase meters (PM) 1 and 2. A digital signal processor (DSP) then compares the signals and drives AOM2 to keep the phase difference between the two arms constant. (b) Grating reading mode. A grating is used in the so-called Littrow condition, where the 0-order reflected beam from one arm coincides with the -1-order back-diffracted beam from the other arm. Two heterodyne signals, PM3 and PM4, differ in the sense that PM4 contains the spot-averaged phase information from the grating.

heterodyne signals, PM3 and PM4, differ in the sense that PM4 contains the spot-averaged phase information from the grating. Self-calibration procedures, similar to ones proposed in Reference [55], can be implemented to correct systematic errors and translate repeatability into accuracy. Measurement in this mode also allows one to assess the repeatability of the stage displacement interferometer.

The four separate beamsplitters shown in Figure 1-14, circled in dotted lines, are in reality one monolithic piece (Fig. 1-15), designed to reduce the optics packaging and rid unnecessary air paths. The fact that both the stage and the fringe locking employ heterodyne interferometry allows the two to be effectively integrated into one control system, the details of which is described by another Ph.D. thesis [48]. Figure 1-16 shows a schematic of the SBIL control system architecture.

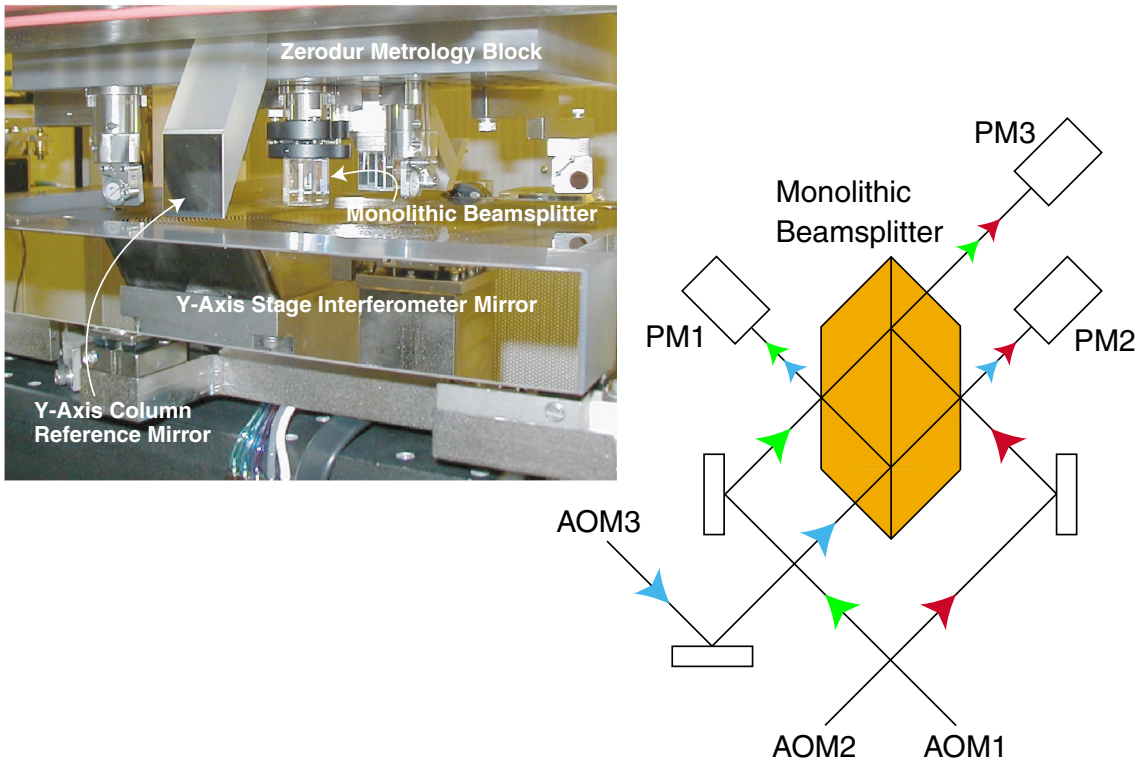

Figure 1-15: The monolithic beamsplitter design. Schematic only. Beam path bending due to refraction is not shown.

Substrate and metrology frame

Substrate and metrology frame errors refer to those from substrate distortion and the inability of the metrology reference surfaces, such as the stage interferometer mirrors and the column reference mirrors, to accurately measure the displacement between the interference fringes and the substrate.

Thermal and mechanical considerations led to the design and installation of a rigid Zerodur metrology block, to which the x- and y-axis column reference mirrors (also made of Zerodur), and all critical phase measurement optics are attached (Fig. 1-17). Critical optical mounts, both on the metrology block and on the stage, have all been machined out of Invar, a low CTE material. A Super-Invar vacuum chuck, lapped to a flatness of 25 μin, or less than 1 μm, can hold substrates with diameters of 100 mm, 150 mm, 200 mm and 300 mm. The design of the metrology block as well as the vacuum chuck are also described in Reference [48].

Period control and beam alignment

Eq. (1.6) shows that the period of the grating image (p) will change if the wavelength of the laser (λ) or the angle of interference (θ) varies. The goal of SBIL period control is to set, stabilize and measure the grating image period at the part-per-

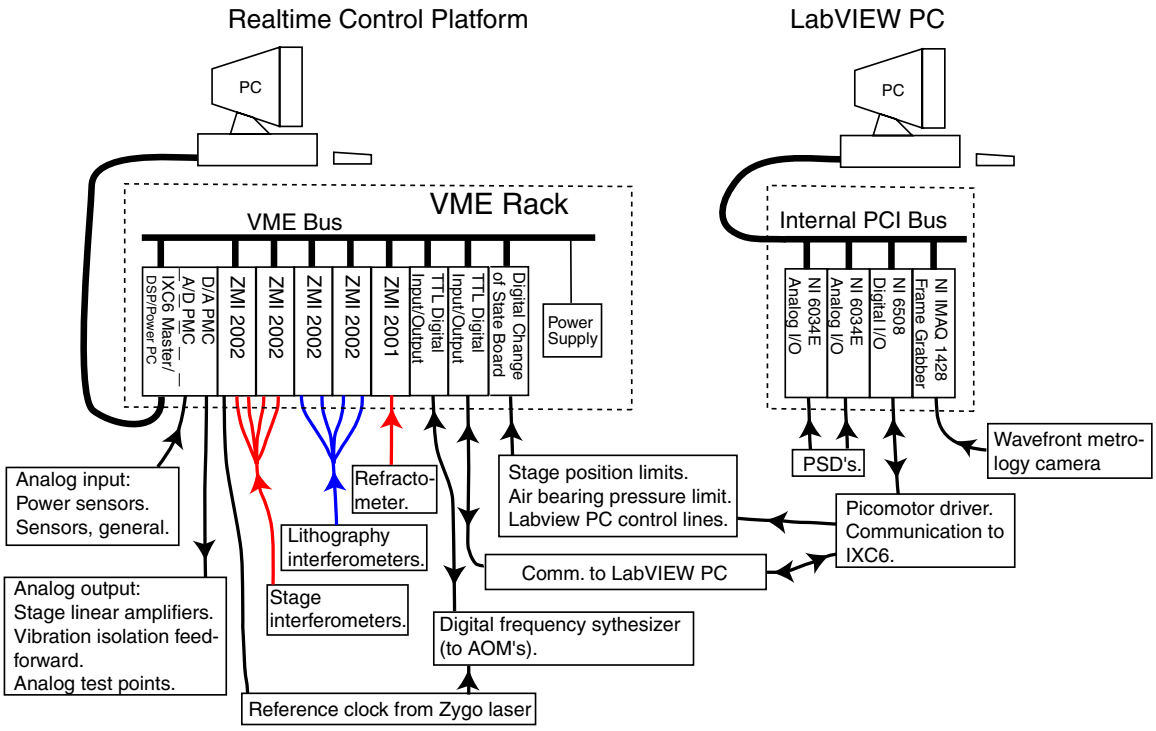

Figure 1-16: SBIL system architecture. The use of two separate platforms allows parallel software and hardware development.

million (ppm) level, i.e., period control with picometer precision. If achieved, as I will show later on, nonlinearity in the resist grating due to any period measurement error can be limited to subnanometers. As mentioned earlier, the application of a grating beamsplitter theoretically alleviates the restriction on beam stability. The stabilizing effect, however, must be experimentally verified. For 1 nm of accumulated phase error across a 1 mm image radius, one must measure the grating period to around 1 ppm. Reference [47] documents a simple interferometric technique that I used to measure the grating image period *in-situ* and with high accuracy.

Beam angle misalignment introduces additional phase errors due to substrate unflatness, and position misalignment, if too large, ruins the fringe contrast. Therefore, both must be controlled. Beam alignment is also critical for SBIL wavefront metrology, fringe period measurement, and grating reading mode. To achieve beam angle and position alignment on the μrad and μm level, respectively, an automated beam alignment system has been built, based on the so-called iterative beam alignment principle [56]. Repeatability experiments show that the system fulfills the alignment requirements for ppm-level period setting.

This thesis will document all aspects of the beam alignment system, as well as the

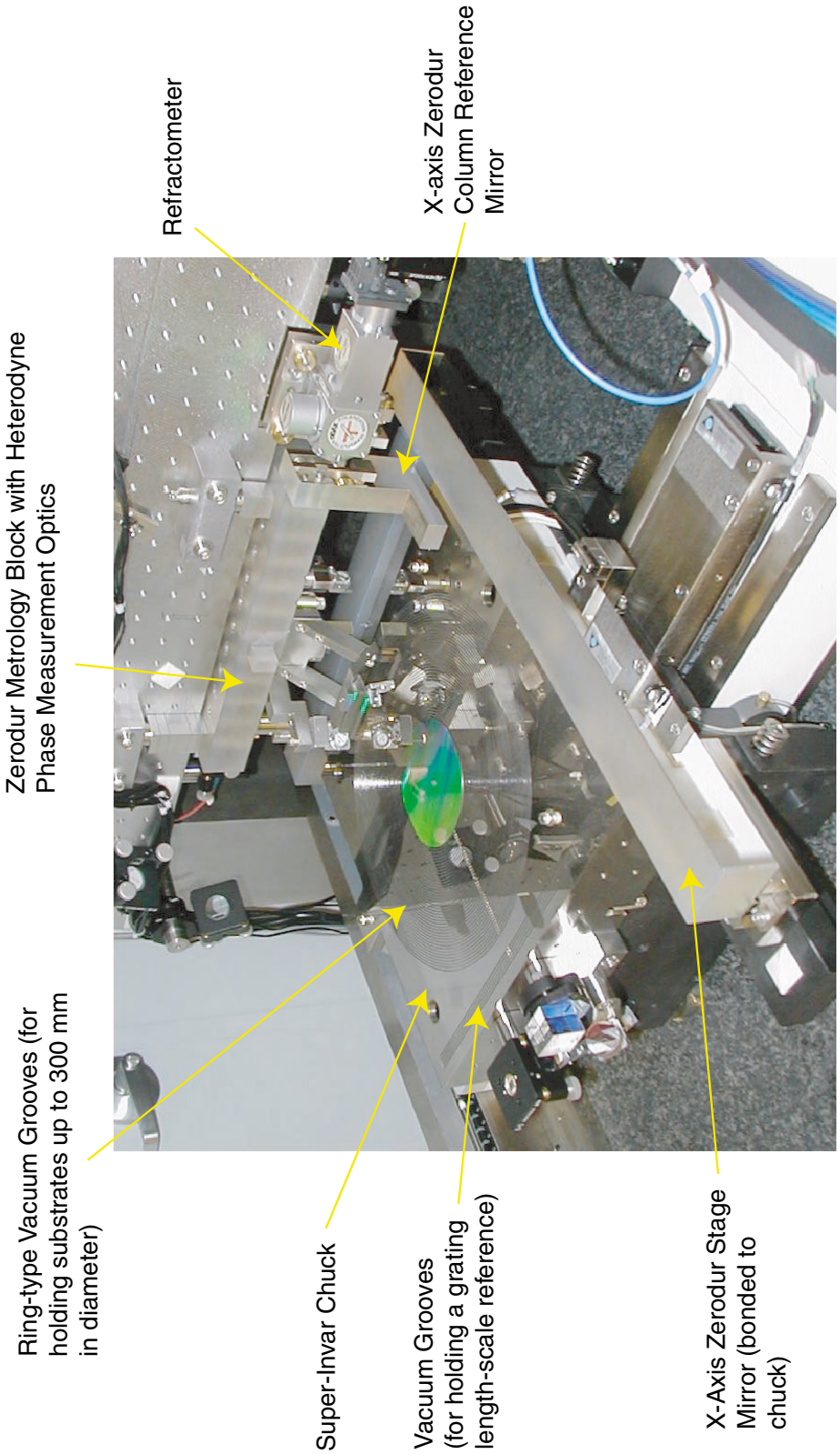

Figure 1-17: Photo showing the Super-Invar chuck and the Zerodur metrology block, which together define the heart of the SBIL substrate and metrology frame. A 100 mm wafer with gratings can be seen on the chuck.

period measurement system, in Chapters 3 and 4, respectively. Most importantly, Section 4.5 will argue in detail that as a result of overlapping scans, no accumulating nonlinear phase error results in the resist grating because of a ppm-level period measurement error. In fact, it will show that the resist grating period can be controlled at the picometer level by stepping the stage by an appropriate amount without changing the grating image period.

Wavefront metrology

During SBIL, grating phase distortions along the scan direction can be somewhat averaged out. Overlap of adjacent scans provides even further averaging. Despite the averaging, excess phase distortions in the grating image is undesirable as it limits the system throughput and sacrifices the image contrast, thus must be minimized.

An experimental procedure to map and reduce the phase nonlinearities across a grating image via phase shifting interferometry (PSI) is developed in detail in Chapter 5. The procedure essentially compares the phase of the grating image to that of a linear metrology grating. The difference between the two, i.e., the so-called moiré phase, is obtained through PSI. The small beams used in SBIL are intrinsically Gaussian in nature. Lowest possible phase distortion is achieved when Gaussian beams interfere at their waists. I build a Gaussian beam interference model specifically for the description of the SBIL wavefront metrology system. By simulating moiré patterns produced by the "beating" of the grating image against an ideal linear grating, I am able to determine how various system setup parameters influence the phase nonlinearities in the image. Phase measurement repeatability is demonstrated at eight thousandth of a period, or 3.2 nm, three-sigma. Due to the lack of a good linear metrology grating, the minimum grating image nonlinearity achieved thus far is 12 nm across a $1/e^2$ beam diameter of 1.92 mm.

Section 5.6 discusses quantitatively the printed phase error in the resist grating. Despite the image nonlinearities, it is shown that subnanometer peak-to-valley printed errors can be achieved by overlapping scans.

1.4.5 Patterned gratings

At the writing of this document, the SBIL prototype is fully functional. I have successfully patterned cosmetically flawless gratings of 400 nm period over substrates of a variety of sizes—100 mm, 150 mm and 300 mm. For the particular recipe that I used (Appendix A), the 300 mm-diam. wafers take just over one hour to produce. By permitting adjustments of the stage scan speed, overlapping step size, and beam power, SBIL allows good dose control.

Figure 1-18 is a scanning electron micrograph (SEM) of the cross section of a

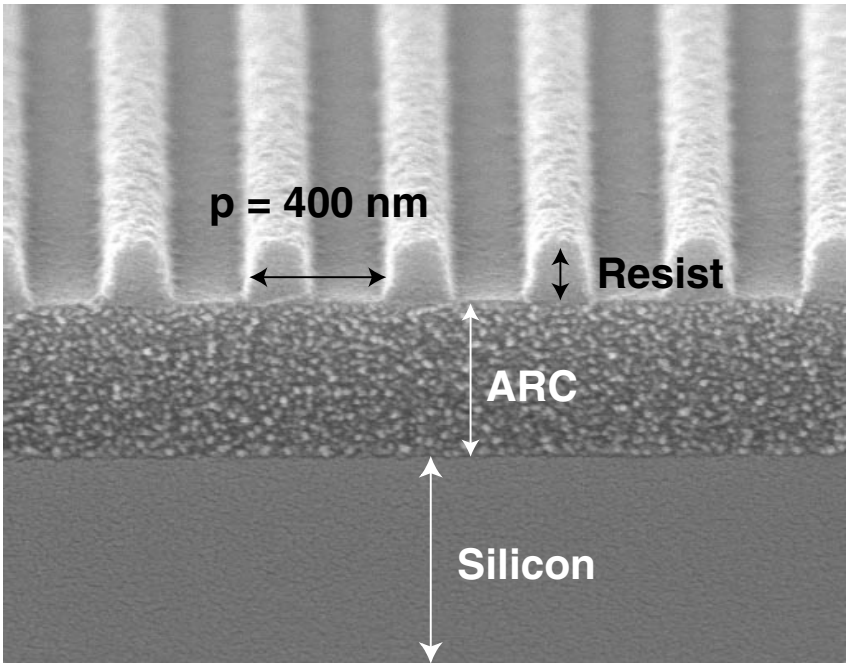

Figure 1-18: A scanning electron micrograph (SEM) of the cross section of a grating written by SBIL. ARC is the acronym for anti-reflection coating. The resist, ARC and developer used are Sumitomo PFI-34 i-line resist, Brewer ARC-XL and Arch Chemicals OPD 262 positive resist developer, respectively.

grating written by SBIL. Modeling results in this thesis will show that given the current performance of period control and wavefront metrology, any phase nonlinearities in the resist grating due to period control inaccuracies or wavefront distortions are subnanometer in amplitude, thanks to the efficient averaging by step-and-scanning a small Gaussian image, which reduces the nonlinearities dramatically.

All modeling is done by assuming perfect stage scan and fringe locking. In reality of course, nothing is perfect. Phase jitters due to nonideal fringe locking and stage motion do exist, although only low-frequency jitters print through to the resist, thanks again to averaging. Reference [48] reports the initial findings in trying to read the phase of a written grating.

To appreciate the full scope and intricacy of the SBIL project, an interested reader should study this thesis, which centers on the optical aspect of the project, in conjunction with Reference [48], which focuses on the mechanical aspect.

Chapter 2

SBIL optics

The current SBIL optical layout is for patterning 400 nm period gratings. Throughout the thesis, I will use the phrase "grating image" or "image grating" interchangeably to describe the millimeter-sized patch of standing waves made by interfering two narrow Gaussian laser beams.

The SBIL lithography laser is an argon-ion laser[1], emitting in ultra-violet (UV) at a wavelength of $\lambda = 351.1$ nm with a maximum continuous-wave (CW) output of over 1 W. The output power is adjustable by changing the tube current. For my experiments, I normally use a power setting of 300 mW. The laser, together with its power supply and heat exchanger, are located remotely so as to remove a major source of thermal and mechanical disturbance. The beam is intrinsically Gaussian in nature and propagates some 10 m to arrive at the SBIL system. On arrival, a small portion of it is sampled by a wedged pickoff window and redirected to the backside of the vertical optical bench (Fig. 1-11), where a beam steering system is used to stabilize the beam in both position and angle.

The optical design of the SBIL lithography interferometer must incorporate means to split and polarize the beam. The beam power in each arm must be separately adjustable. Appropriate spatial filters must be designed to clean the beams of any non-Gaussian irradiance (i.e., intensity) variations before they interfere. To minimize nonlinear phase distortions in the interference image, collimating lenses are used to condition the spatially filtered Gaussian beams so that the interference occurs at their waists, where the wavefronts are the most planar.

In this chapter, I describe the design and layout of the SBIL lithography optics, as well as those used for carrying out beam alignment, fringe period measurement and wavefront metrology.

[1]Innova Sabre argon-ion laser by Coherent, Inc.

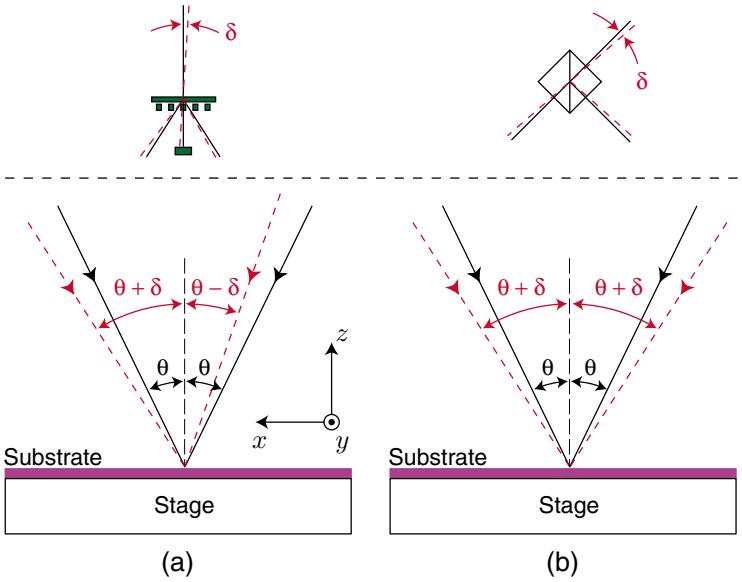

Figure 2-1: (a) For a grating beamsplitter, beam angular variations along the x-direction are antisymmetrically correlated. The figure is schematic only. (b) For a cube beamsplitter, variations are symmetrically correlated.

2.1 Introduction

2.1.1 Grating beamsplitter

To incur a phase error of 1 nm across a 1 mm-radius beam spot, SBIL must stabilize the image grating period to 1 nm/1 mm, or 1 part per million (ppm). The goal is accomplished by using a grating beamsplitter to split the laser and form the lithography interferometer. While the beam steering system performs admirably to stabilize the pointing of the laser [49], residual beam angle instabilities do exist. The measured angular noise is $\delta = 11.4$ μrad, three-sigma (Sec. 3.5.1).

Appendix B discusses period variations due to angle shifts and why using a grating to split the laser is better than using a cube beamsplitter. In essence, the use of a grating allows the angular variations in the interference arms to be "antisymmetrically" correlated, that is, if the angle shift in one arm is $+\delta$, it is $-\delta$ in the other. This provides greater tolerance over angle shift-induced period variations. Figure 2-1 illustrates the antisymmetry schematically. According to Eq. (B.2), with a grating beamsplitter, the period varies by approximately 65 parts per trillion for $\delta = 11.4$ μrad, much smaller than the 1 ppm SBIL period control requirement. On the other hand, if a cube were used, for the same δ, the period would vary by as much as 23 ppm for a nominal fringe period of 400 nm [Eq. (B.3)], and worse, the variation is also dependent upon the sign of the angular noise. Experimental proof of the antisymmetry is provided in Section 3.4. Along the x-axis, which is the direction

perpendicular to the image grating, the angular variations in the two arms are shown to be antisymmetrically correlated to the sub-μrad level. Prior work has also argued that the use of a grating provides a partially achromatic setup where small changes in the lithography laser's wavelength can be accommodated. Furthermore, the spatial phase of the interference fringes are also preserved and the centroids of the beam spots always overlap [52].

2.1.2 Optics

Interference lithography occurs with maximum fringe contrast when the beams are s-polarized (or TE-polarized), i.e., when their polarization vectors lie parallel to the substrate. If the beams were p-polarized (or TM-polarized), the electric field components perpendicular to the substrate would result in a DC intensity background. This would diminish the overall fringe contrast. S-polarization of the UV laser is achieved with a polarizer[2] (Fig. 1-13), whose polarization axis is set parallel to the substrate.

The SBIL laser is itself linearly polarized. A half-wave ($\lambda/2$) plate is inserted in front of the polarizer, such that the power of the s-polarized beam exiting the polarizer can be controlled (Fig. 1-13). The physics of the half-wave plate is described in detail elsewhere [57]. Briefly, the plate is made of birefringent material, which passes light at different speed depending on whether the light is aligned with respect to the so-called optic axis (also known as the fast axis) of the birefringent crystal, or perpendicular to it. By design, the half-wave plate produces a 180° phase lag between the component of the incident light that is parallel to the optic axis and that which is perpendicular. Assuming the UV laser is initially polarized in a direction that makes an angle θ with respect to the optic axis, in passing through the $\lambda/2$-plate, the laser sees its polarization rotated through 2θ from the original polarization direction. To vary the power of the beam after the polarizer, one needs only to rotate the half-wave plate, causing the original polarization state of the laser to rotate with respect to the axis of the polarizer. In particular, if the polarization is rotated and aligned with respect to the polarizer's axis, then the power in the original laser is completely transferred to the final s-polarized beam.

As mentioned earlier in Section 1.4.4, three acousto-optic modulators (AOMs) are used in the so-called lithography mode to generate the two writing beams and a third beam, which when mixed with the former two, produces two signals required for heterodyne fringe locking. In addition to enabling high-bandwidth stabilization of the interference fringes, the two AOMs used in generating the writing beams [AOM1 and 2 in Fig. 1-14(a)] offer a further advantage. To obtain good fringe contrast, beam

[2]Glan-laser calcite polarizer by Newport Corporation.

powers in the lithography arms must be balanced. By changing the amplitude of the radio-frequency (RF) signal driving either AOM, one can regulate the power in the first-order diffracted beam, thus controlling the power incident upon the substrate. The maximum power is determined by the input laser power and the diffraction efficiency of the AOM, while the minimum is simply zero, obtained by nulling the RF amplitude.

Two relaying lenses, one located near the UV laser and the other on the vertical optical bench, help to ensure that the beam does not expand significantly having traversed a distance of approximately 10 m. Each lithography arm has a spatial filter assembly, constituting a focusing (convex) lens and a pinhole (Fig. 1-13). Spatial filtering is a well-known concept [23]. The pinhole, situated at the lens's focal plane, i.e., the Fourier transform plane, blocks undesired high spatial frequency component. This low-pass action cleans the beam of any high frequency contaminants that may be due to unwanted scattering off particulates in the air and imperfections in prior optics. Before the filtered beams finally interfere with each other, two more lenses collimate them so that the collimated Gaussian beam waists are located at the substrate. Since the wavefront at the waist of a Gaussian beam is planar, this helps to ensure the lowest possible phase nonlinearities in the grating image.

The setup also employs a complex network of beamsplitters and mirrors to divide and redirect the beams as necessary.

Because the lenses alone determine the profiles of the propagating Gaussian beams, their selections and placements guide the design of the SBIL optical layout. Section 2.1.3 briefly describes the theory behind the modification of a Gaussian beam by a thin lens. Section 2.2 discusses the SBIL optical design and layout.

2.1.3 Thin lens equation for Gaussian beams

The paraxial Gaussian beam model [58], also known as the scalar Gaussian beam model (Sec. 5.2.2), is used to describe the propagation of the SBIL laser beam. Four parameters are of interest: the wavelength of the laser λ, the $1/e^2$ beam waist diameter d, the full beam divergence angle θ, and the so-called Rayleigh range b (Fig. 2-2). Knowing any two of the four quantities, one can completely characterize the beam. Reference [57] provides two relations linking the four parameters,

$$d = \frac{4\lambda}{\pi\theta} \ , \tag{2.1}$$

$$b = \frac{d}{\theta} \ . \tag{2.2}$$

The Rayleigh range, also known as the confocal parameter, essentially defines the extent of the beam waist region. The curvature radius (R) is a measure of the phase

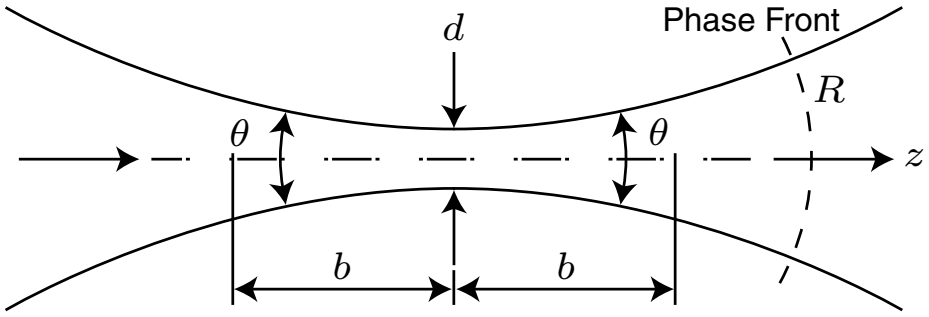

Figure 2-2: Various physical parameters defining a Gaussian beam. The beam is propagating along the z direction. The beam irradiance varies along z and achieves a minimum at the beam waist.

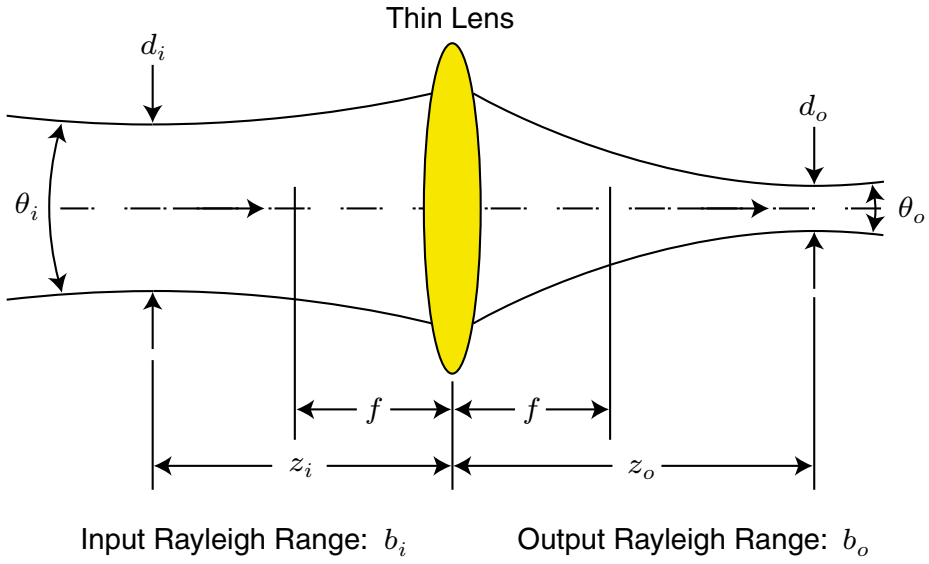

Figure 2-3: Transformation of a Gaussian beam by a thin lens. Beam size is exaggerated.

front curvature intrinsic to the Gaussian beam, which takes on a minimum at the Rayleigh range ($z = b$) and becomes infinite at the beam waist ($z = 0$) and at $z = \infty$. An infinite R implies that the wavefront is strictly planar at the Gaussian beam waist. This is the reason why one wants to interfere the beams at their waists, so as to minimize the nonlinear distortions in the resulting grating image.

Reference [57] derives in detail the transformation of a Gaussian beam by a thin lens. Figure 2-3 shows the geometry. The focal length of the lens is f. The subscripts "i" and "o" denote the input and output, respectively. For better illustration, the beam size has been grossly exaggerated. Starting with the Newtonian form of the thin lens equation from ray optics, the derivation also takes into account the effects of diffraction. In the end, four equations relate the output beam characteristics to

the input:

$$z_o = f + \alpha^2 \, (z_i - f) \ , \tag{2.3}$$

$$d_o = \alpha \, d_i \ , \tag{2.4}$$

$$\theta_o = \frac{\theta_i}{\alpha} \ , \tag{2.5}$$

$$b_o = \alpha^2 \, b_i \ , \tag{2.6}$$

where the parameter α is defined as

$$\alpha = \frac{|f|}{\sqrt{(z_i - f)^2 + b_i^2}} \ . \tag{2.7}$$

The absolute value sign signifies that the equation applies equivalently well to any lens with a negative focal length, e.g., a concave lens.

2.2 Optical design and layout

I am primarily interested in the design and layout of the lithography interferometer optics introduced in Section 2.1, and those used for carrying out beam alignment, fringe period measurement and wavefront metrology. Phase measurement optics, which are attached to a Zerodur metrology block (Figs. 1-13 and 1-17), are a part of the heterodyne fringe locking system. Their design and layout are not covered here. See Reference [48] instead.

2.2.1 Lithography interferometer

The SBIL lithography interferometer is situated on a vertical optical bench (Figs. 1-10 and 1-11). The bench is machined from a solid slab of stainless steel, 0.75 in, or 19 mm thick. Experiments indicate that such construction is superior to a commercial breadboard, which flexes too easily as the temperature changes, thus introducing unwanted drifts to the attached optics.

The interferometer is currently set up to write gratings with a period of approximately 400 nm.

Since lenses are the only optical elements used to modify the beam profiles in SBIL, their selections and placements guide the rest of the optical design. Figure 2-4 shows the final lens layout. For better illustration, the light path has been unfolded so that the laser reaches the substrate in a straight line. The incident angle at the substrate depends on the desired fringe period. For a period of 400 nm, the angle is 26°. The two relaying lenses have the same focal length, $f = 5.41$ m at $\lambda = 351.1$ nm. The focusing lens in the spatial filter has an at-wavelength focal length of $f = 108.2$ mm, and so does the collimating lens after the spatial filter. The distance between the substrate and the collimating lens is approximately 328 mm.

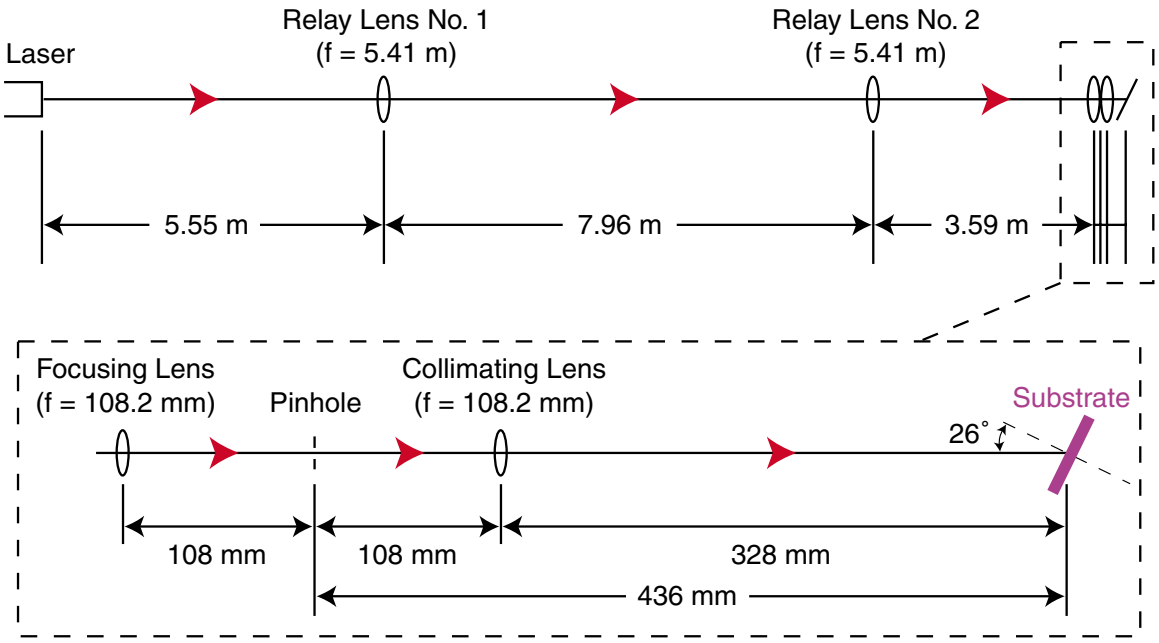

Figure 2-4: Lens layout. For better illustration, the light path has been unfolded to a straight line. To write 400 nm period gratings, the beam must be incident upon the substrate at an angle of 26°.

At $\lambda = 351.1$ nm, the UV laser has a measured initial divergence angle of 0.31 mrad and a measured initial beam waist diameter (at $1/e^2$ points) of 1.6 mm, based on specifications from Coherent, Inc. [59] On the other hand, given the Gaussian beam assumption and the measured divergence angle, Eq. (2.1) predicts an initial beam waist of 1.44 mm in diameter, which is close to but different from the measured value of 1.6 mm. Ignoring this slight inconsistency, I adopt both measured values to describe the beam's initial characteristics. The reader can verify that an alternate model, e.g., one with an initial angle of 0.31 mrad and a calculated waist diameter of 1.44 mm, yield similar modeling results.

Given the lens layout and Eqs. (2.2)–(2.7), Tables 2.1 through 2.4 list the modeled input and output beam parameters at all four lenses. At the spatial-filter pinholes, the focused $1/e^2$ beam waist diameter is 38 μm. By design, the waist of the collimated Gaussian beam is located at the substrate. Its geometrical elongation due to the laser's oblique incidence notwithstanding, the waist at the substrate has a radius of approximately 0.7 mm. A wavefront metrology system has been developed to ensure that the waist can be precisely positioned so as to generate a grating image that has the least amount of nonlinear phase, a topic covered in detail in Chapter 5. Modeled results from this section will provide numerical values to parameters that will be used to simulate the image phase nonlinearities.

Relay Lens No.1 ($f = 5.41$ m)	
Input	Output
$d_i = 1.6$ mm	$d_o = 1.676$ mm
$\theta_i = 0.31$ mrad	$\theta_o = 0.296$ mrad
$z_i = 5.55$ m	$z_o = 5.564$ m
$b_i = 5.161$ m	$b_o = 5.667$ m
$\lambda = 351.1$ nm, $\alpha = 1.048$	

Table 2.1: Beam modification by Relay Lens No.1.

Relay Lens No.2 ($f = 5.41$ m)	
Input	Output
$d_i = 1.676$ mm	$d_o = 1.413$ mm
$\theta_i = 0.296$ mrad	$\theta_o = 0.351$ mrad
$z_i = 2.396$ m	$z_o = 3.269$ m
$b_i = 5.667$ m	$b_o = 4.026$ m
$\alpha = 0.843$	

Table 2.2: Beam modification by Relay Lens No.2.

Focusing lens ($f = 108.2$ mm)	
Input	Output
$d_i = 1.413$ mm	$\boldsymbol{d_o = 37.9\ \mu m}$
$\theta_i = 0.351$ mrad	$\theta_o = 13.079$ mrad
$z_i = 0.321$ m	$z_o = 108.35$ mm
$b_i = 4.026$ m	$b_o = 2.90$ mm
$\alpha = 0.0268$	

Table 2.3: Beam modification by the focusing lens in the spatial filter. The beam waist diameter at the pinhole is 37.9 μm.

Collimating lens ($f = 108.2$ mm)	
Input	Output
$d_i = 37.9\ \mu$m	$\boldsymbol{d_o = 1.413}$ **mm**
$\theta_i = 13.079$ mrad	$\theta_o = 0.351$ mrad
$z_i = 108.36$ m	$z_o = 327.64$ mm
$b_i = 2.90$ mm	$b_o = 4.026$ m
$\alpha = 37.260$	

Table 2.4: Beam modification by the collimating lens. Ignoring the geometrical elongation of the beam due to the laser's oblique incidence, the $1/e^2$ spot radius at the substrate is approximately 0.71 mm.

The design of the lithography interferometer is carried out with Pro/Engineer (ProE), a computer aided design (CAD) program. Figures 2-5 through 2-8 present some sample drawings. During the actual layout of the optics, one can refer to these drawings for precise locations of the optics.

Figure 2-5 shows the lithography interferometer used in the so-called beamsplitter mode. The setup is almost identical to the lithography mode. The difference is that instead of having the beams interfere on a resist-covered substrate, they are to propagate through a beamsplitter mounted on the air-bearing stage and be steered towards the SBIL beam alignment and wavefront metrology optics. See Figure 2-7 for an illustration of the beam path. Similarly, Figure 2-6 shows the lithography interferometer used in the so-called grating mode. Figure 2-8 illustrates the beam path. Both the laser noise eater and the lens prior to the CCD camera are unused currently. The noise eater is an electro-optic feedback device designed to reduce laser amplitude variations. The lens helps to enlarge the beams and may be used to provide conjugate imaging if necessary, during wavefront metrology.

2.2.2 Spatial filtering

Both spatial-filter pinholes are mounted in XY-adjustable pinhole mounts[3], which provide movements in the transverse direction. Each mount is itself attached to a single-axis translation stage that provides the longitudinal adjustment (Fig. 2-6).

The focusing lens simply performs a spatial Fourier transform on the incoming beam [58]. If the pinhole has a radius a, any variation in the irradiance of the original beam with a spatial frequency greater than

$$\omega_{\mathrm{sp}} = \frac{ka}{f} \tag{2.8}$$

is eliminated due to the pinhole's blockage, where $k = 2\pi/\lambda$ is the wave number and f is the focal length of the lens. In other words, any variation with a spatial period of less than

$$p_{\mathrm{sp}} = \frac{2\pi}{\omega_{\mathrm{sp}}} = \frac{\lambda f}{a} \tag{2.9}$$

is eliminated. If the pinhole diameter is large compared to its thickness, the fractional beam power that propagates through the pinhole is

$$F = \frac{\displaystyle\int_0^a \exp\left[-\frac{2r^2}{w_0^2}\right] r\,dr}{\displaystyle\int_0^\infty \exp\left[-\frac{2r^2}{w_0^2}\right] r\,dr} = 1 - \exp\left[-\frac{2a^2}{w_0^2}\right] = 1 - \exp\left[-\frac{8a^2}{d^2}\right] \ , \tag{2.10}$$

[3]X-Y lens holders by Melles Griot, Inc.

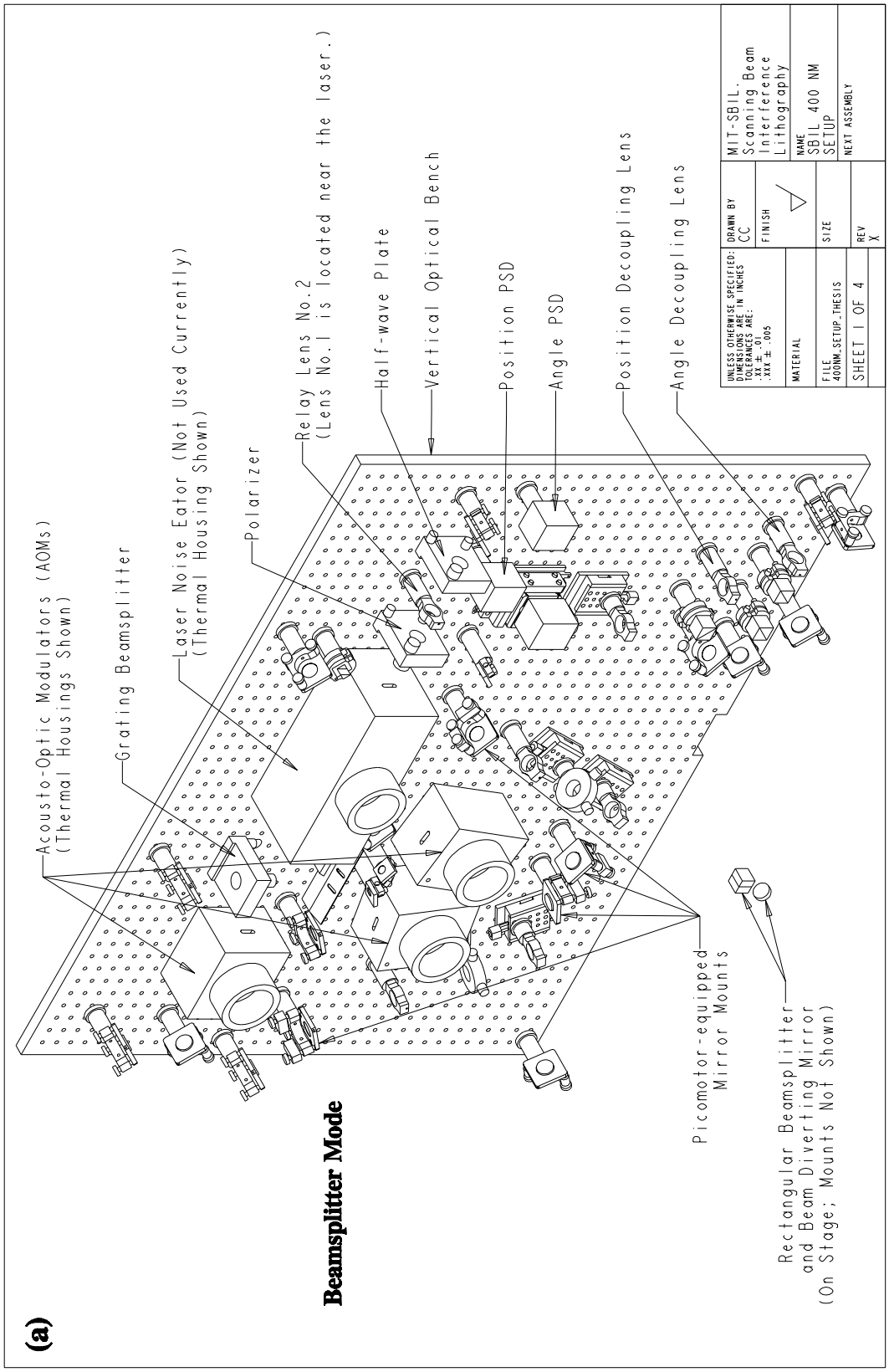

Figure 2-5: Drawing of the SBIL optics layout in the beamsplitter mode.

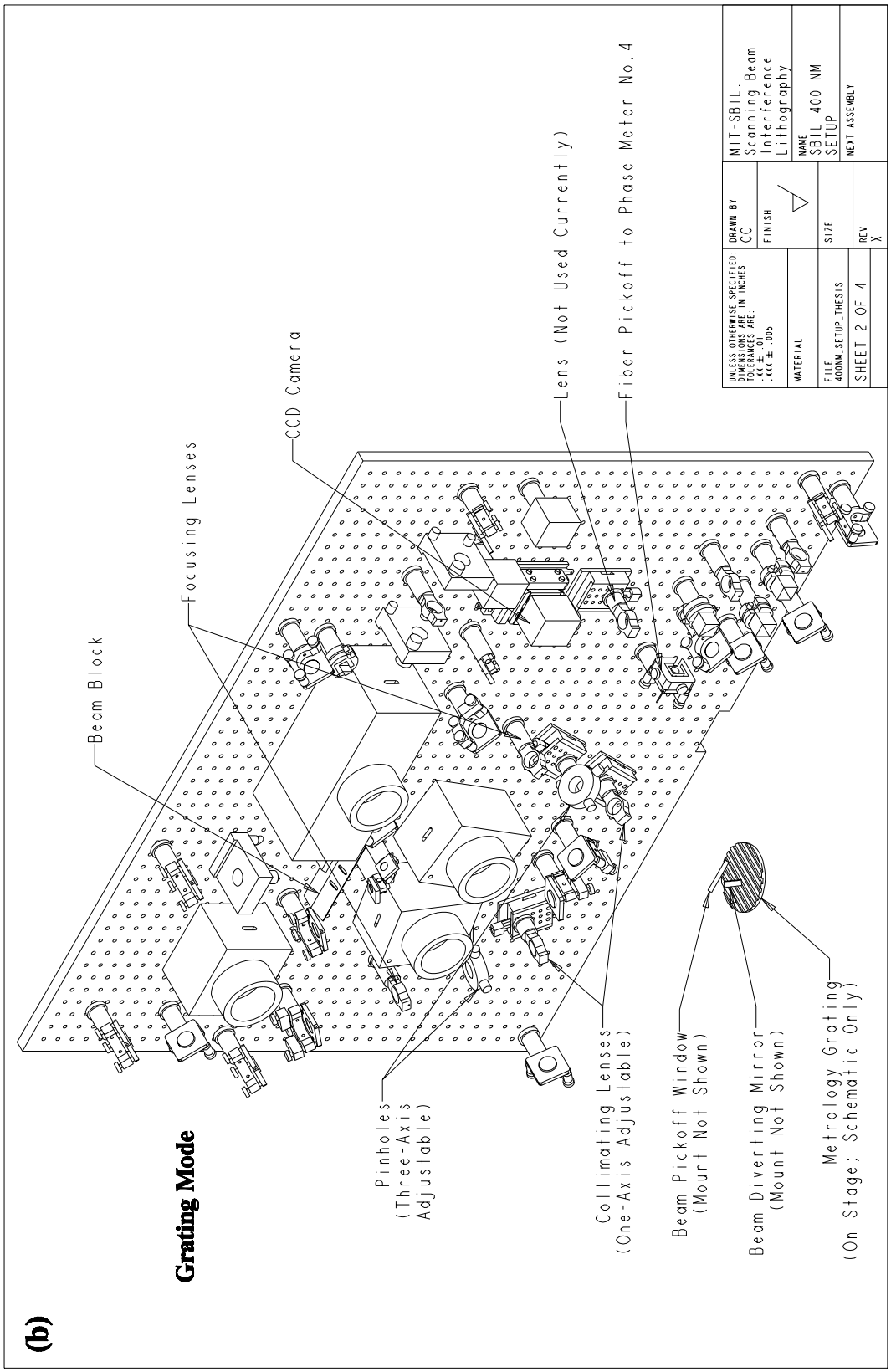

Figure 2-6: Drawing of the SBIL optics layout in the grating mode.

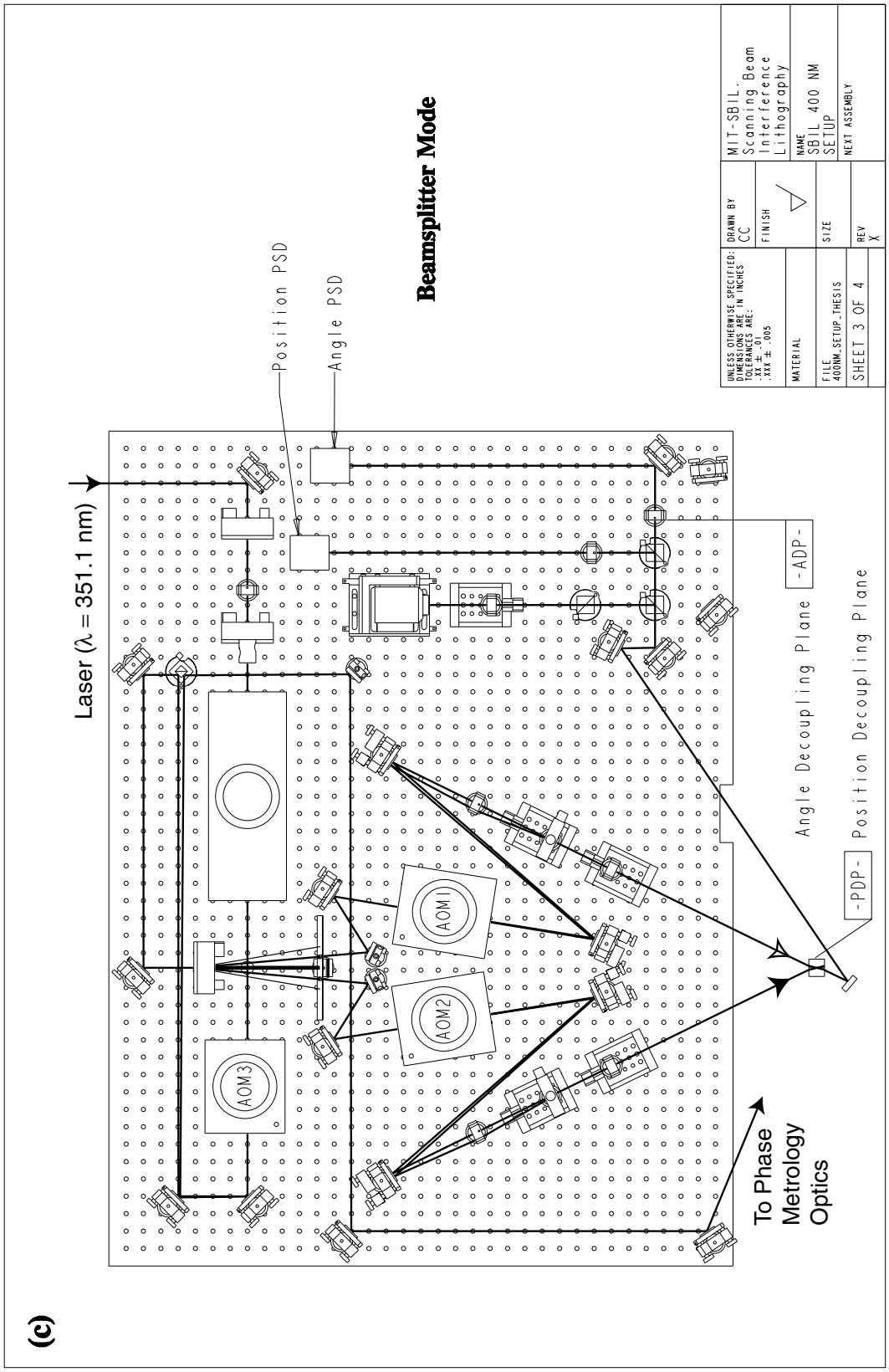

Figure 2-7: Drawing of beam paths in the beamsplitter mode.

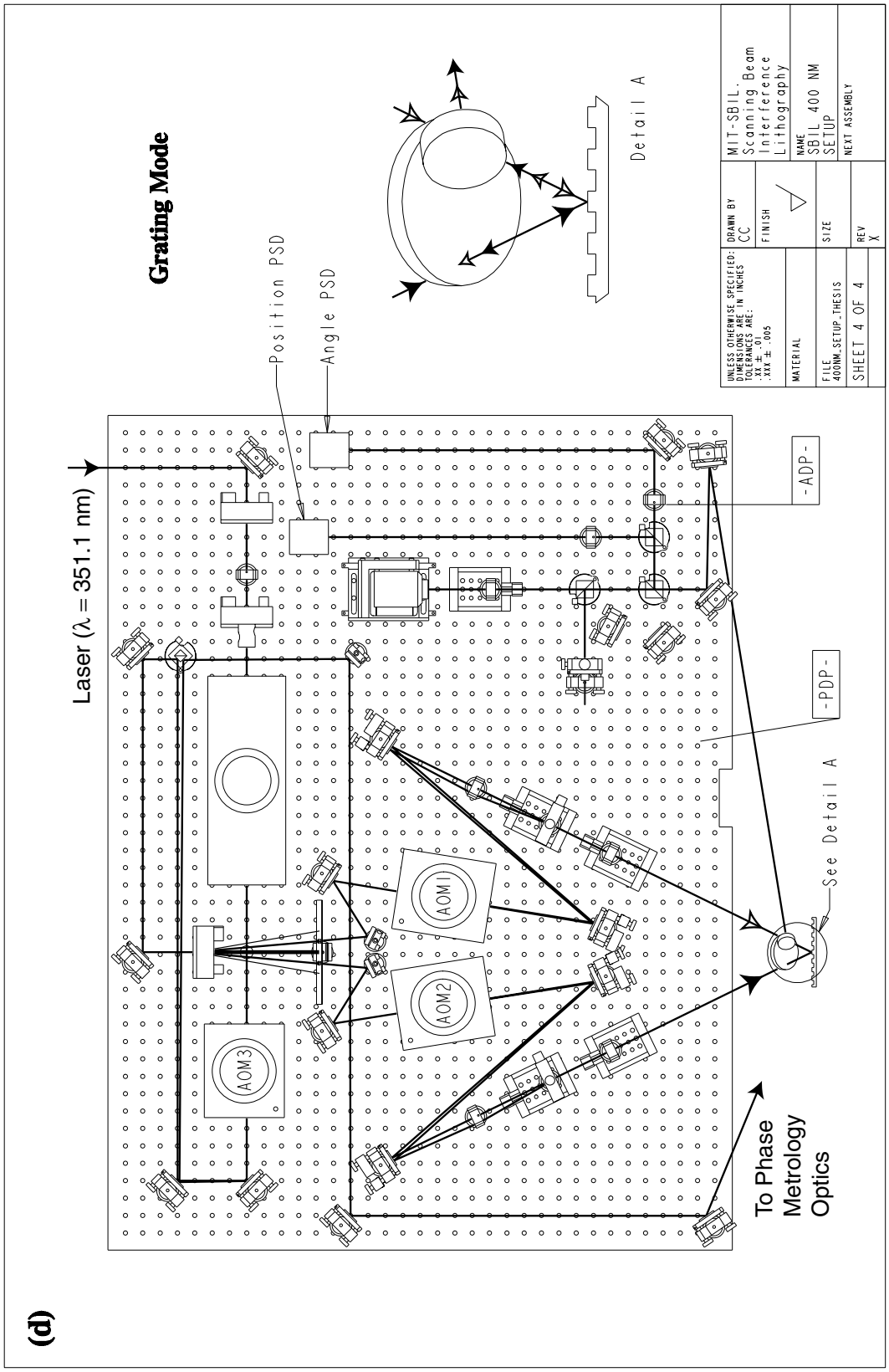

Figure 2-8: Drawing of beam paths in the grating mode.

where w_0 is the beam waist radius (at the $1/e^2$ intensity points) and $d = 2w_0$ is the diameter.

According to Table 2.3, at the pinhole, the focused beam waist diameter is approximately $d = 38$ μm. A common design rule is to set the pinhole aperture to a radius $a = \pi d/4$, which transmits slightly more than 99% of the incident Gaussian beam power, according to Eq. (2.10). Applying the rule yields a desired pinhole diameter of 60 μm. Due to commercial availability, the pinholes used currently[4] have a diameter of 50 μm, smaller than the desired diameter. The pinhole thickness is approximately 12.5 μm. Given $\lambda = 351.1$ nm, $a = 25$ μm and $f = 108.2$ mm, Eq. (2.8) gives $\omega_{\text{sp}} = 4.13$ mm^{-1} and Eq. (2.9) gives $p_{\text{sp}} = 1.52$ mm. In words, the pinhole blocks all spatial frequencies greater than 4.13 mm^{-1}, or equivalently, it stops all spatial periods smaller than 1.52 mm. According to Eq. (2.10), close to 97% of the incident beam power passes through the pinhole.

Beam angular instabilities may result in position instabilities of the focused beam waist. The measured three-sigma angular instability of the laser is $\delta = 11.4$ μrad (Sec. 3.5.1). The beam waist position instability is therefore $\Delta = f\delta$ where f is the focal length of the lens. For $f = 108.2$ mm, one has $\Delta = 1.2$ μm. Such small waist position fluctuations have little impact on the overall power passing through the pinhole if the beam is well centered, which varies by roughly 1% as a result.

2.2.3 Beamsplitter mode

The beamsplitter mode (Figs. 2-5 and 2-7) is engaged prior to the actual lithography. One uses it to align the beams, meaning to overlap the beams in the substrate plane and to equalize the two angles of incidence. One also employs it to measure *in-situ* the period of the grating image. The SBIL beam alignment and period measurement systems are discussed in detail in Chapters 3 and 4, respectively. I focus mainly on the optical aspect here.

Figure 2-7 shows that the laser diffracts after passing through the Acousto-Optic Modulator No.3 (AOM3). An AOM is a device that can generate a bulk acoustic wave across some crystal—fused quartz in the case of SBIL—to diffract and shift the frequency of the incoming light. The theory behind acousto-optic interactions is covered elsewhere [54]. Set by a frequency synthesizer, the RF signal driving AOM3 has a frequency of 120 MHz. The first-order diffracted beam, shifted up in frequency by 120 MHz compared to the zero-order beam, is steered towards the phase measurement optics on a Zerodur metrology block (Fig. 1-13). For clarity of illustration, the CAD drawings do not show the metrology block. The zero-order beam from AOM3

[4]Stainless steel pinholes from Thorlabs, Inc.

diffracts after going through the grating beamsplitter. The grating currently in use has a period of 4 μm. A beam block allows only the $\pm$1-order beams to continue and form the lithography interferometer. AOM1 and 2, driven at 100 MHz, further diffract the right and the left arm, respectively. The first-order diffracted beams, shifted up in frequency by 100 MHz, get collimated before arriving at a rectangular beamsplitter—a fused silica cube made up by two rectangular halves—mounted on the stage. During beam alignment, the spatial-filter pinholes are temporarily removed. Irises are installed just before the first picomotor-equipped[5] mirrors to block the zero-order beams coming out of the AOMs. The beamsplitter's interface is aligned parallel to the x-axis interferometer stage mirror, which is perpendicular to the substrate. Just prior to reaching the beamsplitter, portions of both beams are sent to the phase measurement optics on the metrology block by a beam pickoff window (Fig. 1-13). There, they mix with the 120 MHz diffracted beam from AOM3 and generate two 20 MHz signals required for heterodyne fringe locking at Phase Meter No.1 (PM1) and No.2 (PM2) [Fig. 1-14(a)]. Note that both collimating lenses are mounted on single-axis translation stages that provide adjustments in the longitudinal direction. This degree of freedom is critical for conducting SBIL wavefront metrology, as I will explain in Chapter 5.

During beam alignment, one arm is turned on at a time. Nulling the amplitude of the RF signal driving the corresponding AOM can turn off the unwanted arm. Fringe locking is not possible and is unnecessary during beam alignment. The beam propagates through a maze of mirrors, lenses and beamsplitters, before reaching two duolateral position sensing detectors (PSDs). A PSD reads not only the beam power like a typical photodiode, but also the x and y locations of the beam on the detector by dividing the photocurrent in two resistive layers. The resistivity of the ion-implanted layers is extremely uniform so that the current is inversely proportional to the distance between the incident light spot and the readout electrodes. One of the two PSDs is configured solely for beam angle sensing, and the other for beam position sensing. The theory behind position and angle decoupling is discussed in Section 3.1.1.

Figure 2-5 notes the locations of the position and angle decoupling lenses, with focal lengths of 270.5 mm and 540.9 mm, respectively. Figure 2-7 shows the whereabouts of the position and angle decoupling planes. The optical configuration is such that the angle PSD senses only the beam angle shift in the angle decoupling plane (ADP), and the position PSD sees only the beam position change in the position decoupling plane (PDP). Using the position and angle feedback from the PSDs, the

[5] A picomotor is essentially a piezoelectric actuator that turns a fine-pitched screw.

appropriate picomotor-powered mirrors are actuated to steer the beam and yield desired position and angle alignment. Once one arm is aligned, the other can be aligned in a similar fashion by actuating a different set of picomotors. In the end, the beams overlap in space and have equal angles of incidence. To ensure that the beams overlap not just anywhere in space but at the substrate, a third PSD is used to verify the substrate-plane beam overlap. I describe the SBIL beam alignment system in detail in Chapter 3. Upon the completion of the alignment process, the pinholes are reinserted, which are then adjusted so that the zero-order beams from AOM1 and 2 get blocked but the first-order diffracted beams pass through.

During lithography, accurate period information is required to stitch together adjacent scans. Once the beams are aligned, fringe period measurement can proceed. Both beams are turned on and so is fringe locking. After passing through the rectangular beamsplitter on the stage, the beams propagate coincidently onto the two PSDs. Fringe period is measured by counting the number of oscillations in the power signal from the angle PSD, while the stage, carrying the rectangular beamsplitter, moves a known distance. The SBIL period measurement system is discussed in detail in Chapter 4.

Assuming wavefront metrology has been carried out prior to beam alignment, the system is then ready to perform lithography.

2.2.4 Lithography mode

During lithography, the heterodyne fringe locking is on. AOM1, 2 and 3 are set to frequencies of 100 MHz, 100 MHz, and 120 MHz, respectively. The beams interfere and the interference pattern exposes the photoresist-covered substrate. Stepping over an integer number of fringe periods in the x direction, the stage scans along y (Fig. 1-9). Uniform exposure dose is achieved by overlapping adjacent scans. The light path is the same as shown in Figure 2-7, the only difference being that the beams now fall to the substrate instead.

Since both stage control and fringe locking are based on heterodyne interferometry, which errs if the air index changes, it is critical to have the entire SBIL tool housed in an environmental enclosure (Fig. 1-12).

2.2.5 Grating mode

The grating mode (Figs. 2-6 and 2-8) is for conducting wavefront metrology or reading the phase of a patterned grating. When the mode is used to read a grating, it is also known as the grating reading mode. Figure 2-8 illustrates the light path. Compared to the beamsplitter mode, the most salient difference is the insertion of a grating in place of the beamsplitter.

During wavefront metrology, the inserted grating is a "metrology grating", so named because it has a close-to-ideal linear phase. The grating is used in the so-called Littrow condition (Detail A in Figure 2-8), where after beam alignment, the reflected beam from the left arm coincides with the back-diffracted beam from the right arm. This requires the nominal period of the grating image to match the period of the metrology grating. As in the lithography mode, AOM1, 2 and 3 are set to frequencies of 100 MHz, 100 MHz, and 120 MHz, respectively. Heterodyne fringe locking is on. The goal is to map out the spatial phase nonlinearities in the grating image. Based on the observed distortion values, one can then adjust the positions of the collimating lenses to minimize the distortion. In other words, wavefront metrology is a quantitative way to ensure that the Gaussian beams interfere at their waists, where the phase fronts are planar. A CCD camera captures the intensity pattern due to the interference of the reflected and back-diffracted beams. Phase shifting interferometry (PSI) is performed to extract the nonlinear phase distortion map out of a sequence of phase-shifted intensity patterns. Phase shifting is achieved by stepping the frequency of AOM2. I describe the SBIL wavefront metrology system in detail in Chapter 5.

In the grating reading mode, the lithography interferometer is configured to read the phase of an existing grating through a heterodyne scheme, as mentioned previously in Section 1.4.4. The optics layout is identical to that used for wavefront metrology. AOM3 is turned off. The beam simply transmits through the device without getting diffracted. AOM1 and 2 are set to frequencies of 110 MHz and 90 MHz, respectively. Again, the beams have to be aligned and the grating is used under the Littrow condition. Again, parts of the beams are sampled by the beam pickoff window and redirected to the metrology block where they mix and produce a 20 MHz signal at a phase meter—Phase Meter No.3 or PM3, whose fiber pickoff is mounted on the Zerodur metrology block (Figs. 1-13 and 1-17). The reflected and back-diffracted beams coincide upon the fiber pickoff to PM4 (Fig. 2-6), and produce a second 20 MHz signal, which differs from PM3 in that it contains the averaged phase information from the grating. A comparison of the two signals then yields the grating phase. Details on the grating reading mode, as well as the results from some reading experiments, can be found in Reference [48].

2.3 Summary

Designing the lithography interferometer with ProE removes any inaccuracy associated with an otherwise trial-and-error process. It improves the compactness and the efficiency of the layout, and allows the interferometer arms to be set up mirror-symmetrically about the grating beamsplitter. More importantly, it provides a way

to model the SBIL optics at a system level. Data obtained from such modeling will prove essential to build a simulation for the wavefront metrology system (Sec. 5.2).

The interferometer incorporates means for spatial filtering and adjustment of polarization, intensity and wavefront curvature. The beamsplitter mode is engaged for beam alignment prior to lithography and for fringe period measurement. The rectangular beamsplitter is used in both cases. The grating mode is engaged for conducting wavefront metrology and reading the phase of a patterned grating.

Chapter 3

Beam alignment

A system for carrying out automated beam alignment for SBIL has been implemented. The SBIL design goals call for tight beam alignment tolerances, where the mean beam position and angle alignment errors must be controlled to the μm and the μrad level, respectively. In this chapter, I first discuss the theory behind beam position and angle decoupling, and the so-called iterative beam alignment principle, focusing specifically on deriving a mathematical formalism that can guide the development of similar systems in the future (Sec. 3.1). I then describe the beam alignment system setup in detail (Sec. 3.2). Section 3.3 investigates the noise-limited position and angle measurement accuracy. Section 3.4 conceives an experiment to explicitly verify that the two arms of the lithography interferometer are antisymmetrically correlated, as expected from the use of a grating beamsplitter. Finally, in Section 3.5, I present experimental measurements of the beams' position and angle instabilities. I also show repeatability experiments, which demonstrate that the system fulfills the alignment requirements for nanometer-level SBIL writing.

Throughout the chapter, I use the phrase "grating image", or equivalently, "image grating", to refer to the small patch of standing wave pattern produced by the interference of two coherent Gaussian beams.

All substrates are unflat to some extent. A 300-mm-diam. silicon wafer may have a total thickness variation of 25 μm. In comparison, the SBIL vacuum chuck is lapped to a flatness of 25 μin, or less than 1 μm. Assuming that an unflat substrate is mounted on the vacuum chuck, if angles of incidence in the two arms are unbalanced by an amount δ (Fig. 3-1), the direction along which interference fringes orient will deviate from the normal to the vacuum chuck by an amount $\delta/2$. Due to the intrinsic substrate thickness variation, this slight tilt would introduce a phase error to the written grating. For instance, if the substrate thickness varies by 20 μm from one end

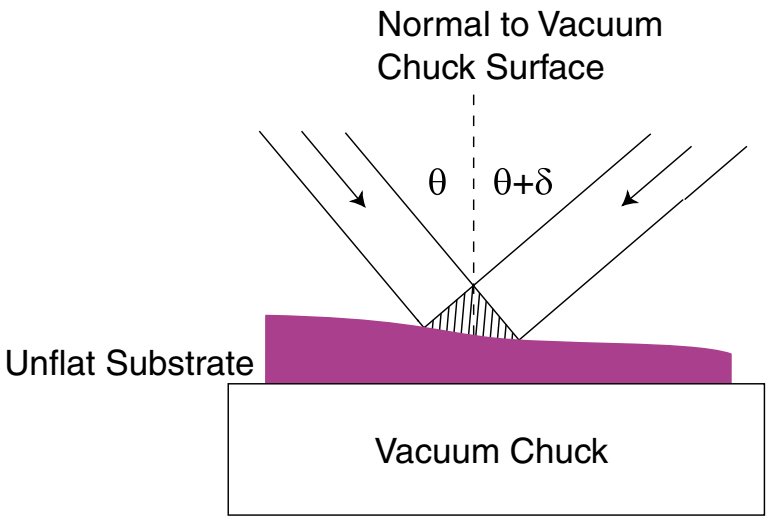

Figure 3-1: Fringe tilt results in phase error if the substrate is unflat.

to the other, one can verify that an unbalance of $\delta = 10$ μrad introduces 0.1 nm of accumulated phase error, regardless of the grating period. Note that SBIL employs a wavefront metrology system (Ch. 5) to ensure that the grating image is essentially produced by interfering two plane waves. Because of its use of large spherical waves, "traditional" interference lithography suffers from substrate nonflatness more severely [23]. While reducing nonflatness-induced phase errors to the subnanometer level requires angle alignment to $\sim$ 10 μrad, the part-per-million (ppm) grating image period control requires even tighter alignment tolerance. In Section 3.5.2, I will demonstrate mean angle alignment to better than 2 μrad, which translates into an adjustability of 4 ppm at a period of 400 nm.

To obtain good interference fringe contrast, beam position overlap is also very important. A general rule of thumb is to overlap the two beam centroids to roughly 1% of the beam spot radius, i.e., for a radius of approximately 1 mm, the centroids should be overlapped to about 10 μm of each other.

In addition, during SBIL period measurement, wavefront metrology or grating reading, the two interfering beams must align so as to be coincident upon photodetectors after traversing various optical components.

3.1 Theory

To automatically align the beams in both position and angle, first one needs to measure these quantities. Beam position decoupling is defined as using an optical setup to isolate and measure the beam position on a position sensing detector (PSD). A PSD is a fancier photodiode which reads not only the beam power but also the x and y beam locations on the detector. Beam angle decoupling is similarly defined as

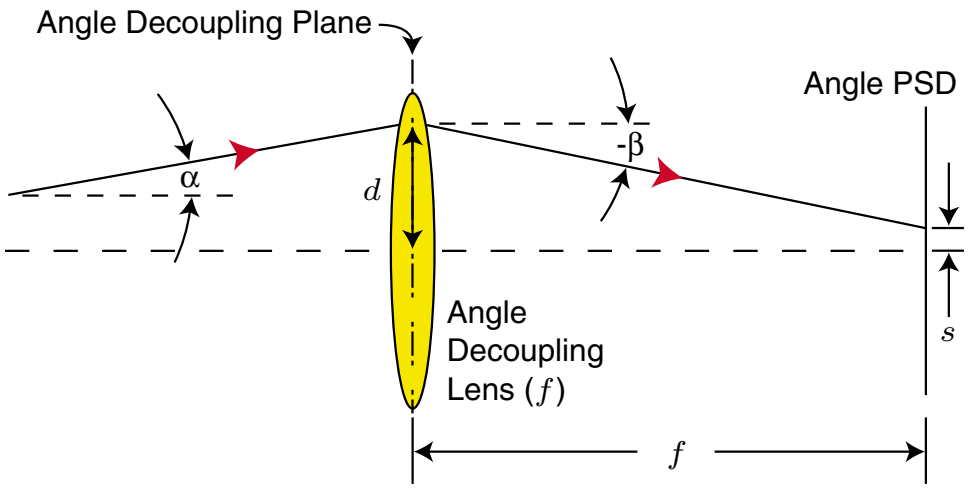

Figure 3-2: Angle decoupling topology.

using an optical setup to isolate and measure the beam angle. An alignment process can then be initiated, which must be capable of driving the beam towards any desired position and angle effectively.

3.1.1 Beam position and angle decoupling

The SBIL beam alignment system uses a similar position and angle decoupling topology as that described in Reference [49]. To best understand the theory of beam position and angle decoupling, one should be familiar with the ABCD matrix formalism from ray optics [58].

Figure 3-2 illustrates the angle decoupling topology. After passing through a thin lens of focal length f, a beam's angle (α) and its position (d) at the angle decoupling plane, are converted to a displacement (s) and an angle (β) at the back focal plane of the lens, where a PSD (so-called angle PSD) is located. In terms of ABCD matrices, one can write

$$\begin{pmatrix} s \\ \beta \end{pmatrix} = \begin{bmatrix} 1 & f \\ 0 & 1 \end{bmatrix} \begin{bmatrix} 1 & 0 \\ -1/f & 1 \end{bmatrix} \begin{pmatrix} d \\ \alpha \end{pmatrix} \quad , \tag{3.1}$$

where the matrix describing the thin lens action is followed by that describing the free space propagation. The PSD detects the displacement s. Solving Eq. (3.1), one finds

$$s = f\alpha \quad . \tag{3.2}$$

Therefore, by sensing s, the PSD is actually detecting the beam angle α. Note that Eq. (3.2) does not contain d—the beam's angle has been decoupled from its position. For SBIL, the focal length of the angle decoupling lens is 540.9 mm.

Figure 3-3 illustrates the position decoupling topology. A beam's position (d)

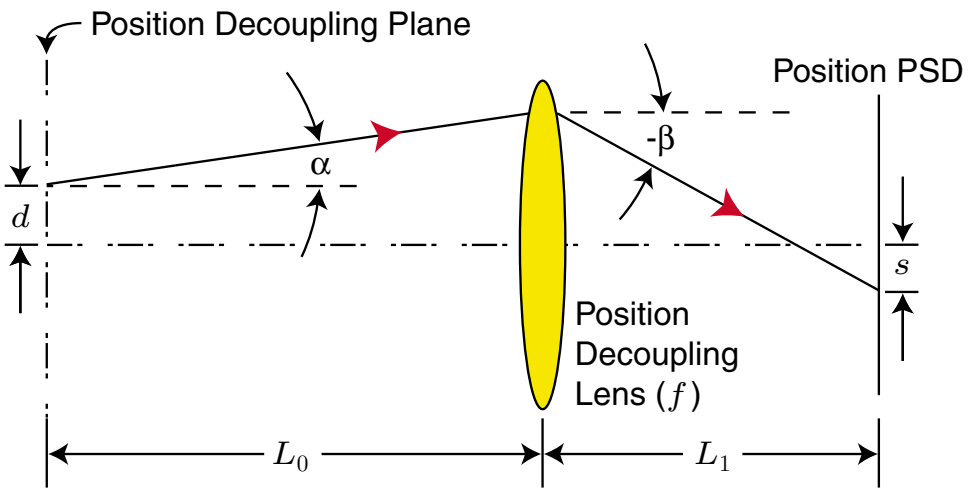

Figure 3-3: Position decoupling topology.

and angle (α) at the position decoupling plane, located a distance L_0 from a lens, are converted to a displacement s and an angle β at the output plane, located at a distance L_1 from the lens. A PSD (so-called position PSD) sits at the output plane. In terms of matrices, s and β can be expressed as

$$\begin{aligned}\begin{pmatrix} s \\ \beta \end{pmatrix} &= \begin{bmatrix} 1 & L_1 \\ 0 & 1 \end{bmatrix} \begin{bmatrix} 1 & 0 \\ -1/f & 1 \end{bmatrix} \begin{bmatrix} 1 & L_0 \\ 0 & 1 \end{bmatrix} \begin{pmatrix} d \\ \alpha \end{pmatrix} \\ &= \begin{bmatrix} d\,(1 - L_1/f) + \alpha\,[L_1 + L_0(1 - L_1/f)] \\ -d/f + \alpha\,(1 - L_0/f) \end{bmatrix} \quad . \end{aligned} \tag{3.3}$$

Setting the second term in s to zero, one has

$$L_0 = \frac{L_1}{M} \quad , \tag{3.4}$$

where the magnification factor M is defined as

$$M = \frac{L_1}{f} - 1 \quad . \tag{3.5}$$

The displacement s at the position PSD is therefore

$$s = -M\,d \quad , \tag{3.6}$$

which is a function of d only—the beam's position has been decoupled from its angle.

Note that M relates the size of s to that of d. It is interesting to also note that one can rewrite s and β by starting at a different input plane instead—Plane 2 in Figure 3-4 for example,

$$\begin{pmatrix} s \\ \beta \end{pmatrix} = \begin{bmatrix} 1 & L_1 \\ 0 & 1 \end{bmatrix} \begin{bmatrix} 1 & 0 \\ -1/f & 1 \end{bmatrix} \begin{bmatrix} 1 & L_0 - \Delta \\ 0 & 1 \end{bmatrix} \begin{pmatrix} d + \Delta\alpha \\ \alpha \end{pmatrix} \quad , \tag{3.7}$$

where Δ is the separation between the position decoupling plane and Plane 2. The

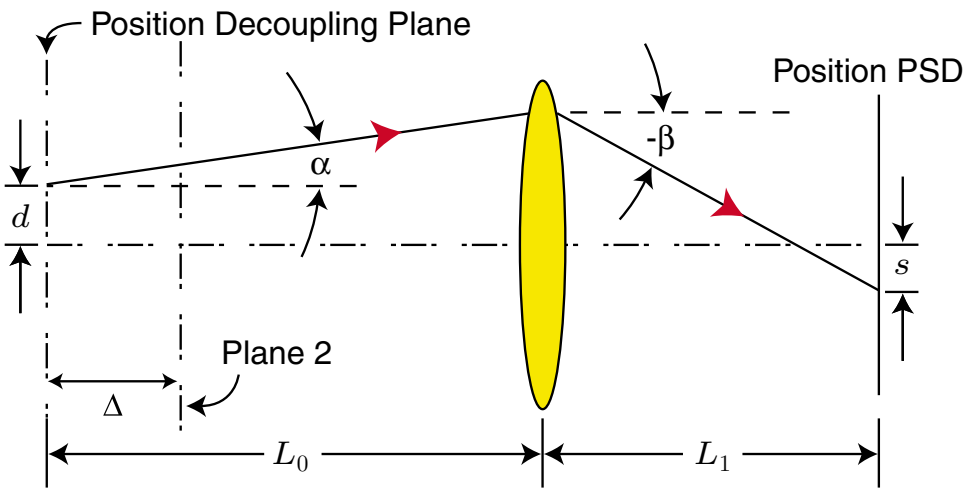

Figure 3-4: Position decoupling topology continued.

derived expression for s is the same as Eq. (3.6). In other words, once the optical layout is completed, the position decoupling happens strictly in the position decoupling plane, no matter which other plane one chooses to use as the input.

For SBIL, the focal length of the position decoupling lens is 270.5 mm and the distance L_1 is 405.75 mm, giving rise to $M = 0.5$. According to Eq. (3.4), the distance L_0 is twice that of L_1 at 811.5 mm.

Locations of the position and angle decoupling planes for the beamsplitter and grating modes (Secs. 2.2.3 and 2.2.5) have been labeled in Figures 2-7 and 2-8, respectively.

3.1.2 Angle PSD placement error

The SBIL angle PSD senses the beam location in two dimensions. The size of the sensor is 2×2 mm^2. Given that the focal length of the angle decoupling lens is $f = 540.9$ mm, one can calculate that the angle PSD has an angle sensing range of approximately 3.7 mrad per axis. Strict angle decoupling happens when the PSD is located at the focal plane of the lens [Eq. (3.2)]. In reality, a small PSD placement error exists, which impacts the accuracy of the decoupled angle readout. I explore the issue in this section.

Suppose that the angle PSD is misplaced by a distance Δ from the focal plane. Instead of Eq. (3.2), one now has

$$s = (f + \Delta)\,\alpha - \frac{\Delta}{f}\,d \quad . \tag{3.8}$$

The angle measurement range is only 3.7 mrad. Differentiation leads to

$$\delta s = (f + \Delta)\,\delta\alpha - \frac{\Delta}{f}\,\delta d \quad . \tag{3.9}$$

The quantities δd and $\delta\alpha$ are related via the relation

$$\delta d = L\,\delta\alpha \quad , \tag{3.10}$$

where L is the distance from the position decoupling plane (of the position PSD) to the angle decoupling plane (of the angle PSD). In writing down Eq. (3.10), I am comparing two scenarios: one with $\Delta = 0$ (no placement error) and the other with $\Delta \neq 0$ (with error). I am assuming that these two scenarios see their beam positions overlapped, but because the latter has a small PSD placement error, an angle readout error is thereby induced. For the current setup, the distance L is approximately 0.77 m. Plugging Eq. (3.10) into Eq. (3.9), one gets

$$\delta s = \left[f + \left(1 - \frac{L}{f}\right) \Delta \right] \delta\alpha \quad , \tag{3.11}$$

or inversely,

$$\delta\alpha = \frac{\delta s}{f\,[1 + (1 - L/f)(\Delta/f)]} \quad . \tag{3.12}$$

Expanding Eq. (3.12) in powers of Δ/f leads to

$$\delta\alpha = \delta\alpha_{\rm corr} \left[1 - \left(1 - \frac{L}{f}\right) \frac{\Delta}{f} + \mathcal{O}[\Delta/f]^2 \right] \quad , \tag{3.13}$$

where $\delta\alpha_{\rm corr} = \delta s/f$ is the exact angle readout if there is no placement error, and $\mathcal{O}[\Delta/f]^2$ denotes terms with orders $(\Delta/f)^2$ and higher. The leading error is

$$\epsilon = \left(\frac{L}{f} - 1\right) \frac{\Delta}{f} \quad . \tag{3.14}$$

For $L = 0.77$ m, $f = 540.9$ mm and a placement error of $\Delta = 5$ mm, Eq. (3.14) yields an angle readout error of 3.9 parts per thousand. When $\delta s = 0$, i.e., at the center or the origin of the PSD, $\delta\alpha$ coincides with $\delta\alpha_{\rm corr}$. Both read zero. However, as one proceeds away from the origin to the edge of the angle sensor, the error between $\delta\alpha$ and the true value $\delta\alpha_{\rm corr}$ may mount to a maximum of 7.2 μrad. For comparison, the SBIL laser angular instability is 11.4 μrad, three-sigma. In reality, I rarely align the beams to the edge of the PSD where a bigger concern is the spot partially falling off the sensor, therefore leading to a false reading. In fact, I rarely align the beams to more than 0.2 mm from the origin—1/10 the size of the PSD. The placement error $\Delta = 5$ mm is a generous overestimate as well. With care and proper tooling, achieving $\Delta \approx 1$ mm should not be a challenge. Hence, the angle readout error due to the PSD misplacement is quite negligible.

Position PSD placement error is not important. As a result of the misplacement, the distance L_1 in Figure 3-3 changes slightly, leading to a slight shift in the location of the position decoupling plane (Sec. 3.1.1).

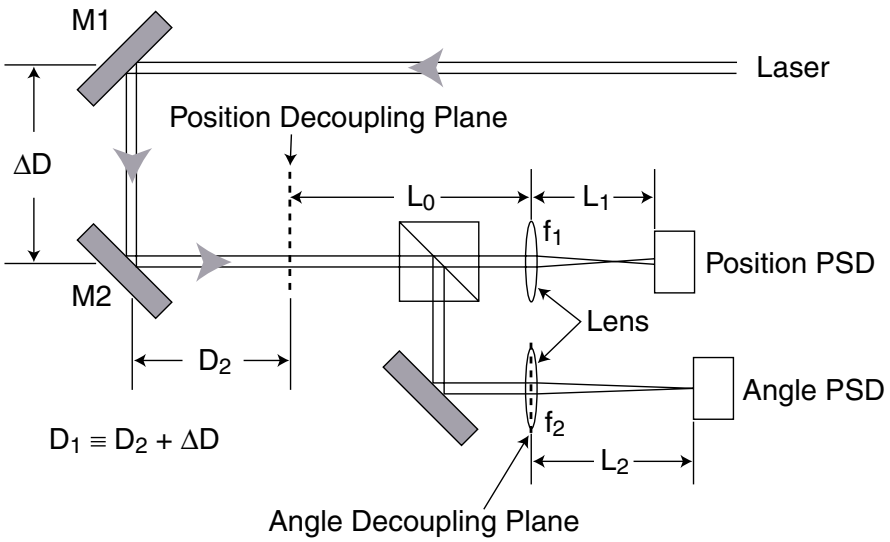

Figure 3-5: Design for a general beam alignment system.

3.1.3 Iterative beam alignment

Figure 3-5 depicts the optical layout of a general-purpose beam alignment system. The position and angle decoupling topologies are the same as described in Section 3.1.1. Though other topologies may also be used, the theme remains the same: a position PSD senses only beam position fluctuations in a position decoupling plane, and an angle PSD senses only beam angle shifts at an angle decoupling plane. In the case of SBIL, the beam alignment system uses two picomotor-controlled tip-tilt mirrors per arm to direct the beam to the position and angle PSDs. Section 3.2 discusses the alignment hardware in detail. The system applies the following set of optical parameters: $f_1 = 270.5$ mm, $f_2 = 540.9$ mm, $L_1 = 405.75$ mm, $L_0 = 2\,L_1 = 811.5$ mm and $L_2 = f_2$. The distances D_1 and D_2 are defined as those from the position decoupling plane to the mirror M1, and to M2, respectively. In the beamsplitter mode (Sec. 2.2.3), from Figure 2-7, one finds $D_1 = 1196$ mm and $D_2 = 806$ mm. In the grating mode (Sec. 2.2.5), from Figure 2-8, one finds $D_1 = 1414$ mm and $D_2 = 1024$ mm. It is noted in Section 3.1.2 that the positioning tolerance on the angle PSD is quite lenient, and any error in placing the position PSD merely shifts the position decoupling plane slightly.

The so-called iterative beam alignment principle is intuitive. For the same amount of angle change at the angle decoupling plane, Mirror M1 shifts the position (in the position decoupling plane) more than M2. In the beamsplitter mode for example, for the same 1.5 μrad beam angle change, the position shift due to M1 is approximately 1.8 μm, and that due to M2 is 1.2 μm. On the other hand, for the same amount of position shift in the position decoupling plane, M2 changes the angle (at the angle

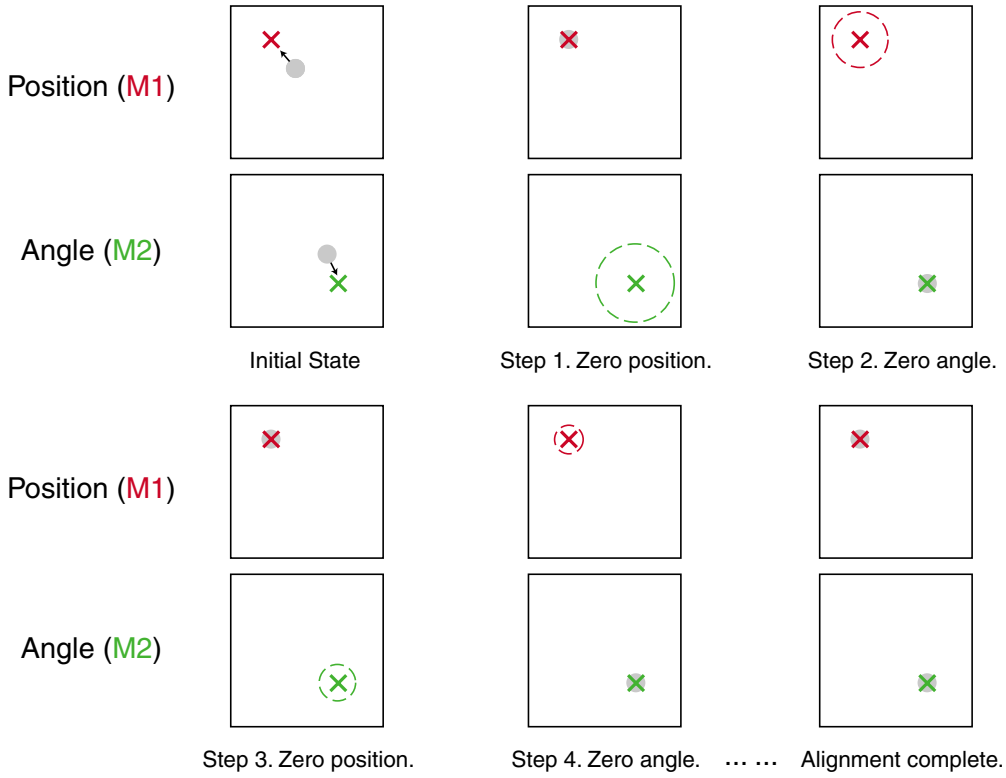

Figure 3-6: Cartoon demonstrating the iterative beam alignment principle. The two-axis outputs from the position and angle PSDs are graphically represented as square boxes. Mirrors M1 and M2 are driven iteratively to zero the beam spots, marked by solid circles, in both position and angle to the desired locations, marked by crosses. Dashed lines circle the regions where the spots may lie in.

decoupling plane) more than M1. Therefore, one can get a desired alignment result by iteratively using M1 to align position and M2 to align angle. Figure 3-6 uses a cartoon to illustrate the iterative beam alignment principle.

I now develop a mathematical formalism, which can be used to design general iterative beam alignment systems. As one will see, the speed at which the alignment converges to the desired angle and position is a strong function of the distances D_1 and D_2 (Fig. 3-5).

For simplicity, I consider beam alignment using one-dimensional position and angle PSDs. The results so derived can be easily generalized to systems using two-dimensional sensors. Suppose initially the beam in the position decoupling plane is at a distance Δd from a desired position, and the beam at the angle decoupling plane makes an angle that differs by $\Delta\theta$ from a desired angle. Consider an algorithm where one iteration involves first aligning the beam's position and then angle. At the start of the first iteration, one actuates M1 to zero position, after which, the respective outputs in the position and angle decoupling planes become

$$O_{\mathrm{p}}^{(1,1)} = 0 \ , \tag{3.15}$$

$$O_{\mathrm{a}}^{(1,1)} = \Delta\theta + \frac{\Delta d}{D_1} \ . \tag{3.16}$$

The first iteration is complete after one actuates M2 to zero angle, with outputs

$$O_{\mathrm{p}}^{(1,2)} = D_2 \left(\Delta\theta + \frac{\Delta d}{D_1} \right) \ , \tag{3.17}$$

$$O_{\mathrm{a}}^{(1,2)} = 0 \ . \tag{3.18}$$

After the n-th iteration, the position and angle outputs are

$$O_{\mathrm{p}}^{(n,1)} = 0 \ , \tag{3.19}$$

$$O_{\mathrm{a}}^{(n,1)} = \left(\frac{D_2}{D_1} \right)^{n-1} \left(\Delta\theta + \frac{\Delta d}{D_1} \right) \ , \tag{3.20}$$

$$O_{\mathrm{p}}^{(n,2)} = \left(\frac{D_2}{D_1} \right)^{n-1} \left(D_2 \, \Delta\theta + \frac{D_2}{D_1} \, \Delta d \right) \ , \tag{3.21}$$

$$O_{\mathrm{a}}^{(n,2)} = 0 \ . \tag{3.22}$$

For $D_2 < D_1$, one has guaranteed convergence in both angle [Eq. (3.20)] and position alignment [Eq. (3.21)]. The speed of convergence is directly a function of the ratio of D_2 to D_1—the smaller the ratio, the faster the convergence.

For completeness, I give output expressions for the other iterative alignment algorithm, where an iteration is defined by first zeroing the beam's angle and then position:

$$O_{\mathrm{p}}^{(n,1)} = \left(\frac{D_2}{D_1} \right)^{n-1} (D_2 \, \Delta\theta + \Delta d) \ , \tag{3.23}$$

$$O_{\mathrm{a}}^{(n,1)} = 0 \ , \tag{3.24}$$

$$O_{\mathrm{p}}^{(n,2)} = 0 \ , \tag{3.25}$$

$$O_{\mathrm{a}}^{(n,2)} = \left(\frac{D_2}{D_1} \right)^{n-1} \left(\frac{D_2}{D_1} \, \Delta\theta + \frac{\Delta d}{D_1} \right) \ . \tag{3.26}$$

Once again, the speed of convergence is a function of the ratio of D_2 to D_1.

Let $r = D_2/D_1$. Define R to be the ratio of the desired alignment tolerance to the initial displacement (either in position or angle), e.g., if the initial displacement from a desired position is 1 mm, and the desired position alignment tolerance is 10 μm, then $R = 100$. Then the number of iterations, n, is related to r and R by

$$n \approx -\log_r(R) \ . \tag{3.27}$$

If one knows the desired performance specifications (n and R values), Eq. (3.27) can be used to calculate r, from which, the optical design for the iterative beam

alignment system can proceed. Alternatively, if r and R are known, one can estimate the number of cycles (n) needed to attain the required alignment tolerance. For example, beamsplitter-mode alignment has $r = 0.67$ and $R = 100$, leading to $n \approx 12$.

It must be pointed out that other alignment schemes do exist, for example, those based on the principle of decoupling matrix [60]. The main advantage for the decoupling matrix approach is its speed. Assuming one has a controller that can drive all axes in parallel and has obtained a sufficiently accurate decoupling matrix, it is possible that one can align the beam's position and angle in a single operation. However, as Section 3.2 points out, in the current SBIL setup, only one picomotor driver is available so the four picomotors in each arm, two for each tip-tilt mirror, must be addressed in a serial fashion. The speed advantage for the decoupling matrix approach thus becomes much less obvious, because to prevent the spots from falling off the sensors, a single alignment operation may have to be broken into multiple ones. Furthermore, a decoupling matrix is usually only valid for regions of the PSDs that have been previously calibrated. Alignment accuracy and speed may decrease dramatically if one attempts to align beams that fall outside these regions. Iterative alignment, on the other hand, works for the full position and angle ranges as long as the beams remain on the sensors.

The SBIL beam alignment system is implemented by applying the iterative scheme.

3.2 System setup

I now describe the setup of the SBIL beam alignment system. The reader should review Sections 2.2.3 through 2.2.5 for they are complementary to the topic under discussion. In particular, the reader should note the presence and the function of the acousto-optic modulators (AOMs).

3.2.1 Beamsplitter mode

Figure 3-7 presents the beam alignment system concept. As shown, the system is used in the so-called beamsplitter mode. The optical aspect of the beamsplitter mode is discussed in Section 2.2.3. Figure 3-7 is schematic only and the AOMs have been omitted. Figure 2-7 presents the actual engineering drawing of the beamsplitter mode, together with the beam path and the locations of the position and angle decoupling planes. Frequency settings of the AOMs are also covered in Section 2.2.3. Four picomotors, two for each mirror mount[1], provide four axes of beam steering control in each arm. Each picomotor—essentially a piezoelectric actuator that turns a screw—has a step size of approximately 30 nm, which translates into a mount angle resolution

[1]Model 8807 by New Focus, Inc.

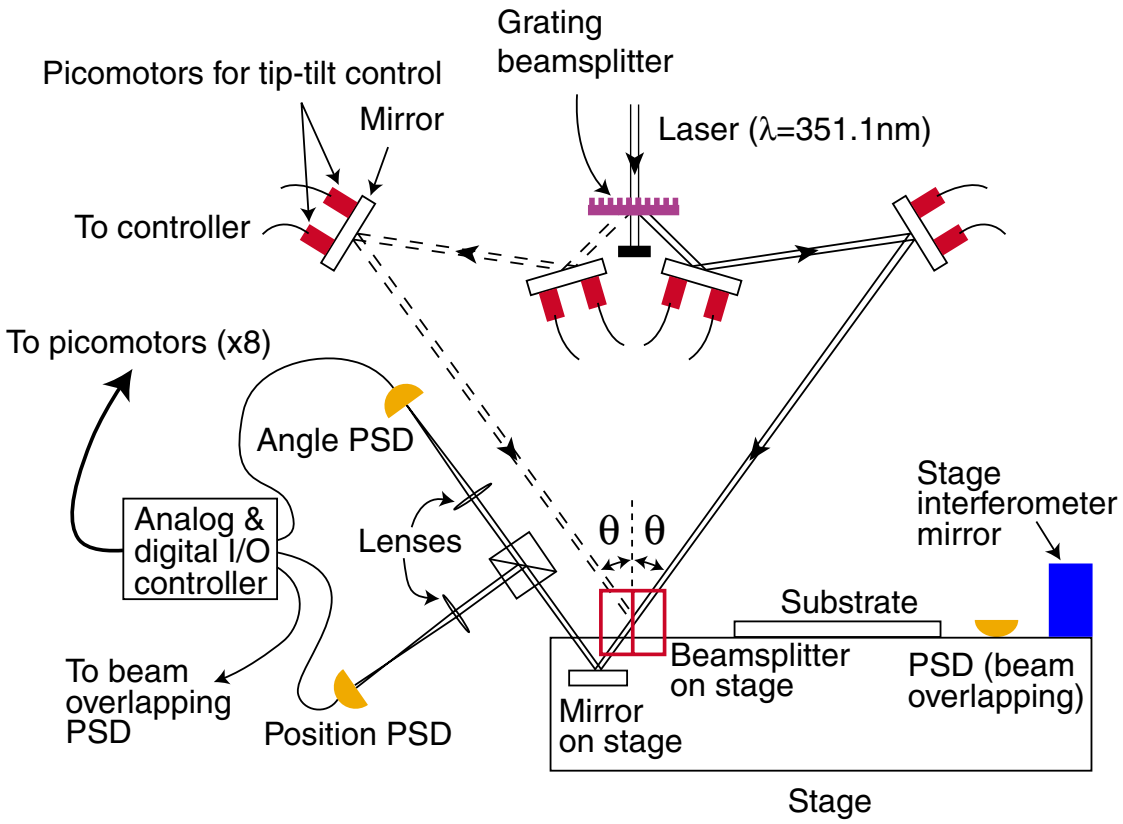

Figure 3-7: SBIL beam alignment system concept (beamsplitter mode).

of 0.75 μrad and a beam angle adjustability of 1.5 μrad. Despite its high resolution, a picomotor is inherently a non-deterministic device. Figure 3-8 shows some measured picomotor angle hysteresis data. For each data point, the picomotor is first driven clockwise by the indicated number of steps, and then driven counterclockwise by the same number of steps. Angle hysteresis is recorded by the angle PSD. A linear fit does not apply in general. Even when it does, the slope of the line is nonrepeatable. The picomotor step size may vary due to load, aging, temperature, and differences in mechanical parts, etc. Hence, any picomotor-based alignment scheme must have a feedback setup if precision control is required. In the case of SBIL, the position PSD provides two axes of beam position feedback, and the angle PSD provides two axes of angle feedback.

As shown in Figure 3-7, a grating splits the incoming laser into two beams. Compared to a cube beamsplitter, the grating provides greater tolerance over the laser's spatial incoherence as well as its temporal incoherence (Sec. 2.1.1). I choose to explain the alignment process for the left arm, noting that the alignment for the right arm proceeds in a similar fashion. While aligning the left arm, the right beam is temporarily turned off. After being reflected by the two picomotor-mounted mirrors,

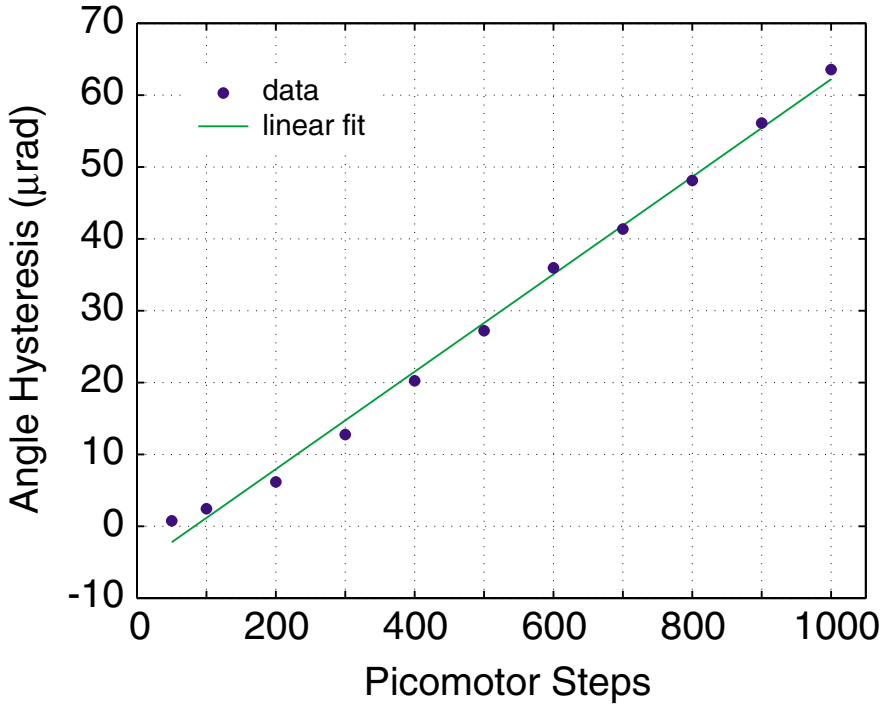

Figure 3-8: Open-loop control impossible due to picomotor step nonuniformity.

the beam is incident upon a custom rectangular beamsplitter—a cube consisting two rectangular halves, which is mounted on the stage. The beamsplitter is positioned nominally to the location where the arms are designed to interfere. The splitter interface is aligned parallel to the stage interferometer mirror, which is perpendicular to the substrate. After transmitting through the beamsplitter, another cube splits the beam in two: one falling onto the position PSD and the other onto the angle PSD. Position and angle readouts from the PSDs are fed into an input-output (I/O) PC controller, which uses the information to adjust the picomotors through a picomotor driver[2].

If one aligns the left and right beams to the same locations on both the position and angle PSDs, the beams then overlap in space, but not necessarily at the substrate, and have equal angles of incidence. Subsequent calibrations are needed to ensure that the beams overlap in the substrate plane. This is done via the use of a third PSD, the so-called beam overlapping PSD. I will come back to this point shortly.

The position and angle PSDs are On-Trak Photonics UV2L2 duolateral PSDs. They are 2×2 mm^2 in dimension. Given the optical parameters of Section 3.1.1, one can calculate that the measurement range for the position PSD is 4 mm and that for the angle PSD is 3.7 mrad. Analog outputs from the PSDs are handled by a National

[2]Model 8732 by New Focus, Inc.

Instruments (NI) board with 16-bit analog-to-digital (A/D) conversion, leading to a beam position resolution of 61 nm per axis and an angle resolution of 56 nrad per axis. Measurement accuracy, not resolution, is the real figure of merit. I present in Section 3.3 experimental results that establish the system's position and angle measurement accuracies, which are approximately 1.3 μm and 1.2 μrad per axis[3], three-sigma, respectively. The picomotor driver is controlled via external transistor-transistor logic (TTL) signals from a NI digital I/O board. All control software, including the picomotor driver software, is written in LabVIEW.

The spatial filter pinholes must be removed prior to any alignment attempt, and reinstalled after the alignment is complete. While the pinholes are absent, irises are installed just before the first set of picomotor-equipped mirrors to block out the zero-order beams from the AOMs. The operator must manually position the beams onto both PSDs, before the alignment can proceed under computer control. Note also that the system aligns the beams exiting from the rectangular beamsplitter. It does not act directly on the entry beams. The same beamsplitter is also used to conduct the fringe period measurement, which is the subject of study in Chapter 4.

As mentioned earlier, four picomotors provide control over four degrees of freedom (DOF) in each arm. The four-axis readouts from the position and angle PSDs help closing the feedback loop. It is important that one understands which four DOFs are being controlled in order to correctly utilize the alignment system in the beamsplitter mode. Figure 3-9 shows the four DOFs defining an incoming laser beam. As drawn, xOy defines the substrate plane. The four DOFs—angles θ and φ, and position coordinates y_a and z_a—are all defined with respect to the beamsplitter interface. At the completion of a successful beamsplitter-mode alignment, the left and right beams hit the same spot (y_a, z_a) at the interface and achieve the same angle orientations (θ, φ). In general, $\varphi \neq 0$ and $z_a \neq 0$, meaning that the plane defined by the two interferometer arms has a slight tilt with respect to the plane yOz, and the beams do not overlap on top of the substrate. The former condition causes no concern for it only entails a small rotation of the grating image along the direction of the interference fringes. The latter is more troublesome for if z_a is sufficiently large, the beams do not overlap in the substrate plane effectively. Recall that the goal is to overlap the beam centroids to around 1% of the radius. To overcome this shortcoming, a third PSD is placed at the substrate plane to explicitly verify the beam overlap (Sec. 3.2.3). The PSD is mounted on the stage and has its protective window removed to prevent multiple reflections from introducing readout errors. The face of the PSD is carefully

[3]These figures are obtained when the PSD amplifier is used at the highest gain setting. Much better accuracies are expected at lower gains.

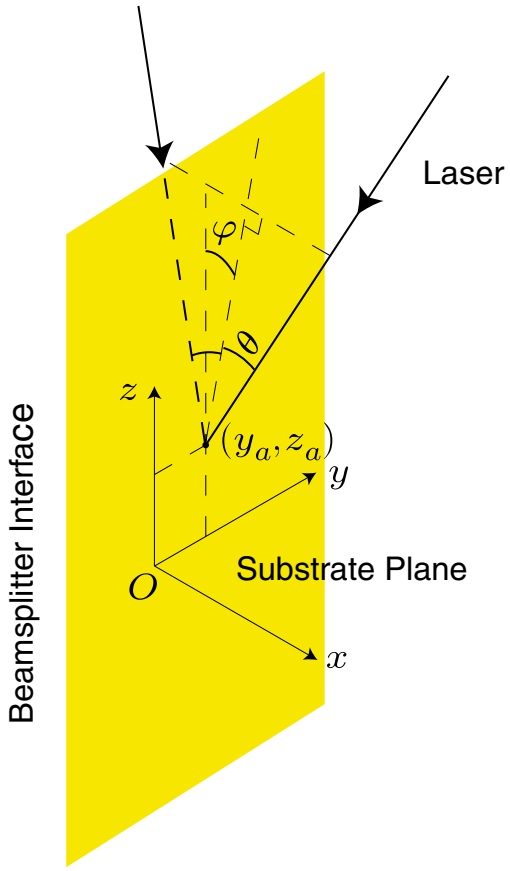

Figure 3-9: Four degrees of freedom defining each arm during the beamsplitter-mode alignment.

positioned to the same plane as the top surface of the substrate.

3.2.2 Rectangular beamsplitter design, installation and non-ideality

Figure 3-10 shows the design of the rectangular beamsplitter. Figure 3-11 shows the quality-control (QC) test results that the beamsplitter manufacturer must provide upon delivery. The listed pre- and post-assembly specifications are constrained by the financial budget. The beamsplitter currently in use is custom-made by Optimax Systems, Inc. It met and exceeded all specifications. Table 3.1 lists the QC test results. The numbers should be read in conjuction with Figures 3-10 and 3-11.

The rectangular shape of the beamsplitter allows the parallelism and perpendicularity specifications to be achieved relatively easily. More importantly, it allows easy alignment of the beamsplitter interface to the x-axis interferometer stage mirror, which has been aligned perpendicular to the surface of the vacuum chuck. Perpendicularity of the fringes is thereby assured. In theory, aligning the interface to the stage mirror also avoids the need to experimentally establish the scan direction, i.e.,

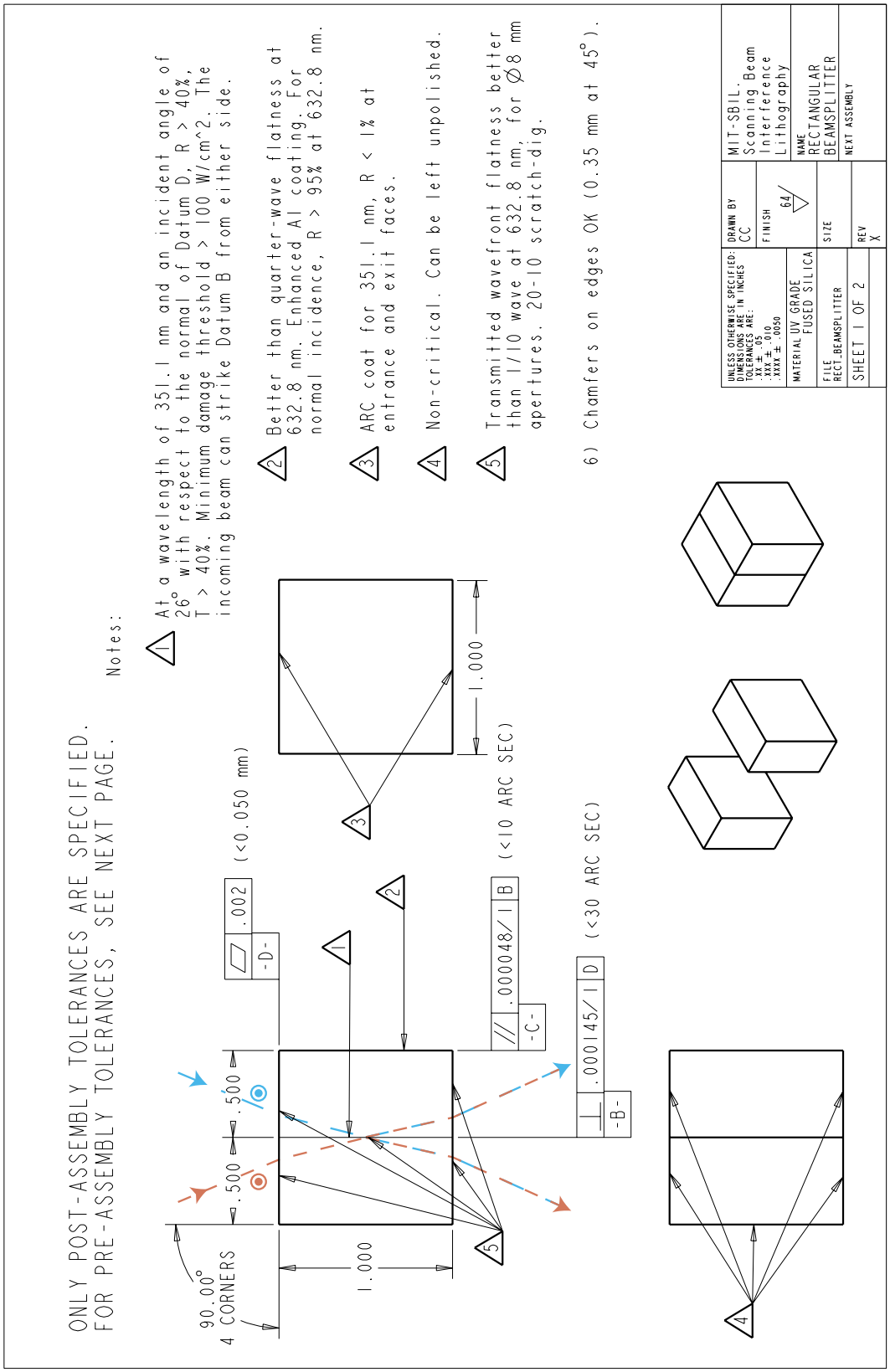

Figure 3-10: Rectangular beamsplitter design.

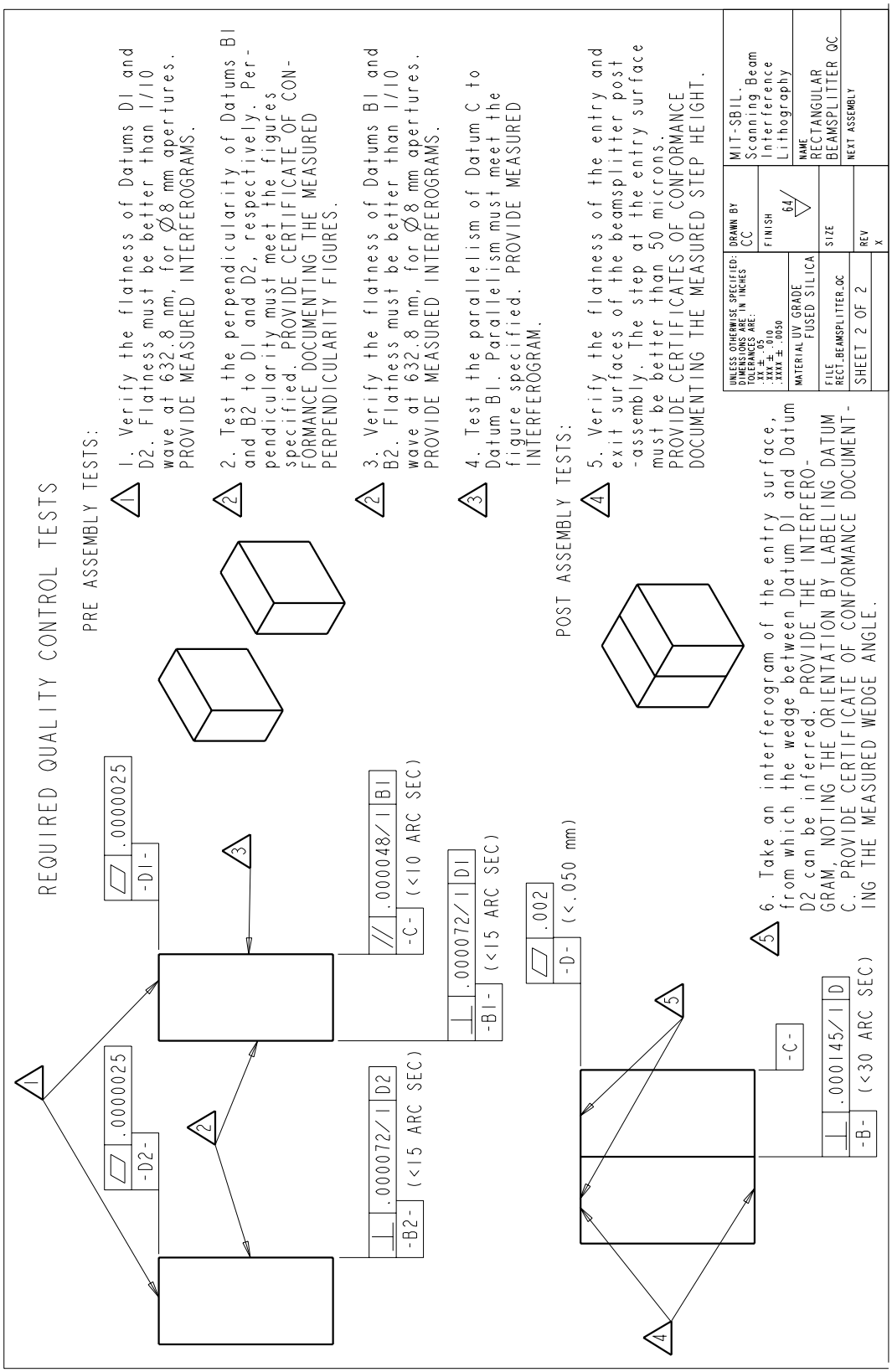

Figure 3-11: Rectangular beamsplitter design continued. Quality-control (QC) tests.

Rectangular beamsplitter QC test results	
Perpendicularity of Datum B1 to Datum D1	2 arcsec (9.7 μrad)
Perpendicularity of Datum B2 to Datum D2	8 arcsec (38.8 μrad)
Parallelism of Datum C to Datum B1	4.1 arcsec (19.9 μrad)
Wedge angle between Datum D1 and Datum D2	10.4 arcsec (50.4 μrad)
Flatness of Datum B1	20.9 nm at 8 mm diam.
Flatness of Datum B2	57.0 nm at 8 mm diam.
Transmitted wavefront through Datum D1	17.0 nm at 8 mm diam.
Transmitted wavefront through Datum D2	14.3 nm at 8 mm diam.
Step height (Datum D)	9 μm

Table 3.1: Rectangular beamsplitter quality-control (QC) test results. The numbers should be read in conjuction with Figures 3-10 and 3-11.

the direction of fringe orientation. The alignment ensures that the stage x axis is the step direction and the y axis is the scan direction. In practice however, beamsplitter non-idealities combined with interface alignment errors dictate that the scan direction must be experimentally verified. The observed deviation is around 10 μrad from the stage y axis.

During installation, the beamsplitter interface must be aligned perpendicular to the vacuum chuck surface. To facilitate the alignment, one face of the beamsplitter (Datum C in Fig. 3-10) has an enhanced aluminum coating. The alignment is done with the help of a Newport autocollimator that has a 0.1 μrad angle resolution and outputs a 1 in-diam. collimated beam at $\lambda = 670$ nm. First, the beamsplitter assembly is mounted on the side of the vacuum chuck (Fig. C-1). Commercial optical mounts from New Focus, Inc. (NF) are used whenever possible. Chuck attachments are machined out of Super Invar, a low coefficient-of-thermal-expansion (CTE) material. Alignment Mirror Assembly No.1 is then attached, its mirror aligned to the x-axis interferometer stage mirror. Mirror Assembly No.2 is attached to direct the autocollimator beam to the beamsplitter and to Assembly No.1. The beamsplitter, with its coated surface facing the beam, is aligned to No.1's mirror. When the alignment is complete, both mirror assemblies are removed. Figure C-2 shows the engineering drawing of the rectangular beamsplitter assembly. The estimated alignment error is around 10 μrad in both pitch and yaw—angles defined with respect to the x-axis stage mirror.

From QC test results (Table 3.1), one can reconstruct the shape of the beamsplitter, whose non-ideality introduces a systematic substrate-plane fringe tilt, in addition to any due to beam alignment inaccuracies. The shape-distortion angles γ, ρ and α,

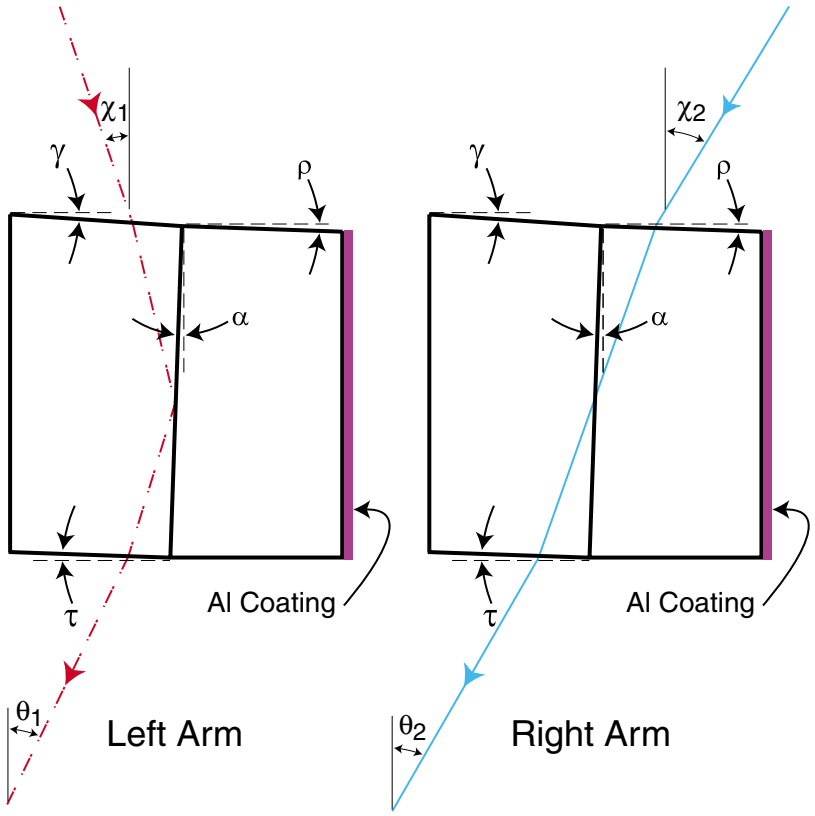

Figure 3-12: Rectangular beamsplitter shape distortions.

as defined by Figure 3-12, are approximately $58 + 10 = 68$ μrad, $10 + 10 = 20$ μrad and $20 + 10 = 30$ μrad, respectively, where I have included an estimated pitch alignment error of $+10$ μrad. The beams' entry angles are χ_1 for the left arm and χ_2 for the right. Their corresponding exit angles are θ_1 and θ_2. Even if the beam alignment system equalizes the exit angles perfectly, the entry angles cannot be equal due to the imperfect splitter geometry. Fringe tilt develops as a result. Unfortunately, no parallelism data is available to infer the magnitude of the angle τ. Nevertheless, expectation is that Optimax has made the exit surface parallel to the entry surface to within 10 arcsec, or 48 μrad. As far as the fringe tilt is concerned, the magnitude of τ is not an important quantity because both arms exit from that surface. As a result, χ_1 and χ_2 change by roughly the same amount, leaving the direction of the fringe tilt unchanged. Suppose $\theta_1 = 26^\circ$ and θ_2 differs from θ_1 by $+6$ μrad due to an imperfect beam alignment. The resulting fringe tilt away from the substrate-plane normal is about 25 μrad, based on mathematics that will be introduced in Section 4.1.10. In a worst-case scenario where the thickness of the substrate varies monotonically by 25 μm across, fringe tilt will introduce an unflatness induced phase error of about 0.6 nm.

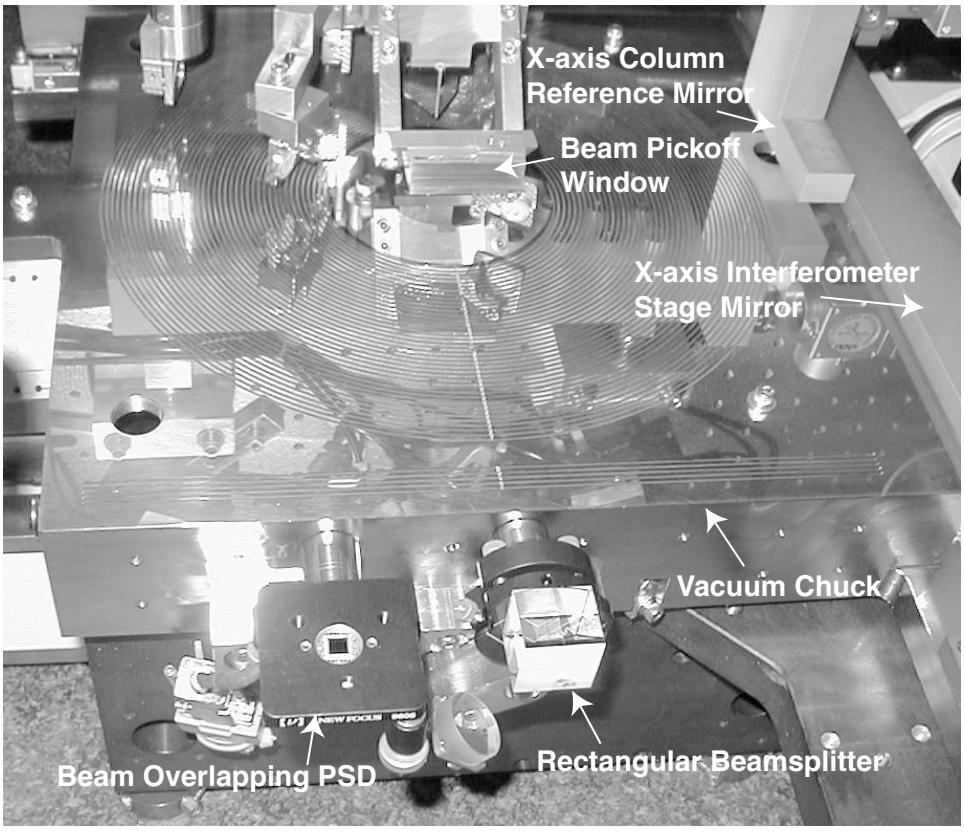

Figure 3-13: Photo of the vacuum chuck with the rectangular beamsplitter and the beam overlapping PSD attached. The chuck is machined out of a single block of Super Invar, and is flat to within 1 μm.

3.2.3 Beam overlapping PSD

When used in the beamsplitter mode, the SBIL beam alignment system is essentially overlapping the beams and equalizing the incident angles at the interface of the beamsplitter. However, at the end of the alignment, there is no guarantee that the spots will overlap at the substrate. To solve the problem, a third PSD is placed in the substrate plane to verify the beam overlap. The beam spot radius at the substrate is usually around 1 mm. The PSD used for checking the beam overlap must be large enough to accommodate the spot. An On-Trak UV2L4 detector is used. It has a dimension of 4×4 mm^2, which translates into an A/D-limited position resolution of 61 nm. Measurement accuracy is more important than resolution. According to findings from Section 3.3, the readout accuracy of the PSD is approximately 1.3 μm per axis, three-sigma, determined primarily by the performance of the PSD amplifier. The desired beam overlap tolerance is about 10 μm. The PSD's protective window is removed to prevent multiple reflections from impacting the measurement accuracy.

Figure C-3 shows the location of the beam overlapping PSD on the vacuum chuck,

next to the rectangular beamsplitter. Figure C-4 shows the PSD assembly drawing. Wires are omitted. Figure 3-13 shows a photo of the SBIL vacuum chuck, with the beam overlapping PSD and the rectangular beamsplitter attached.

To accurately sense the beam position overlap, the face of the PSD sensor must be placed in the same plane as the substrate. The placement is done via the following procedure. First, one moves the stage so that the beam from the left arm is incident upon the substrate (the right arm can be used as well). The substrate may be a dummy uncoated silicon wafer that is the same type as the one waiting to be exposed. After being sampled by the beam pickoff window (Fig. 1-13) and redirected towards the optical bench, the reflected beam goes into the position and angle PSDs. Position and angle readouts are recorded. One then moves the stage so that the same beam is now incident upon the beam overlapping PSD. The proper placement is achieved by adjusting the PSD mount so that the reflected beam aligns with that previously from the substrate surface.

Another often-used feature of the beam overlapping PSD is to verify equal power in each arm to assure an optimal exposure dose.

3.2.4 Grating mode

Section 2.2.5 has discussed the grating mode in some length. The mode is engaged when one wants to conduct wavefront metrology (Ch. 5) or to read the phase of an existing grating. When used to read a grating, it is also known as the grating reading mode. Grating mode alignment uses the same alignment scheme as illustrated in Figure 3-7, except that the beams are now incident upon a grating placed on the vacuum chuck. The beam path is shown in Figure 2-8. Note that due to path difference, the locations of the position and angle decoupling planes have shifted, compared to those from the beamsplitter mode (Fig. 2-7). For the alignment to work, the periods of the grating image and of the material grating on the chuck must match closely to yield the so-called Littrow condition, where the reflected beam from the left arm (0-order) and the back-diffracted beam from the right arm (-1-order) coincide. Both of them are sampled by the beam pickoff window and directed to the position and angle PSDs. The automated beam alignment process can then be initiated. Since the alignment directly takes place at the grating substrate, it is no longer necessary to use the beam overlapping PSD to check for spot overlap.

Even though the alignment ensures the coincidence of the reflected and back-diffracted beams, it does not guarantee equal angles of incidence for the two arms (Fig. 3-14). Section 5.2.8 discusses the effect quantitatively, showing that it does not negatively impact SBIL wavefront metrology. In the grating reading mode, the phase

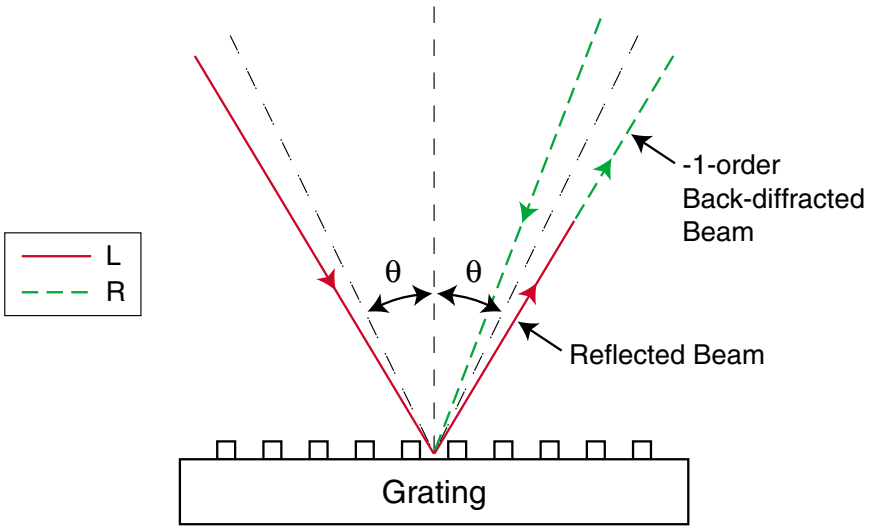

Figure 3-14: Beam alignment in the grating mode does not necessarily guarantee equal angles of incidence for the left and the right arms. It does guarantee that the beams are on top of each other at the grating.

of the intensity signal due to the interference of the reflected and back-diffracted beams is a direct representation of the spot-averaged grating phase. A displacement of one grating period corresponds to one cycle of the intensity signal. In other words, the signal phase does not depend on the incident angles being exactly equal.

Often times, one desire to switch the system from conducting wavefront metrology to reading the phase of a grating, without having to take out the pinholes and manually readjusting the optics. Recall that during wavefront metrology, AOM1 and AOM2 shift both arms in frequency by 100 MHz, and during the grating reading mode, AOM1 and AOM2 operate at 110 MHz and 90 MHz, respectively (Sec. 2.2.5). The angle shift $\Delta\theta$, due to a shift in the AOM's frequency, is given by

$$\Delta\theta = \frac{\lambda}{n\, v_s}\, \Delta\nu_s \quad , \tag{3.28}$$

where λ is the laser wavelength, n is the refractive index of fused silica, v_s is the speed of sound in fused silica and $\Delta\nu_s$ is the frequency shift [54]. For $\lambda = 351.1$ nm, $n = 1.48$, $v_s = 5.97$ km/s and $\Delta\nu_s = 10$ MHz, one has $\Delta\theta = 0.4$ mrad. In changing to the grating reading mode, the left arm, generated by AOM2, shifts down in angle by 0.4 mrad and the right arm, generated by AOM3, shifts up by the same amount. Given that the focal length of the lenses used in the spatial filter assemblies is 108.2 mm, the angle shift translates into a focal spot position shift of 43 μm. Therefore, if a 10 MHz frequency step is commanded, either beam will get blocked by its pinhole.

To switch the mode without removing the pinhole, the trick is to shift the AOM's

frequency gradually in steps, and realign the beam after each step. During actual experiment, a step size of 1 MHz is chosen, which corresponds to an angle shift of 40 μrad and a focal spot position shift of only 4.3 μm per step. Enough light passes through the pinhole to allow the alignment system to function.

3.3 Noise study

Each data acquisition (DAQ) device used by the SBIL beam alignment system outputs a certain amount of electronic noise. Together, they influence the accuracy of the beam position and angle readouts, and must be characterized.

3.3.1 Digitization noise floor

Two PSDs are configured as beam position and angle sensors. Both are UV2L2 duolateral PSDs purchased from On-Trak Photonics, Inc. They are 2×2 mm^2 in dimension. Using the technical data furnished by On-Trak and standard formula from Horowitz and Hill [61], one can calculate the noise-limited resolution of the PSD sensor to be around 15 nm under a modest 2 mW SBIL laser illumination. Note that increased light intensity results in better signal-to-noise ratio in the photocurrent, hence finer resolution, but it may also cause saturation and nonlinear operation of the PSD. On-Trak advises a sensor power density threshold of 3 W/cm^2.

The PSD used to check the beam position overlap at the substrate is an On-Trak UV2L4 detector. It has the same specification as the UV2L2, except for its dimension, which is 4×4 mm^2. The estimated sensor resolution is at 30 nm.

The analog-to-digital (A/D) conversion is handled by two 16-bit National Instruments (NI) A/D boards (Model 6034E), each is wired with 8 differential input channels to minimize the line noise. All channels are programmed to have an input range of $\pm$10 V, which translates into a voltage resolution of 305.2 μV. Taking into account the position and angle decoupling topologies (Sec. 3.1.1), the beam position and angle resolutions are 61 nm and 56 nrad per axis, respectively.

Data accuracy is more important than resolution, and is the real figure of merit here. NI advertises a better than $\pm$3 least-significant-bit (LSB) relative accuracy for the 6034E. The sampling noise is defined by a uniform probability distribution, and has a variance [62]

$$\sigma^2 = \frac{\Delta^2}{12} \quad , \tag{3.29}$$

where Δ is the quantization interval. If $\Delta = 3$ LSB is used, one comes up with a noise variance estimate of 6.98×10^{-8} V^2. At a sampling rate of 100 kHz, i.e., a Nyquist frequency of 50 kHz, the power spectrum should be that of a white noise source with a spectral density of 1.18×10^{-6} V/$\sqrt{\text{Hz}}$. Figure 3-15 shows the digitization noise

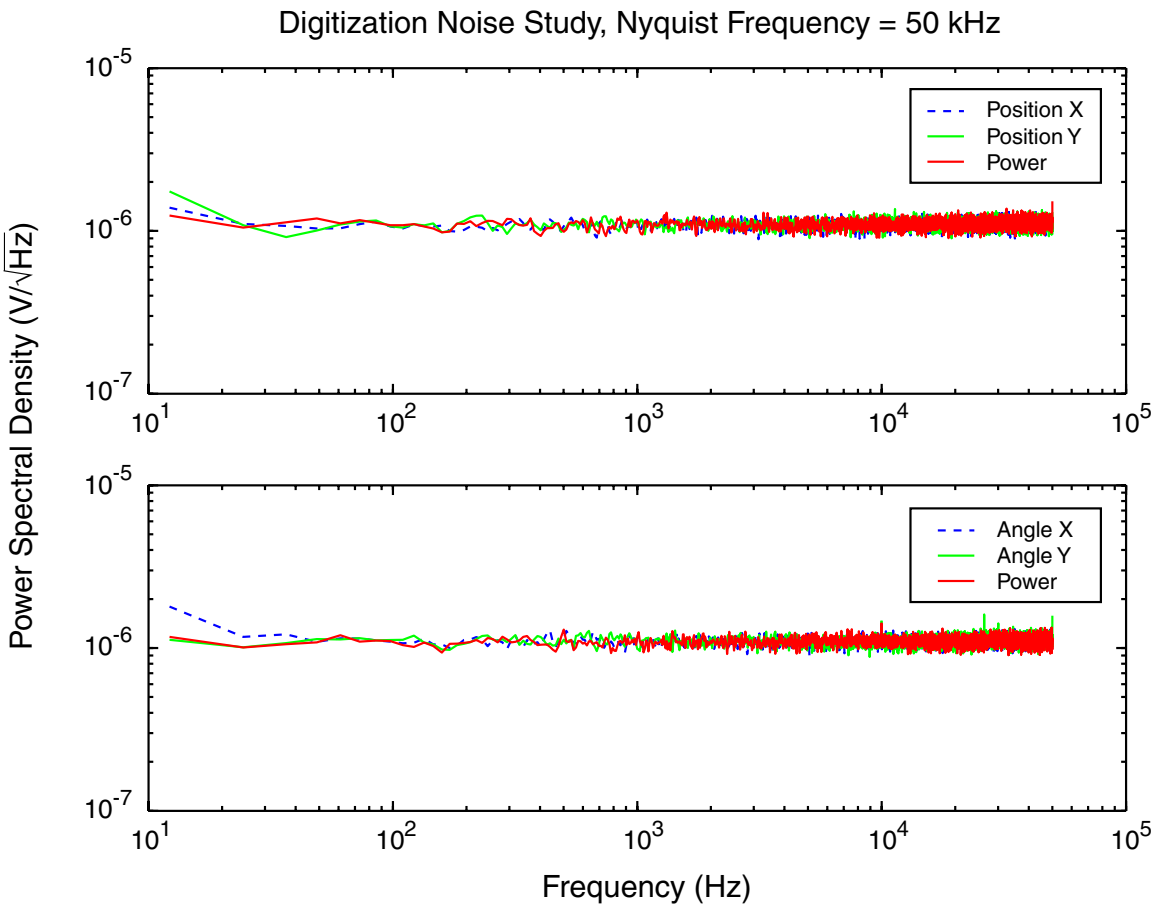

Figure 3-15: Digitization noise study. The A/D board is sampled at 100 kHz for 6 s while all six input channels dedicated to beam position and angle sensing are shorted.

when all six channels dedicated to sense the beam position and angle are shorted. The board is set to sample at 100 kHz for 6 s. As expected, the measured power spectrum is flat, and the spectral density is at 1.11×10^{-6} V/$\sqrt{\text{Hz}}$, meaning that the board is within specification.

The digitization noise dominates over the PSD sensor noise and sets the DAQ system noise floor.

3.3.2 DAQ system accuracy

The photocurrents generated by the PSDs are converted into analog voltage signals via On-Trak OT-301 transimpedance amplifiers. Each amplifier has three analog outputs: x and y positions of the beam with a range of ± 10 V, and the beam power with a range between 0 and 6 V. Each is also equipped with six gain settings (G1 through G6), varying from 4×10^3 to 4×10^6 V/A to accommodate input current ranges from 1.5 μA to 1.5 mA.

In this section, an experiment is performed to measure the relative accuracy of the

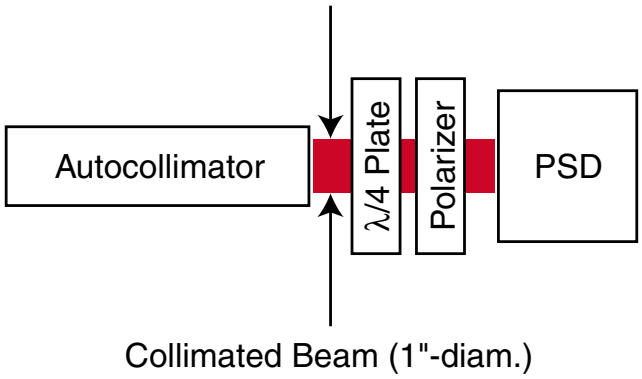

Figure 3-16: Optical setup for determining the DAQ system accuracy.

DAQ system, as limited by the sum of the noises from the PSD sensor, the amplifier, the wiring and the A/D board. Not surprisingly, the measured figure lies above the digitization noise floor (Sec. 3.3.1) and is determined primarily by the noise of the amplifier.

A collimated laser beam, approximately 25 mm in diameter, is pointed at one of the PSDs, with an attenuator in between to allow intensity adjustment. The reason why I use such a large and collimated beam is to rid position fluctuations due to any mount-drift induced beam drift. The analog design of the amplifier allows it to output x and y positions of the beam, independent of intensity fluctuations. The source section from an old Newport autocollimator produces the beam nicely with a circular polarization at $\lambda = 670$ nm. The attenuator is made up of a quarter-wave plate, followed by a polarizer. Figure 3-16 shows the setup. Because the laser diode is dying due to age, only with the amplifier at its highest gain (G6) can I reach 5 V at the power output, under which On-Trak recommends to optimally operate the PSDs. It means the measured system accuracy strictly applies only to one out of the six transimpedance gain settings. However, there is every reason to believe that the highest gain generates the most noise. The accuracy thus established represents a worst-case estimate on the system performance.

Figure 3-17 shows the DC-subtracted power spectral densities for the x and y outputs from the amplifier. The data is an average of five sets, each 1 s-long at a sample rate of 100 kHz. Although no anti-aliasing procedure is adopted, both signals reach the digitization noise floor at high frequencies. In other words, any aliased power lies within the noise and can be safely ignored. The measured variances in x and y are $\sigma_x^2 = 4.66 \times 10^{-6}$ V^2 and $\sigma_y^2 = 5.06 \times 10^{-6}$ V^2, respectively. The total variance is

$$\sigma_{\text{tot}}^2 = \sigma_x^2 + \sigma_y^2 = 9.72 \times 10^{-6} \text{ V}^2 \quad . \tag{3.30}$$

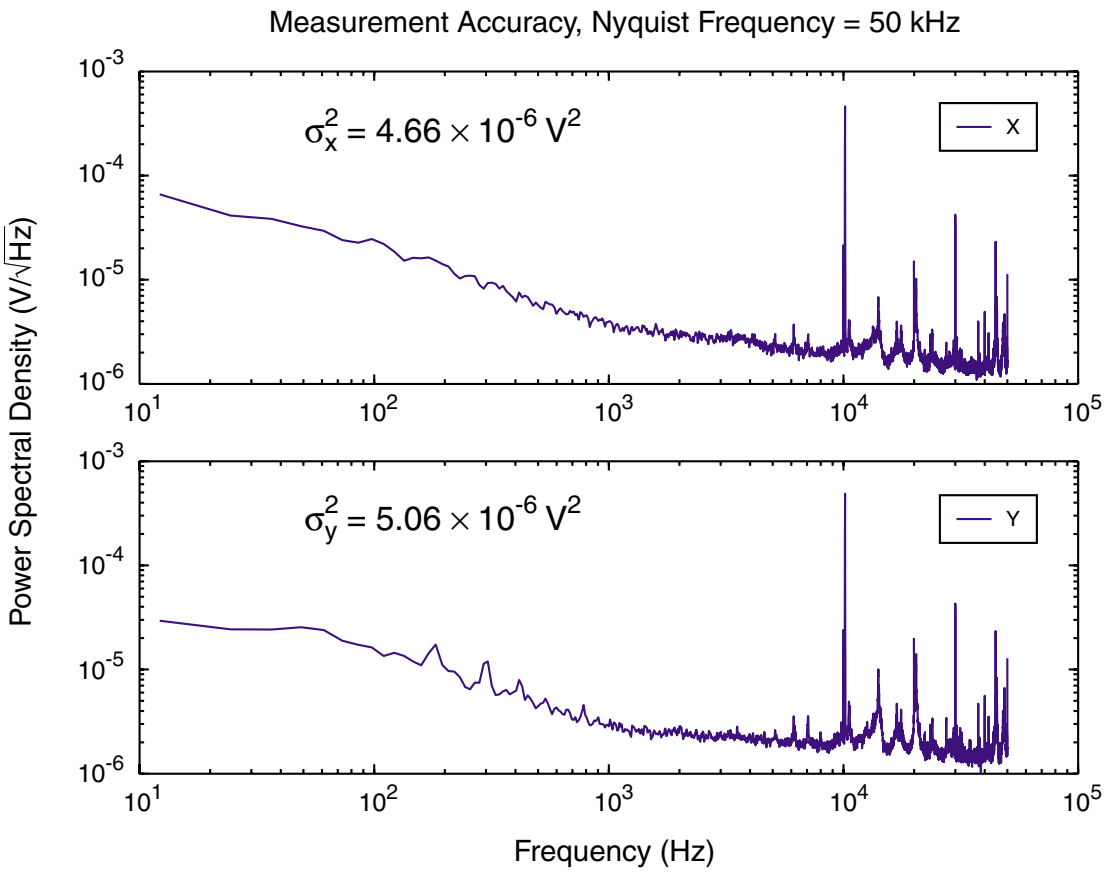

Figure 3-17: DAQ system accuracy study. The DC-subtracted power spectral density plots are averaged from five data sets. Each is 1 s long and sampled at 100 kHz.

Table 3.2 translates the above figures into relative accuracies in beam position and angle readouts. The listed numbers correspond to worst-case values. During actual beam alignment, the amplifiers are routinely used at lower gain settings. The readouts from the x and y axes are closely matched. The slight mismatch may be caused by minute differences in the x and y amplifier circuits.

I emphasize that these are relative accuracy numbers. Both the position and angle readouts change in absolute values when different amplifier gain-settings are used. However, as long as all measurements can be done under the same gain setting, which is the case during SBIL alignment, absolute accuracy should not be a concern.

3.4 Period stabilization

An experiment is performed to verify that for a grating beamsplitter, the angular instabilities in the two lithography arms are "antisymmetrically" correlated, i.e., if the beam varies in angle by $+\delta$ in one arm, it varies by $-\delta$ in the other. The antisymmetry is important for providing the required 1 ppm period stabilization of the grating image (Sec. 2.1.1). Results from this section will show that the antisymmetry does exist and

Relative accuracy (three-sigma)	
Position x	1.30 μm
Position y	1.35 μm
Angle x	1.20 μrad
Angle y	1.25 μrad
Overall position	1.87 μm
Overall angle	1.73 μrad

Table 3.2: System measurement accuracy. The numbers are maximum values obtained under a worst case when the amplifier is set to the highest gain (G6).

the period stabilization is at 1 ppm.

3.4.1 Experimental setup

The setup must be able to measure the angular noise of the beams in the two arms simultaneously. The lithography interferometer is used in the beamsplitter mode with the pinholes in place (Fig. 2-7), the position PSD is temporarily converted into another angle PSD, and the position decoupling lens ($f = 270.5$ mm) is temporarily replaced by another angle decoupling lens ($f = 540.9$ mm). I call the converted detector Angle PSD No.1, and the other, Angle PSD No.2. No.1 is used to sense the angular noise in the left arm, and No.2 the right arm. The axis of the PSD sensor that is parallel to the vertical optical bench is the x axis, and the one perpendicular is y.

The measured axis rotation between the two PSDs is 1.4°. Based on the beam instability data (Sec. 3.5.1), one can estimate that this slight rotation contributes a coordinate-mixing induced measurement error of at most 0.2 μrad, which is incorporated in the measurement consistency results that will be presented in Section 3.4.2.

My objective is to study the angular noise correlation. A DC offset between the readouts of the two angle PSDs is of no concern. For instance, when the same beam gets routed to the PSDs, if the beamsplitter and the mirror before the PSDs (Fig. 2-7) are not adjusted, one of them may yield a voltage readout in the x direction of +0.1 V DC and the other −0.2 V DC. This small offset is not important because I am only interested in the AC noise variance. Large offsets however are undesirable since PSD position nonlinearities do exist across the length of the detector.

Both PSD amplifiers are used under the same transimpedance gain—G3. All experimental data in this section is originally sampled at 100 kHz, then digitally resampled at 25 kHz to prevent aliasing.

3.4.2 Measurement consistency

Before the correlation experiment, the system's measurement consistency must be established. Given the same input, how well do the two angle PSDs match in output?

In addition to electronic noise, other factors also limit the measurement consistency. As mentioned earlier, there are errors associated with the relative rotation of the PSD sensors and sensor nonlinearities. The NI 6034E board is not a simultaneous-sampling board, which is required if one truly wants to obtain two angle readouts at any one instant of time. Nevertheless, the board allows a meaningful experiment because it can switch between two different channels with a fast settling time of less than 5 μs [63]. Thirdly, different amplifiers are used to convert the signals from the PSDs. The fact that the amplifiers are used under the same nominal gain not withstanding, their noise characteristics may well be different. The gains, despite being nominally equal, may be slightly off, resulting in a scale factor. Furthermore, PSD sensors may not be located precisely at the focal planes of the decoupling lenses. As a result, small amounts of beam position noise may contaminate the angle readouts (Sec. 3.1.2). Finally, thermal and mechanical disturbances experienced by the optical bench, the mounts and the optics themselves may lead to additional inaccuracies.

With the same beam—the right arm—propagating onto both angle PSDs, Figure 3-18(a) and (b) show a set of time-domain DC-subtracted signals from the amplifiers' x outputs (angle-x), while (c) shows the difference between (a) and (b). The shape of (c) suggests the existence of a scale factor between the gains of the amplifiers. Using the least-squares method [64], one finds the scale factor to be approximately $a_x = 1.27$, defined as the gain of PSD No.1 divided by No.2. Figure 3-18(d) shows the difference between (a) and (b) while taking into account a_x. Similarly, for angle-y, the scale factor is approximately $a_y = 0.95$. Figure 3-19 presents the power spectral density plots for both angle-x and angle-y difference signals. When the same beam is incident upon both angle PSDs, the three-sigma measurement consistency of the system is 1.51 ± 0.23 μrad along x and 1.39 ± 0.26 μrad along y, based on the analysis of 10 data sets. In other words, the x outputs from the angle PSDs are matched to about 1.51 μrad and y to 1.39 μrad. Note that I have specified the experimental uncertainties. To the uncertainties present, the measurement consistency in x agrees with that in y.

3.4.3 Angular noise correlation

With both arms on, the system is adjusted so that only the left arm is incident upon Angle PSD No.1, and only the right arm is incident upon Angle PSD No.2. The adjustment is done by purposely misaligning the incident angles of the two arms,

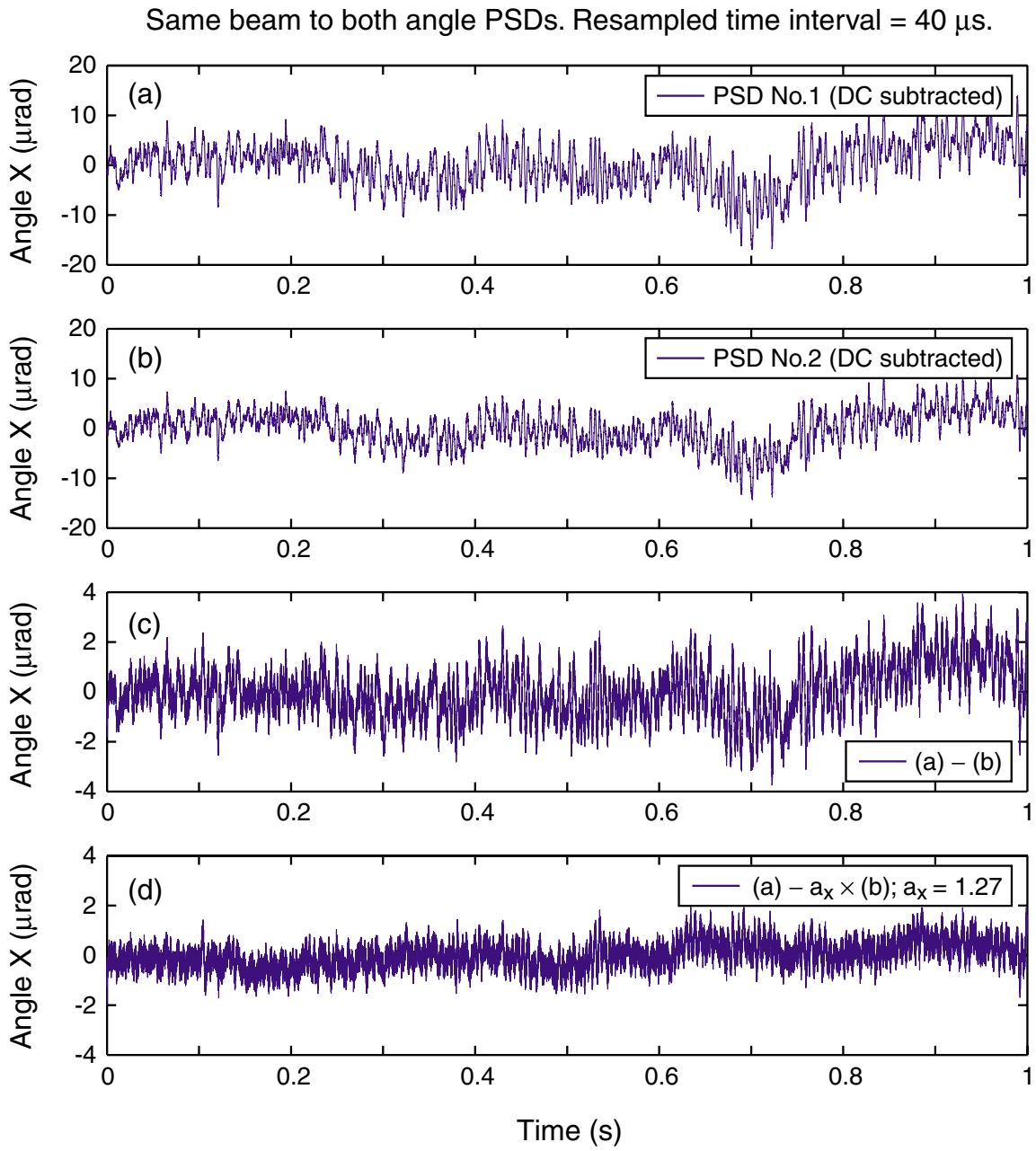

Figure 3-18: Same beam—the right arm—onto both angle PSDs. (a) DC-subtracted angle-x readout from Angle PSD No.1. (b) DC-subtracted angle-x readout from Angle PSD No.2. (c) Difference between a and b without gain adjustment. (d) Difference between a and b with gain adjustment.

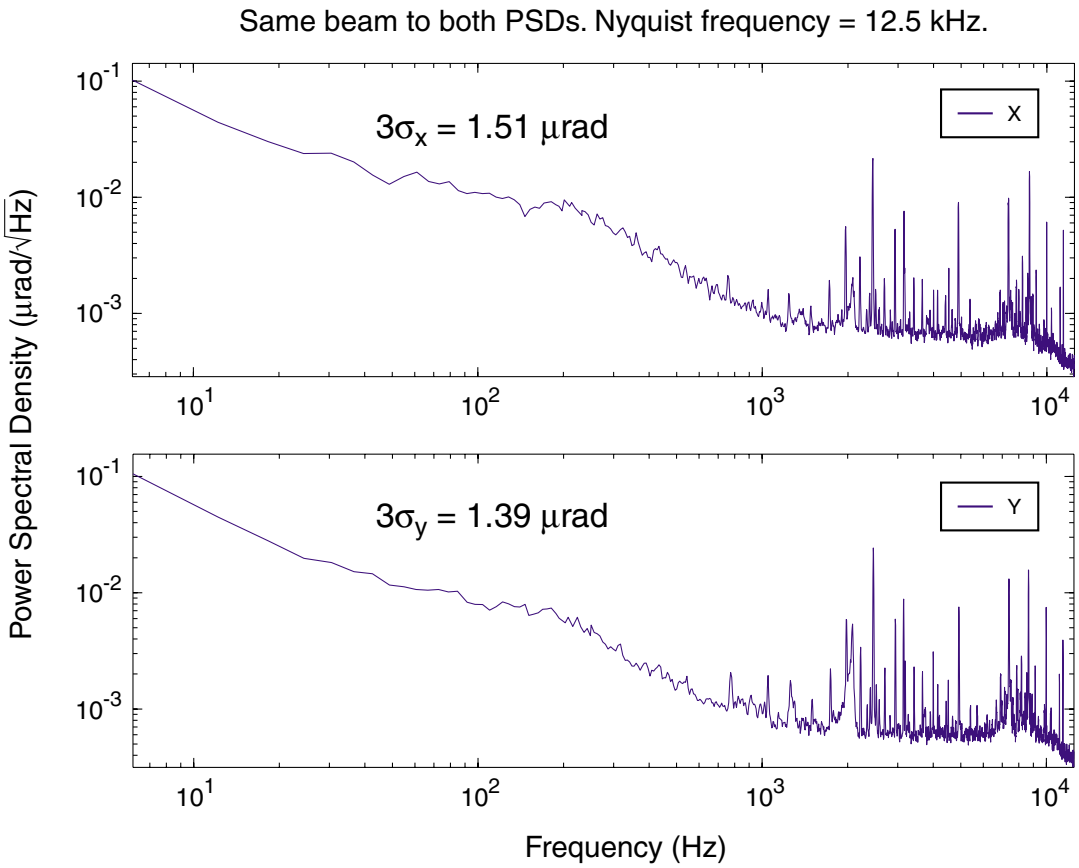

Figure 3-19: Measurement consistency. The DC-subtracted power spectral density plots for the angle-x and angle-y difference signals, averaged from 10 data sets.

separating the beams spatially and blocking the appropriate ones behind the angle decoupling lenses. It is done by exploiting the fact that I am only interested in AC noise variance. In theory, a polarizing beamsplitter cube can be used to separate and redirect the beams as they propagate to the PSDs on top of one another. This of course requires independent polarization controls in both arms. However, in reality, the polarizing effect due to the other optics and the polarization mixing of the cube itself renders the scheme useless.

Figure 3-20(a) shows a sample angle-x signal for the left arm, and (b) for the right arm. The antisymmetric nature of the angular noise correlation between the arms is evident. Adjusting for the amplifier-gain mismatch, Figure 3-20(c) shows the sum of (a) and (b). The three-sigma standard deviation of the angle-x sum signal is 2.02 ± 0.27 μrad, averaged from 10 such data sets. Again, I have noted the experimental uncertainty.

Figure 3-21(a) shows a sample angle-y signal for the left arm, and (b) for the right arm. No antisymmetry is observed, which is expected as the grating beamsplitter,

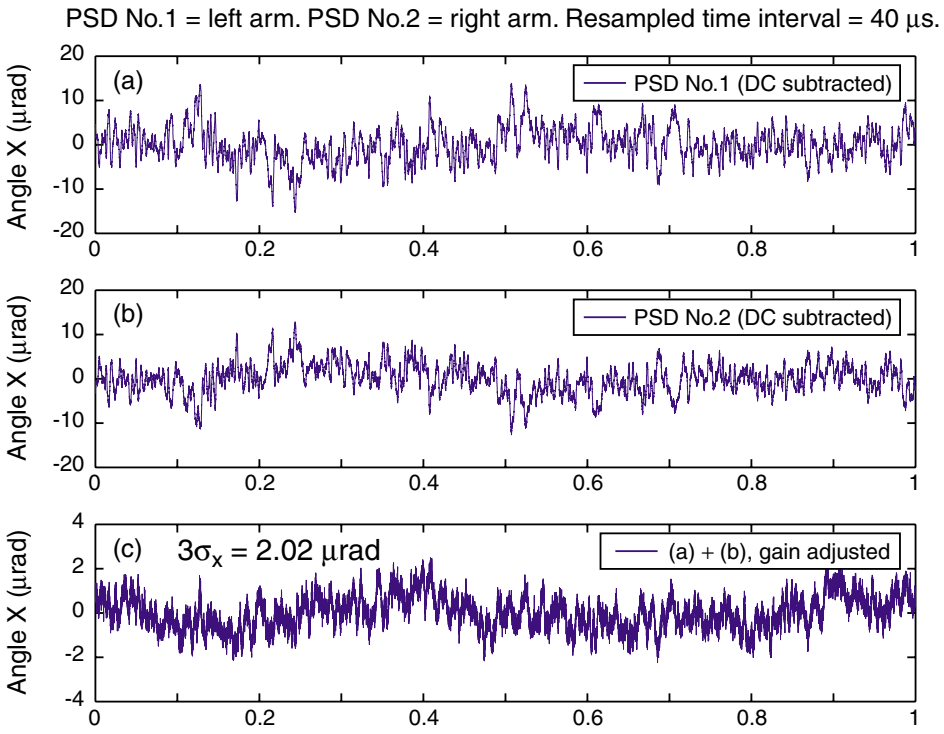

Figure 3-20: Angular noise correlation along x. (a) Angle-x noise in the left arm, and (b) in the right arm. (c) Gain adjusted sum of (a) and (b).

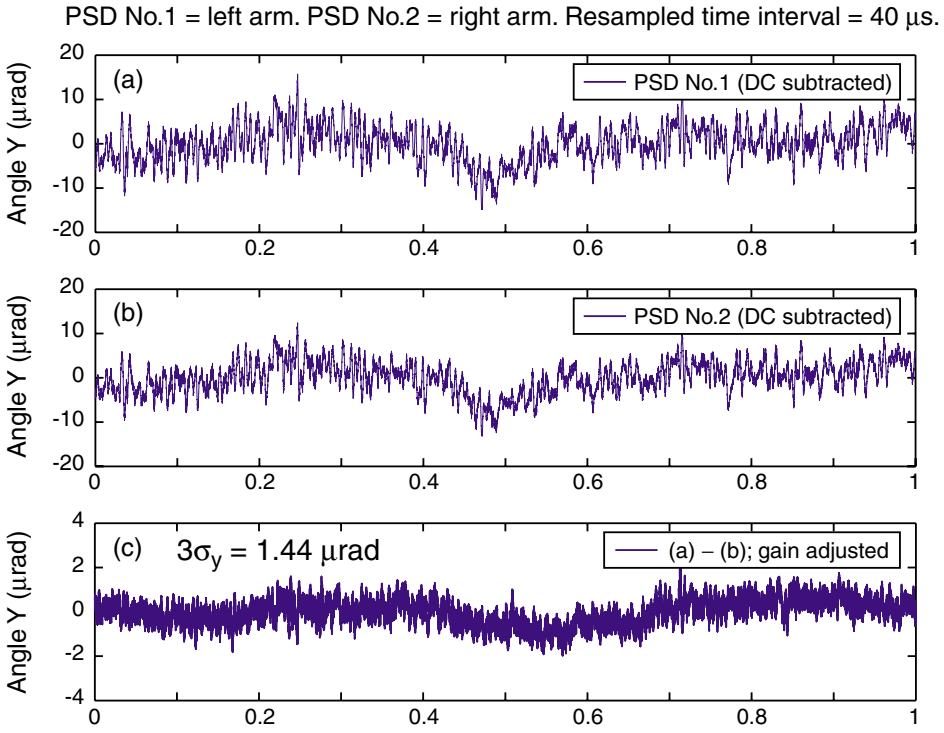

Figure 3-21: Angular noise correlation along y. (a) Angle-y noise in the left arm, and (b) in the right arm. (c) Gain adjusted difference between (a) and (b).

with its vector oriented along the x direction, exerts no influence along y. Figure 3-21(c) shows the difference of (a) and (b), again adjusted for the gain mismatch. The three-sigma standard deviation of the angle-y difference signal is 1.44 ± 0.21 μrad, averaged from 10 data sets.

I have demonstrated quantitatively that the two arms are antisymmetrically correlated in angle-x and symmetrically correlated in angle-y. The correlation in y fits comfortably within the measurement consistency of 1.39 ± 0.26 μrad established in Section 3.4.2. The 2.02 ± 0.27 μrad correlation figure in x, on the other hand, seems just slightly larger than the consistency of 1.51 ± 0.23 μrad. While an exact number is out of reach, it is reasonable to suspect that any non-antisymmetrically-correlated component in x, if it even exists, is on the order of sub-μrad. Since the consistency figures (Sec. 3.4.2) already take into account errors due to sensor orientation and nonlinearity, non-simultaneous sampling and amplifier noises, the most plausible explanation for any non-correlation may be attributed to mechanical disturbances experienced by the optical mounts in the two widely separated lithography arms. In particular, since mirrors reflect the beams instead of transmitting them, if the mirror mounts vibrate or are subject to other forms of random external excitations despite the quelling of the environmental enclosure, that will introduce uncorrelated beam angle noises on the sub-μrad level.

Suppose that the non-antisymmetrically-correlated angle-x component is 0.5 μrad. Assuming one arm is fixed at angle θ and the other at $(\theta + \delta)$, a similar expansion to Eq. (B.3) predicts an angle-change induced period variation of $\frac{1}{2} \cot \theta \, \delta$. For a nominal grating period of 400 nm, i.e., $\theta = 26°$, and $\delta = 0.5$ μrad, the estimated period variation is only 0.5 ppm. This is a ceiling estimate as SBIL exposure requires a relatively long dose build-up time, which means that high-frequency errors do not print through. Reference [48] contains a good discussion of SBIL's immunity to high-frequency phase jitters. Later, this thesis will also delve into detailed discussions on how overlapping scans can provide highly efficient averaging of the resist-grating phase.

3.5 Results

Position and angle instabilities in both lithography arms have been experimentally characterized. Section 3.5.1 presents the results. I demonstrate the performance of the SBIL beam alignment system in Section 3.5.2 by measuring the system's repeatability.

3.5.1 Beam position and angle instabilities

Despite the use of a beam steering system to stabilize the pointing of the lithography laser in real time, the beam has some residual angle instability. An experiment is

Left arm beam instability (three-sigma)	
Position x	32.3 μm
Position y	24.1 μm
Angle x	8.3 μrad
Angle y	10.3 μrad
Overall position	40.3 μm
Overall angle	13.2 μrad

Table 3.3: Left arm beam instability, averaged from 10 data sets.

Right arm beam instability (three-sigma)	
Position x	27.2 μm
Position y	22.1 μm
Angle x	7.4 μrad
Angle y	8.6 μrad
Overall position	35.1 μm
Overall angle	11.4 μrad

Table 3.4: Right arm beam instability, averaged from 10 data sets.

performed to measure it. Such a quantitative knowledge is critical for analyzing and predicting the SBIL performance.

Data presented in this section are all sampled at 16 kHz, then digitally resampled at 2 kHz. Figure 3-22 shows a sample data set from the left arm. The experiment is performed with the system in the beamsplitter mode. Readouts from the position and angle PSDs are recorded. Amplifier gains are set at G3.

Tables 3.3 and 3.4 summarize the findings. By first transforming the time-domain data into their respective power spectral densities, and then averaging over 10 such data sets, one gets the mean power spectral density curve. Numerical integration leads to the variance of the respective signal.

Given the noise present in the DAQ system (Sec. 3.3.2), angular instabilities in the two arms agree as expected. The measured distance between the two position decoupling planes, one for the beam steering system and the other for the beam alignment system (used in beamsplitter mode), is approximately 3 m. Based on the angular instability values, the predicted position instabilities are 34 μm for the right arm and 40 μm for the left arm. This is indeed confirmed by the experiment.

Throughout the thesis, when I need to quote a figure for the beam angular instability δ, I will use $\delta = 11.4$ μrad, three-sigma. This, according to Eq. (B.2), gives rise to a theoretically-predicted period variation of 65 parts per trillion, well within

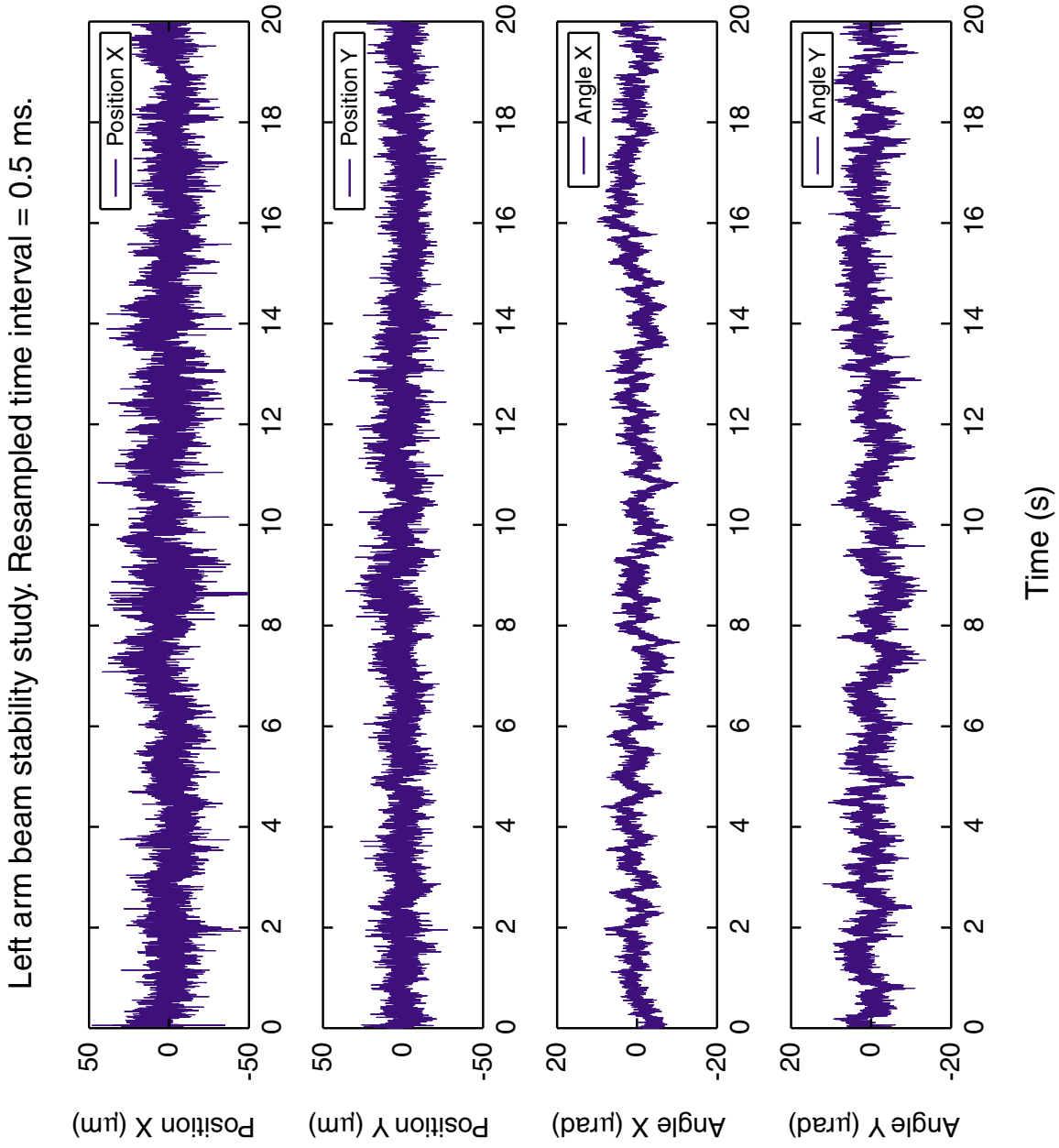

Figure 3-22: A sample data set from the beam instability study for the left arm. All data are DC-subtracted.

the 1 ppm SBIL period stabilization requirement. In reality of course, the fantastic theoretical limit is not approached, nevertheless, results from Section 3.4.3 show that the 1 ppm goal is achieved.

3.5.2 Beam alignment performance

The observed one-sigma beam position and angle instabilities are $\sigma_{\text{pos}} = 12$ μm and $\sigma_{\text{ang}} = 3.8$ μrad, respectively.

I determine through a series of repeatability experiments whether or not one can align the mean beam angle and position to better than the noise present. Recall that the goal is to overlap the beam centroids and equalize the mean beam angles to the μm and the μrad level, respectively.

Figure 3-23 shows the results from 52 sets of alignment repeatability experiments, conducted using the left arm of the lithography interferometer. In each experiment, the spots are commanded to return to the origins on both the position and angle PSD's. The alignment is complete when the controller senses that the mean position has returned to within a full σ_{pos} from the origin and the mean angle has returned to within $\sigma_{\text{ang}}/2$. The time interval dedicated to sensing the means in between consecutive picomotor commands is 0.1 s, at a sampling rate of 10 kHz. When the alignment is complete, a 5 s-long data set is sampled. The means from this data set are used to plot Figure 3-23.

All position means fall within the $\sigma_{\text{pos}} = 12$ μm circle as commanded. Most of the angle means fall within the $\sigma_{\text{ang}}/2 = 1.9$ μrad circle. Small spillovers are observed, caused most likely by inaccuracies in determining the means while the alignment is in progress. From elementary statistics theory [65], the error on the mean (μ) is related to the error of a single measurement (σ) by

$$\mu = \frac{\sigma}{\sqrt{N}} \quad , \tag{3.31}$$

where N is the number of measurements used to determine the mean. Given the measured angle noise of 11.4 μrad, during the alignment process, 1000 data points (0.1 s $\times$ 10 kHz) are used to obtain the arithmetic mean, which translates into $\mu =$ 0.36 μrad. Eq. (3.31) assumes that only random errors exist, whereas in reality, small systematic errors are present as well and will ultimately limit the measurement accuracy of the mean.

Recall that the picomotors enable a beam angle adjustability of approximately 1.5 μrad. Being able to align the mean beam angle to 2 μrad means that I am aligning to the picomotor resolution. At 400 nm period, angle setting at the 2 μrad level allows a grating image period adjustability of around 4 ppm.

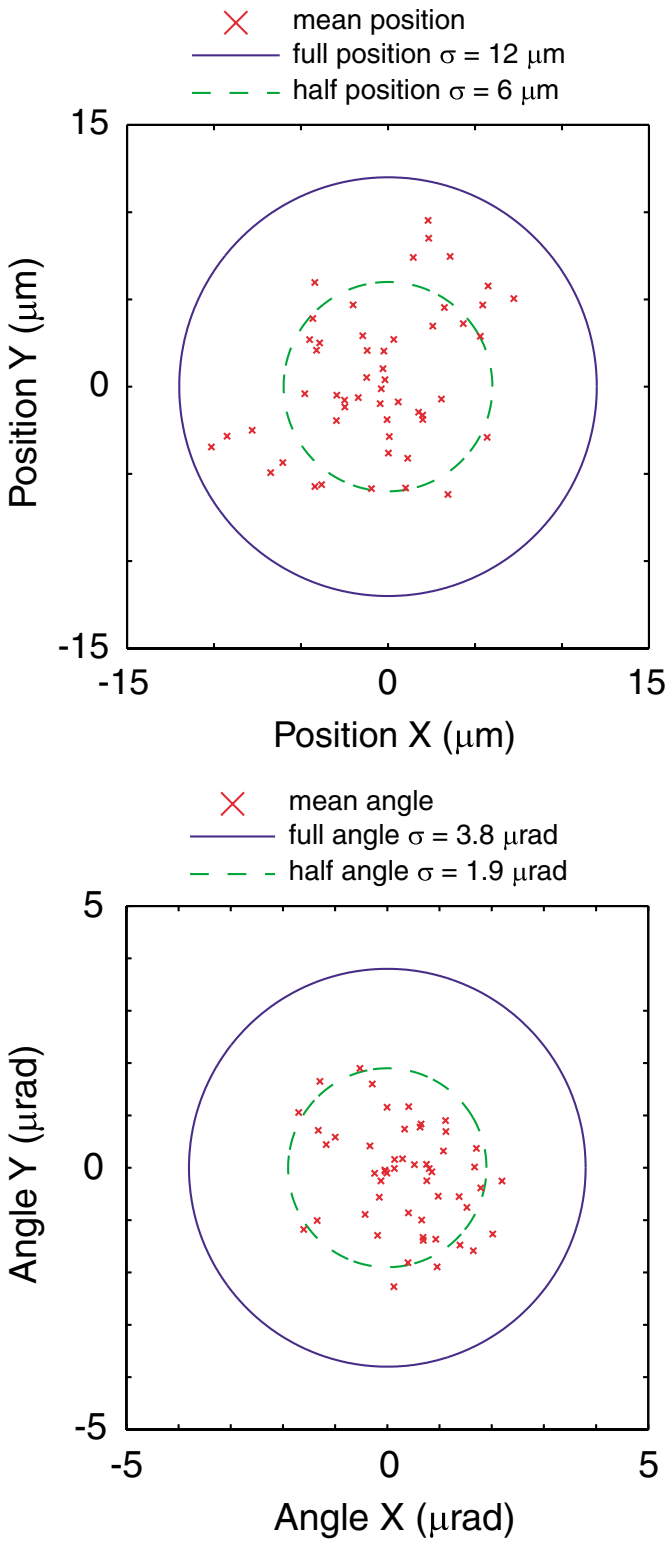

Figure 3-23: Beam alignment results.

3.6 Summary

SBIL "period control" refers to one's ability to establish, stabilize and measure the grating image period.

In this chapter, I have described the design and implementation of an automated beam alignment system. The system can align mean beam angles to 2 μrad, which means the grating image period can be established with an adjustability of 4 ppm at 400 nm. An experiment is also performed to verify explicitly that the angular noise in the two interferometer arms are correlated antisymmetrically. Measurement results show that period stabilization is at 1 ppm.

The measured three-sigma beam angle instability is 11.4 μrad. Taking into account the beamsplitter manufacturing and installation imperfections, a worst-case projection gives a substrate unflatness induced phase error of 0.6 nm over a 300 mm wafer.

As I will describe in the next chapter, the rectangular beamsplitter used for beam alignment is also employed for fringe period measurement. This dual function ensures that the splitter measures the correct period as seen by the substrate.

Chapter 4

Period measurement

By the phrase "grating image" or "image grating", I refer to the small patch of standing wave pattern produced by the interference of two Gaussian laser beams.

For SBIL to succeed in writing large gratings with nanometer level phase nonlinearities, it is critical that the stage steps over by an integer number of fringe periods between adjoining scans. This is the only way to ensure good exposure contrast. The concept is illustrated schematically in Figure 4-1. In an ideal case, the stage moves by an exact integer multiple of the fringe period. Dose builds up correctly and the contrast is maximized. In a worst case, the stage moves by an additional one-half of the period. Resist contrast is lost and grating lines are completely "washed out".

I use "period control" to describe efforts to establish, stabilize and measure the grating image period. In the previous chapter, I described a beam alignment system that can equalize mean beam angles to 2 μrad, which is important for setting the fringe period to the part-per-million (ppm) level. I also conducted an experiment to verify explicitly that the two interferometer arms are correlated antisymmetrically in angle noise, which is essential to maintain a stable period. The topic of discussion for this chapter is how to measure the period *in-situ* and with extreme accuracy. Having obtained the right period, how to control the stage such that it does move over by an integer multiple of the period is a critical problem as well. That is the subject of another Ph.D. thesis [48].

The error budget allocated to period measurement is stringent. To ensure optimal stitching between scans, and more importantly, to ensure period control at the picometer level, the placement of the grating image must be controlled to $\sim$1 nm at the edge of a 1 mm radius spot. In other words, one must measure the fringe period to approximately 1 nm/1 mm = 10^{-6}, or 1 ppm. At this level, phase nonlinearity in the resist grating due to any period measurement error is confined to subnanometers

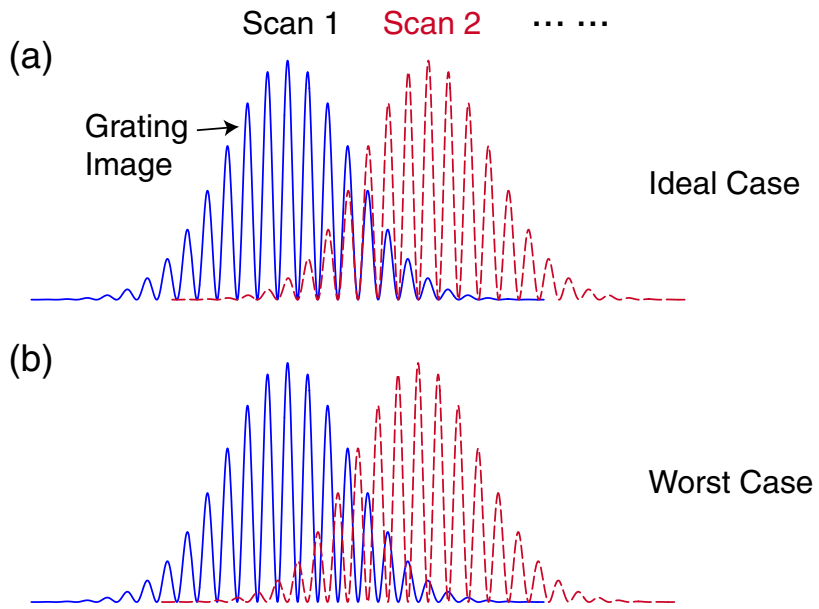

Figure 4-1: Stitching scans. (a) The ideal case where the stage moves by an integer number of fringe periods. Contrast is optimal. (b) The worst case where the stage moves by an additional one-half of a fringe period. Contrast is completely lost. Fringe period grossly exaggerated for illustration.

(Sec. 4.5).

Exposing the interference pattern in resist and measuring the period of the developed grating with a scanning electron microscope (SEM) is an extremely slow, laborious and inaccurate process. Moreover, it yields period measurement in units traceable to the SEM used, whereas I desire length units defined by SBIL's stage displacement measuring interferometer. A direct aerial image measurement utilizing a slit artifact [66] is difficult to implement for small grating periods, due to energy throughput and fabrication reasons.

A couple of simple interferometric techniques have been developed at MIT to measure the grating image period *in-situ* and with high accuracy [47, 67]. Figure 4-2 schematically demonstrates the one currently in use. The left and right beams are incident upon a beamsplitter mounted on the stage. SBIL beam alignment system adjusts the beams so that they coincide in space and interfere at a photodetector. The voltage readout from the detector duplicates the light intensity variation. Let the stage be displaced by a distance D. The number of signal oscillations observed at the detector corresponds to the number of fringes in the grating image that the beamsplitter has traversed. Let the number be N. The fringe period p is given by

$$p = \frac{D}{N} \quad . \tag{4.1}$$

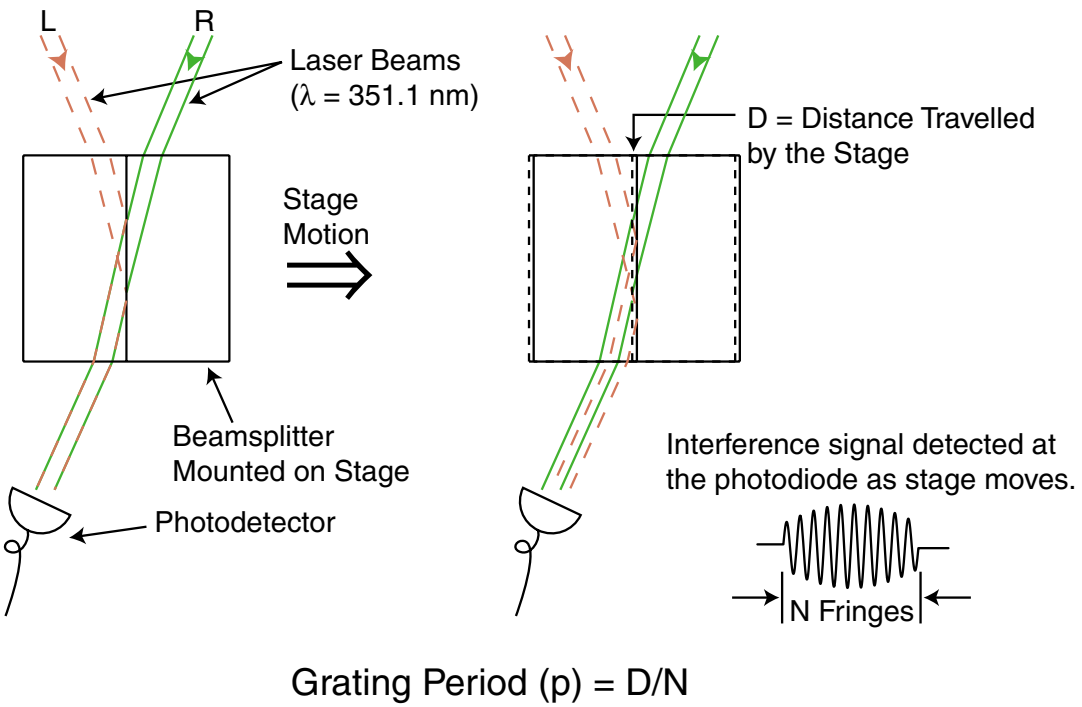

Figure 4-2: Beamsplitter period measurement scheme.

For gratings with a period of 400 nm, a 1 ppm measurement error translates into 0.4 pm, a tiny number indeed. Is the beamsplitter, which can neither be manufactured nor installed with perfection (Sec. 3.2.2), capable of measuring the fringe period to this level of accuracy? Section 4.1 sets out to explore the theoretical limits of the scheme.

4.1 Theory

At first glance, measuring the fringe period with a beamsplitter seems so straightforward an idea that it needs no further discussion, till one realizes that SBIL demands a measurement accuracy of 1 ppm. Intuitively, the scheme works since the fringes in the grating image are oriented parallel to the beamsplitter interface—remember that the same beamsplitter is also used for beam alignment. But, what happens if they are not, due to errors in aligning the beams? And what happens if the beamsplitter interface is not aligned exactly perpendicular to the substrate, or if the beamsplitter itself has a non-ideal shape? Could the beamsplitter still measure, with the required accuracy, the fringe period that is seen by the substrate during lithography? In this section, I answer these questions.

To intuit the discussion and to make the math tractable, I limit myself to consider uniform plane waves most of the time. In Section 4.1.7 where it is necessary to investigate the light irradiance, i.e., intensity distribution over a non-point photodetector,

the incident beams are assumed to have Gaussian amplitude profiles and planar phase fronts. Up to Section 4.1.8, an ideal world is assumed where the beamsplitter is made to perfection. In Sections 4.1.9 and 4.1.10, I consider the non-ideal scenario where the beamsplitter has certain defects in its shape. Section 4.1.11 briefly discusses the fringe nonlinearity-induced stitching error. Throughout the discussion, all mechanical parts and attachments are assumed to be infinitely rigid.

A point photodetector is an imagined, physically unrealizable device that can sample light at a single point in space. In other words, it is an intensity detector. A real-world photodetector, on the other hand, is a power sensor that integrates the light intensity over a certain area. In an approach that tackles the problem with increasing sophistication, I start by considering period measurement with a point detector, which can be analyzed straightforwardly with ray tracing. Building on the basic result, I then generalize the theory to describe physical non-point detectors.

A detector can be fixed in the laboratory frame, e.g., on the vertical optical bench where it is always stationary, or, be mounted on the interferometer stage, in which case, it moves with the beamsplitter. Practicality requires that SBIL uses the former layout. Whenever necessary, a section is divided into two case studies based on the two mounting schemes—the case where the detector is fixed and the beamsplitter is moving, and the case where the detector and the beamsplitter move in unison. For a point detector, depending on which mounting scheme is used, the measured period can be either exactly or only approximately the actual fringe period. When a physical detector such as a photodiode is used, I show that both mounting schemes give the correct fringe period as far as SBIL measurement accuracy is concerned, though measurement errors that are negligible to SBIL do exist.

A quick note on nomenclature: Often, I will call a non-point photodetector a physical detector, or alternatively, a photodiode.

4.1.1 Principle of operation

The principle of operation for *in-situ* fringe period measurement via a beamsplitter is quantitatively discussed in this section.

Case I. Point detector fixed; beamsplitter moving

Figure 4-3 shows the ray tracing for the ideal case where the left and the right beams, both plane waves, have been aligned perfectly with equal angle of incidence θ. The point detector is fixed while the beamsplitter moves. In practice, the topology as drawn may not be implemented since it entails fixing the detector to the granite surface on which the air-bearing stage floats. A mirror must be inserted to divert the beams elsewhere, e.g., to the vertical optical bench on which the detector can then

be attached. The addition of a moving mirror necessarily complicates the analysis when the left and the right beams have different angles of incidence (Sec. 4.1.3). For the current case however, the presence of a mirror is inconsequential, because the beams propagate coincidently after the beamsplitter, and see the same optical path length (OPL) change after reflecting off the mirror. In other words, the presence of a mirror does not alter the resulting phase of the interference signal at the detector. For simplicity, I proceed without the mirror.

As the rectangular beamsplitter is displaced by a distance D, the change in OPL in the left arm is

$$\Delta L = 2\ D\ \sin\theta\ \ , \tag{4.2}$$

where a unity air index is assumed and will be assumed throughout Section 4.1. The change in the right arm is zero since the beam transmits through the beamsplitter and experiences no phase shift before and after the displacement. The difference between the two yields the net change in OPL, which is simply ΔL. At the detector, the change in spatial phase is

$$\Delta\phi = 2\ \pi\ \frac{\Delta L}{\lambda}\ \ , \tag{4.3}$$

where λ is the laser wavelength. The number of phase cycles N is related to $\Delta\phi$ by

$$N = \frac{\Delta\phi}{2\ \pi} = \frac{D}{p}\ \ , \tag{4.4}$$

where $p = \frac{\lambda}{2\ \sin\theta}$ is the period of the grating image formed by the interference of two plane waves. Reversely, by counting the number of phase cycles at the point detector and knowing the beamsplitter displacement, one can calculate the period of the grating image

$$p = \frac{D}{N}\ \ . \tag{4.5}$$

Case II. Point detector moving with the beamsplitter

Figure 4-4 shows a configuration where the point detector is mounted on the stage, and moves with the beamsplitter as it is displaced. The change in OPL in the left arm is

$$\Delta L = \Gamma_1 + \Sigma_1 - \Pi_1 = D\ \sin\theta\ \ , \tag{4.6}$$

where Γ_1, Σ_1 and Π_1 are path length segments graphically defined in the Figure 4-4. Note that no messy OPL analysis inside the cube is needed because of the simple rectangular geometry. Similarly, the change in the right arm is

$$\Delta R = -\Gamma_2 + \Sigma_2 - \Pi_2 = -D\ \sin\theta\ \ . \tag{4.7}$$

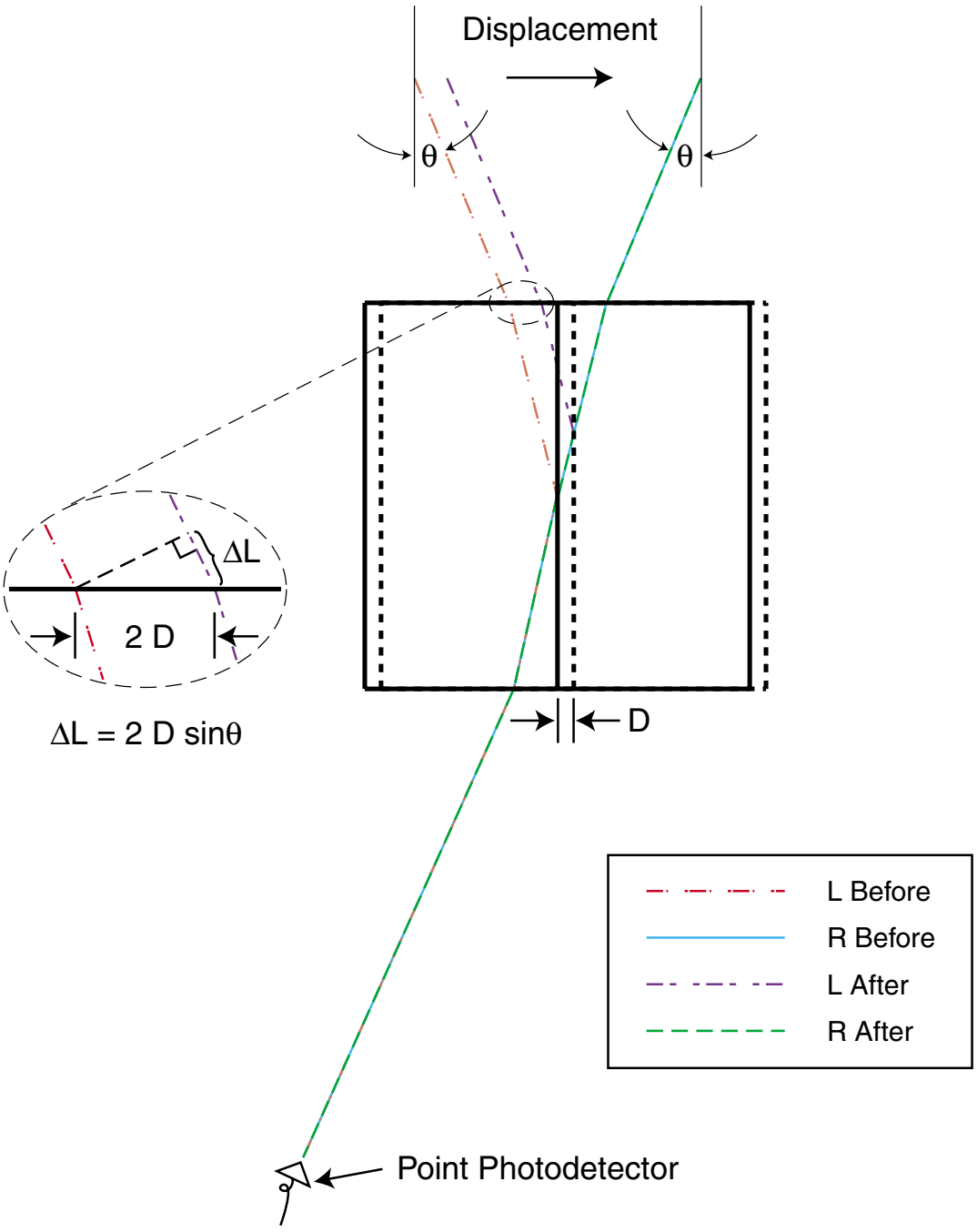

Figure 4-3: Ray trace for the case where the point detector is fixed while the beam-splitter is displaced by a distance D. The left and right incident angles are equal.

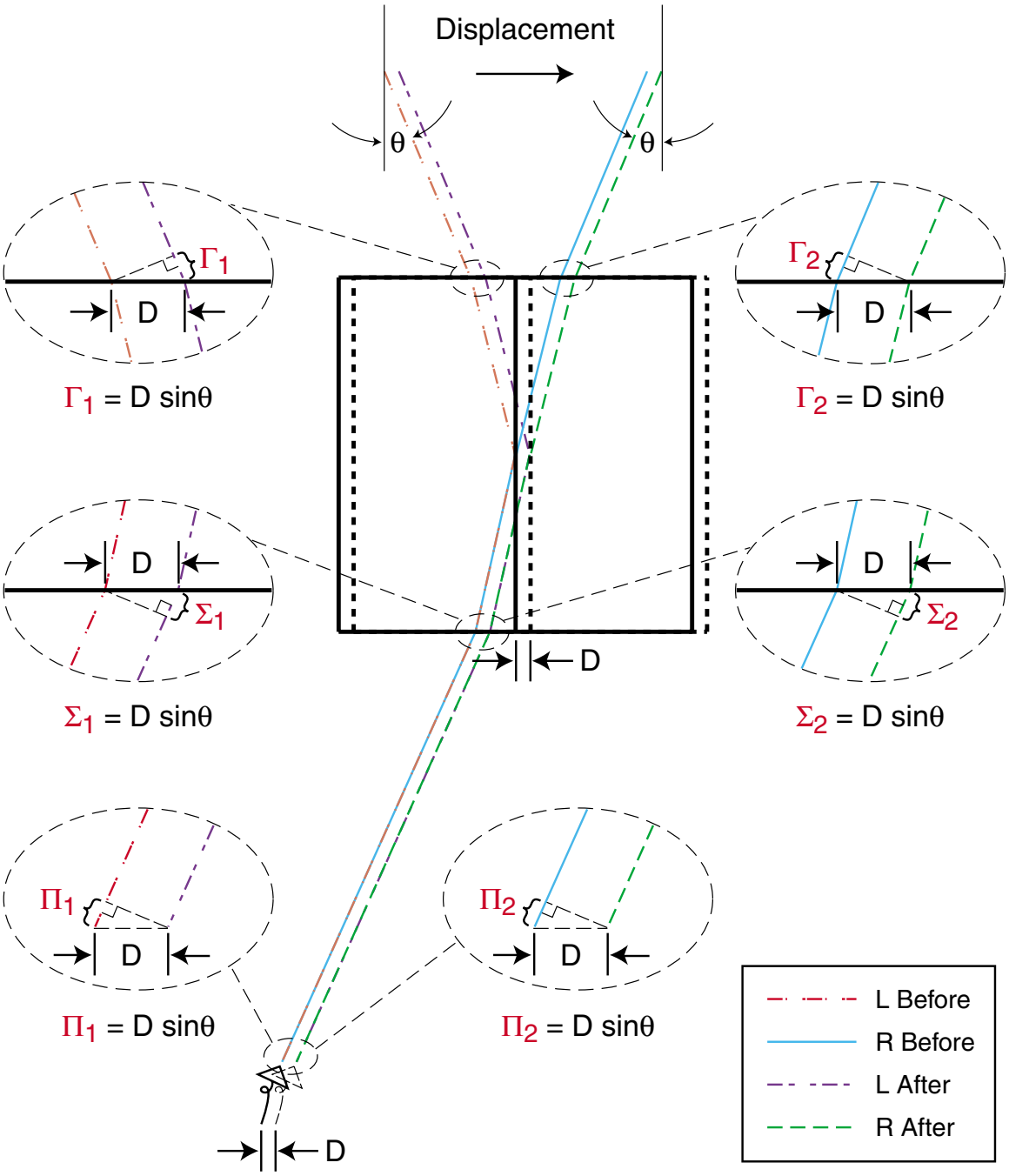

Figure 4-4: Ray trace for the case where the point detector and the beamsplitter move together. The left and right incident angles are equal.

The net change in OPL is

$$\delta \mathrm{L} = \Delta L - \Delta R = 2\ D\ \sin\theta\ \ , \tag{4.8}$$

which is identical to Eq. (4.2) and again leads to the correct period.

A subtle difference should be noted. Whereas in Case I, the net OPL change is due entirely to change in path length of the left arm, Case II sees equal contributions from both the left and the right arms. In a situation where the beams' incident angles are no longer equal (Sec. 4.1.2), the subtlety explains why mounting the detector on the stage, i.e., it moving with the beamsplitter, yields the exact fringe period, whereas fixing it while the beamsplitter moves does not.

4.1.2 Point detector without beam diverting mirror

What happens if the beams' angles are unequal? To keep the discussion simple yet physically revealing, I again omit the beam diverting mirror. It will, however, be the center of discussion in Section 4.1.3.

Case I. Detector fixed; beamsplitter moving

Figure 4-5 presents the ray tracing. The measurement topology is the same as that of Figure 4-3 except the angle of incidence for the left arm, θ_1, is now different from that for the right, θ_2.

Due to unequal angles, the interference fringes are now tilted with respect to the substrate. The actual fringe period in the substrate plane is

$$p_{\mathrm{corr}} = \frac{\lambda}{\sin\theta_1 + \sin\theta_2}\ \ , \tag{4.9}$$

an expression first appeared in Section 1.4.1 [Eq. (1.5)]. The topology will not yield a measured period that is in agreement with Eq. (4.9). It is graphically evident that the dependence on the angle θ_2 will be missing, because as the beamsplitter moves, only the left arm sees a change in OPL; the right does not. The net change in optical path length is

$$\Delta L = 2\ D\ \sin\theta_1\ \ , \tag{4.10}$$

which is a function of θ_1 only and leads to a measured period

$$p_{\mathrm{m}} = \frac{D}{N} = \frac{\lambda}{2\ \sin\theta_1}\ \ . \tag{4.11}$$

Eq. (4.11) is not the same as Eq. (4.9). They match only when θ_1 equals θ_2 (Sec. 4.1.1). Physically, the interferometric setup in Figure 4-5 can be thought of as having the right beam as a reference beam and the left a measurement beam. The reference transmits through the beam splitting interface. It records no path length change. The measurement beam reflects off the interface and detects the beamsplitter movement.

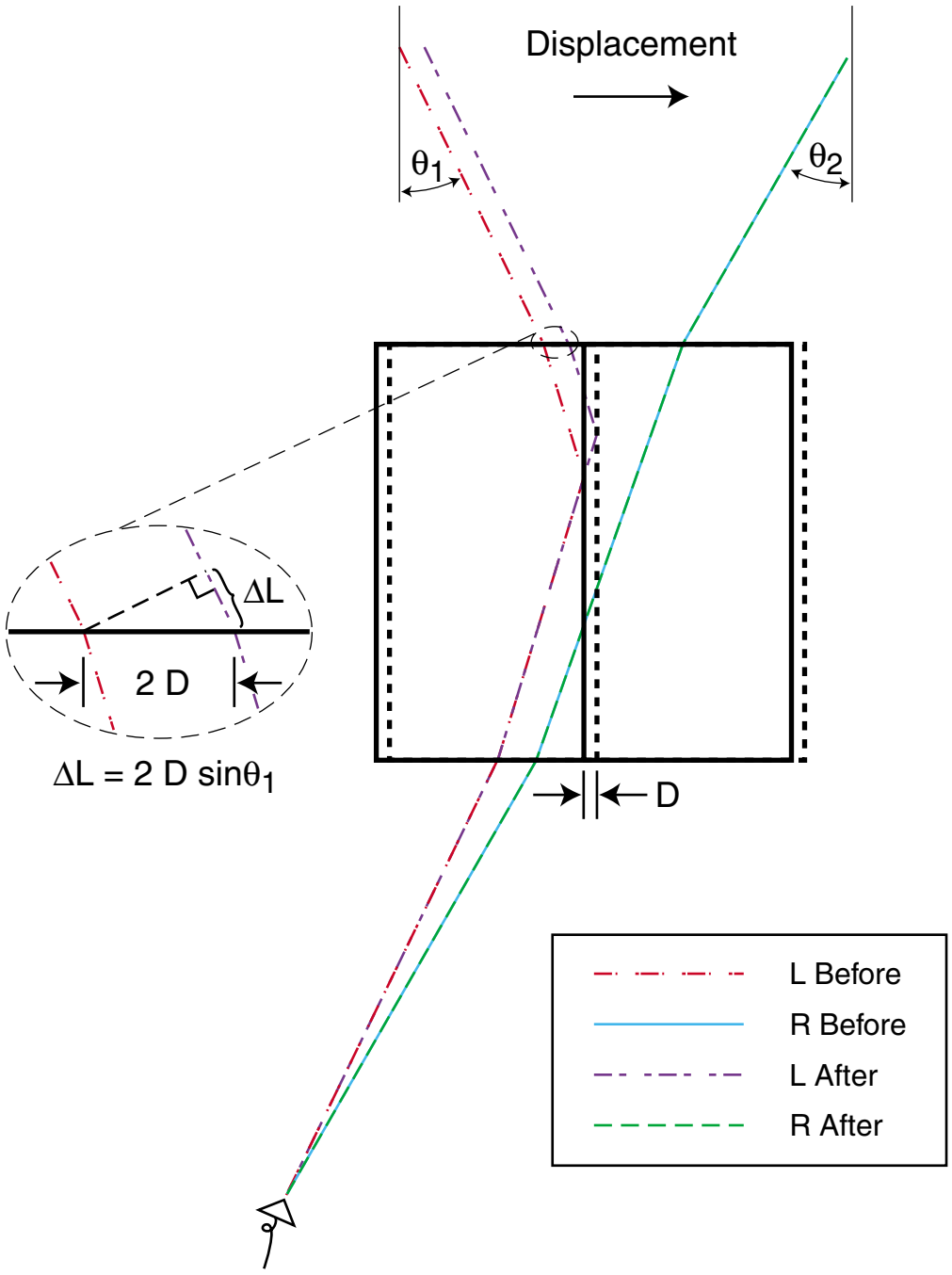

Figure 4-5: Ray trace for the case where the point detector is fixed while the beam-splitter is displaced by a distance D. The left and right incident angles are not equal.

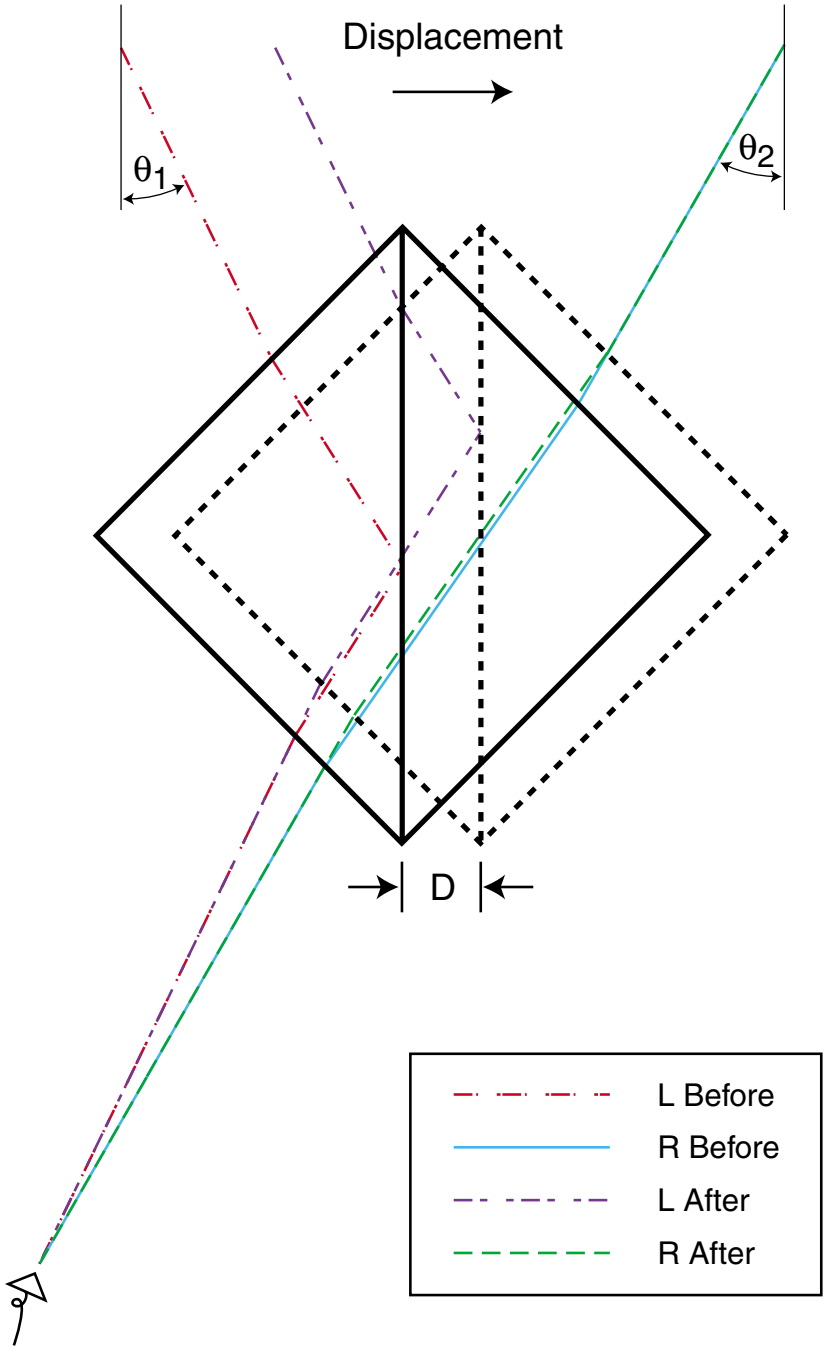

Figure 4-6: Period measurement with a common beamsplitter cube. The point detector is fixed while the beamsplitter is displaced by a distance D. The left and right incident angles are not equal. Appendix D presents a detailed analysis.

The signal variation at the detector corresponds solely to this change of path length in the measurement arm, which is why the measured period is only a function of θ_1.

One may guess that the error occurs because the rectangular beamsplitter cube has a peculiar geometry. Figure 4-6 shows the ray tracing for a conventional beamsplitter cube. While the resulting change in OPL can no longer be decided with ease and requires considerable exercise in refractive optics and analytical geometry (Appendix D), the measured period, Eq. (4.11), remains unchanged. It is interesting to note that in this case, even though ray tracing shows that the right arm undergoes a slight modification in geometry before and after the displacement, no net OPL change accumulates. In essence, it remains a reference arm.

Case II. Detector moving with the beamsplitter

The analysis for the case where the photodetector moves with the beamsplitter is almost identical to that of Case II in Section 4.1.1, except that the incident angles are now unequal. Figure 4-7 presents the ray trace. The change in optical path length in the left arm is

$$\Delta L = \Gamma_1 + \Sigma_1 - \Pi_1 = D\ \sin\theta_1\ \ , \tag{4.12}$$

where Γ_1, Σ_1 and Π_1 are all graphically defined in Figure 4-7. Similarly, the OPL change in the right arm is

$$\Delta R = -\Gamma_2 + \Sigma_2 - \Pi_2 = -D\ \sin\theta_2\ \ . \tag{4.13}$$

The difference between ΔL and ΔR gives a net change

$$\delta \mathrm{L} = \Delta L - \Delta R = D\ (\sin\theta_1 + \sin\theta_2)\ \ , \tag{4.14}$$

which translates into a measured period

$$p_{\mathrm{m}} = \frac{\lambda}{\sin\theta_1 + \sin\theta_2} \tag{4.15}$$

that is in agreement with the correct fringe period [Eq. (4.9)].

Physically, having the point detector move with the beamsplitter transforms the right arm from a reference into a measurement arm. Similar to the left arm, the right senses an angle dependent path length change. Measurements from both arms, when combined, give rise to the correct fringe period.

4.1.3 Point detector with beam diverting mirror

In reality, to implement the beamsplitter period measurement scheme, one needs to attach a mirror, in addition to the beamsplitter, to the moving stage. The mirror serves to divert the beams to a location where the photodetector can be conveniently mounted. As noted in Sections 4.1.1 and 4.1.2, one possible location is on the vertical

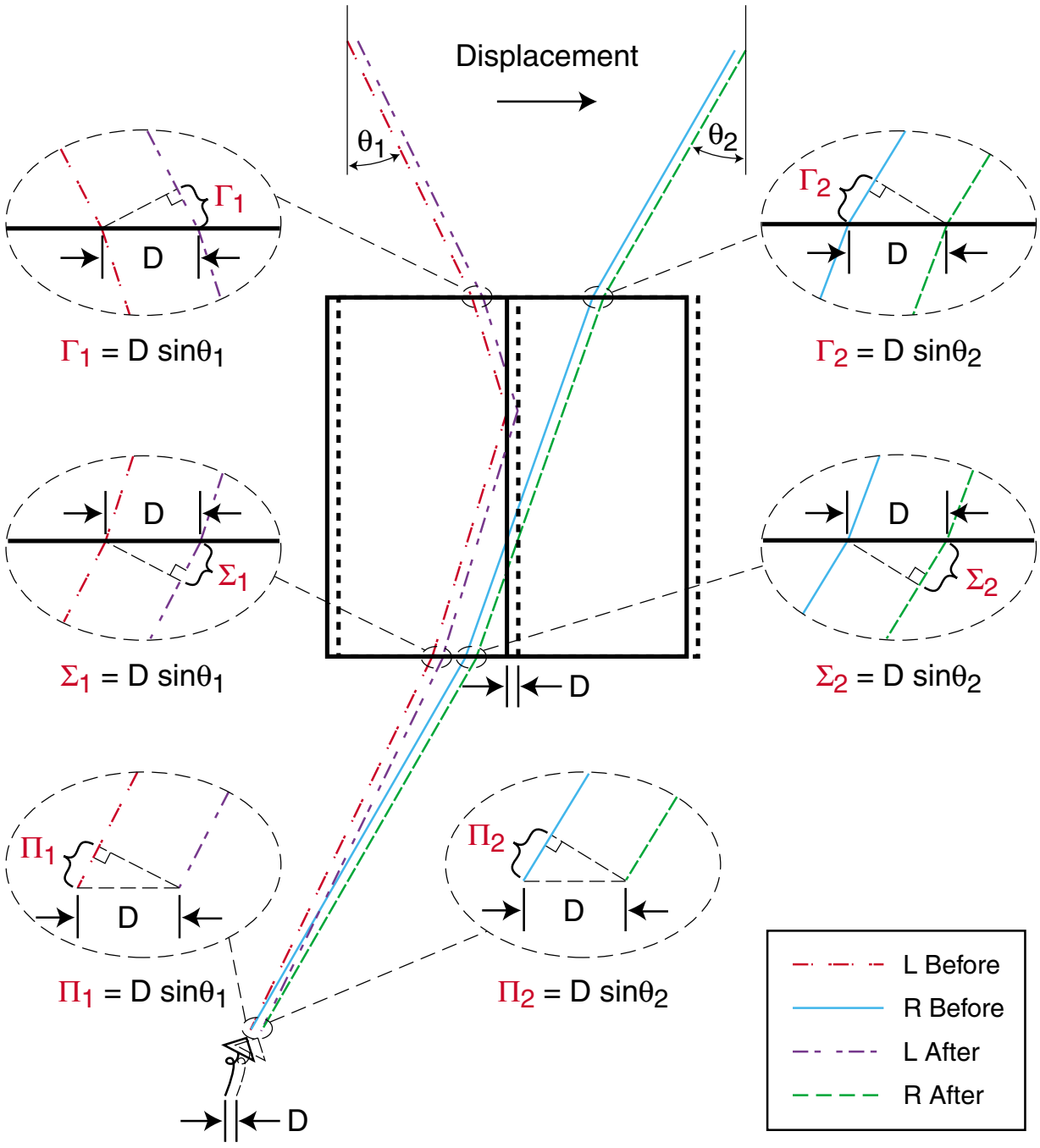

Figure 4-7: Ray trace for the case where the point detector and the beamsplitter move together. The left and right incident angles are not equal.

optical bench and the other is on the stage itself. In the former configuration, the detector remains still when the beamsplitter-mirror assembly moves. The latter sees the beamsplitter, the mirror and the photodetector move in unison. A moving mirror significantly complicates the ray tracing analysis in the case where the detector is fixed. To tackle the easier problem first, I reverse the usual order of discussion and analyze the case where the detector moves with the beamsplitter-mirror assembly.

Case I. Detector moving with the beamsplitter-mirror assembly

This case is trivial to analyze if one unfolds the reflected rays about the mirror before and after the displacement. As shown in Figure 4-8, the fictitious points P_1' and P_2' are reflections about mirrors M1 and M2, of points P_1 and P_2 before and after the displacement of the whole assembly, respectively. The spatial points P_1 and P_2 mark the starting and end locations of the point detector as it moves. With the reflected rays unfolded, one reproduces Figure 4-7 and concludes right away that the measured period is once again Eq. (4.15), in agreement with the actual fringe period. The introduction of a mirror here does not induce any additional net change in optical path length.

Case II. Detector fixed; beamsplitter-mirror assembly moving

Figure 4-9 shows the ray tracing for the scenario where the detector is mounted on the optical bench, i.e., it remains still when the stage, carrying the beamsplitter and the mirror, is displaced by a distance D. Note that while the ray tracing is rigorous, the location of the detector is schematic only. Two regions, marked (a) and (b), are presented in closeup in Figure 4-10.

The interference fringe phase shift at the point detector is proportional to the net change in optical path length. The fact that the detector is fixed while the beamsplitter and the mirror is moving complicates the ray tracing analysis. The beam-unfolding trick used in Case I is of no value here. The OPL changes in the left and the right arms must be analyzed independently. The mathematics, though elementary trigonometry, is tedious, involving many intermediate variables, all of which have been graphically defined in Figures 4-9 and 4-10. I simply present the end result here. The change in OPL in the left arm is

$$\begin{aligned} \Delta L &= \Gamma_1 + \Sigma_1 + \Delta_1 - 2L_1 \\ &= D\ \sin\theta_1 - D\ \sin(2\varphi - \theta_1)\ , \end{aligned} \tag{4.16}$$

where Γ_1, Σ_1, Δ_1 and L_1 are path segments defined in Figures 4-9 and 4-10. Similarly, the change in the right arm is

$$\begin{aligned} \Delta R &= -\Gamma_2 + \Sigma_2 + \Delta_2 - 2L_2 \\ &= -D\ \sin\theta_2 - D\ \sin(2\varphi - \theta_2)\ . \end{aligned} \tag{4.17}$$

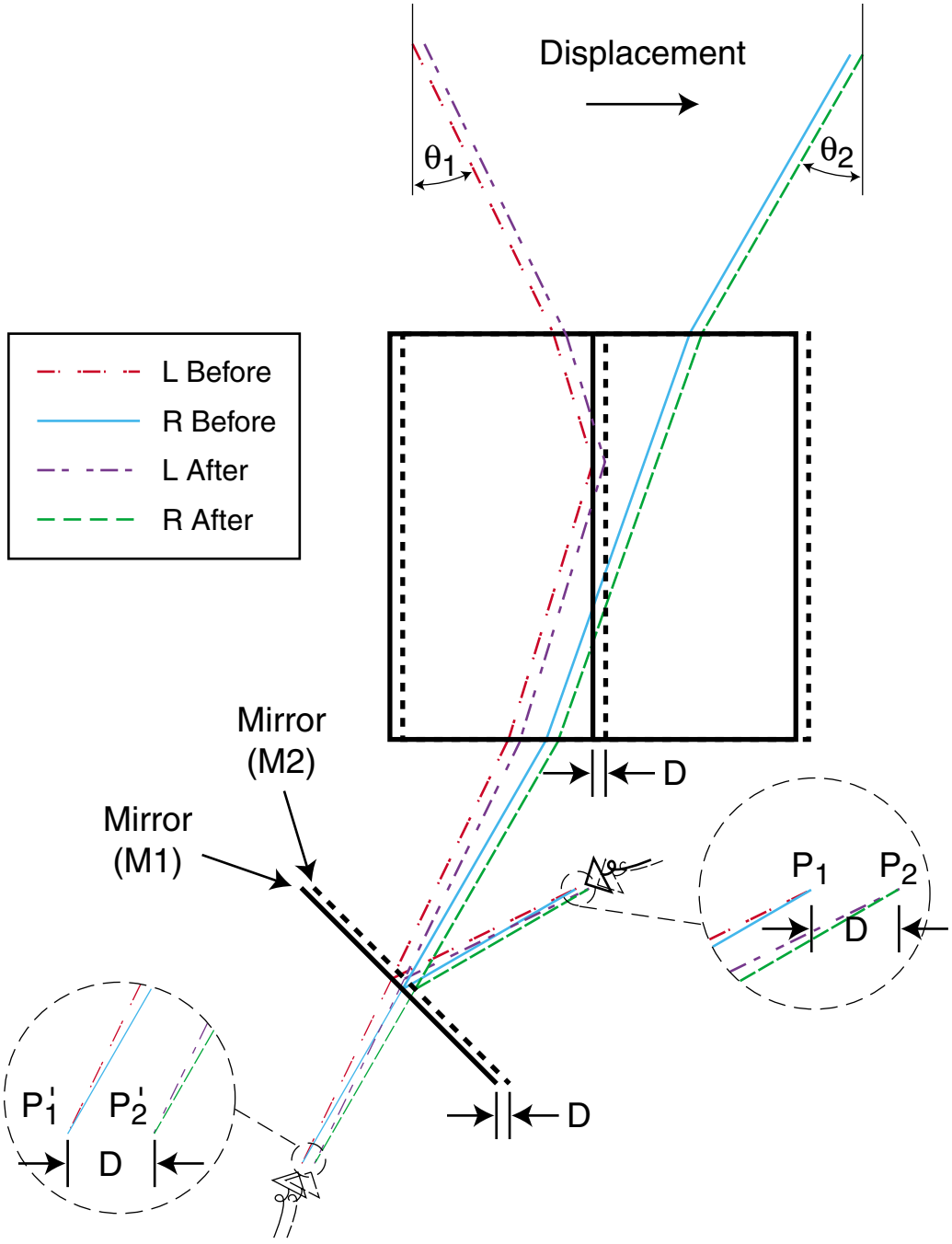

Figure 4-8: Ray trace for the case where the point detector and the beamsplitter move together. A beam diverting mirror is used. The rays have been unfolded to reveal the equivalence to Figure 4-7.

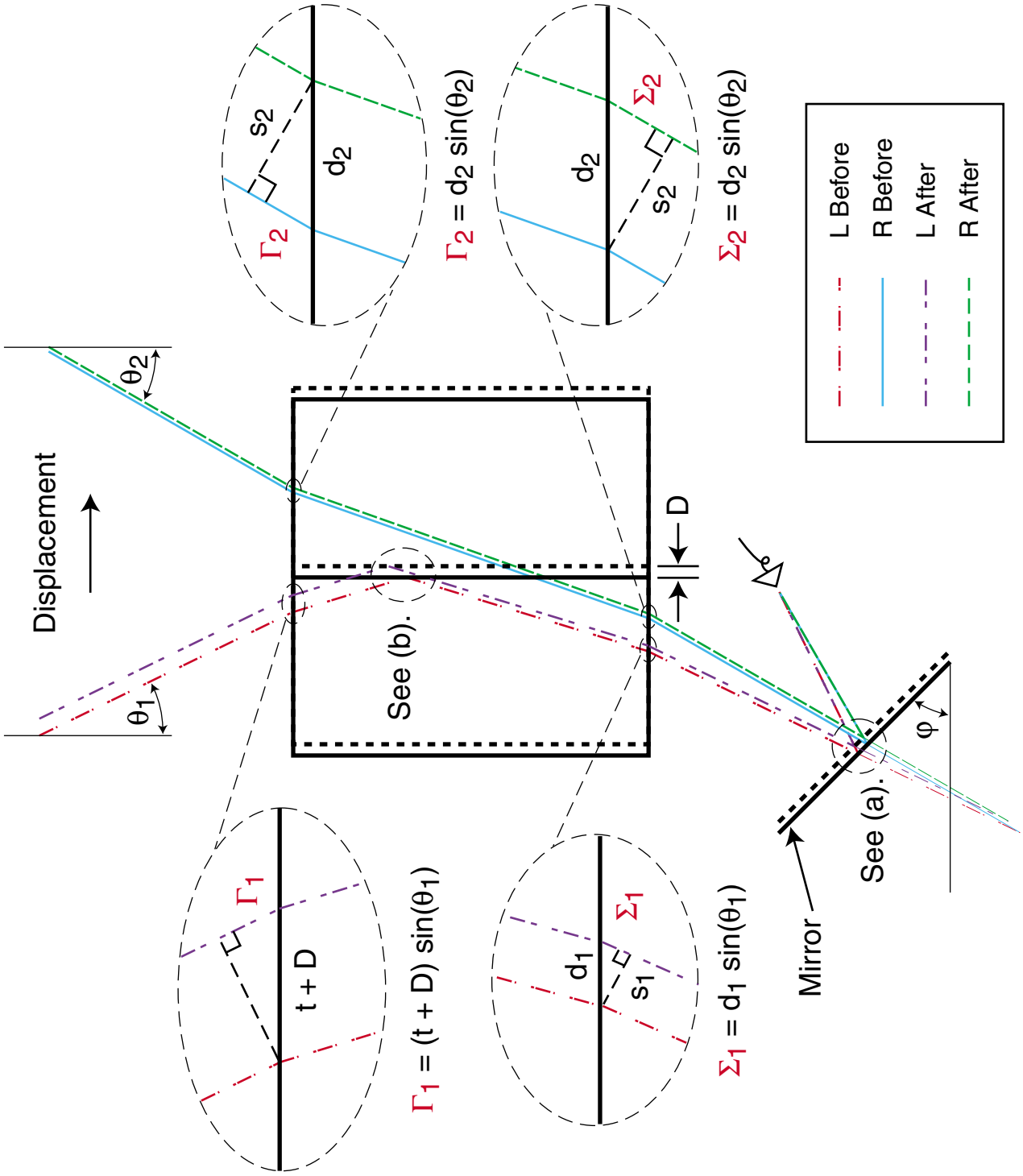

Figure 4-9: Ray trace for the case where the point detector is fixed while the beamsplitter-mirror assembly moves. To be continued in Figure 4-10.

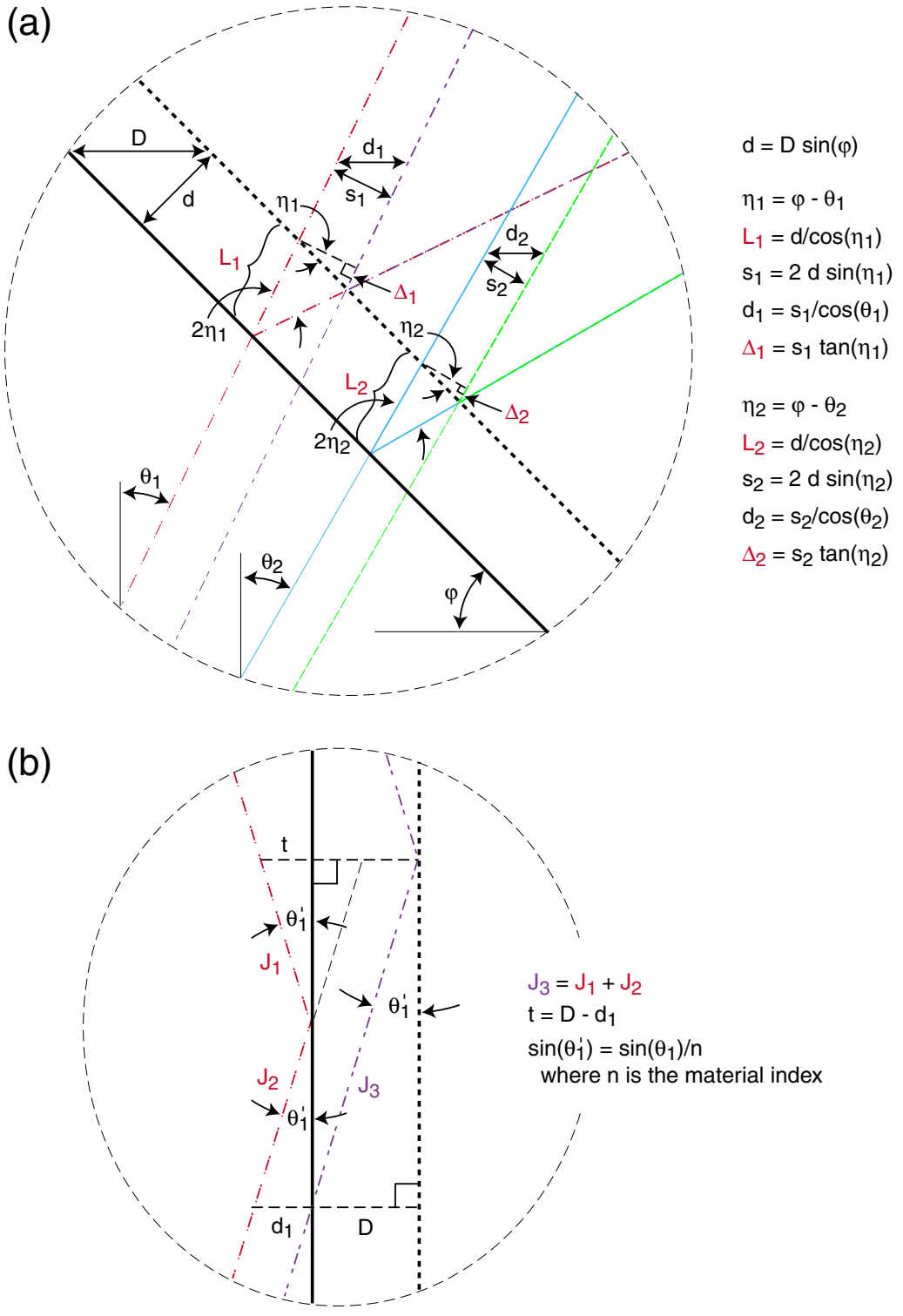

Figure 4-10: Ray trace for the case where the point detector is fixed while the beamsplitter-mirror assembly moves. Continued from Figure 4-9.

The net change in OPL is

$$\begin{aligned}\delta \mathrm{L} &= \Delta L - \Delta R \\ &= D\,(\sin\theta_1 + \sin\theta_2) - D\,[\sin(2\varphi - \theta_1) - \sin(2\varphi - \theta_2)] \quad .\end{aligned} \tag{4.18}$$

Eq. (4.18) has two terms. The first term reproduces Eq. (4.14). It alone gives rise to a measured period that equals the actual fringe period [Eq. (4.15)]. The second term is an error term, deviating the measured period from the actual. The error depends on the mirror's tilt angle φ, as well as the two incident angles θ_1 and θ_2. So long as θ_1 and θ_2 are not equal, this measurement error will exist.

Hence, in using a point detector, one must note the difference between mounting it on the stage and mounting it in the laboratory frame. The former measures the correct period whereas the latter does not.

4.1.4 Measurement error for a point detector

Given that the number of passing fringes at the detector is

$$N = \frac{\delta \mathrm{L}}{\lambda} \quad , \tag{4.19}$$

one can derive the measured period from Eq. (4.18),

$$p_{\mathrm{m}} = \frac{D}{N} = \frac{\lambda}{(\sin\theta_1 + \sin\theta_2) - [\sin(2\varphi - \theta_1) - \sin(2\varphi - \theta_2)]} \quad . \tag{4.20}$$

The second term in the denominator leads to a period measurement error. As a consistency check, in the special case where $\varphi = 0$, the measured period becomes $p_{\mathrm{m}} = \frac{\lambda}{2\,\sin\theta_1}$, an expression that coincides with Eq. (4.11). This is hardly surprising for when the mirror is placed horizontal (Fig. 4-9), unfolding the reflected rays reproduces Figure 4-5, from which Eq. (4.11) is obtained.

I now derive an expression for the period measurement error when the two beams are only slightly misaligned. Without loss of generality, the angle for the right beam is assumed larger than that of the left, i.e., $\theta_1 = \theta$ and $\theta_2 = \theta + \delta$ where $\delta/\theta \ll 1$. The correct period in the substrate plane is given by Eq. (4.9),

$$p_{\mathrm{corr}} = \frac{\lambda}{\sin\theta + \sin(\theta + \delta)} = \frac{\lambda}{2\,\sin(\theta + \delta/2)\,\cos(\delta/2)} \quad . \tag{4.21}$$

The measured period, Eq. (4.20), can be expanded in powers of δ as

$$p_{\mathrm{m}} = p_{\mathrm{corr}} \left[1 + \frac{\cos(2\varphi - \theta)}{2\,\sin\theta}\delta + \mathcal{O}[\delta]^2\right] \quad , \tag{4.22}$$

where the symbol $\mathcal{O}[\delta]^2$ indicates terms with orders δ^2 and higher. To the first order in δ, the percentage error in period measurement is

$$\mathcal{E} = \frac{\cos(2\varphi - \theta)}{2\,\sin\theta}\delta \quad . \tag{4.23}$$

Note that if the mirror is tilted such that $2\varphi - \theta = 90°$, $\mathcal{E}$ vanishes.

4.1.5 Wave model for a non-point detector

Although a point photodetector is a textbook curiosity rather than a real-world device, by considering period measurement with the point detector, I have established the basics from which a generalized theory, applicable to physical non-point detectors such as a photodiode, can be developed.

A photodiode is a power sensor. It integrates the light irradiance (i.e., intensity) over an active area. To model the signal coming out of the diode, one must know the intensity distribution over the diode. In the case of a two-beam interference, the intensity is proportional to the magnitude square of the total electric field, i.e.,

$$I(\mathbf{r}) \propto |\mathbf{E}_{\text{tot}}(\mathbf{r})|^2 = |\mathbf{E}_L(\mathbf{r}) + \mathbf{E}_R(\mathbf{r})|^2 \quad , \tag{4.24}$$

where $\mathbf{E}_L$ and $\mathbf{E}_R$ are electric fields describing the two incoming beams, and $\mathbf{r}$ is the displacement vector.

A photodiode can be viewed as composed of many individual point detectors. Pick any one of the points. Through analytical ray tracing, relative path length changes of the two rays intersecting at that point detector can be established (Secs. 4.1.1–4.1.3). I now show that these path length changes can be encoded as planar wavefronts. The resulting wave model is equivalent to the ray model and allows proper calculation of the light intensity distribution over the entire photodiode.

Figure 4-11 shows the schematic. The point at which path length information is known is labeled O and chosen as the coordinate origin. Suppose in reaching O, the left (L) and the right (R) rays have seen changes in optical path lengths of ΔL and ΔR, respectively. The net change in OPL is therefore $\delta\mathrm{L} = \Delta L - \Delta R$. In the wave model, two plane waves replace the rays,

$$\mathbf{E}_L(\mathbf{r}) = \exp(-j\mathbf{k}_L \cdot \mathbf{r} - jk\ \Delta L - j\phi_L) \quad , \tag{4.25}$$

$$\mathbf{E}_R(\mathbf{r}) = \exp(-j\mathbf{k}_R \cdot \mathbf{r} - jk\ \Delta R - j\phi_R) \quad , \tag{4.26}$$

where for convenience, unity amplitudes are assumed; $\mathbf{k}_L$ and $\mathbf{k}_R$ are the wave vectors for the left and the right plane waves, respectively; $k = 2\pi/\lambda$ is the wave number and ϕ_L and ϕ_R are some arbitrary initial phases.

Applying Eq. (4.24) and substituting in the wave vectors

$$\mathbf{k}_L = (k \sin\psi_1,\ 0,\ -k\cos\psi_1) \quad , \tag{4.27}$$

$$\mathbf{k}_R = (k \sin\psi_2,\ 0,\ -k\cos\psi_2) \quad , \tag{4.28}$$

one finds the intensity distribution in the plane of the photodiode ($z = 0$) is, up to some proportionality constant,

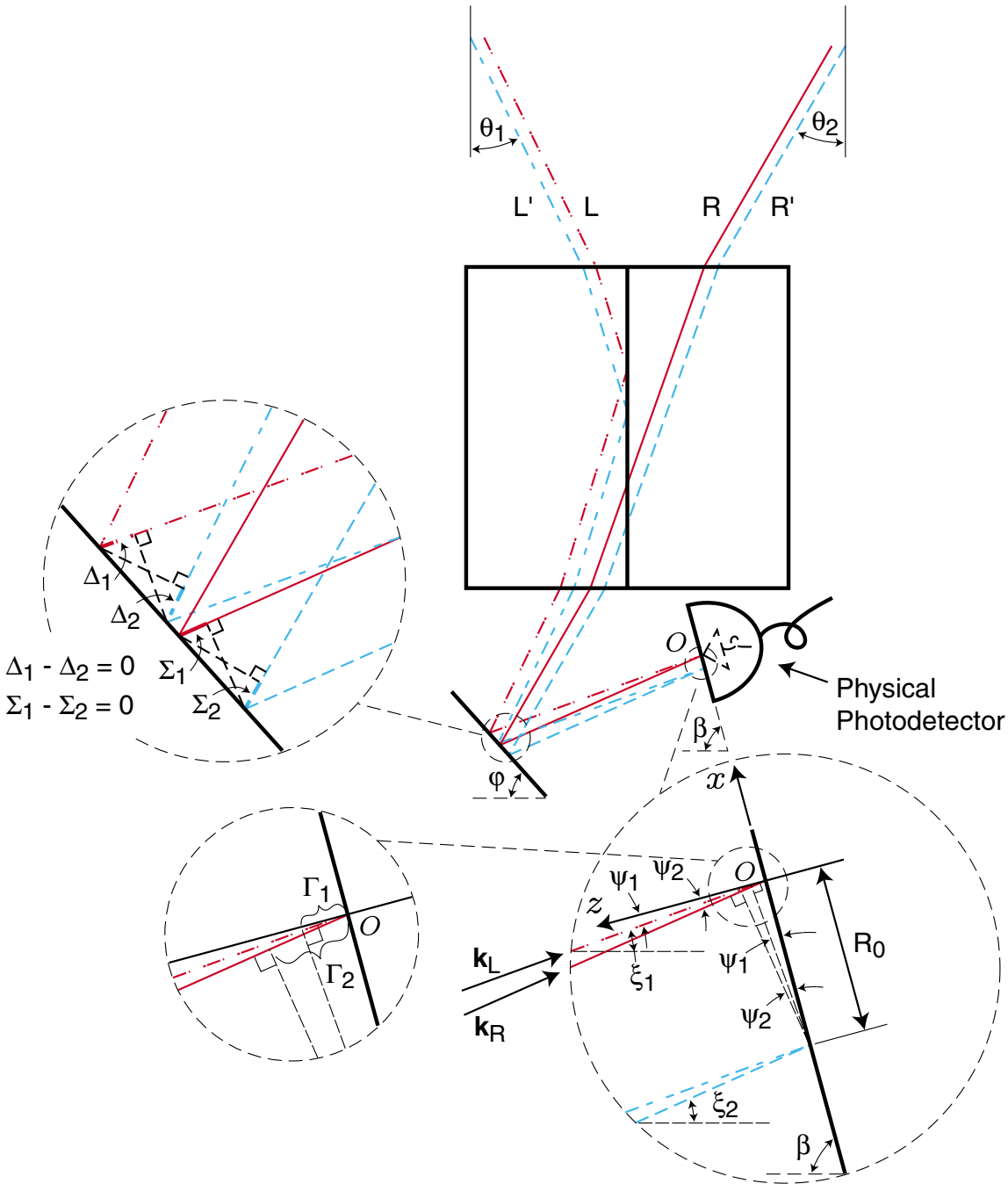

Figure 4-11: Wave model development. Optical path length changes are encoded as planar wavefronts.

$$I(x) = 2 + 2\cos\left[k(\sin\psi_1 - \sin\psi_2)x + k(\Delta L - \Delta R) + (\phi_L - \phi_R)\right] \quad . \tag{4.29}$$

When two plane waves with different wave vectors interfere, the intensity is that of a linear fringe pattern. It has a period of $\lambda/(\sin\psi_1 - \sin\psi_2)$. At the origin O, the spatial phase is

$$\phi(0) = \frac{2\pi}{\lambda}(\Delta L - \Delta R) + (\phi_L - \phi_R) \quad , \tag{4.30}$$

which shows a net OPL change of $\delta \mathrm{L} = \Delta L - \Delta R$. It fits the initial condition from ray tracing.

There is one more consistency check. Pick any point in the plane of the diode that is not the origin, for instance, $x = -R_0$. The spatial phase at that point, from Eq. (4.29), is

$$\phi(-R_0) = k(\sin\psi_1 - \sin\psi_2)(-R_0) + \phi(0) \quad . \tag{4.31}$$

In other words, the phase at $x = -R_0$ leads that at $x = 0$ by an amount

$$\Delta\phi = \phi(-R_0) - \phi(0) = \frac{2\pi}{\lambda}(\sin\psi_2 - \sin\psi_1)R_0 \quad . \tag{4.32}$$

The same result can be obtained from ray tracing (Fig. 4-11). Rays L and L' differ in OPL only at the diode, so do Rays R and R'. There are no net path length differences in their traversing the beamsplitter cube or reflecting off the mirror. Simple trigonometry shows that the net change in OPL going from the unprimed to the primed set of rays matches Eq. (4.32).

4.1.6 Locations of Gaussian beam centroids

SBIL uses small-diameter Gaussian beams to produce a grating image, which then gets recorded in photoresist. Even though in describing the period measurement scheme, it is difficult to produce an analytical model that incorporates the Gaussian wavefront, a Gaussian intensity profile can be readily modeled with no problem. As the beamsplitter and the mirror move, the centroids of the interfering Gaussian beams move in the detector plane. A correct model must take into account the centroid movements. I end up simulating either incident beam with an electric field that has a plane wavefront and a Gaussian amplitude whose centroid moves as the beamsplitter is displaced.

In this section, I calculate the locations for the moving beam centroids. Similar to that for a point detector, the discussion is divided into two parts, that of a photodiode moving and of it fixed.

Case I. Detector fixed; beamsplitter-mirror assembly moving

Figures 4-12 and 4-13 show the setup and its closeups. Here, the rays label the centroids of the beams as they propagate through the beamsplitter and reflect off

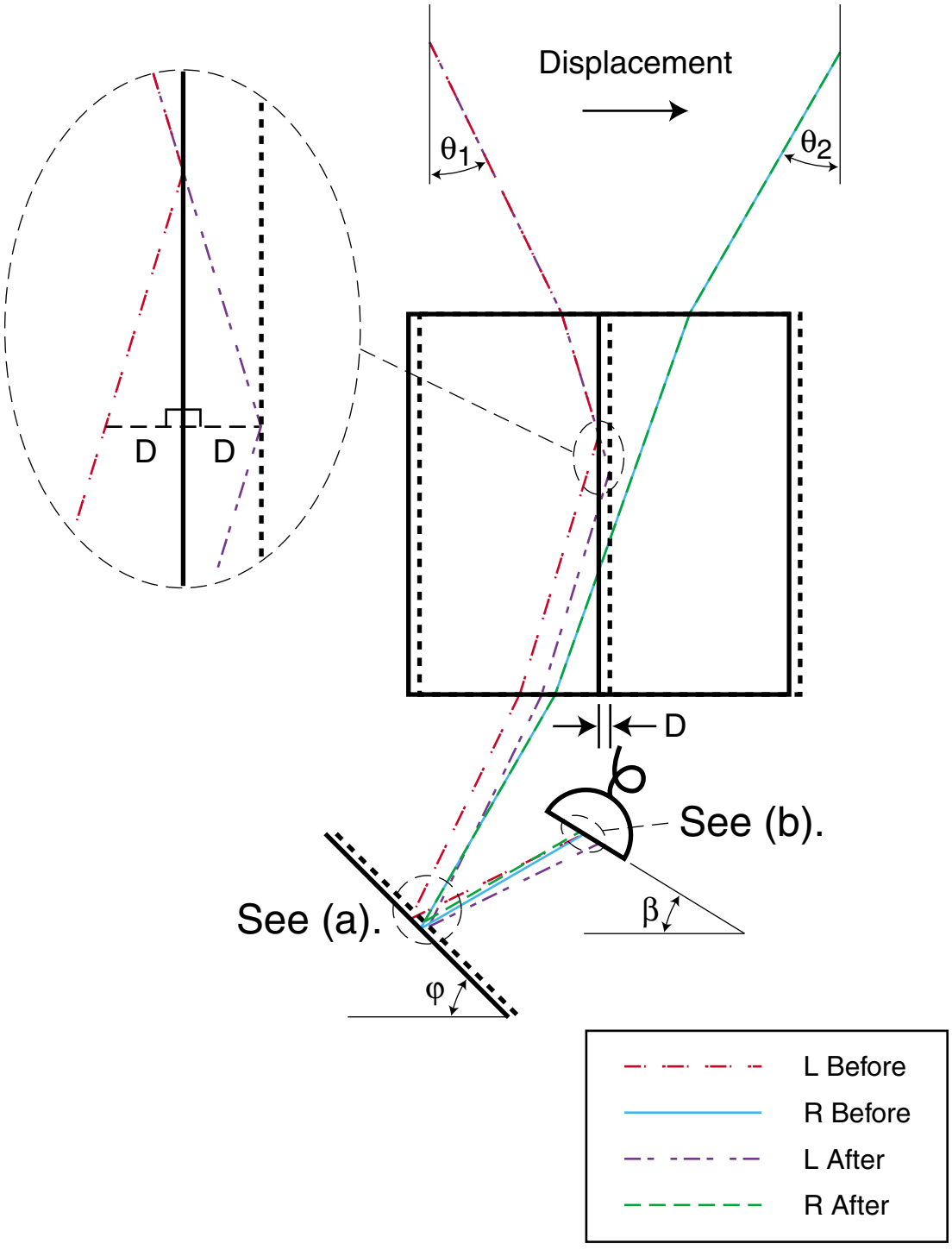

Figure 4-12: Ray trace showing the movements of the Gaussian beam centroids, for the case where the photodiode is fixed while the beamsplitter-mirror assembly moves. To be continued in Figure 4-13.

(a)

$d = D \sin(\varphi)$

$d_1 = 2D$
$s_0 = d_1 \cos(\theta_1) = 2D \cos(\theta_1)$
$\eta_1 = \varphi - \theta_1$
$T = s_0/\cos(\eta_1)$
$s_1 = [T - 2d \tan(\eta_1)] \cos(\eta_1)$

$\eta_2 = \varphi - \theta_2$
$s_2 = 2d \tan(\eta_2) \cos(\eta_2)$

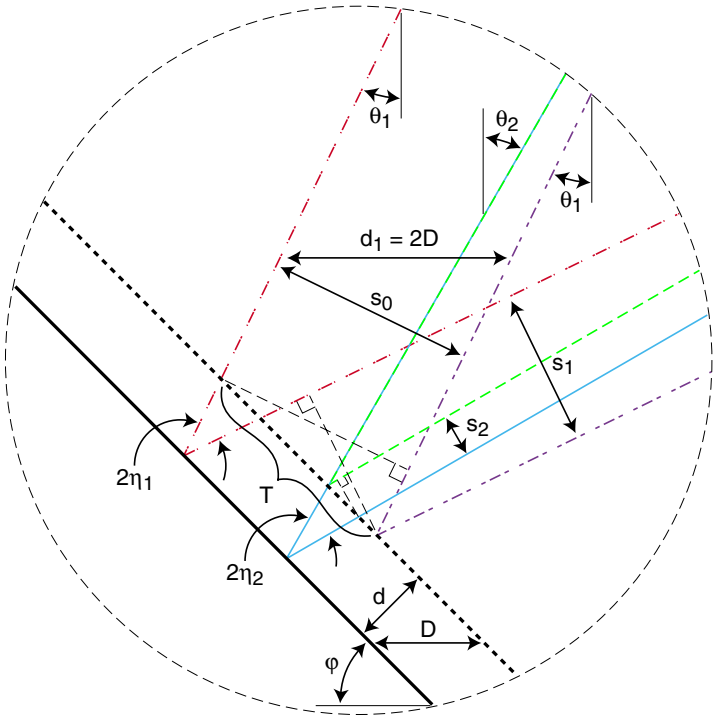

(b)

$\xi_1 = 90^\circ - 2\varphi + \theta_1$
$\gamma_1 = 90^\circ - \beta - \xi_1 = 2\varphi - \beta - \theta_1$
$X_L = s_1/\cos(\gamma_1)$

$\xi_2 = 90^\circ - 2\varphi + \theta_2$
$\gamma_2 = 90^\circ - \beta - \xi_2 = 2\varphi - \beta - \theta_2$
$X_R = s_2/\cos(\gamma_2)$

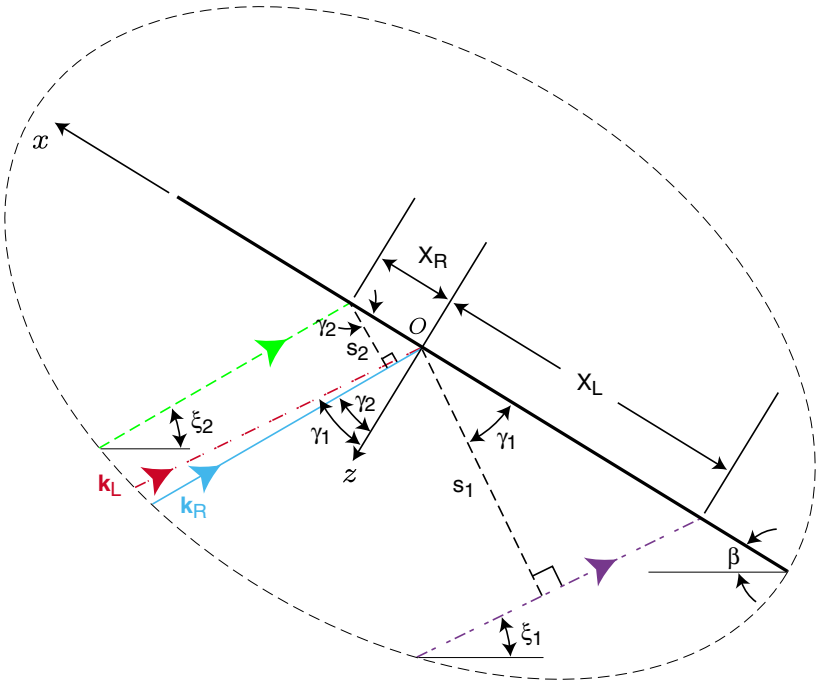

Figure 4-13: Ray trace showing the movements of the Gaussian beam centroids, for the case where the photodiode is fixed while the beamsplitter-mirror assembly moves. Continued from Figure 4-12.

the mirror towards the photodiode. For convenience, the two beams are assumed to overlap before the displacement. As the beamsplitter-mirror assembly is displaced, centroid movements for both arms in the detector plane are evident [Fig. 4-13(b)]. All important intermediate steps are written down in Figure 4-13. I record here only X_L and X_R, the resulting centroid locations for the left and the right beams, respectively,

$$X_L(D) = -\frac{2D\cos\varphi\cos(\varphi-\theta_1)}{\cos(2\varphi-\beta-\theta_1)} \ , \tag{4.33}$$

$$X_R(D) = \frac{2D\sin\varphi\sin(\varphi-\theta_2)}{\cos(2\varphi-\beta-\theta_2)} \ , \tag{4.34}$$

where β is the detector tilt angle. I note specifically that locations X_L and X_R are functions of the displacement D.

Case II. Detector moving with the beamsplitter-mirror assembly

The photodiode is mounted on the stage. In the coordinate frame xOz (Fig. 4-14), the left and the right centroid locations are

$$X_L(D) = -\frac{2D\cos\varphi\cos(\varphi-\theta_1) - D\cos(2\varphi-\theta_1)}{\cos(2\varphi-\beta-\theta_1)} \ , \tag{4.35}$$

$$X_R(D) = \frac{2D\sin\varphi\sin(\varphi-\theta_2) + D\cos(2\varphi-\theta_2)}{\cos(2\varphi-\beta-\theta_2)} \ . \tag{4.36}$$

Ray geometries inside the beamsplitter and nearby the mirror are identical to those from Figures 4-12 and 4-13. Therefore, compared to the earlier case where the detector is fixed, changes in X_L and X_R are due entirely to the displacement of the coordinate frame from $x_0O_0z_0$ to xOz.

4.1.7 Period measurement with a non-point detector

Together, Sections 4.1.5 and 4.1.6 provide the tools with which I now tackle the problem of period measurement with a real-world photodetector. In Section 4.1.5, it is shown that any path length information derived from ray tracing can be encoded in the phase carried by an electromagnetic wave. This allows one to develop a wave model necessary for describing a real photodiode, based on results obtained earlier for a point detector. Section 4.1.6 finds the locations for the moving Gaussian beam centroids, which must be incorporated into the wave model to help define the electric field amplitudes.

Case I. Detector fixed; beamsplitter-mirror assembly moving

See Figures 4-12 and 4-13 for reference. Prior to the displacement, the beams incident upon the photodiode are modeled as

$$\mathbf{E}_L(\mathbf{r}) = A_L \exp\left(-\frac{x^2+y^2}{w_0^2}\right)\exp(-j\mathbf{k}_L\cdot\mathbf{r} - j\phi_L) \ , \tag{4.37}$$

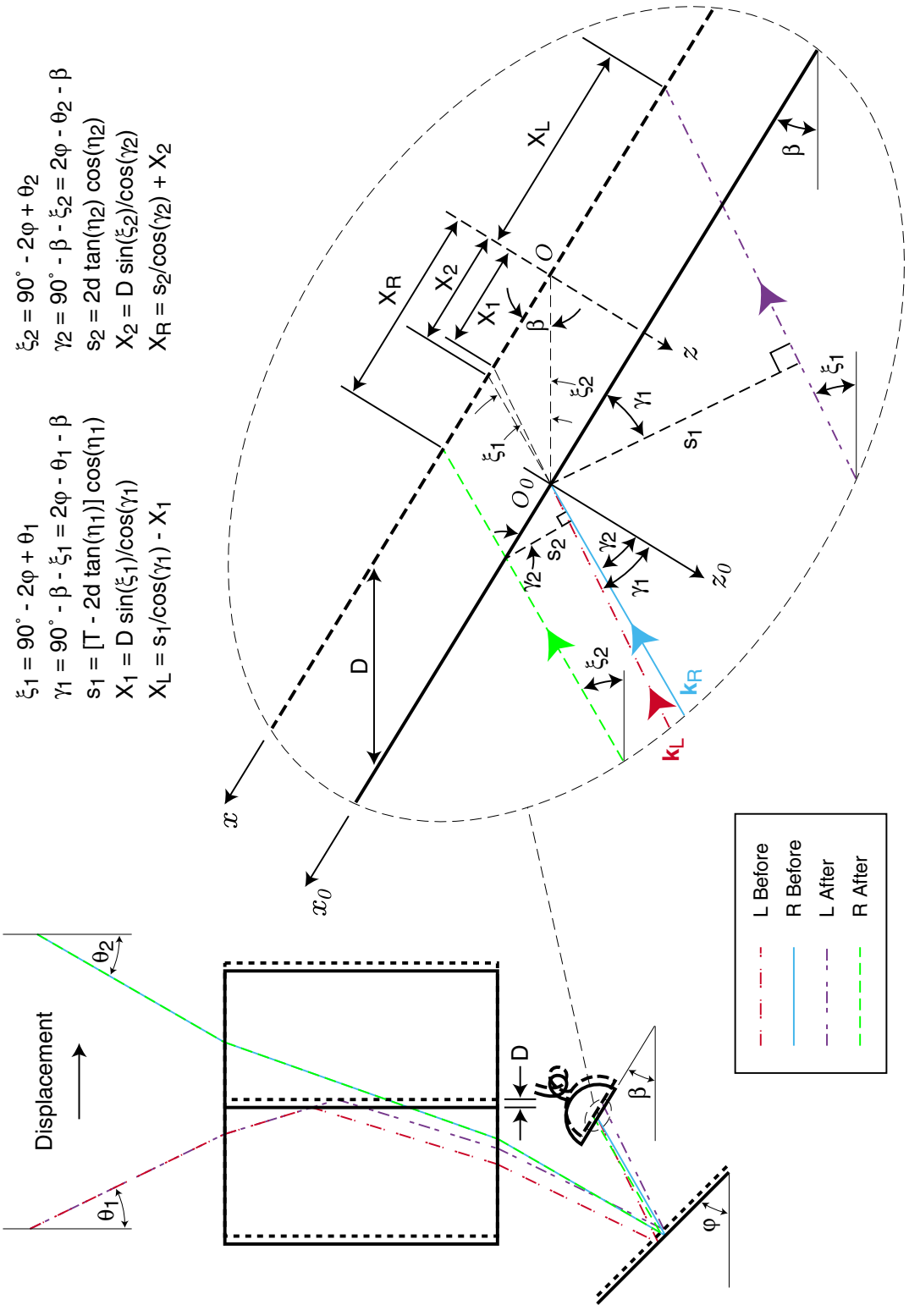

Figure 4-14: Ray trace showing the movements of the Gaussian beam centroids, for the case where the photodiode and the beamsplitter-mirror assembly move together.

$$\mathbf{E}_R(\mathbf{r}) = A_R \exp\left(-\frac{x^2+y^2}{w_0^2}\right) \exp(-j\mathbf{k}_R \cdot \mathbf{r} - j\phi_R) \ , \tag{4.38}$$

where A_L and A_R are real numbers, ϕ_L and ϕ_R are arbitrary initial phases, and w_0 is the $1/e^2$ beam intensity radius. Each field carries a planar phase front and has a Gaussian amplitude profile. The wave vectors $\mathbf{k}_L$ and $\mathbf{k}_R$ are

$$\mathbf{k}_L = (-k\sin\gamma_1,\ 0,\ -k\cos\gamma_1) \ , \tag{4.39}$$

$$\mathbf{k}_R = (-k\sin\gamma_2,\ 0,\ -k\cos\gamma_2) \ , \tag{4.40}$$

where the angles $\gamma_1 = 2\varphi - \beta - \theta_1$ and $\gamma_2 = 2\varphi - \beta - \theta_2$ [Fig. 4-13(b)]. For simplicity, the Gaussian beam radii are assumed equal and constant as the waves propagate. The constancy assumption is not a problem here because in the end, the intensity is evaluated only at the detector plane, i.e., $z = 0$ where the two radii are indeed constant. Any geometrical elongation of the beam spots due to oblique incidence is also ignored.

After a displacement D, the beams pick up additional phase factors due to changes in optical path length, and their centroids shift as well. The electric fields become

$$\mathbf{E}_L(\mathbf{r}, D) = A_L \exp\left(-\frac{[x - X_L(D)]^2 + y^2}{w_0^2}\right) e^{-j\mathbf{k}_L\cdot\mathbf{r} - jk\,\Delta L(D) - j\phi_L} \ , \tag{4.41}$$

$$\mathbf{E}_R(\mathbf{r}, D) = A_R \exp\left(-\frac{[x - X_L(D)]^2 + y^2}{w_0^2}\right) e^{-j\mathbf{k}_R\cdot\mathbf{r} - jk\,\Delta R(D) - j\phi_R} \ , \tag{4.42}$$

where OPL changes ΔL and ΔR are derived in Section 4.1.3 [Eqs. (4.16) and (4.17)], and X_L and X_R are given by Eqs. (4.33) and (4.34), respectively. Note that when $D = 0$, these expressions reduce to our initial conditions, Eqs. (4.37) and (4.38).

The beams interfere at the photodiode, i.e., in the plane $z = 0$. The resulting light irradiance is (up to a proportionality constant),

$$\begin{aligned} I(x, y, D) &= [\mathbf{E}_L(\mathbf{r}, D)^* + \mathbf{E}_R(\mathbf{r}, D)^*] \cdot [\mathbf{E}_L(\mathbf{r}, D) + \mathbf{E}_R(\mathbf{r}, D)]|_{z=0} \\ &= I_0(x, y, D) + I_1(x, y, D) \ , \end{aligned} \tag{4.43}$$

where the functions I_0 and I_1 are

$$I_0(x, y, D) = |\mathbf{E}_L(x, y, D)|^2 + |\mathbf{E}_R(x, y, D)|^2 \ , \tag{4.44}$$

$$I_1(x, y, D) = 2\,\mathcal{R}e\left\{\mathbf{E}_L(x, y, D)^* \cdot \mathbf{E}_R(x, y, D)\right\} \ . \tag{4.45}$$

The operator $\mathcal{R}e\{A\}$ takes the real part of a complex number A. The I_0 term represents the sum of individual field intensities. The term I_1 represents the interaction between the two fields and contains the phase information associated with the interference pattern. Substituting in the field expressions [Eqs. (4.41) and (4.42)], one gets

$$I_0(x,y,D) = A_L A_R\, e^{-2\,\frac{[x-X_L(D)]^2+y^2}{w_0^2}} + A_L A_R\, e^{-2\,\frac{[x-X_R(D)]^2+y^2}{w_0^2}} \quad , \tag{4.46}$$

$$I_1(x,y,D) = 2A_L A_R\, e^{-\frac{[x-X_L(D)]^2+y^2}{w_0^2}}\, e^{-\frac{[x-X_R(D)]^2+y^2}{w_0^2}} \cos\{k(\sin\gamma_2 - \sin\gamma_1)x + k[\Delta L(D) - \Delta R(D)] + (\phi_L - \phi_R)\} \quad . \tag{4.47}$$

The photodiode integrates the intensity and yields a power readout. Assuming the active area of the diode is much larger than the Gaussian beam size, integration of Eq. (4.46) leads to

$$P_0(D) = \int_{-\infty}^{+\infty}\int_{-\infty}^{+\infty} I_0(x,y,D)\, dx\, dy = A_L A_R \pi w_0^2 \quad , \tag{4.48}$$

which is a constant. The term simply provides a DC offset to the output power. Integrating Eq. (4.47) yields the so-called AC power. The math is much more involved (Appendix E), yet the final expression is exact and compact

$$\begin{aligned} P_1(D) &= \int_{-\infty}^{+\infty}\int_{-\infty}^{+\infty} I_1(x,y,D)\, dx\, dy \\ &= C\, \exp\left(-\frac{[X_L(D) - X_R(D)]^2}{2w_0^2}\right) \cos[\Delta\phi(D) + (\phi_L - \phi_R)] \quad , \end{aligned} \tag{4.49}$$

where the constant is

$$C = A_L A_R \pi w_0^2 \exp\left[-\frac{1}{8}k^2(\sin\gamma_2 - \sin\gamma_1)^2 w_0^2\right] \quad . \tag{4.50}$$

The exponential term, originating from the beam centroid movements, defines an envelope for the AC power oscillation. My interest lies with the cosine term, for it contains the phase of the oscillation from which, the measured period can be derived. Ignoring the constant $(\phi_L - \phi_R)$, the phase is

$$\Delta\phi(D) = \frac{2\pi}{\lambda}\left\{\frac{1}{2}(\sin\gamma_2 - \sin\gamma_1)\,[X_L(D) + X_R(D)] + [\Delta L(D) - \Delta R(D)]\right\} \quad . \tag{4.51}$$

Note specifically the functional dependence on the displacement D.

Eq. (4.4) relates the number of signal oscillations N to $\Delta\phi$. Substituting in expressions for ΔL, ΔR, X_L, X_R from Eqs. (4.16), (4.17), (4.33) and (4.34), respectively, one obtains the measured period for the case where the photodiode is fixed and the beamsplitter is moving,

$$p_{\mathrm{m}}^{(I)} = \frac{D}{N} = \frac{\lambda}{\alpha_I} \quad , \tag{4.52}$$

where

$$\alpha_I = (\sin\theta_1 + \sin\theta_2) + \left\{[\sin(2\varphi - \beta - \theta_2) - \sin(2\varphi - \beta - \theta_1)] \cdot \left[-\frac{\cos\varphi\cos(\varphi - \theta_1)}{\cos(2\varphi - \beta - \theta_1)}\right.\right.$$

$$+\frac{\sin\varphi\sin(\varphi-\theta_2)}{\cos(2\varphi-\beta-\theta_2)}\Bigg]-[\sin(2\varphi-\theta_1)-\sin(2\varphi-\theta_2)]\Bigg\}\quad. \tag{4.53}$$

The expression inside the curly brackets must vanish for $p_{\mathrm{m}}^{(I)}$ to match the exact fringe period [Eq. (4.9)]. It happens only when θ_1 and θ_2 are equal.

Case II. Detector moving with the beamsplitter-mirror assembly

For the case where the photodiode is moving together with the beamsplitter, Eq. (4.51) remains valid, though different expressions of ΔL, ΔR, X_L and X_R must be used. Substituting in Eqs. (4.12), (4.13), (4.35) and (4.36), one gets

$$p_{\mathrm{m}}^{(II)}=\frac{D}{N}=\frac{\lambda}{\alpha_{II}}\quad, \tag{4.54}$$

where

$$\begin{aligned}\alpha_{II}=(\sin\theta_1+\sin\theta_2)+\frac{1}{2}[&\sin(2\varphi-\beta-\theta_2)\\&-\sin(2\varphi-\beta-\theta_1)]\cdot\left[-\frac{2\cos\varphi\cos(\varphi-\theta_1)-\cos(2\varphi-\theta_1)}{\cos(2\varphi-\beta-\theta_1)}\right.\\&\left.+\frac{2\sin\varphi\sin(\varphi-\theta_2)+\cos(2\varphi-\theta_2)}{\cos(2\varphi-\beta-\theta_2)}\right]\quad.\end{aligned} \tag{4.55}$$

For $p_{\mathrm{m}}^{(II)}$ to equal the exact fringe period, the second term in α_{II} must vanish, which can only happen when $\theta_1=\theta_2$.

4.1.8 Measurement error for a non-point detector

If neither mounting scheme is capable of measuring the exact fringe period when the two beams have different angles of incidence, what is the measurement error and can SBIL tolerate it?

Suppose that the beams are only slightly misaligned. Without loss of generality, assume the right beam has the larger angle of incidence, i.e., $\theta_1=\theta$ and $\theta_2=\theta+\delta$ where $\delta/\theta\ll 1$. The correct fringe period, p_{corr}, is given by Eq. (4.21). Both Eqs. (4.52) and (4.54) can be expanded in powers of δ,

$$p_{\mathrm{m}}^{(I)}=p_{\mathrm{corr}}\left(1-\frac{\sin(2\varphi-\beta)}{4\ \sin\theta\cos(2\varphi-\beta-\theta)}\delta^2+\mathcal{O}[\delta]^3\right)\quad, \tag{4.56}$$

$$p_{\mathrm{m}}^{(II)}=p_{\mathrm{corr}}\left(1-\frac{\sin(2\varphi-\beta)}{4\ \sin\theta\cos(2\varphi-\beta-\theta)}\delta^2+\mathcal{O}[\delta]^3\right)\quad, \tag{4.57}$$

where the symbol $\mathcal{O}[\delta]^3$ indicates terms with orders δ^3 and higher.

This is a somewhat surprising result. It says that both detector mounting schemes, be the diode stationary on the optical bench or moving with the stage, lead to the same measured period, up to the second order in δ. The leading percentage error is

$$\mathcal{E}=\frac{\sin(2\varphi-\beta)}{4\ \sin\theta\cos(2\varphi-\beta-\theta)}\delta^2\quad. \tag{4.58}$$

As a comparison, one should revisit Section 4.1.4 where the measurement error for a point detector is discussed. There, when the detector gets displaced together with the beamsplitter, it measures the exact fringe period, but when it remains stationary, an error proportional to δ incurs [Eq. (4.23)].

The SBIL tool employs the mounting scheme where the photodiode is fixed on the optical bench. The SBIL beam alignment system can quite safely align the mean beam angles to within 10 μrad (Sec. 3.5.2). Based on Eq. (4.58), this gives an alignment induced period measurement error of approximately 100 parts per trillion. This is four-order-of-magnitude smaller than the required 1 ppm SBIL period measurement accuracy. It is safe to assert that for SBIL, the beam alignment induced period measurement error is negligible, at least when a perfect beamsplitter is used.

4.1.9 Period measurement with a pseudo-ideal beamsplitter

As mentioned in Section 3.2.2, the rectangular shape of the beamsplitter is chosen for manufacturing and alignment reasons. One face of the beamsplitter has an enhanced aluminum coating [Fig. 4-15(a)]. This face is aligned to the x-axis interferometer stage mirror via a 0.1 μrad-resolution autocollimator. The stage mirror has been previously aligned perpendicular to the vacuum chuck surface. If the beamsplitter interface is parallel to the coated surface, then by implication, it is perpendicular to the chuck surface as well. When the beamsplitter is used to align the beams, the fringe perpendicularity is thereby assured. In practice however, beamsplitter shape non-ideality and alignment error incurred during the splitter installation do exist. The interface's perpendicularity to the substrate can only be assured to around 30 μrad.

The same beamsplitter is also used for *in-situ* fringe period measurement. Up to now, the discussion on period measurement has been grounded on the assumption that the beamsplitter is made to perfection. What if the interface is tilted with respect to the substrate, either because of imperfect manufacturing or because of errors in alignment? Intuitively, this seems to be a problem. The SBIL beam alignment system ensures that the two arms have equal angles of incidence by aligning the beams exiting from the beamsplitter. It does not align the angles at the beamsplitter's entry surface. If the interface is tilted, equalizing the exit angles necessarily leads to unequal entry angles, which results in a slight tilt of the interference fringes during lithography. The fringe tilt leads to a substrate-nonflatness induced phase error (Sec. 3.2.2). A more grave concern however is on the accuracy of the fringe period measurement. If measuring with an imperfect beamsplitter can not detect the proper period in the substrate plane, which is determined by the beams' entry angles not the exit ones, the scheme does not work and can not be used by SBIL.

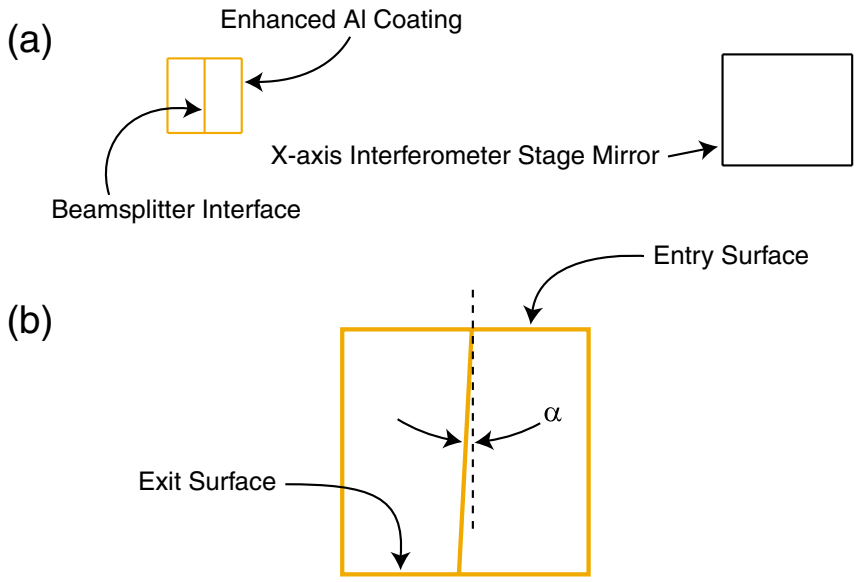

Figure 4-15: An imperfect beamsplitter. (a) Interface tilt may develop as a result of misalignment. (b) Tilt may also exist because of non-ideal optics manufacturing.

In this section, I study period measurement with a pseudo-ideal beamsplitter, where the splitter has a perfect exterior geometry, but its interface is tilted by a slight angle α [Fig. 4-15(b)]. When the case is solved, I move on to describe period measurement with a non-ideal beamsplitter that has not only an interface tilt, but also tilts in its entry and exit surfaces. It probably does not surprise the reader that the two cases are related in their mathematical derivations. Results show that in both, the beamsplitter period measurement scheme works and in theory exceeds the 1 ppm SBIL accuracy requirement.

I only investigate the case where the photodiode is fixed, for it is the mounting scheme currently in use. First, the net change in optical path length (OPL) must be established. As before, I consider an imaginary point photodetector. Suppose after beam alignment, the exit angles of the beams after the beamsplitter are θ_1 for the left arm and θ_2 for the right. Figures 4-16 and 4-17 show the ray trace. Comparing them with Figures 4-9 and 4-10, one discovers that the only difference exists in the left arm, due to reflections off the tilted interface. In particular, since the entry angle is now χ_1, which is not equal to θ_1, the OPL segment Γ_1 is different from before. An additional OPL segment also emerges due to an imbalance of path length inside the beamsplitter. Overall, the OPL change in the left arm is

$$\begin{aligned} \Delta L &= \Gamma_1 + n\,\vartheta_1 + \Sigma_1 + \Delta_1 - 2L_1 \\ &= D\ \sin\chi_1 - D\ \sin(2\varphi - \theta_1)\ \ , \end{aligned} \tag{4.59}$$

where Γ_1, Σ_1, Δ_1 and L_1 are path segments defined in Figures 4-16 and 4-17; $n\,\vartheta_1$ is the

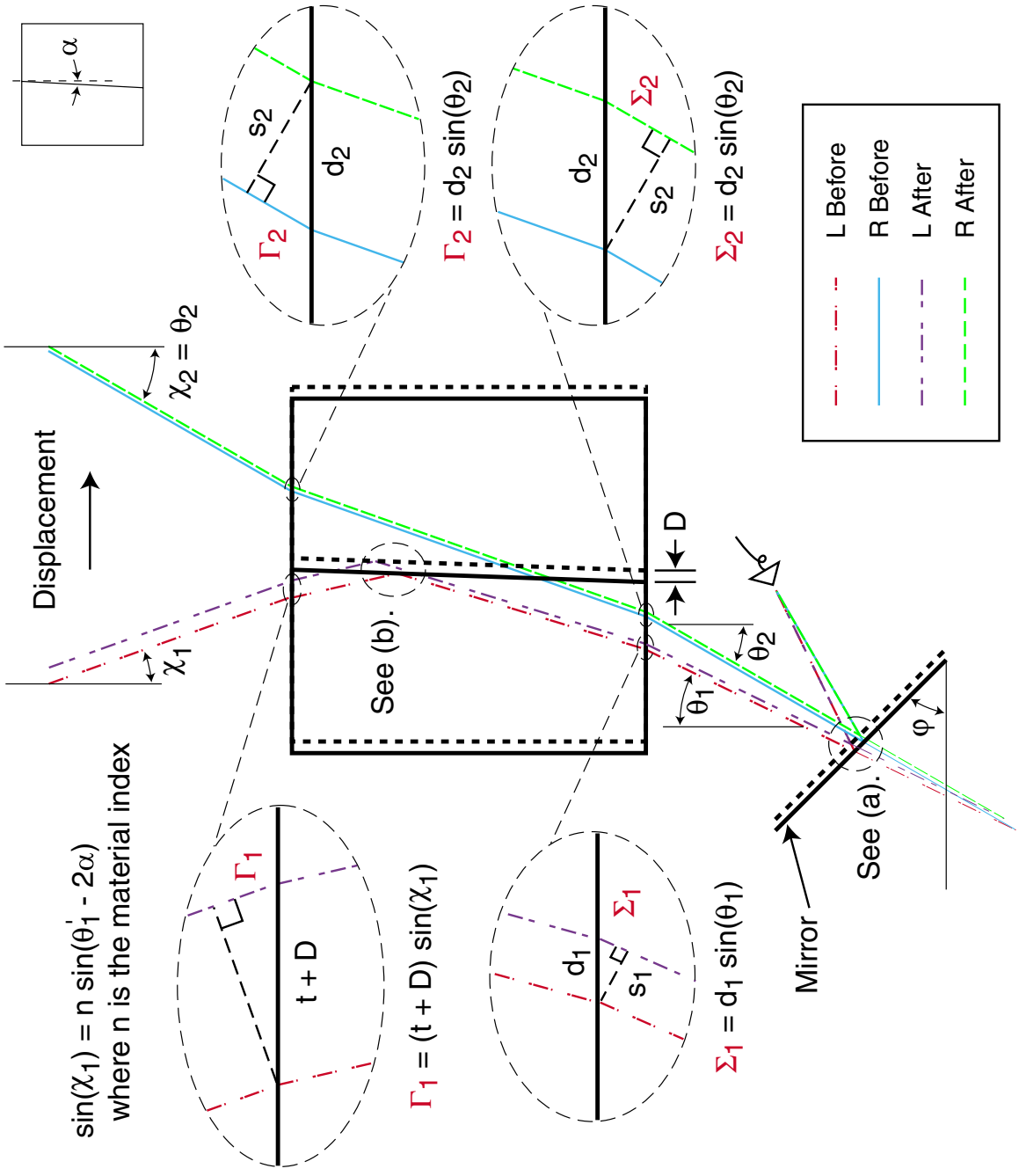

Figure 4-16: Period measurement with a pseudo-ideal beamsplitter. Ray trace showing the OPL variations. To be continued in Figure 4-17.

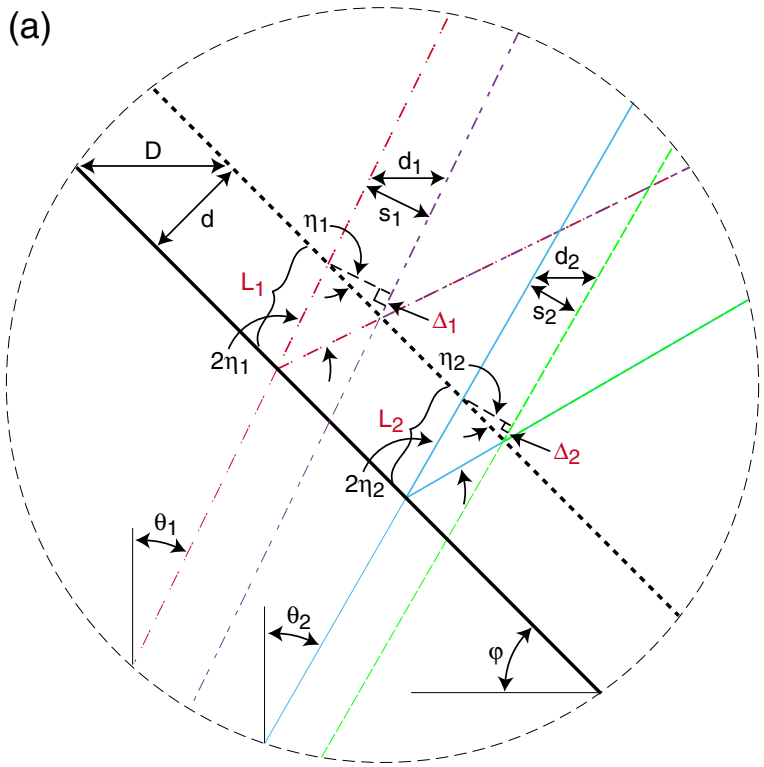

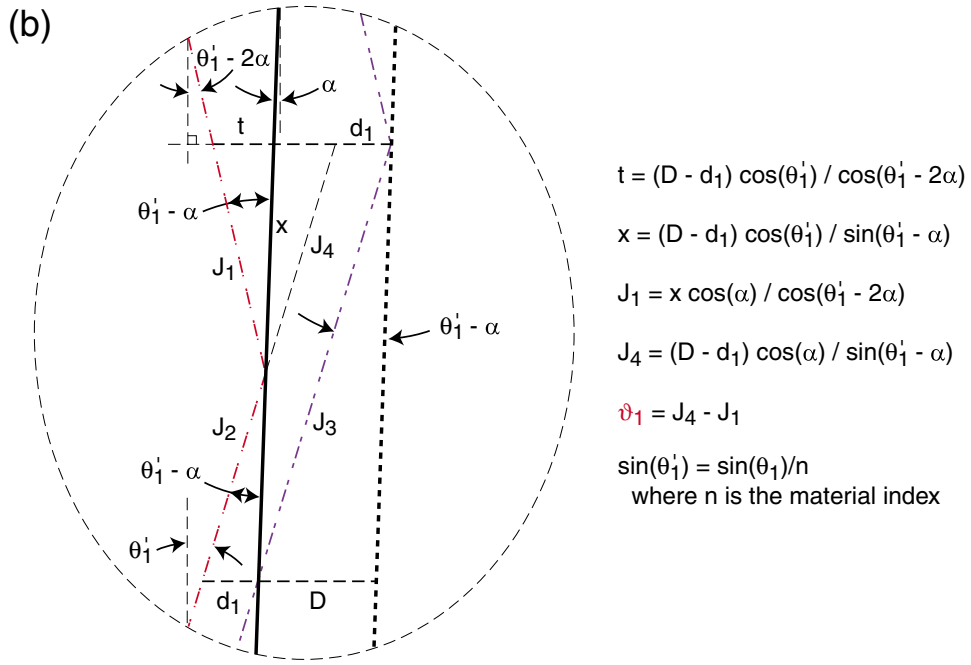

Figure 4-17: Period measurement with a pseudo-ideal beamsplitter. Ray trace showing the OPL variations. Continued from Figure 4-16.

segment due to the OPL imbalance inside the beamsplitter and n is the beamsplitter's refractive index. The change in the right arm is

$$\begin{aligned} \Delta R &= -\Gamma_2 + \Sigma_2 + \Delta_2 - 2L_2 \\ &= -D\ \sin\theta_2 - D\ \sin(2\varphi - \theta_2)\ \ , \end{aligned} \tag{4.60}$$

which is identical to Eq. (4.17). Physically, this makes sense because the right beam simply transmits through the interface and is unaware of its tilt. The net change in OPL is the difference between ΔL and ΔR,

$$\begin{aligned} \delta\mathrm{L} &= \Delta L - \Delta R \\ &= D\ (\sin\chi_1 + \sin\theta_2) - D\ [\sin(2\varphi - \theta_1) - \sin(2\varphi - \theta_2)]\ \ . \end{aligned} \tag{4.61}$$

Eq. (4.61) differs from Eq. (4.18) only in one term—the term $D\sin\theta_1$ is replaced by $D\sin\chi_1$. The beams' entry angles into the beamsplitter are χ_1 and θ_2 for the left and the right arm, respectively. The angle χ_1 is related to the exit angle θ_1 by

$$\sin\chi_1 = n\ \sin(\theta_1^{'} - 2\alpha)\ \ , \tag{4.62}$$

$$\sin\theta_1^{'} = \sin\theta_1/n\ \ . \tag{4.63}$$

Since the entry angles set the fringe period in the substrate plane, an expression of both inside δL raises the hope that the correct period may be measured.

The movements of the Gaussian beam centroids are traced out in Figures 4-18 and 4-19. Comparing them to Figures 4-12 and 4-13, one notes that the distance d_1 is now dependent on the tilt angle α. As a result, the location of the left beam centroid (X_L) changes slightly, whereas that of the right (X_R) remains the same,

$$X_L(D) = -\frac{2D\left[\dfrac{\cos\alpha\cos\theta_1\cos(\theta_1^{'} - \alpha)}{\cos\theta_1^{'}} - \sin(\varphi - \theta_1)\sin\varphi\right]}{\cos(2\varphi - \beta - \theta_1)}\ \ , \tag{4.64}$$

$$X_R(D) = \frac{2D\sin\varphi\sin(\varphi - \theta_2)}{\cos(2\varphi - \beta - \theta_2)}\ \ . \tag{4.65}$$

Plug expressions for ΔL, ΔR, X_L and X_R into Eq. (4.51), derive the measured period p_m, and expand p_m for the case when the exit angles are only slightly misaligned, i.e., when $\theta_1 = \theta$ and $\theta_2 = \theta + \delta$. One has in powers of δ and α

$$p_\mathrm{m} = p_\mathrm{corr}\left(1 - \frac{\cos\theta}{2\,n\,\cos\theta'}\,\delta\,\alpha - \frac{\sin(2\varphi - \beta)}{4\ \sin\theta\cos(2\varphi - \beta - \theta)}\delta^2 + \mathcal{O}[3]\right)\ \ , \tag{4.66}$$

where

$$p_\mathrm{corr} = \frac{\lambda}{\sin\chi + \sin(\theta + \delta)}\ \ , \tag{4.67}$$

and from Eqs. (4.62) and (4.63),

$$\sin\chi = n\ \sin(\theta^{'} - 2\alpha)\ \ , \tag{4.68}$$

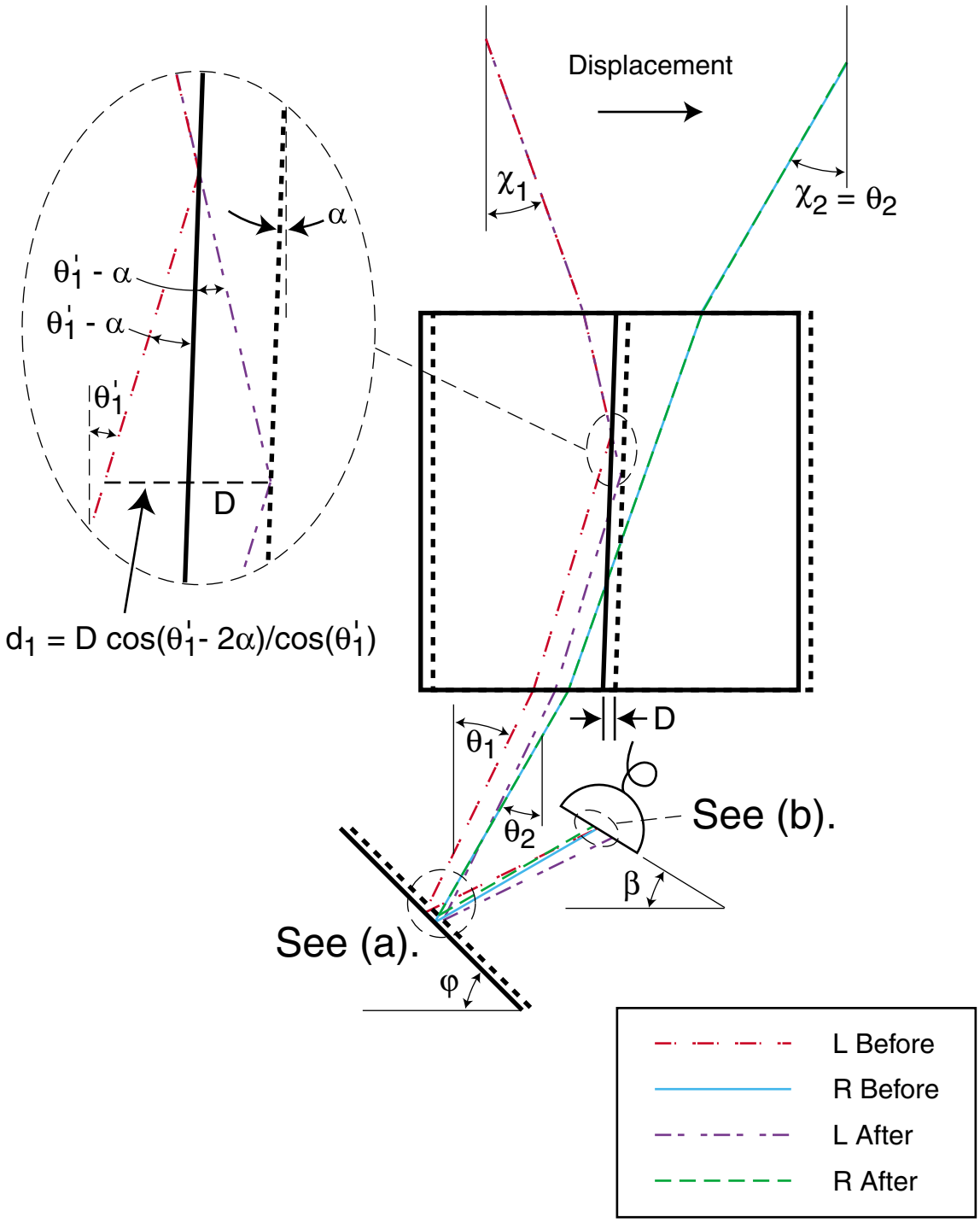

Figure 4-18: Period measurement with a pseudo-ideal beamsplitter. Ray trace showing the movements of the beam centroids. To be continued in Figure 4-19.

(a)

$d = D \sin(\varphi)$

$d_1 = D + D \cos(\theta_1' - 2\alpha)/\cos(\theta_1')$
$s_0 = d_1 \cos(\theta_1)$
$\eta_1 = \varphi - \theta_1$
$T = s_0/\cos(\eta_1)$
$s_1 = [T - 2d \tan(\eta_1)] \cos(\eta_1)$

$\eta_2 = \varphi - \theta_2$
$s_2 = 2d \tan(\eta_2) \cos(\eta_2)$

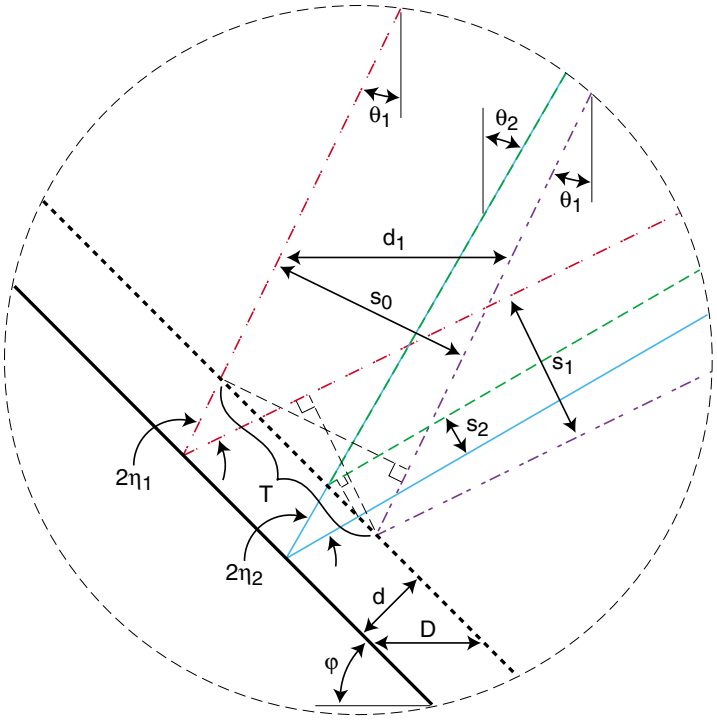

(b)

$\xi_1 = 90^\circ - 2\varphi + \theta_1$
$\gamma_1 = 90^\circ - \beta - \xi_1 = 2\varphi - \beta - \theta_1$
$X_L = s_1/\cos(\gamma_1)$

$\xi_2 = 90^\circ - 2\varphi + \theta_2$
$\gamma_2 = 90^\circ - \beta - \xi_2 = 2\varphi - \beta - \theta_2$
$X_R = s_2/\cos(\gamma_2)$

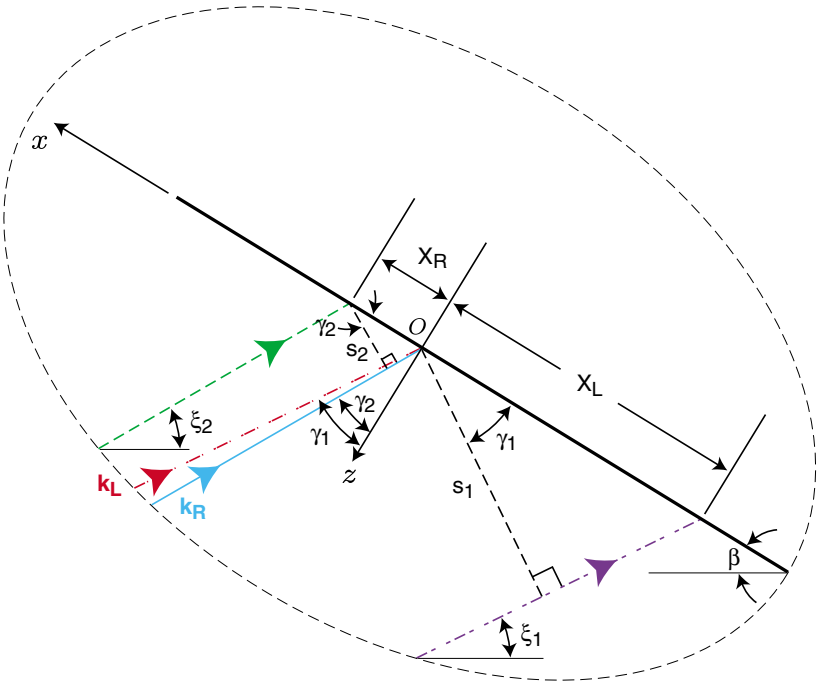

Figure 4-19: Period measurement with a pseudo-ideal beamsplitter. Ray trace showing the movements of the beam centroids. Continued from Figure 4-18.

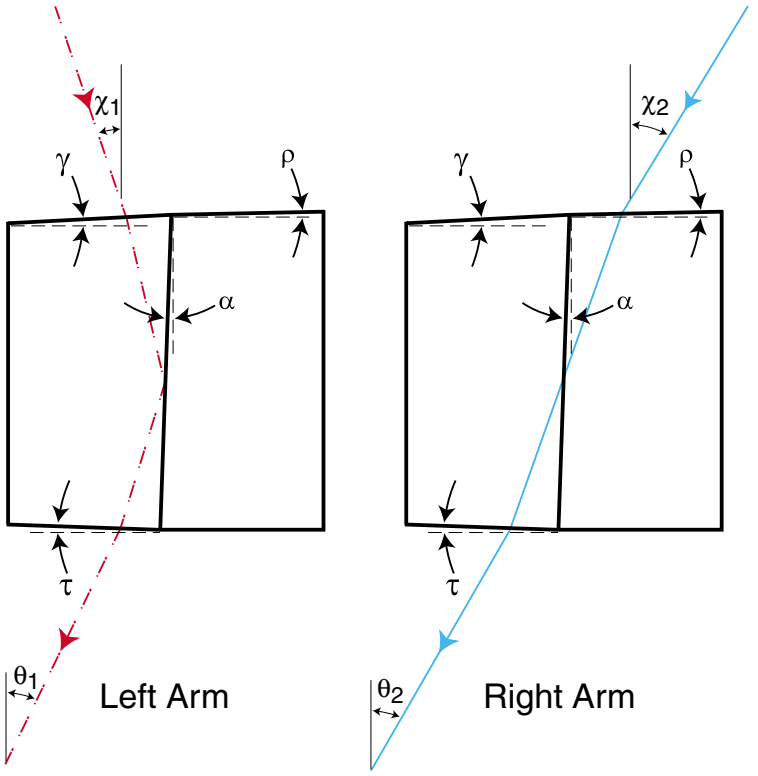

Figure 4-20: A non-ideal beamsplitter has both interface and surface tilts.

$$\sin\theta' = \sin\theta/n \quad . \tag{4.69}$$

The symbol $\mathcal{O}[3]$ denotes terms with orders three or higher—terms proportional to $\delta^2\alpha$ and $\delta\,\alpha^2$, for example. The period p_{corr} is determined by the angles of the beams prior to entry into the beamsplitter. It corresponds to the actual fringe period in the substrate plane. The leading percentage error is proportional to the product of δ and α. From Section 3.2.2, the value for α is approximately 30 μrad, which includes both the manufacturing error and the alignment error incurred during the beamsplitter installation. Together with $\theta \approx 26°$, $\delta \approx 10$ μrad and $n \approx 1.48$, one has the leading percentage error at about 95 parts per trillion, negligible given the 1 ppm required accuracy.

So in the case of a pseudo-ideal beamsplitter with only an interface tilt, the beamsplitter period measurement scheme continues to work. I now move on to describe the most general case.

4.1.10 Period measurement with a non-ideal beamsplitter

In general, the beamsplitter, due to manufacturing reasons, has not only an interface tilt, but also tilts in its entry and exit surfaces. Given that the exit angles are θ_1 and θ_2, from Figure 4-20, one can calculate the incident angles χ_1 and χ_2, for the left and

the right arm, respectively,

$$\chi_1 = \gamma - \sin^{-1}\left[n\,\sin\left(2\,\alpha + \gamma - \tau - \sin^{-1}\left[\frac{\sin(\theta_1 - \tau)}{n}\right]\right)\right] \quad , \tag{4.70}$$

$$\chi_2 = -\rho + \sin^{-1}\left[n\,\sin\left(\rho + \tau + \sin^{-1}\left[\frac{\sin(\theta_2 - \tau)}{n}\right]\right)\right] \quad . \tag{4.71}$$

While it is not very instructive to stare at these expressions, one thing is clear: The problem is now a lot more complicated. Instead of working out the exact OPL change and beam centroid movements, I need an alternative approach to calculate the measured fringe period.

The approach that I have in mind is inspired by the so-called perturbation theory from quantum mechanics, where for instance, a particular energy state of an atom is known by its quantum wavefunction, and when an external electric field is applied, that base state splits into two or more whose energies are slightly "perturbed" from the base energy and whose wavefunctions can be modified from the base wavefunction by adding small perturbation terms.

In my case, the "base wavefunction" is the solution obtained for the pseudo-ideal beamsplitter (Sec. 4.1.9). The small perturbation terms originate from the tiny distortions in the splitter's shape—the tilts γ, ρ and τ in the entry and exit surfaces, graphically defined in Figure 4-20.

First, I derive an expression for the correct fringe period in the substrate plane, which will be used later to check the measured period. Given the incident angles χ_1 and χ_2, the period is

$$p_{\text{corr}} = \frac{\lambda}{\Upsilon_{\text{corr}}} = \frac{\lambda}{\sin\chi_1 + \sin\chi_2} \quad . \tag{4.72}$$

The numerator is simply the wavelength of the laser, a constant. The denominator Υ_{corr} contains everything of interest. Expanding Υ_{corr} perturbatively around its base value and keeping terms that are first-order in γ, ρ and τ, one gets

$$\Upsilon_{\text{corr}} = \left[\sin\chi_1^{(0)} + \sin\chi_2^{(0)}\right] + C_\gamma\,\gamma + C_\rho\,\rho + C_\tau\,\tau + \mathcal{O}[2] \quad , \tag{4.73}$$

where

$$\sin\chi_1^{(0)} = n\,\sin\left[\sin^{-1}\left(\frac{\sin\theta_1}{n}\right) - 2\alpha\right] \quad , \tag{4.74}$$

$$\sin\chi_2^{(0)} = \sin\theta_2 \quad , \tag{4.75}$$

$$C_\gamma = \cos\theta_1 - n\sqrt{1 - \frac{\sin^2\theta_1}{n^2}} \quad , \tag{4.76}$$

$$C_\rho = -\cos\theta_2 + n\sqrt{1 - \frac{\sin^2\theta_2}{n^2}} \quad , \tag{4.77}$$

$$C_\tau = -\cos\theta_1 + n\sqrt{1-\frac{\sin^2\theta_1}{n^2}} - \cos\theta_2 + n\sqrt{1-\frac{\sin^2\theta_2}{n^2}} \ , \tag{4.78}$$

and $\mathcal{O}[2]$ symbolizes terms with orders two or higher—terms proportional to the products $\gamma\alpha$, $\tau\alpha$, $\gamma\tau$, or $\rho\tau$, for instance. The base term in Eq. (4.73) corresponds to the substrate-plane fringe period found earlier for the pseudo-ideal beamsplitter. The three first-order terms correspond to perturbations of the base term due to tilts in the splitter's entry and exit surfaces.

Now I proceed to derive the measured fringe period. When a non-ideal beamsplitter is used to conduct the measurement, the optical paths are considerably more complex (Figs. 4-21 through 4-25). As always, the OPL change in the left arm is the sum of all unbalanced path segments,

$$\begin{aligned}\Delta L &= (\Gamma_1 + \Xi_1 + n\,\Pi_1 - n\,\Lambda_1) + (\Sigma_1 + \Omega_1 + n\,K_1 - n\,\Psi_1) \\ &\quad + n\,\vartheta_1 + \Delta_1 - 2L_1 \\ &= D\,\left\{\left[\sin\chi_1^{(0)} - \sin(2\varphi - \theta_1)\right] + C_\gamma\,\gamma + C_{\tau 1}\,\tau\right\} + \mathcal{O}[2] \ ,\end{aligned} \tag{4.79}$$

where $\chi_1^{(0)}$ and C_γ have been defined in Eqs. (4.74) and (4.76), respectively, and

$$C_{\tau 1} = -\cos\theta_1 + n\sqrt{1-\frac{\sin^2\theta_1}{n^2}} \ . \tag{4.80}$$

Similarly, the OPL change in the right arm is

$$\begin{aligned}\Delta R &= (-\Gamma_2 - n\,\Lambda_2 + \Xi_2 + n\,\Pi_2) + (\Sigma_2 + \Omega_2 + n\,K_2 - n\,\Psi_2) + \Delta_2 - 2L_2 \\ &= -D\,\left\{\left[\sin\chi_2^{(0)} + \sin(2\varphi - \theta_2)\right] + C_\rho\,\rho + C_{\tau 2}\,\tau\right\} + \mathcal{O}[2] \ ,\end{aligned} \tag{4.81}$$

where $\chi_2^{(0)}$ and C_ρ have been defined in Eqs. (4.75) and (4.77), respectively, and

$$C_{\tau 2} = -\cos\theta_2 + n\sqrt{1-\frac{\sin^2\theta_2}{n^2}} \ . \tag{4.82}$$

Note that C_τ, as defined by Eq. (4.78), is the sum of $C_{\tau 1}$ and $C_{\tau 2}$,

$$C_\tau = C_{\tau 1} + C_{\tau 2} \ . \tag{4.83}$$

The net change in optical path length is the difference between ΔL and ΔR

$$\begin{aligned}\delta\mathrm{L} &= \Delta L - \Delta R \\ &= D\,\left\{\left[\sin\chi_1^{(0)} + \sin\chi_2^{(0)}\right] - \left[\sin(2\varphi - \theta_1) - \sin(2\varphi - \theta_2)\right]\right\} \\ &\quad +\ D\,(C_\gamma\,\gamma + C_\rho\,\rho + C_\tau\,\tau) + \mathcal{O}[2] \ .\end{aligned} \tag{4.84}$$

Here, the base term reproduces Eq. (4.61)—the net OPL difference for the pseudo-ideal beamsplitter. The second term corresponds to the perturbation.

The locations of the Gaussian beam centroids are also modified slightly from those for the pseudo-ideal beamsplitter,

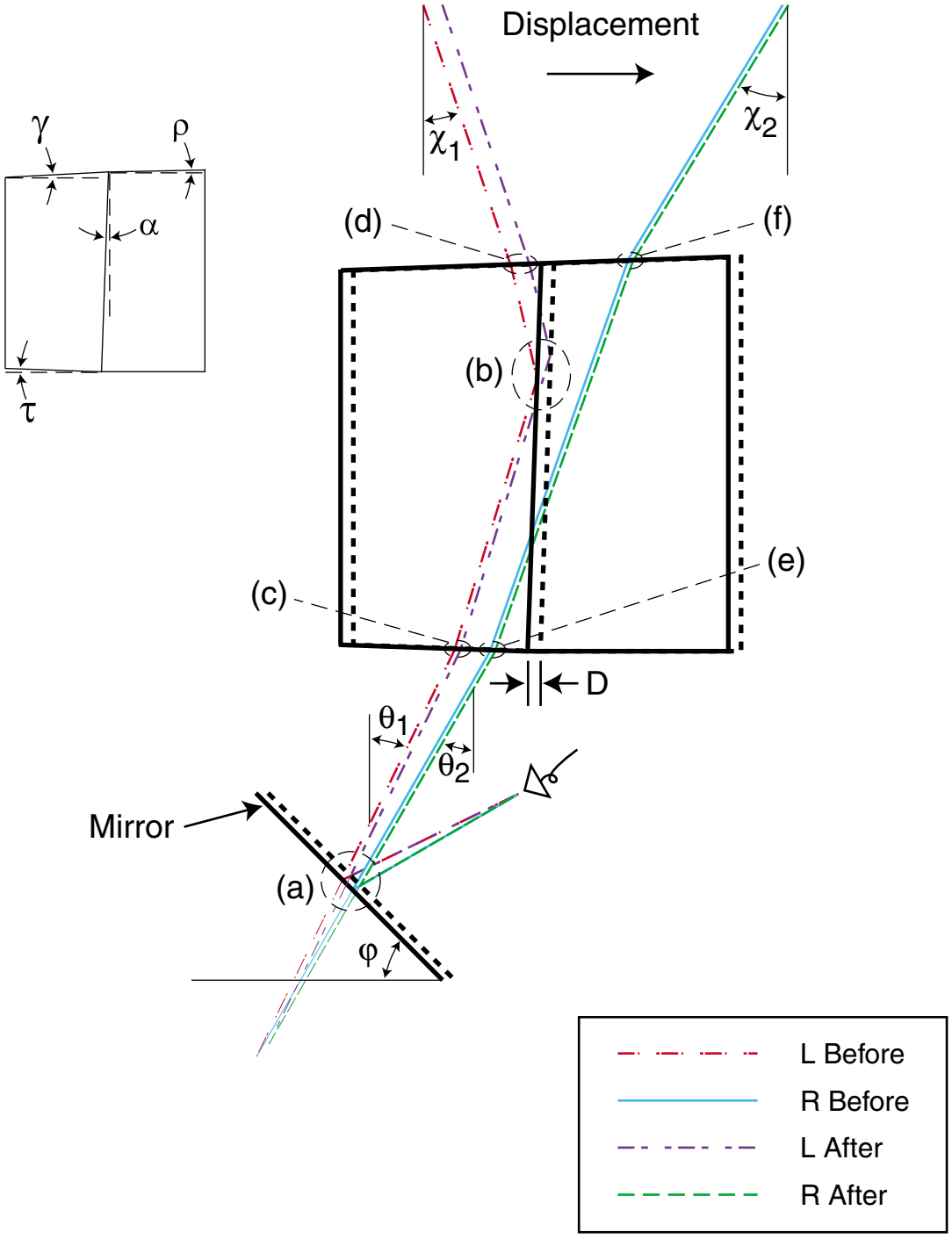

Figure 4-21: Period measurement with a non-ideal beamsplitter. Ray trace showing the OPL variations. To be continued in Figures 4-22–4-26.

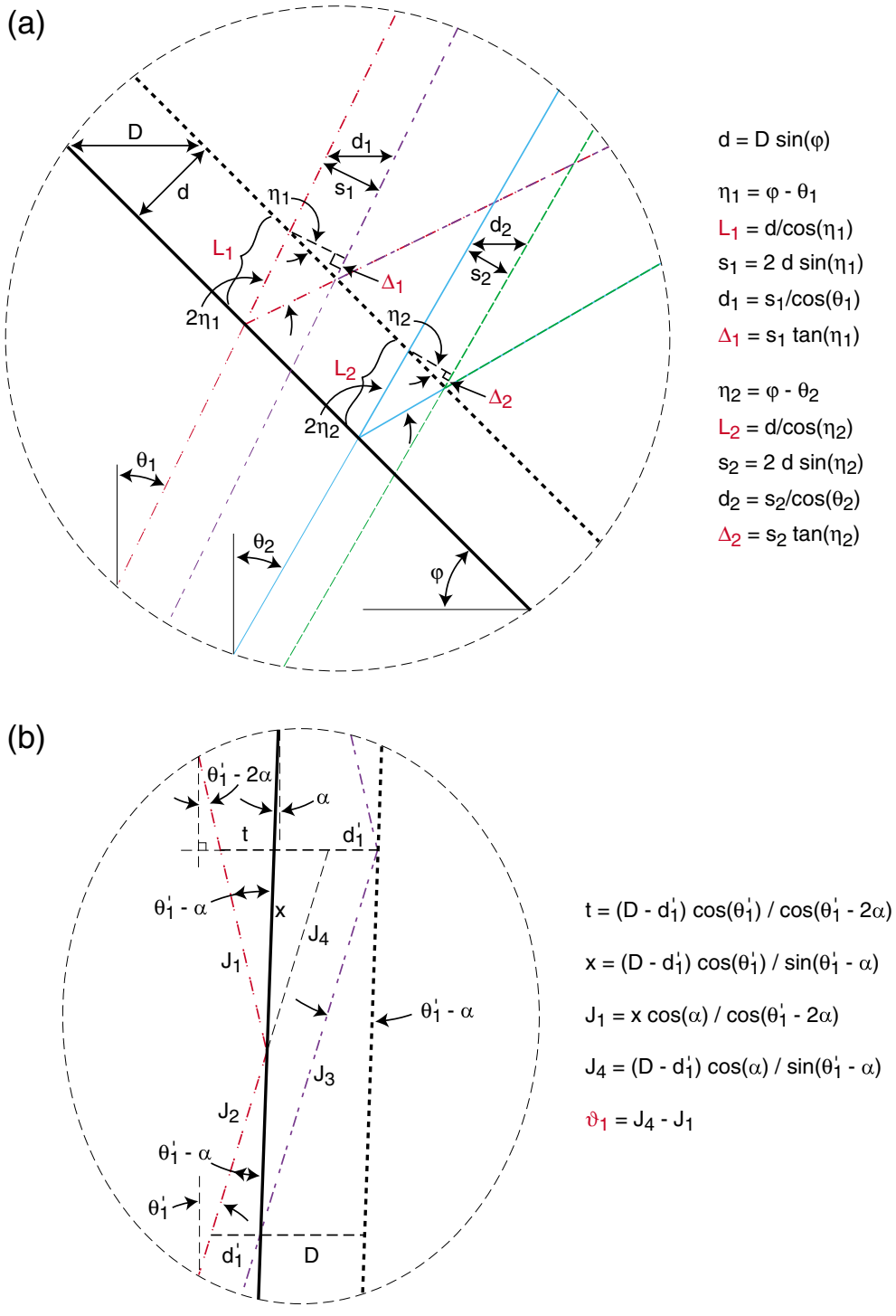

Figure 4-22: Period measurement with a non-ideal beamsplitter. Ray trace showing the OPL variations. Continued from Figure 4-21.

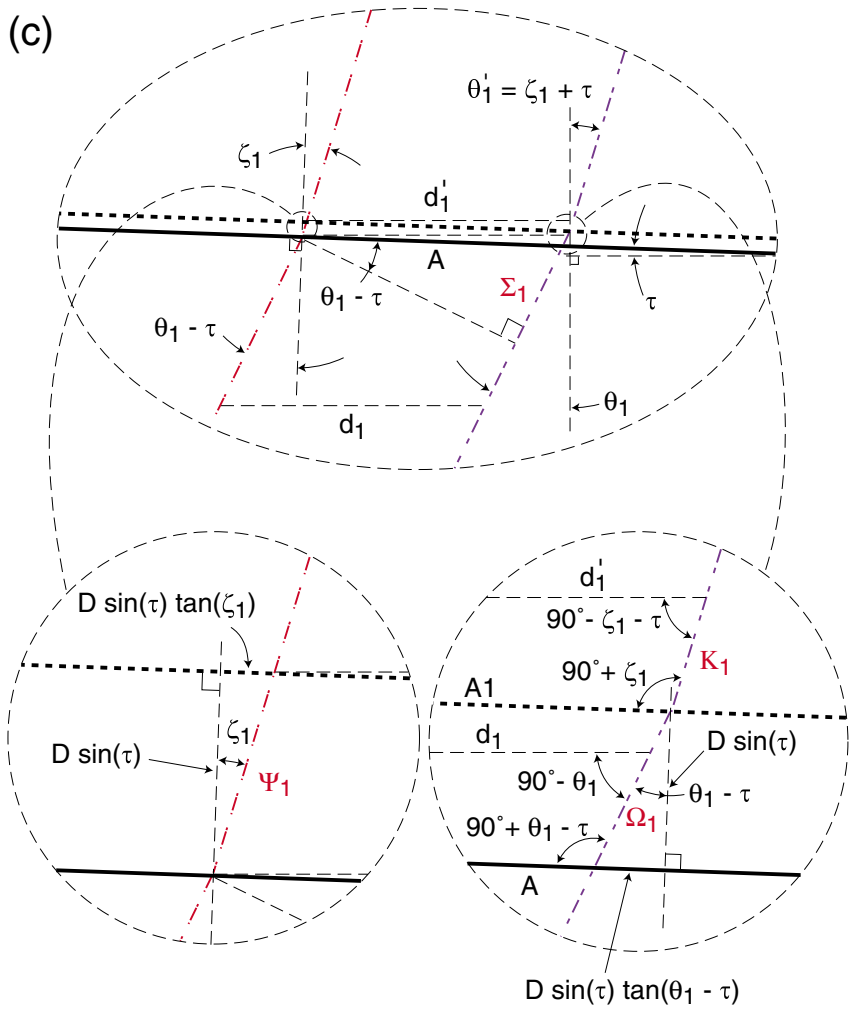

$\Sigma_1 = A \sin(\theta_1 - \tau)$

$A = d_1 \cos(\theta_1) / \cos(\theta_1 - \tau)$

$\Omega_1 = D \sin(\tau) / \cos(\theta_1 - \tau)$

$A1 = A + D \sin(\tau) \tan(\theta_1 - \tau) - D \sin(\tau) \tan(\zeta_1)$

$d'_1 = A1 \cos(\zeta_1) / \cos(\zeta_1 + \tau)$

$n K_1 = n A1 \sin(\tau) / \cos(\zeta_1 + \tau)$

$n \Psi_1 = n D \sin(\tau) / \cos(\zeta_1)$

$\theta'_1 = \zeta_1 + \tau$

$\sin(\zeta_1) = \sin(\theta_1 - \tau) / n$
where n is the material index

Figure 4-23: Period measurement with a non-ideal beamsplitter. Ray trace showing the OPL variations. Continued from Figure 4-21.

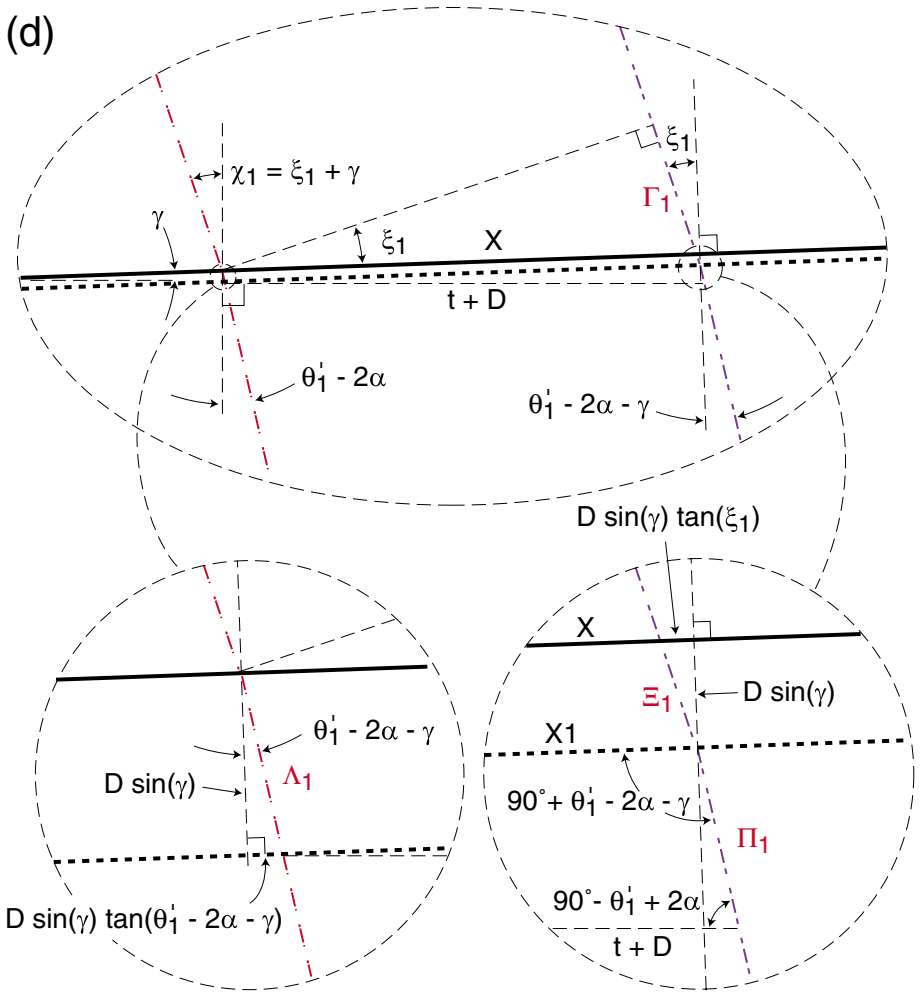

$n\,\Pi_1 = n\,(t + D)\,\sin(\gamma) / \cos(\theta'_1 - 2\alpha - \gamma)$

$X1 = (t + D)\,\cos(\theta'_1 - 2\alpha) / \cos(\theta'_1 - 2\alpha - \gamma)$

$\Xi_1 = D\,\sin(\gamma) / \cos(\xi_1)$

$X = X1 + D\,\sin(\gamma)\,\tan(\theta'_1 - 2\alpha - \gamma) - D\,\sin(\gamma)\,\tan(\xi_1)$

$\Gamma_1 = X\,\sin(\xi_1)$

$n\,\Lambda_1 = n\,D\,\sin(\gamma) / \cos(\theta'_1 - 2\alpha - \gamma)$

$\chi_1 = \xi_1 + \gamma$

$\sin(\xi_1) = n\,\sin(\theta'_1 - 2\alpha - \gamma)$
where n is the material index

Figure 4-24: Period measurement with a non-ideal beamsplitter. Ray trace showing the OPL variations. Continued from Figure 4-21.

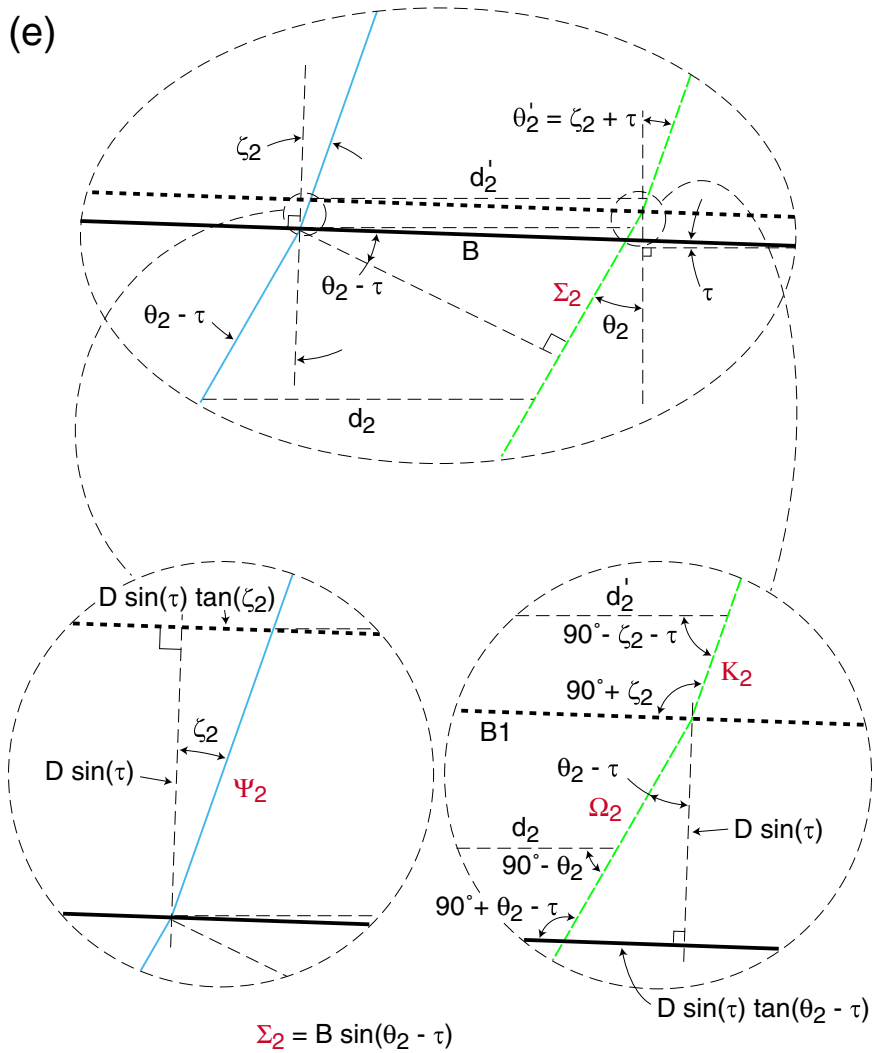

$\Sigma_2 = B \sin(\theta_2 - \tau)$

$B = d_2 \cos(\theta_2) / \cos(\theta_2 - \tau)$

$\Omega_2 = D \sin(\tau) / \cos(\theta_2 - \tau)$

$B1 = B + D \sin(\tau) \tan(\theta_2 - \tau) - D \sin(\tau) \tan(\zeta_2)$

$d_2' = B1 \cos(\zeta_2) / \cos(\zeta_2 + \tau)$

$n K_2 = n B1 \sin(\tau) / \cos(\zeta_2 + \tau)$

$n \Psi_2 = n D \sin(\tau) / \cos(\zeta_2)$

$\theta_2' = \zeta_2 + \tau$

$\sin(\zeta_2) = \sin(\theta_2 - \tau) / n$
where n is the material index

Figure 4-25: Period measurement with a non-ideal beamsplitter. Ray trace showing the OPL variations. Continued from Figure 4-21.

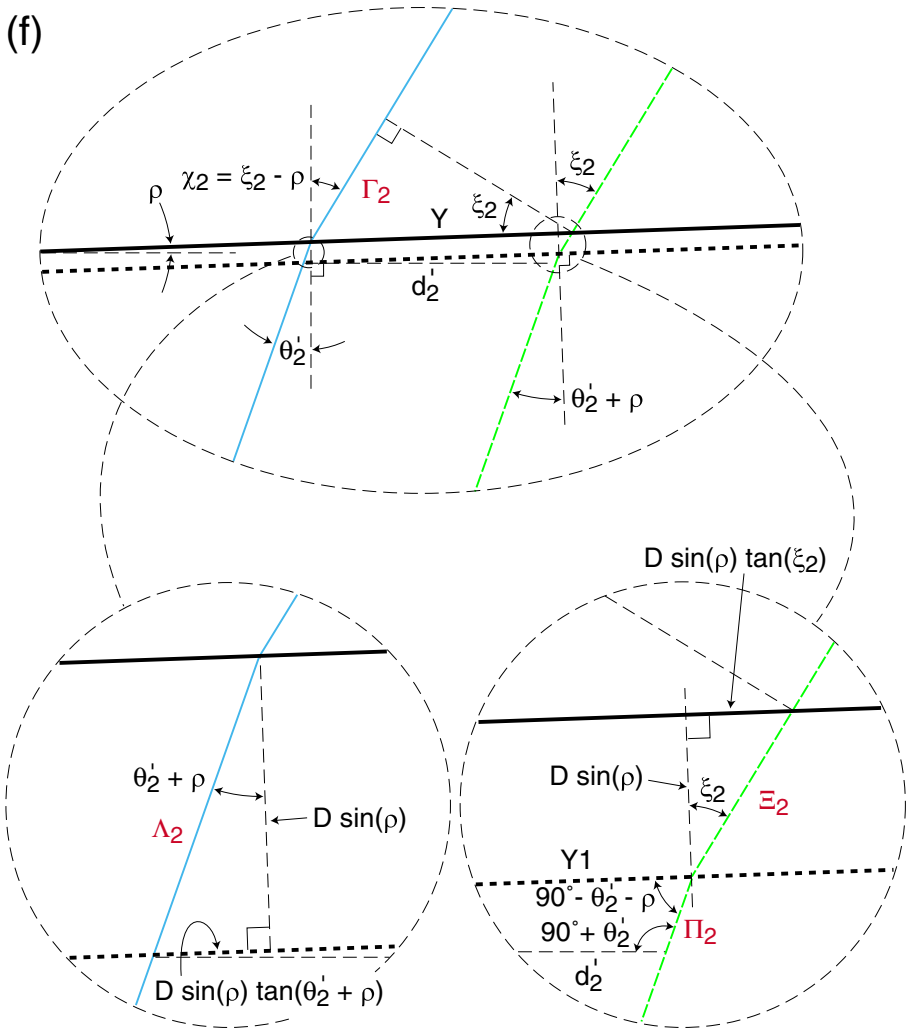

$n\ \Pi_2 = n\ d'_2 \sin(\rho) / \cos(\theta'_2 + \rho)$

$Y1 = d'_2 \cos(\theta'_2) / \cos(\theta'_2 + \rho)$

$\Xi_2 = D \sin(\rho) / \cos(\xi_2)$

$Y = Y1 - D \sin(\rho) \tan(\theta'_2 + \rho) + D \sin(\rho) \tan(\xi_2)$

$\Gamma_2 = Y \sin(\xi_2)$

$n\ \Lambda_2 = n\ D \sin(\rho) / \cos(\theta'_2 + \rho)$

$\chi_2 = \xi_2 - \rho$

$\sin(\xi_2) = n \sin(\theta'_2 + \rho)$
where n is the material index

Figure 4-26: Period measurement with a non-ideal beamsplitter. Ray trace showing the OPL variations. Continued from Figure 4-21.

$$X_L = X_L^{(0)} + F_\gamma\,\gamma + F_{\tau 1}\,\tau + \mathcal{O}[2] \ , \tag{4.85}$$

$$X_R = X_R^{(0)} + F_\rho\,\rho + F_{\tau 2}\,\tau + \mathcal{O}[2] \ , \tag{4.86}$$

where $X_L^{(0)}$ and $X_R^{(0)}$ represent the base solution given by Eqs. (4.64) and (4.65), respectively. The terms linear in γ, ρ and τ are leading-order perturbations to the base solution. As before, the symbol $\mathcal{O}[2]$ denotes all higher-order terms.

Fortunately, in my bid to calculate the measured fringe period, I need not worry about finding the exact expressions for the proportionality constants F_γ, F_ρ, $F_{\tau 1}$ or $F_{\tau 2}$, because of the following simple observation: Applying Eq. (4.52) to the current case, one finds the measured fringe period

$$p_\mathrm{m} = \frac{D}{N} = \frac{\lambda}{\Upsilon_\mathrm{m}} \ , \tag{4.87}$$

where

$$\begin{aligned}\Upsilon_\mathrm{m} = \left[\sin\chi_1^{(0)} + \sin\chi_2^{(0)}\right] &+ (C_\gamma\,\gamma + C_\rho\,\rho + C_\tau\,\tau) \\ &+ \{[\sin(2\varphi - \beta - \theta_2) - \sin(2\varphi - \beta - \theta_1)]\cdot[X_L + X_R]/2 \\ &\quad - [\sin(2\varphi - \theta_1) - \sin(2\varphi - \theta_2)]\} + \mathcal{O}[2] \ .\end{aligned} \tag{4.88}$$

When the exit angles are only slightly misaligned, i.e., when $\theta_1 = \theta$ and $\theta_2 = \theta + \delta$, the expression inside the curly brackets is void of first-order terms. More specifically, as indicated by Eq. (4.66), the base centroid locations $X_L^{(0)}$ and $X_R^{(0)}$, when combined with the trigonometric terms, yield zero first-order contribution—the lowest order terms being those proportional to $\delta\,\alpha$ and δ^2. Therefore, Eq. (4.88) can be rewritten as

$$\Upsilon_\mathrm{m} = \left[\sin\chi_1^{(0)} + \sin\chi_2^{(0)}\right] + C_\gamma\,\gamma + C_\rho\,\rho + C_\tau\,\tau + \mathcal{O}[2] \ . \tag{4.89}$$

Up to the first order, Υ_m coincides exactly with Eq. (4.73), meaning that for small δ, α, γ and τ, the period measured by a non-ideal beamsplitter is the actual fringe period at the substrate plane.

4.1.11 Fringe nonlinearity-induced stitching error

So far, I have considered only beams with planar wavefronts. What happens to the period measurement if the wavefronts are slightly curved or distorted, as is the case in reality?

Curved wavefronts interfere and give rise to a fringe phase that is not strictly linear. As a concrete example, assume the image grating phase varies only along the x axis and is given by

$$\phi(x) = \frac{2\pi}{p_0}x + Bx^2 \ , \tag{4.90}$$

where p_0 is some constant and B is a small constant coefficient. By choice, the phase at the origin is zero. Physically, the first term is the good old linear phase with a nominal period p_0. The second term symbolizes the nonlinear component, which is mirror symmetric about $x = 0$. The grating period as a function of x is given by

$$p(x) = \left(\frac{1}{2\pi}\frac{d\phi}{dx}\right)^{-1} = 2\pi\left(\frac{2\pi}{p_0} + 2Bx\right)^{-1} \approx p_0\left(1 - \frac{Bp_0x}{\pi}\right) \quad . \tag{4.91}$$

Had the nonlinear phase been zero (i.e., $B = 0$), one would have plane-wave interference where the resulting period $p(x)$ is simply the nominal p_0.

During the period measurement, suppose that the beamsplitter, starting at $x = 0$, is displaced by an amount x_0. The number of signal oscillations recorded at the photodiode is

$$N = \frac{\phi(x_0)}{2\pi} = \frac{x_0}{p_0} + \frac{Bx_0^2}{2\pi} \quad . \tag{4.92}$$

The measured fringe period p_m is a constant, and is related to x_0 and N by

$$p_\mathrm{m} = \frac{x_0}{N} \approx p_0\left(1 - \frac{Bp_0x_0}{2\pi}\right) \quad . \tag{4.93}$$

Compare Eq. (4.93) to Eq. (4.91). In a sense, the measured period is the "average" of an otherwise changing period.

The inability of the beamsplitter scheme to trace out $p(x)$ produces a source of systematic error. Suppose that one is interested in stepping the stage by an integer number (N') of fringe periods along x so that a new scan can be started. Based on the measured period, the stage will be displaced by

$$x' = p_\mathrm{m}N' \quad . \tag{4.94}$$

Ideally, over that distance, the grating phase should increment by $2\pi N'$, but phase nonlinearities sabotage the result. Expansion by Mathematica gives

$$\phi(x') = 2\pi N' + N'p_0(N'p_0 - x_0)B + \mathcal{O}[2] \quad . \tag{4.95}$$

The systematic stitching error thus introduced is

$$\Delta\phi \approx N'p_0(N'p_0 - x_0)B \quad . \tag{4.96}$$

As a realistic example, for $N' = 2500$, $p_0 = 400$ nm, $x_0 = 400$ μm and $B = 10$ nm/mm^2, Eq. (4.96) yields $\Delta\phi = 6$ nm over a distance of 1 mm.

A couple of methods can be used to reduce the error. Nonlinear component in the grating image should be minimized to make B smaller—a topic of discussion for the next chapter. The stage scan distance x_0, which is used to determine p_m, can also be increased.

Should the error, which arises from phase nonlinearities in the grating image, cause panic about the applicability of SBIL? No. I shall show in Section 5.6, the printed phase error, which is the nonlinear error in the written grating, can be minimized to less than 1 nm by overlapping scans even if the grating image is distorted at the dozen nanometer level. That said, the nominal grating period must still be determined with high accuracy in order to maximize the contrast. Given the values of p_0, x_0 and B used earlier, Eq. (4.93) predicts a percentage measurement error of only

$$\epsilon = \frac{Bp_0x_0}{2\pi} = 2.5 \times 10^{-13} \quad , \tag{4.97}$$

which is much smaller than the 1 ppm allocated budget. Fringe nonlinearities do not prevent the nominal grating period from being measured accurately. In fact, for a measurement error at the ppm level, Section 4.5 will prove that the resist grating phase is equal to that derived from the measured period.

The beamsplitter suffers not only from surface tilts as considered in Section 4.1.10, but also from figure errors—its surfaces can not be truly flat. The nonflatness induces additional fringe nonlinearities while the measurement is taking place. However, similar to the argument used earlier, this should not prevent the system from measuring the nominal fringe period with the desired accuracy.

4.1.12 Summary

After a somewhat lengthy discussion, here comes a simple conclusion: Physics allows the beamsplitter period measurement scheme to work. Even if the geometry of the splitter is imperfect or its alignment is off a bit, it will measure faithfully the fringe period as seen by the substrate during lithography. The theoretical limit of the measurement accuracy is at the part-per-billion level, far exceeding the 1 ppm SBIL requirement.

In the absence of pure plane waves and the presence of optics figure errors, the beams can very well propagate with distorted or curved wavefronts, giving rise to varying fringe period. The beamsplitter scheme, due to its nature, is not capable of mapping out the period as a function of distance, a problem that can be solved by conducting SBIL wavefront metrology (Ch. 5). The scheme can only yield a constant "averaged" period. Whereas the image grating phase may increase in a nonlinear fashion, the stage can only be displaced by integer multiples of the measured period, thus a systematic stitching error may result. However, as will be demonstrated quantitatively in the next chapter, by flattening the wavefronts at the substrate and by overlapping scans, SBIL can reduce any wavefront distortion induced printed error to the 1 nm level.

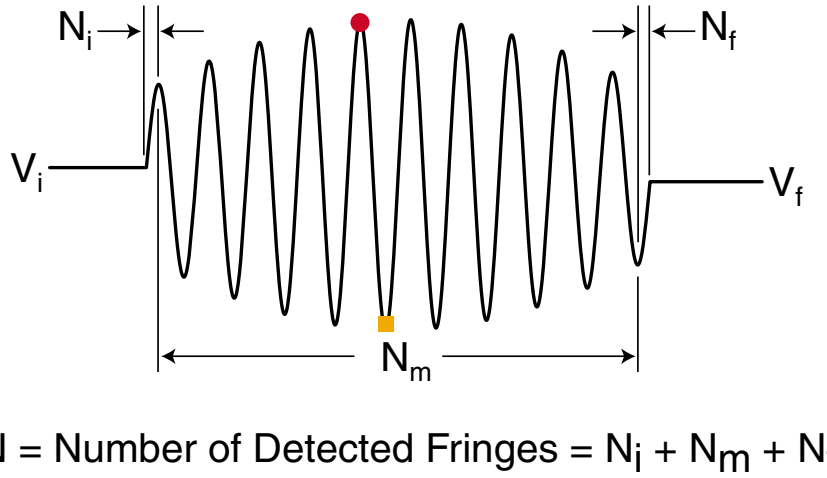

Figure 4-27: Fringe counting. The period is exaggerated. Note that the figure shows the oscillation envelope predicted by Eq. (4.49). The envelope is observed experimentally.

4.2 Error modeling

I establish an error model that can be used to predict the period measurement repeatability from a single experiment.

4.2.1 Fringe counting

The ability to accurately count each signal oscillation from the photodiode is paramount. Figure 4-27 graphically defines some of the quantities that I will be referring to later on. The initial voltage readout from the photodiode, prior to the stage movement, is V_i. The final voltage is V_f, obtained when the stage has come to a complete stop. The total number of detected fringes is N, and is the sum of three terms, the fractional cycles N_i and N_f at the beginning and the end, and the number of completed cycles N_m in the middle. Figure 4-29 illustrates all four wave forms that may be observed at the diode output. Depending on the numbers of peaks (n_p) and valleys (n_v), one can classify them into three different cases. For instance, in Case 1, n_p is greater than n_v by one. The number of completed fringe cycles is equal to n_v. Case 3 sees two wave forms falling under it. The number of completed cycles is exactly one-half short of n_v.

To calculate the fractional cycles, one begins with the formula describing a sine wave,

$$V(t) = A\,\sin(Ct + \varphi) + B \quad , \tag{4.98}$$

where the diode voltage is a function of time t. The quantities A and B define the wave amplitude and the DC offset, respectively. The wave number C is related to the

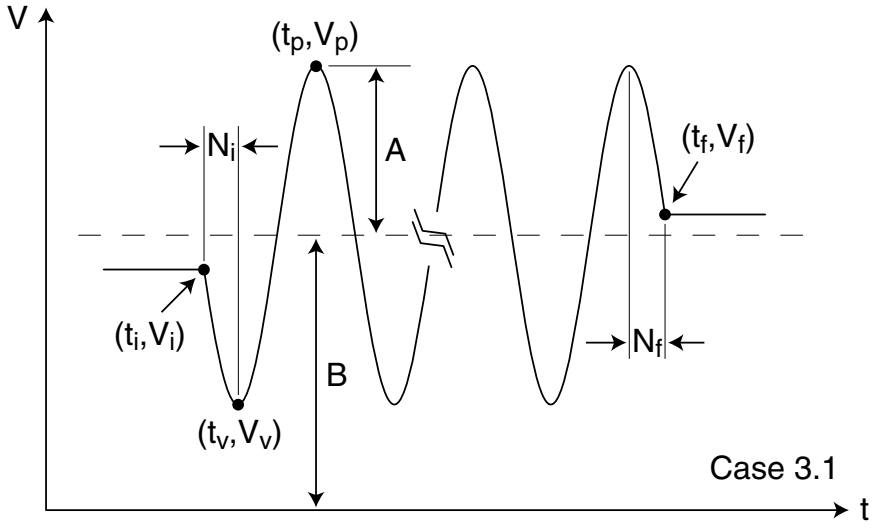

Figure 4-28: Fractional cycles, and related coordinates.

period p by

$$p = \frac{2\pi}{C} \quad , \tag{4.99}$$

and φ is some constant delay. Figure 4-28 presents some of these definitions graphically, using Case 3.1 out of Figure 4-29 as an example. In terms of the first valley and peak magnitudes, V_v and V_p, respectively, the voltage amplitude and the DC offset can be expressed as

$$A = \frac{V_p - V_v}{2} \quad , \tag{4.100}$$

$$B = \frac{V_p + V_v}{2} \quad . \tag{4.101}$$

After some straightforward math, the initial fractional cycle N_i is found equal to the following expression,

$$\frac{1}{4} + \frac{1}{2\pi} \sin^{-1}\left(\frac{V_i - B}{A}\right) \quad . \tag{4.102}$$

Similarly, the final fractional cycle N_f equals to

$$\frac{1}{4} - \frac{1}{2\pi} \sin^{-1}\left(\frac{V_f - B'}{A'}\right) \quad . \tag{4.103}$$

To calculate N_f during an actual experiment, for accuracy reasons, A and B are recalculated from the peak and valley voltages near the point (t_f, V_f), hence the primed notations.

Table 4.1 gives a summary of the findings. It is the centerpiece of the SBIL fringe counting routine. Note that depending on the cases, the subscripts "i" and "f" need to be changed accordingly.

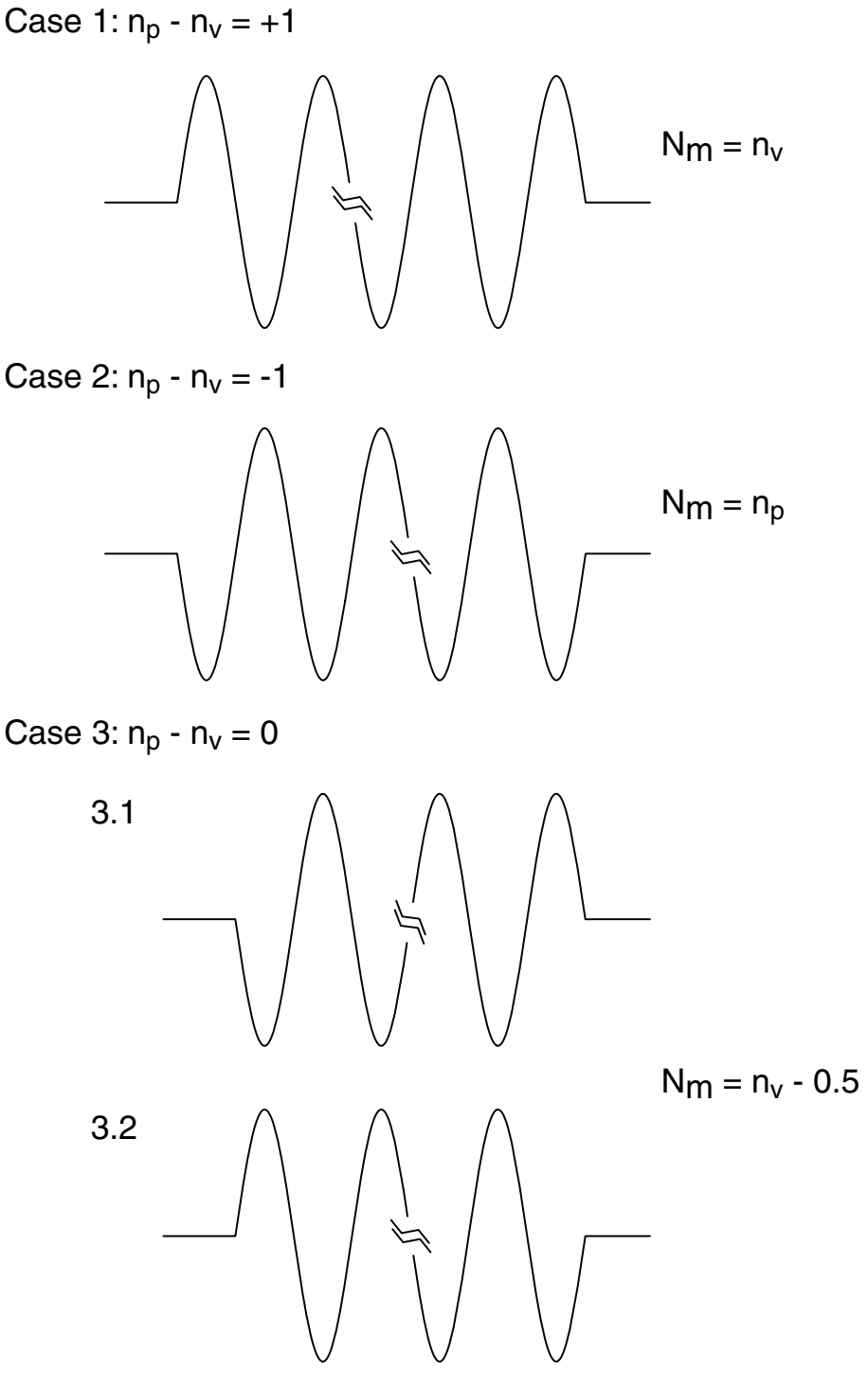

Figure 4-29: Four schematic wave forms that may appear at the output of a photodiode during period measurement. Based on the numbers of peaks (n_p) and valleys (n_v) present, one can classify them into three different cases. Two fall under Case 3 where $n_p = n_v$. The number of completed cycles is N_m, which can be related to either n_p or n_v.

Case No. (Fig. 4-29)	N_m	N_i	N_f
1	n_v	Eq. (4.103)	Eq. (4.103)
2	n_p	Eq. (4.102)	Eq. (4.102)
3.1	$n_v - 0.5$	Eq. (4.102)	Eq. (4.103)
3.2	$n_v - 0.5$	Eq. (4.103)	Eq. (4.102)

Table 4.1: Fringe counting summary. The four cases are graphically illustrated in Figure 4-29.

4.2.2 Noise sensitivity

Note that once the number of signal peaks and valleys have been correctly counted, N_m is unambiguously known. The critical issue now is how to experimentally measure the quantities V_i and V_f, so that the fractional cycles can be determined with the highest accuracy. Put the question in another way: Whereabout on the sine wave should one start and stop the measurement?

I define noise sensitivity as

$$S \equiv \frac{\Delta N_*}{\Delta V_*} \quad . \tag{4.104}$$

where the subscript "$*$" stands for either "i" or "f". Physically, Eq. (4.104) says that given an error ΔV_* in the voltage readout, the error in the fractional cycle determination ΔN_* is minimized if the noise sensitivity S is at the minimum.

From either Eq. (4.102) or Eq. (4.103), differentiation leads to

$$S = \frac{1}{2\pi A\sqrt{1 - \dfrac{(V_* - B)^2}{A^2}}} \quad . \tag{4.105}$$

Noise sensitivity is minimal when $V_* = B$. Looking at Figure 4-28, this means that the initial and final voltage measurements should take place as close as possible to the centerline of the amplitude envelope, i.e., the DC level.

4.2.3 The model

I proceed now to build a theoretical model which can be used to predict the period measurement repeatability $\mathcal{R}$ from a single experiment.

Knowing that the total number of cycles $N = N_i + N_m + N_f$, one obtains in terms of their error variances,

$$\Delta N^2 = \Delta N_i^2 + \Delta N_f^2 \quad . \tag{4.106}$$

The fact that N_m can be determined without ambiguity means that $\Delta N_m^2 = 0$ (Sec. 4.2.1).

For convenience, I again use the notation "$*$" to denote either "i" or "f". The

equation that I am about to derive applies either way. During the period measurement, to determine the voltages—be it the peak, the valley, the initial or the final voltage, I sample a large number of data points and calculate the mean. For example, the experimental results that I will be showing in Section 4.4.2 are obtained when V_i and V_f are averaged from 2000 data points sampled at 4 kHz. The rationale goes back to Eq. (3.31), which states that repeated measurements improve the accuracy on the mean. As a result, a statistical error of the mean ΔV_* exists for the initial or the final voltage. Similar errors exist for A and B since they are calculated from the peak and valley voltages.

Differentiating Eq. (4.102) or Eq. (4.103) with respect to V_*, B and A leads to an estimate of the error on the fractional cycle:

$$\begin{aligned}\Delta N_*^2 = &\left(\frac{\Delta V_*}{2\pi A\sqrt{1-\dfrac{(V_*-B)^2}{A^2}}}\right)^2 + \left(\frac{\Delta B}{2\pi A\sqrt{1-\dfrac{(V_*-B)^2}{A^2}}}\right)^2 \\ &+ \left(\frac{(V_*-B)\,\Delta A}{2\pi A^2\sqrt{1-\dfrac{(V_*-B)^2}{A^2}}}\right)^2 \quad ,\end{aligned} \tag{4.107}$$

where

$$\Delta B^2 = \Delta A^2 = \left(\frac{1}{2}\,\Delta V_p\right)^2 + \left(\frac{1}{2}\,\Delta V_v\right)^2 \quad . \tag{4.108}$$

The period measurement repeatability is defined as

$$\mathcal{R} \equiv \frac{\Delta p}{p} = \frac{\Delta N}{N} \quad , \tag{4.109}$$

where the second half of the equation comes from differentiating $p = D/N$. Eqs. (4.106) through (4.109) give someone a way to estimate the period measurement repeatability from a single experiment.

Algorithmically, given the experimental data, the model can be implemented through the following procedure:

1. Find the mean voltages V_i, V_f, V_p and V_v;
2. Calculate the period p from the beamsplitter displacement D and the total number of observed cycles N;
3. Determine the errors on the voltage means;
4. Calculate ΔA and ΔB via Eq. (4.108);
5. Apply Eq. (4.107) to find ΔN_i^2 and ΔN_f^2;
6. Apply Eq. (4.106) to find $|\Delta N|$;

7. Apply Eq. (4.109) to find the repeatability $\mathcal{R}$;

This analytical model has been implemented (along with the fringe counting algorithm) in LabVIEW. Its prediction agrees well with the repeatability figure derived from multiple experiments (Sec. 4.4.2).

4.2.4 The ideal case

The goal of SBIL period measurement is to reach a repeatability of approximately 1 ppm, or

$$\mathcal{R} = \frac{\Delta p}{p} = \frac{\Delta N}{N} = 1 \times 10^{-6} \quad . \tag{4.110}$$

In the most ideal case, one would obtain a sinusoidal signal from the photodiode with perfect contrast, and with V_* starting dead in the middle of the amplitude envelope, i.e., $A = B = V_*$. Eq. (4.107) reduces to

$$\Delta N_*^2 = \left(\frac{\Delta V_*}{2\pi A}\right)^2 + \left(\frac{\Delta B}{2\pi A}\right)^2 = \frac{1}{4\pi^2}\left[\left(\frac{\Delta V_*}{V_*}\right)^2 + \left(\frac{\Delta B}{B}\right)^2\right] \quad . \tag{4.111}$$

Furthermore, making the assumption that

$$\left(\frac{\Delta V_*}{V_*}\right)^2 = \left(\frac{\Delta B}{B}\right)^2 = \left(\frac{\Delta A}{A}\right)^2 \quad , \tag{4.112}$$

one finds

$$\frac{\Delta V_*}{V_*} = \pi\, \Delta N \quad . \tag{4.113}$$

For $p = 2$ μm and a stage displacement of 400 μm, $N = 200$ leads to a desired error $\Delta N = 2 \times 10^{-4}$. Eq. (4.113) puts a cap on the allowed percentage voltage error: $\Delta V_i/V_i = \Delta V_f/V_f = 6.28 \times 10^{-4}$. The diode that I employ[1] has a readout range of 0–6 V. In the ideal case, $V_i = V_f = 3$ V, which gives a maximal allowed voltage error of $\Delta V_i = \Delta V_f = 1.88$ mV.

Similarly, for $p = 400$ nm, the allowed percentage error is $\Delta V_i/V_i = \Delta V_f/V_f = 3.14 \times 10^{-3}$, or $\Delta V_i = \Delta V_f = 9.42$ mV. Note that the required initial and final voltage resolution is five times more stringent for a grating period of 2 μm than for 400 nm. Intuitively, this makes good sense. Given a fixed scan length, one can fit five times more fringes at the shorter period, hence, the more relaxed specification.

The analysis is valuable because it provides a way to roughly estimate just how many data points are required to determine the voltage means. For instance, for $p = 400$ nm, if the observed initial voltage fluctuation is ± 0.1 V, in order to obtain an error on the mean of 9.42 mV, one needs to average at least 113 data points, assuming of course that the statistics is purely random in nature.

[1] The power readout from the angle PSD.

In practice, because of imperfect fringe contrast due to the football shaped amplitude envelope, offsets of V_i and V_f from their ideal locations, and the presence of systematic errors, the required resolutions must be higher.

4.2.5 Stage displacement error

It may seem that I have discounted any error due to the stage displacement D. That is not the case. The static positioning error of the SBIL stage along the critical x axis is around 30 nm [68]. However, the stage error is corrected in real-time by a heterodyne fringe-locking system, which tries to minimize the image to substrate motion. Reference [48] demonstrates that the short-term[2] fringe stability is one hundredth of a period. The model developed in Section 4.2.3 incorporates the fringe stability implicitly in errors associated with the mean initial and final voltages, V_i and V_f, respectively. By aggressively averaging, the error associated with the mean can be further reduced, which as I will show shortly, enables fringe period determination to the ppm level.

4.3 System setup and experimental procedure

The hardware layout for period measurement is essentially identical to that for beam alignment. The lithography interferometer is used in the beamsplitter mode (Sec. 3.2.1). Figure 4-30 is a photo showing the rectangular beamsplitter and the beam diverting mirror, together with other important hardwares.

In terms of procedure, first, the beam alignment system is used to overlap the left and right arms in position, and to equalize the two angles of incidence. The beam overlapping PSD is used to check the beam overlap at the substrate plane, and to balance the power in each arm. When the alignment is complete, the beams are incident upon the rectangular beamsplitter, coincide on exit and propagate to the optical bench where the angle PSD sits. The power output from the angle PSD is used to monitor the interference signal as the beamsplitter is displaced.

Throughout a measurement, the beams must be fringe locked. The heterodyne fringe-locking controller not only stabilizes the image grating with respect to the stage, but also allows the user to shift the grating phase if necessary. One exploits the feature to shift V_i to the centerline of the signal train without having to experiment with the stage location. To end the measurement with V_f at the centerline, one has no choice but to displace the stage by the proper amount. For the experiments that I will discuss in Section 4.4.2, the stage displacement is 400.05 μm, with the last 50 nm making sure that V_f ends up close to the centerline of the oscillation envelope.

[2]Short term means on the order of a few seconds, which is how long it takes to collect the period measurement data.

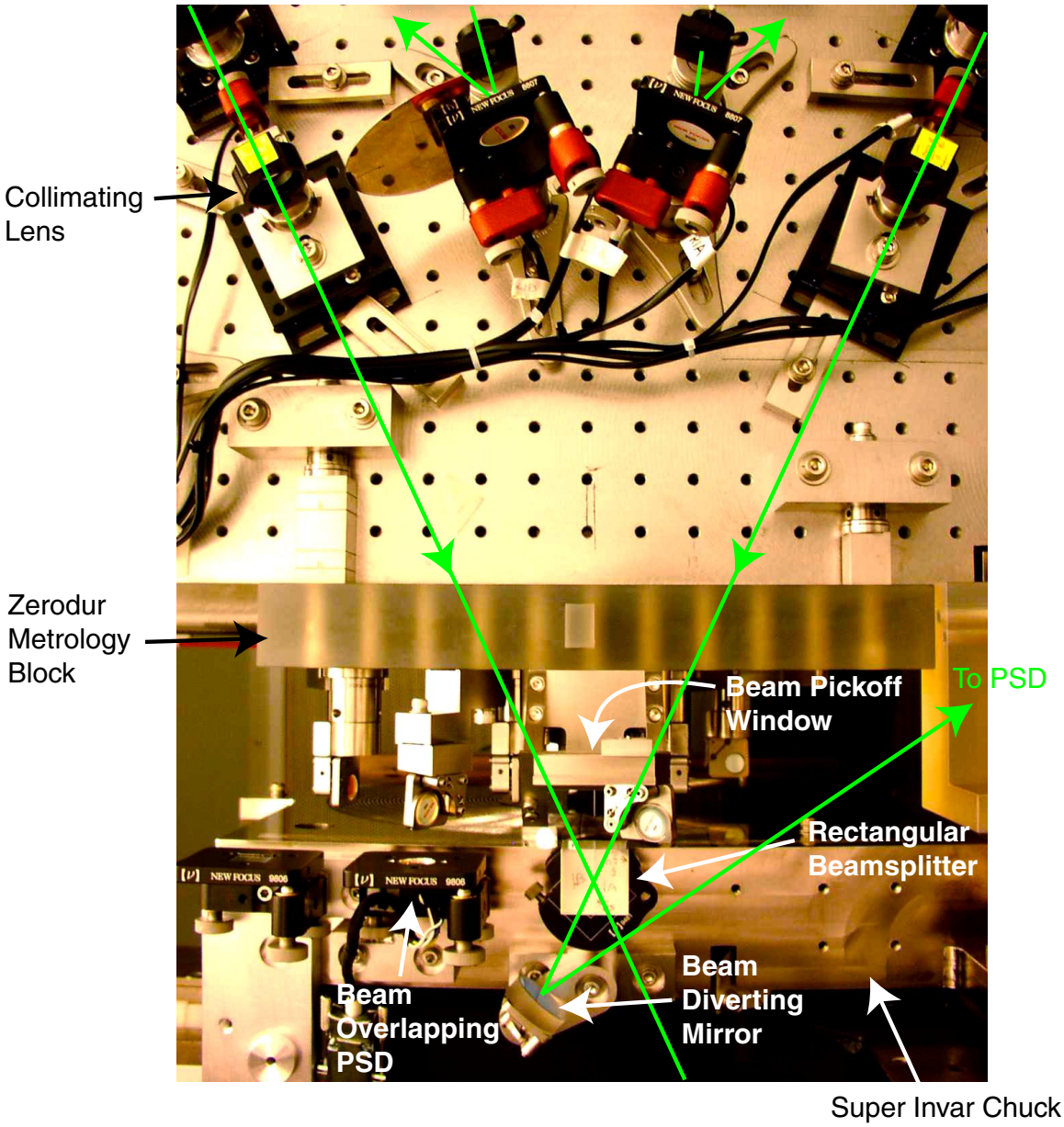

Figure 4-30: Photo of the SBIL period measurement system. The angle PSD used for sensing the interference power signal is not pictured. Figure 2-6 should also be helpful.

Data acquisition is performed by the same National Instruments A/D board that has been the focus of study in Section 3.3.1. Data acquisition, fringe counting and error analysis softwares have all been written in LabVIEW.

4.4 Results

The first systematic SBIL period measurement study was reported in 2001 [47]. The SBIL tool at that time was configured to write gratings with a nominal period of 2 μm. The measured fringe period was 1.7644 μm. The repeatability was 7.35×10^{-4}, three-sigma, which was established empirically from 54 sets of measurements. It was far from the required 1 ppm accuracy. I will not re-report the work in this thesis. Interested reader should go to the paper for detailed error analysis and discussions.

Since those early days, the SBIL tool has gone through some major upgrades. The additions of an environmental enclosure, a low coefficient-of-thermal-expansion (CTE) metrology frame[3], a column-referencing stage interferometer with refractometry correction, together with a more compact fringe locking system have significantly boosted the stage positioning and fringe locking performance. This is the context under which the new period measurement study takes place.

4.4.1 Low-pass digital filter design

Having said that I will not discuss the old study, I do want to present some ancient data to make a point. To implement an accurate fringe counting routine as described in Section 4.2.1, one must be able to determine the number of completed cycles N_m with absolute certainty. To miscount by one cycle means the measurement accuracy can be orders of magnitude off. Table 4.1 relates N_m to the number of peaks (n_p) or valleys (n_v) in the interference signal. Any error made in determining n_p or n_v will render the period thus measured useless.

A clean, jitter-less signal naturally helps when it is time to automate peak and valley counting. However, in those early days, a clean signal from the PSD was something that one could only dream about. Figure 4-31 shows an example of the noisy data. The football shaped oscillation envelope is predicted by Eq. (4.49). Physically, the tapering of the envelope results when the beams slide off one another (Fig. 4-2). The central bulge appears when the beams coincide to maximize the fringe contrast. Upon closer examination, one sees that high-frequency jitters contaminate the signal with all kinds of spurious peaks and valleys. A reader familiar with the fringe-tracking techniques from single interferogram analysis may recall similar headaches [69]. Figure 4-32 presents a power spectral density plot of the raw data with the

[3]The Zerodur metrology block and the stage Super Invar chuck form the centerpiece of the metrology frame (Fig. 4-30)

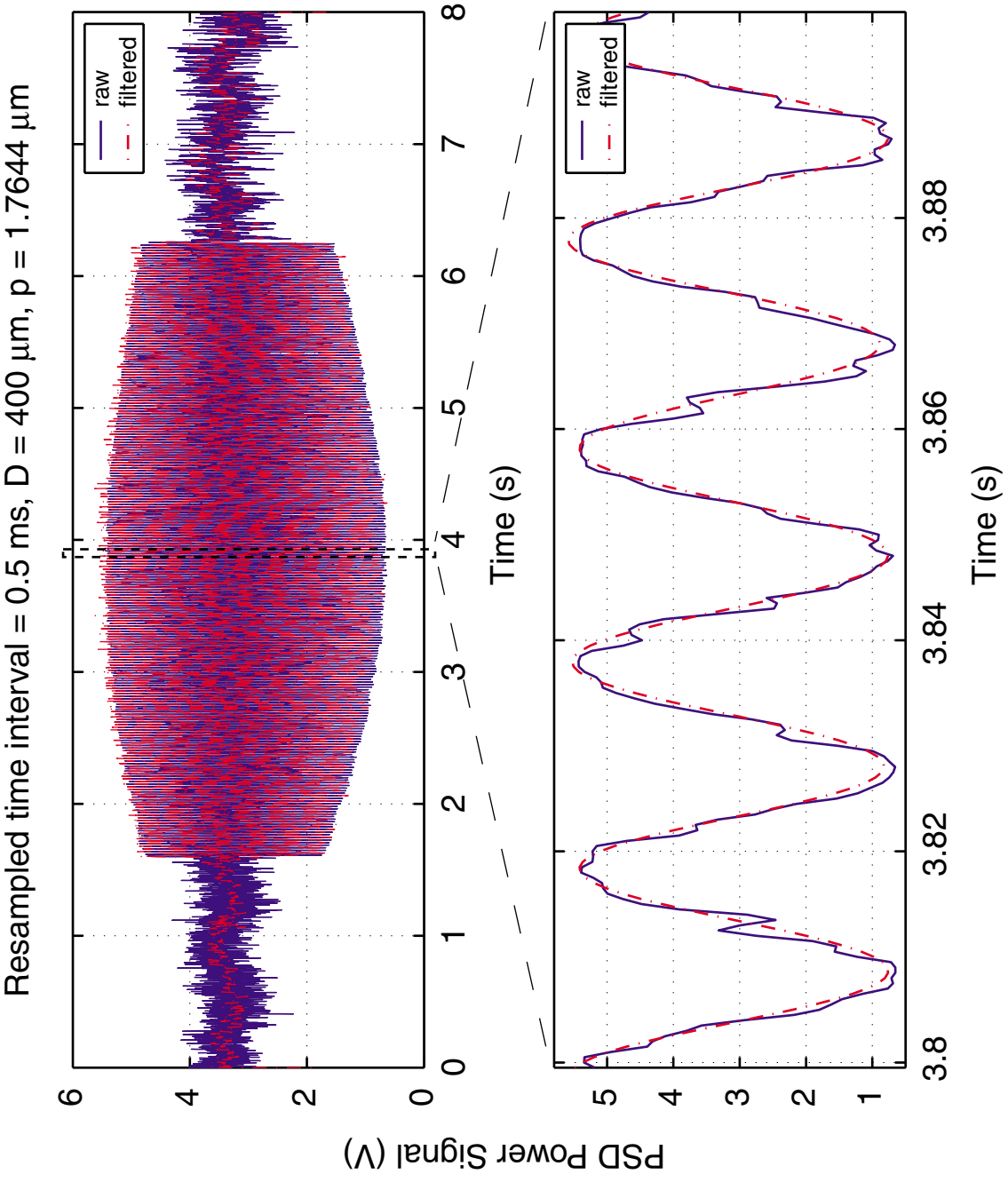

Figure 4-31: Raw and digitally filtered period measurement data. $p = 1.7644$ μm.

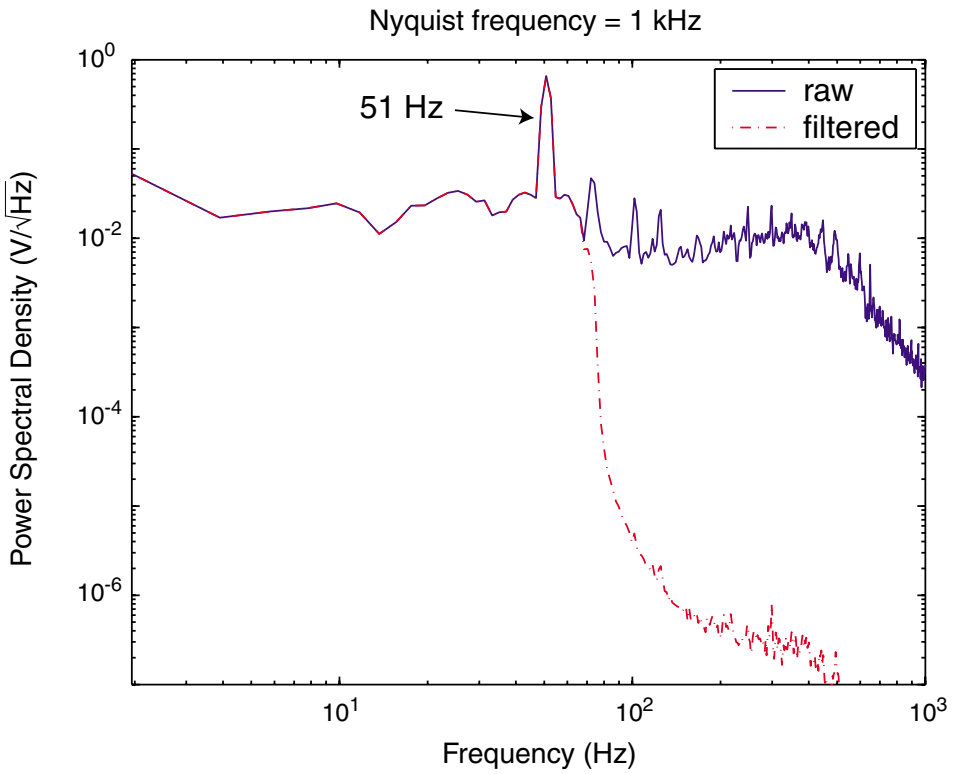

Figure 4-32: AC power spectral densities of the raw and digitally filtered data shown in Figure 4-31.

background removed. The desired signal oscillates at 51 Hz. The fairly peaky and broad "shoulder" (up to 400 Hz) carries significant noise power, which is the source of the time-domain contaminants. The only way to rid of these false extrema is to low-pass filter the data.

Digital signal processing (DSP) has seen many professional lives dedicated to it [62, 70, 71, 72]. For my particular application, the low-pass filter must have a very sharp cutoff—a transition bandwidth of 10 Hz, and a significant attenuation in the stop band—greater than 60 dB is the design criterion that I use. Most importantly, the filter has to preserve the signal phase, i.e., it has to be a finite impulse response (FIR) filter. The final design of the FIR filter uses a Kaiser window, which is known to optimize the trade-off between the window's main lobe width and sidelobe amplitude [62]. Figure 4-33 plots the frequency response of the filter.

Filtered time-domain data is plotted on top of the raw data in Figure 4-31, which shows smooth oscillations that are ideal for automated peak and valley counting. The performance of the filter is perhaps better viewed in the frequency domain. The AC power spectral density of the filtered data is plotted along side the raw data in Figure 4-32. For all practical purposes, the broad shoulder of high-frequency noise has been

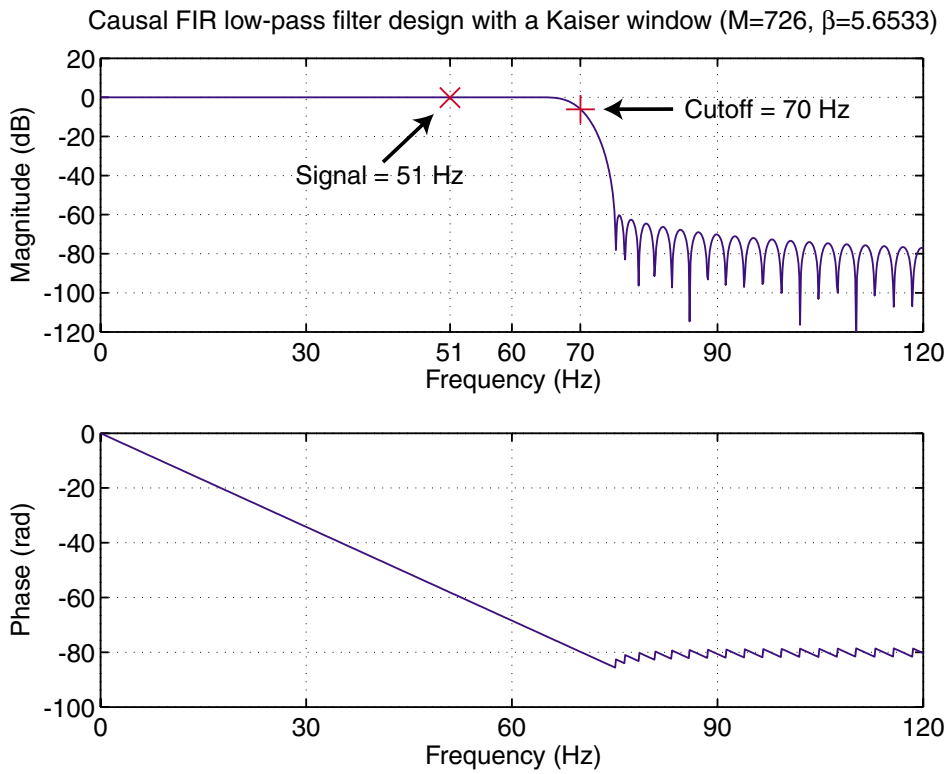

Figure 4-33: Causal FIR low-pass filter design with a Kaiser window (M = 726, b = 5.6533). Cutoff frequency is 70 Hz with a transition bandwidth of 10 Hz.

completely removed.

4.4.2 Period measurement

Currently, the system is configured to write 400 nm period gratings.

Sixteen period measurements are taken. For all, the beamsplitter is displaced by 400.05 μm at a speed of 90 μm/s. One would expect to see the interference signal peaking at a frequency of approximately 225 Hz. This is indeed the case.

Assuming a noisy signal, I designed a FIR filter beforehand with a cutoff frequency at 250 Hz, a 10 Hz transition band and an attenuation of 60 dB in the stop band. Figure 4-34 plots the filter's frequency response. Figure 4-35 shows the filter's performance in the frequency domain, and Figure 4-36 is a plot of the time-domain raw and filtered data. Thanks to much improved fringe locking, the raw data exhibits no artifacts that may impede computerized peak and valley counting. The system locks the fringes to $0.012\,\lambda$, three-sigma. In retrospect, filtering is unnecessary.

Comparing Figure 4-35 to 4-32, one sees two main differences. The overall AC noise power is now much smaller than before. With the variance under the signal peak discounted for up to ± 10 Hz, the 5–1000 Hz AC power is 5.41×10^{-3} V^2 now vs. 8.22×10^{-2} V^2 from before, a 15-fold improvement. The distinct frequency shoulder

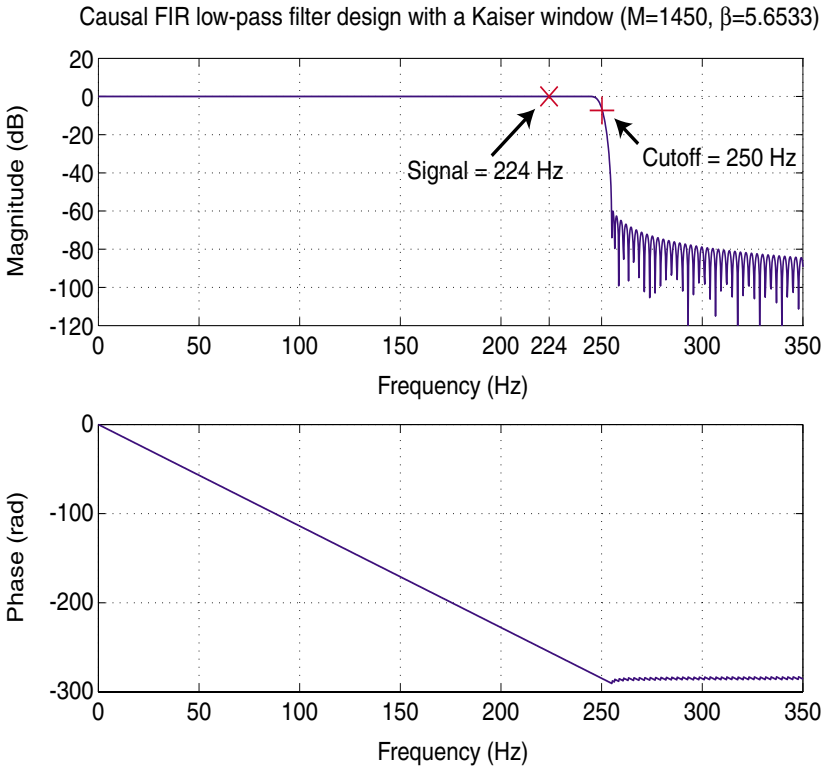

Figure 4-34: Causal FIR low-pass filter design with a Kaiser window (M = 1450, b = 5.6533). Cutoff frequency is 250 Hz with a transition bandwidth of 10 Hz.

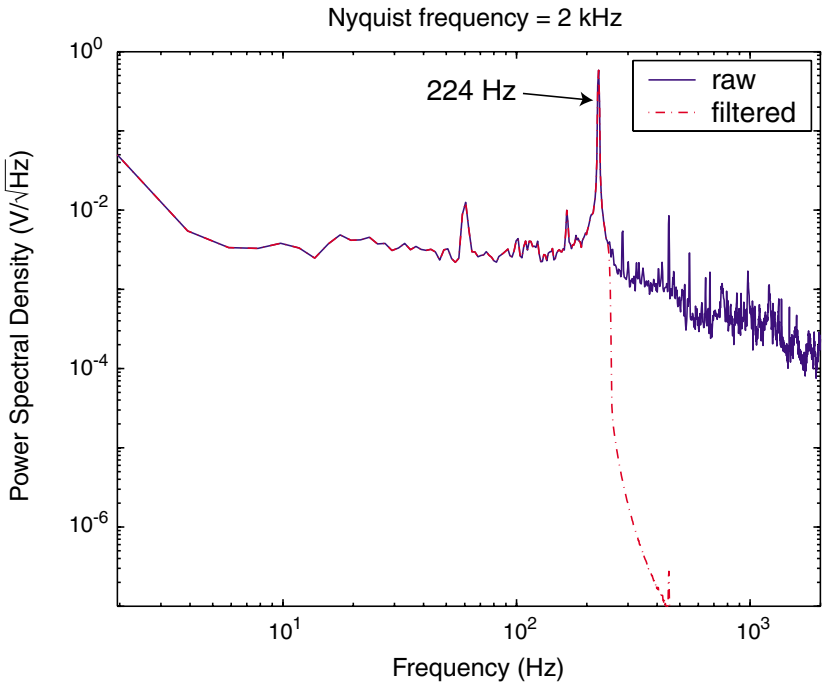

Figure 4-35: AC power spectral densities of the raw and digitally filtered data shown in Figure 4-36.

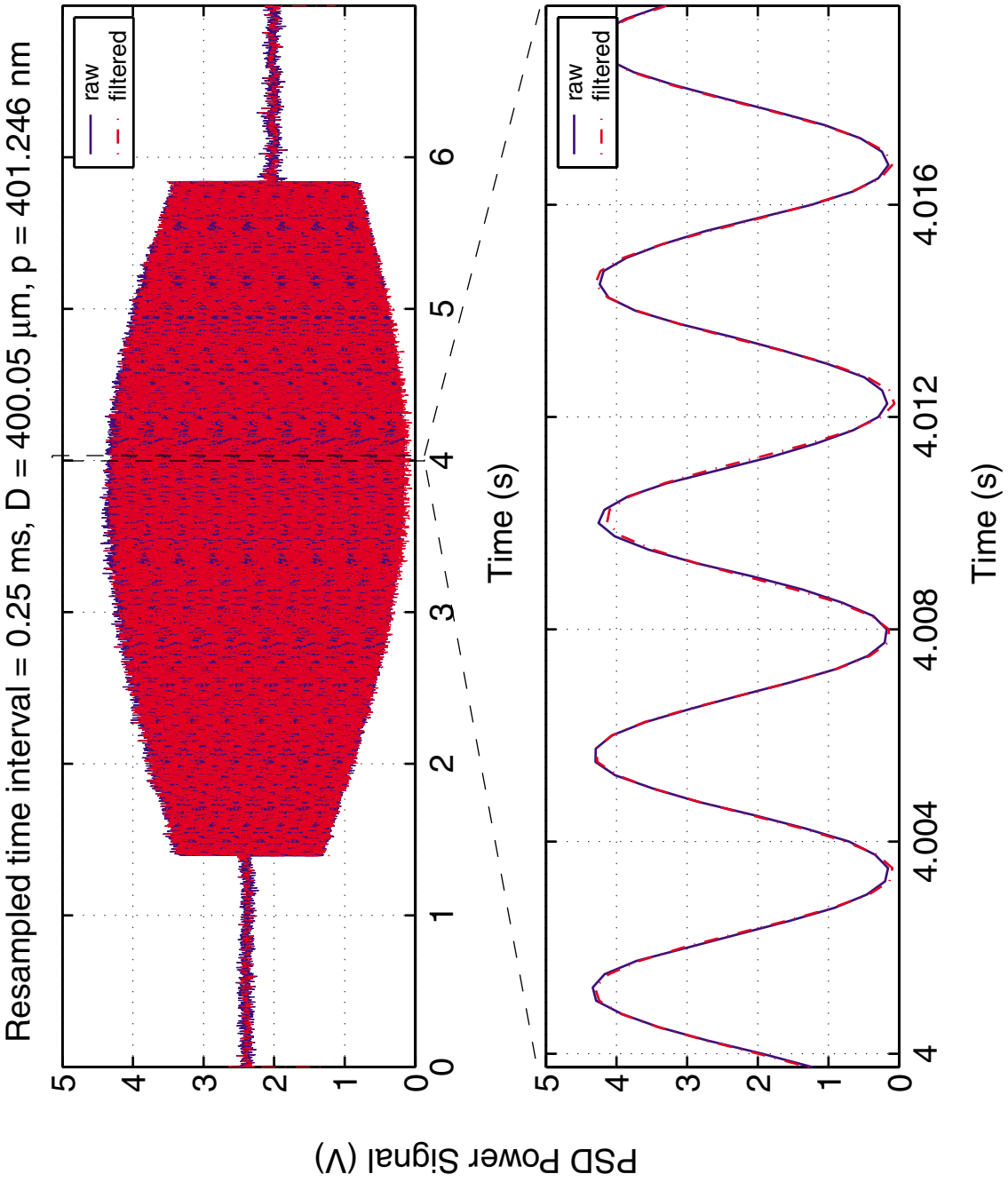

Figure 4-36: Raw and digitally filtered period measurement data. $p = 401.246$ nm.

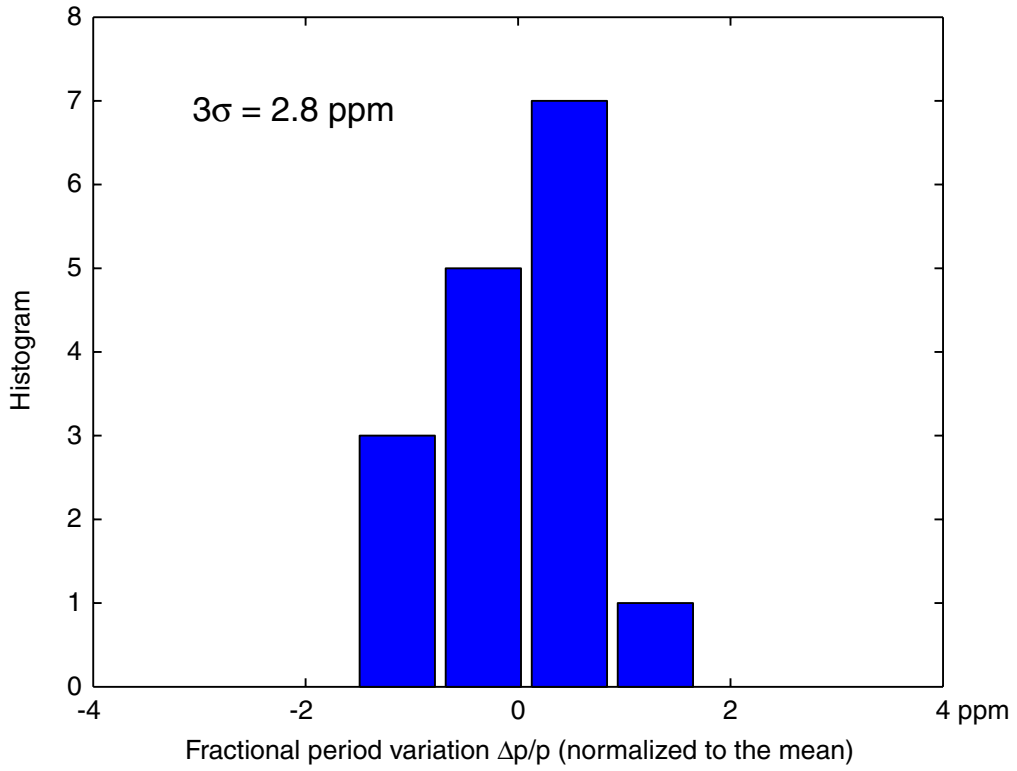

Figure 4-37: Experimental period measurement repeatability, derived from 16 data sets.

which existed before at 400 Hz has disappeared. As a result, in the time domain, the data looks much cleaner. It is obvious that the system upgrade has paid dividend.

After 16 measurements, the mean period is found to be 401.246 nm with a three-sigma standard deviation of 0.0011 nm or 1.1 pm. Measurement repeatability is plotted in Figure 4-37. It is at 2.8 ppm, three-sigma, which meets the SBIL period measurement goal.

The error model established in Sec. 4.2.3 allows one to estimate the measurement repeatability from any individual data set. The predicted three-sigma repeatability is 3.3 ppm on average with 0.6 ppm standard deviation, in agreement with the empirical measurement. In other words, the system behaves as expected, and any measurement inaccuracy is quantitatively accounted for.

It is remarkable that the actual fringe period (401.246 nm) ends up so close to the designed 400 nm. From

$$p = \frac{\lambda}{2\sin\theta} \quad , \tag{4.114}$$

one can estimate that given a change $\Delta p = 1.246$ nm, the offset in incident angle from the design is only $\Delta\theta = 1.5$ mrad, proof again of the benefit in an engineered optical layout.

4.5 Phase error in the resist grating

During SBIL, the stage is commanded to step by an integer number of the measured fringe period p_{m}, not the actual image period p. Although the difference between p_{m} and p is only a few ppm, over the course of writing a large grating hundreds of millimeters in dimension, hundreds of scans may be required. Will the small period measurement inaccuracy accumulate into a significant nonlinear phase error in the finished resist grating? This is an important question that I will address in this section.

Assume perfect stage scan and fringe locking. The dose delivered to the resist by the initial scan can be written mathematically as

$$D^{(0)}(x) = B_D(x) + A_D(x)\,\sin\left(\frac{2\pi}{p}x\right) \quad , \tag{4.115}$$

where B_D is some background dose,

$$A_D(x) = \exp\left(-\frac{2x^2}{R^2}\right) \tag{4.116}$$

is the Gaussian dose amplitude, R is the $1/e^2$ intensity radius, p is the actual fringe period and x defines the coordinate perpendicular to the fringe direction. The dose deposited by the n-th scan is the same as the initial except that it has shifted in position due to the discrete stepping of the stage,

$$D^{(n)}(x - nS) = B_D(x - nS) + A_D(x - nS)\,\sin\left[\frac{2\pi}{p}(x - nS)\right] \quad , \tag{4.117}$$

where the step size S equals some integer N multiplying the measured fringe period p_{m},

$$S = N\,p_{\mathrm{m}} \quad . \tag{4.118}$$

There is a small percentage difference between p_{m} and p. Let it be Δ, i.e.,

$$p_{\mathrm{m}} = p\,(1 + \Delta) \quad . \tag{4.119}$$

Define a shorthand symbol for later convenience

$$\delta \equiv 2\pi N \Delta \quad . \tag{4.120}$$

The total dose in the resist is the sum of all individual ones,

$$\begin{aligned} D^{\mathrm{tot}}(x) &= D^{(0)}(x) + D^{(1)}(x - S) + \cdots + D^{(n)}(x - nS) \\ &= B_D^{\mathrm{tot}}(x) + E(x)\sin\left(\frac{2\pi}{p}x\right) + F(x)\cos\left(\frac{2\pi}{p}x\right) \quad , \end{aligned} \tag{4.121}$$

where

$$B_D^{\mathrm{tot}}(x) = B_D(x) + B_D(x - S) + \cdots + B_D(x - nS) \quad , \tag{4.122}$$

$$E(x) = A_D(x) + A_D(x - S)\cos\delta + \cdots + A_D(x - nS)\cos(n\delta) \quad , \tag{4.123}$$

$$F(x) = -[A_D(x - S)\sin\delta + \cdots + A_D(x - nS)\sin(n\delta)] \quad . \tag{4.124}$$

Applying the math identity

$$E\,\sin\left(\frac{2\pi}{p}x\right) + F\,\cos\left(\frac{2\pi}{p}x\right) = A_D^{\text{tot}}\,\sin\left[\frac{2\pi}{p}x + \Phi_e\right] \quad , \tag{4.125}$$

Eq. (4.121) can be rewritten as

$$D^{\text{tot}}(x) = B_D^{\text{tot}}(x) + A_D^{\text{tot}}(x)\,\sin\left[\frac{2\pi}{p}x + \Phi_e(x)\right] \quad , \tag{4.126}$$

where

$$A_D^{\text{tot}}(x) = \sqrt{E(x)^2 + F(x)^2} \quad , \tag{4.127}$$

$$\Phi_e(x) = \tan^{-1}\frac{F(x)}{E(x)} \quad . \tag{4.128}$$

Note that Eq. (4.126) is exact. No approximation has been made in deriving it. Ideally, there is no period measurement error. If p_{m} matches p exactly, $\Phi_e(x) = 0$ for all x. The resist grating phase is simply $\frac{2\pi}{p}x$. In reality however, period measurement error exists, the phase of the resist grating will therefore deviate from the ideal by a non-zero amount.

From Eq. (4.126), the resist grating phase is

$$\phi_{\text{res}}(x) = \frac{2\pi}{p}x + \Phi_e(x) \quad . \tag{4.129}$$

One worries that the inaccuracy in measuring the actual fringe period p may introduce an accumulating phase nonlinearity in ϕ_{res}. I show now that the worry is needless. To start, I define a linear phase based on the measured fringe period p_{m},

$$\phi_{\text{m}}(x) \equiv \frac{2\pi}{p_{\text{m}}}x \quad . \tag{4.130}$$

I define the difference between ϕ_{res} and ϕ_{m} to be

$$\Delta\phi(x) \equiv \phi_{\text{res}}(x) - \phi_{\text{m}}(x) \quad . \tag{4.131}$$

The mathematical formalism developed thus far is particularly suited for numerical simulations. Appendix F lists the MATLAB source code.

Figure 4-38 shows a sample simulation where $\Delta\phi$ is plotted as a function of x. To minimize any numerical artifact that may arise from an abrupt data cutoff, the radius of the Gaussian amplitude A_D is taken to be five times the $1/e^2$ radius of $R = 1$ mm. The measurement error is assumed at 2.8 ppm, corresponding to the experimental repeatability. The step size is 0.9 mm, 90% of the $1/e^2$ radius. The linear ramps at the beginning and the end of the plot correspond to regions where

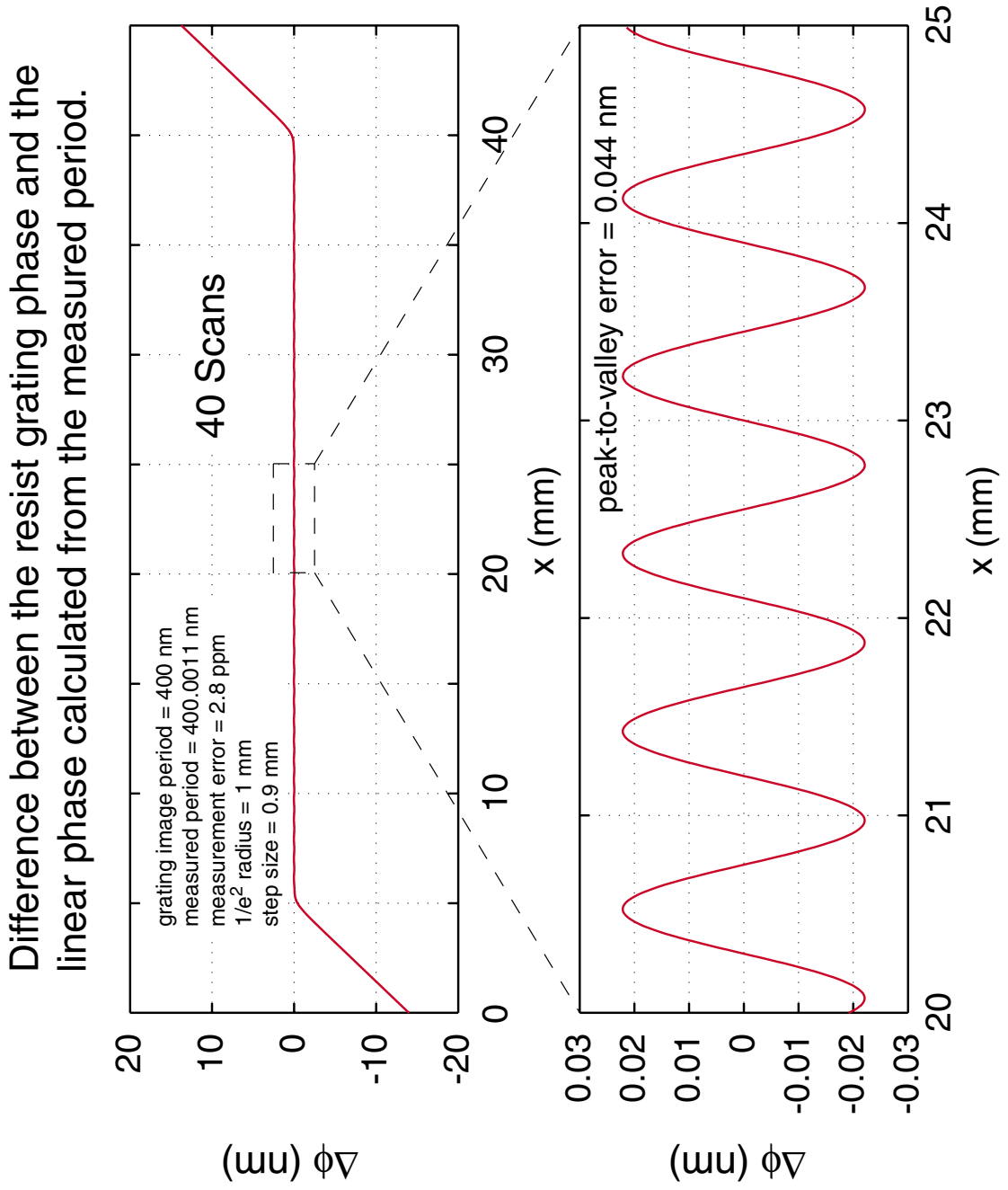

Figure 4-38: Plot of the difference between ϕ_{res} and ϕ_{m} for the following simulated parameters: number of scans = 40, actual grating image period $p = 400$ nm, measured grating image period $p_{\text{m}} = 400.0011$ nm, percentage measurement error $\Delta = 2.8$ ppm, $1/e^2$ intensity radius $R = 1$ mm, and step size $S = 0.9$ mm.

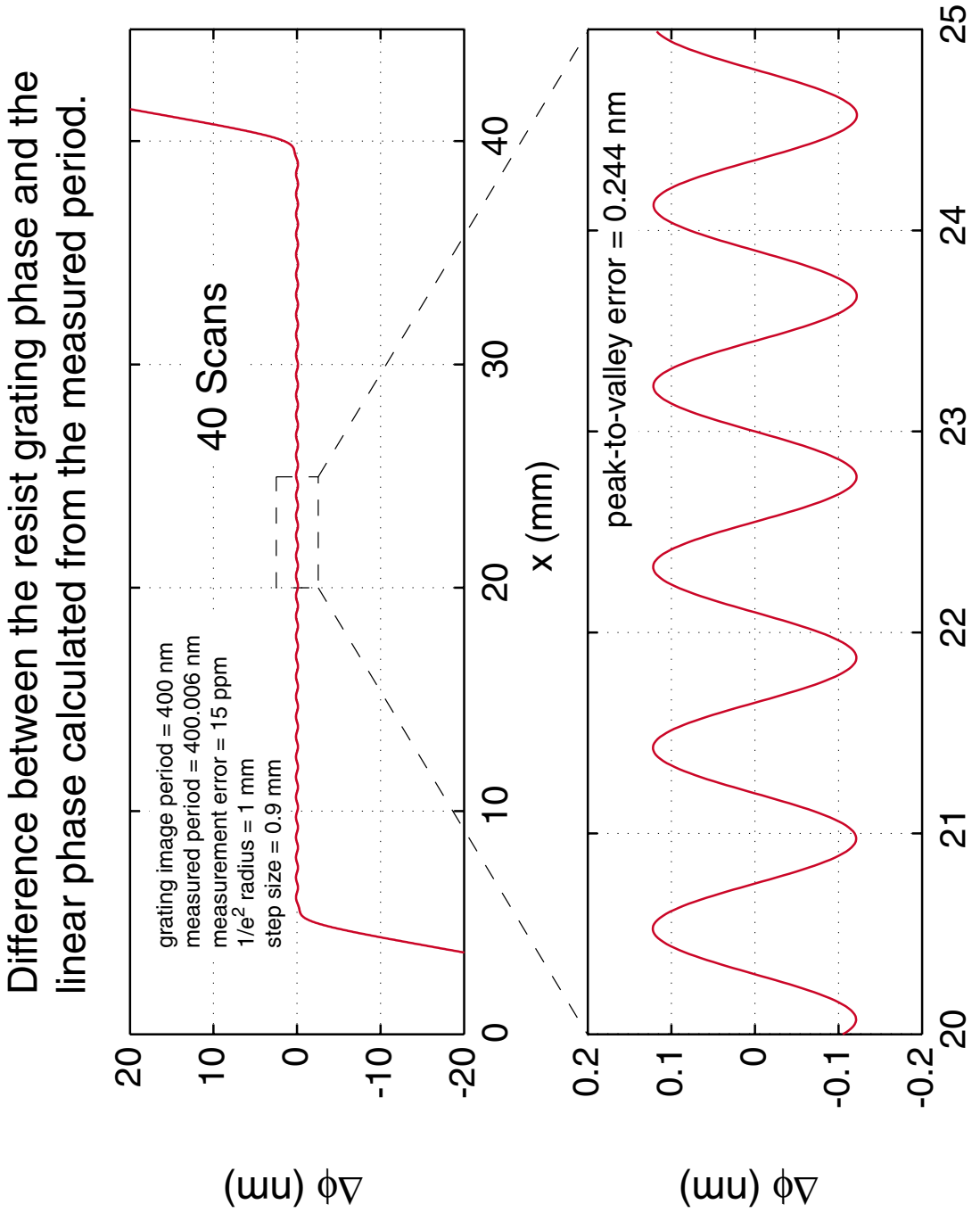

Figure 4-39: Plot of the difference between ϕ_{res} and ϕ_{m}. Same parameters as those used in Figure 4-38, except that the percentage measurement error is increased to 15 ppm.

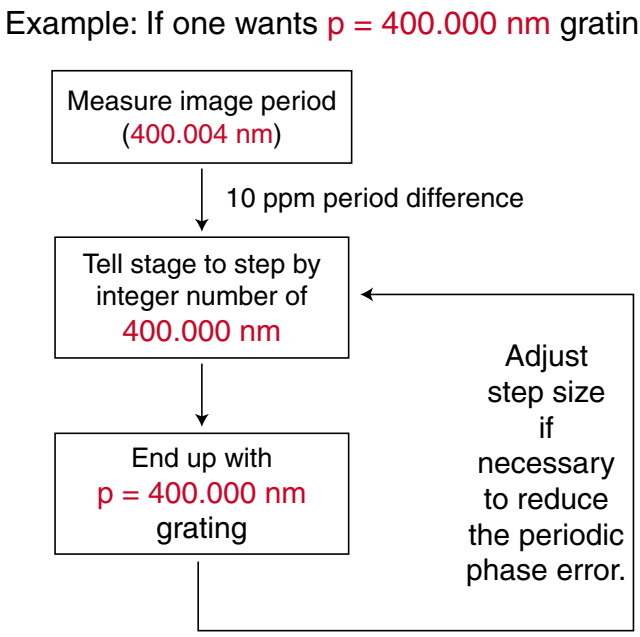

Figure 4-40: Flexibility in setting the resist grating period.

no significant scan overlap has taken place. There, not surprisingly, the resist grating phase is determined very much by the phase of the grating image, which deviates from ϕ_{m} noticeably. However, in the region of interest where scans do overlap, the difference between ϕ_{res} and ϕ_{m} falls effectively to zero. Any residual nonlinear phase error is cyclic with a period corresponding precisely to the 0.9 mm step size. The peak-to-valley amplitude of the error is a mere 0.04 nm. In other words, the phase of the resist grating is essentially ϕ_{m} [Eq. (4.130)], the linear phase calculated from the measured period. Figure 4-39 repeats the simulation with the same parameters except one: The percentage measurement error is now increased to 15 ppm, leading to a measured period that is different from the actual by 6 pm. As a result, the peak-to-valley amplitude of the cyclic nonlinear phase in the resist grating is higher at 0.24 nm, but it is still well within the SBIL error budget. Furthermore, if one reduces the step size, the amplitude of the cyclic error decreases due to finer overlaps.

The significance of the above finding is illustrated graphically in Figure 4-40 through an example flow chart. Suppose that one desires to write a grating with a period of 400.000 nm exactly, and suppose that the measured image period is off slightly by some 10 ppm at 400.004 nm. Instead of fine-tuning the beam alignment to set the grating image period, one can simply command the stage to step by integer number of 400.000 nm and end up with a written grating of the desired period. In other words, by overlapping scans, SBIL has the flexibility to modify the exposed grating period at the picometer level.

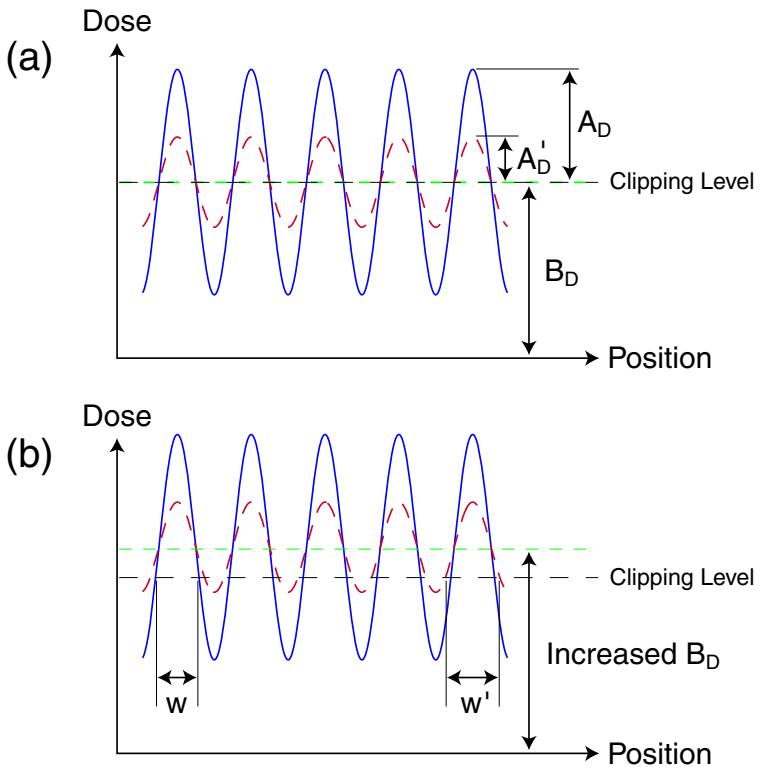

Figure 4-41: Dose contrast variations lead to grating line width variations. (a) Ideal case. Background dose B_D coincides with the resist clipping level. Dose amplitude variations from A_D to A'_D do not have any impact on the grating line width if 1:1 line-space ratio is desired. (b) If B_D is not set correctly, or if the clipping property of the resist varies with position, the line width changes depending on the dose amplitude.

Having considered its impact on the grating phase, I now explore the impact of period measurement inaccuracies on the exposure dose contrast. The question is important since large contrast variations across the wafer may lead to grating line width variations. The dose function is given by Eq. (4.126). Ideally, if the background dose B_D is set to coincide with the clipping level of the photoresist, dose amplitude variations from A_D to A'_D do not have any impact on the 1:1 line-space ratio [Fig. 4-41(a)]. However, if B_D is not set correctly, or if the clipping property of the resist varies with position, the line width will change depending on the dose amplitude. In Figure 4-41(b), line widths W and W', corresponding to amplitudes A_D and A'_D, respectively, are noticeably different.

I define the normalized dose amplitude error as

$$e_A(x) \equiv \frac{A_D^{\text{tot}}(x)}{A_{D,0}^{\text{tot}}(x)} - 1 \quad , \tag{4.132}$$

where A_D^{tot} is the total dose amplitude [Eq. (4.127)] and $A_{D,0}^{\text{tot}}$ is the nominal dose amplitude when no period measurement error exists, i.e.,

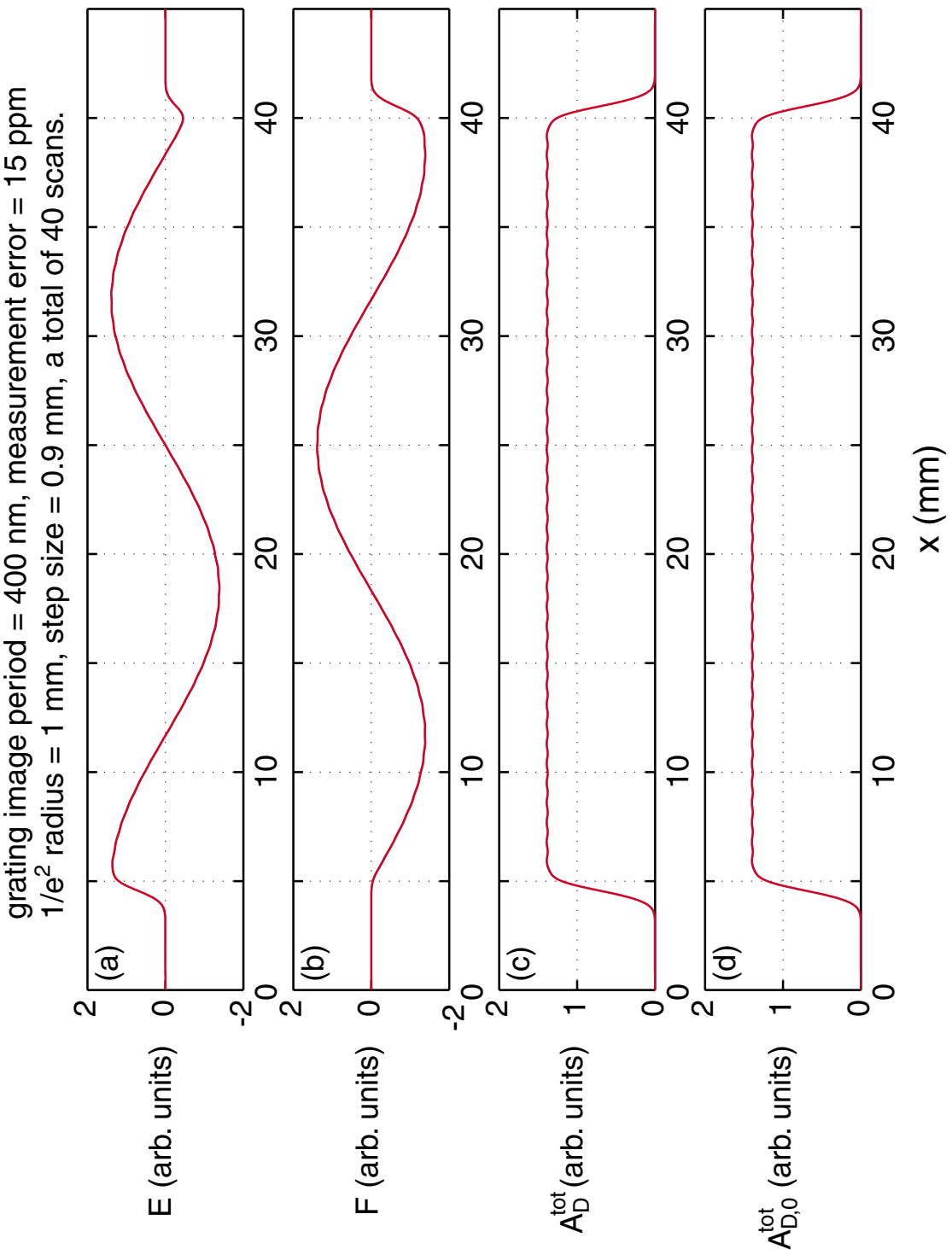

Figure 4-42: Subplots (a) and (b) are the quantities E and F, respectively, which together make up the total dose amplitude A_D^{tot} [Eq. (4.127)]. Subplots (c) and (d) correspond to the total dose amplitude A_D^{tot} and the nominal dose amplitude $A_{D,0}^{\text{tot}}$ [Eq. (4.133)], respectively. The set of simulated parameters is the same as that used in Figure 4-39.

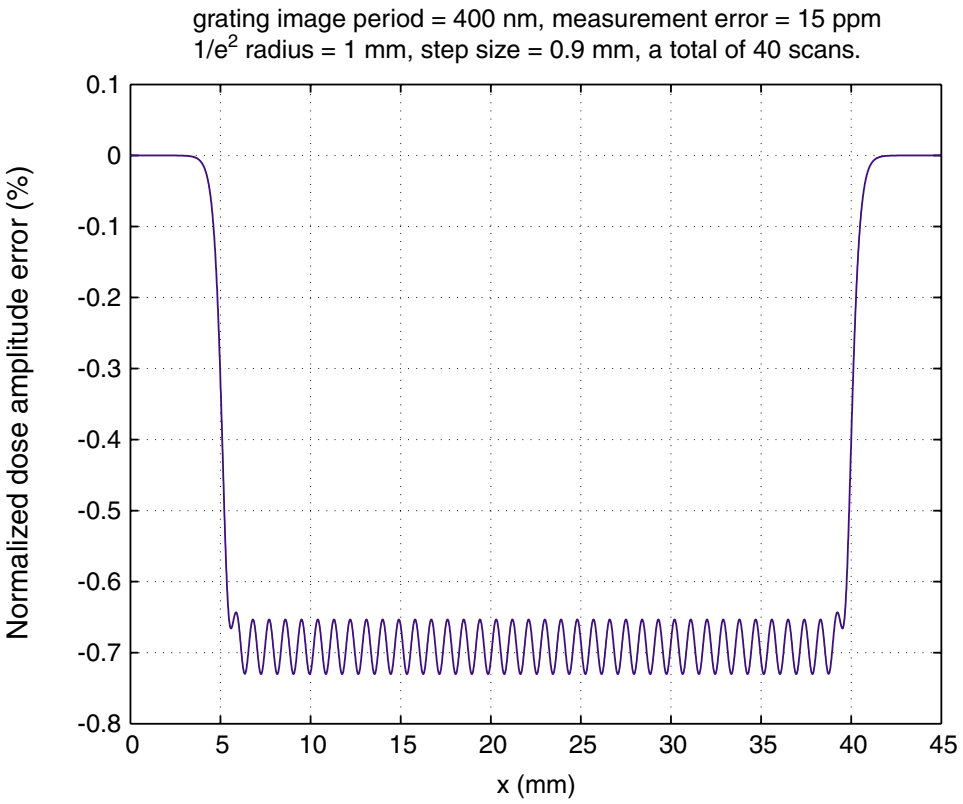

Figure 4-43: Continued from Figure 4-42. Plot of the normalized dose amplitude error e_A.

$$A_{D,0}^{\text{tot}}(x) = \sum_{i=0}^{n} A_D(x - iS) \quad . \tag{4.133}$$

Figures 4-42(c) and (d) plot A_D^{tot} and $A_{D,0}^{\text{tot}}$, respectively, for the same set of simulated parameters used in Figure 4-39. The difference between the two quantities is minute, much better observed in Figure 4-43, which plots the normalized dose amplitude error e_A. Despite a rather large 15 ppm assumed period measurement error, the dose amplitude varies from the error-free nominal by less than -1%—the minus sign indicates that any measurement error only reduces the dose amplitude, or equivalently, the contrast. Much of that variance is simply a DC offset at around -0.7%. The actual AC variance has a peak-to-valley of about 0.1%.

The impact of period measurement inaccuracies on the exposure dose contrast is therefore quite negligible. Here is an interesting observation on the side: Figures 4-42(a) and (b) plot the quantities E and F, respectively, which together make up the total dose amplitude A_D^{tot} [Eq. (4.127)]. Both E and F are periodic with a period given by the grating image period divided by the measurement error[4], i.e., p/Δ. For

[4]One would not have easily guessed this from Eqs. (4.123) and (4.124).

Figure 4-42, this period is around 27 mm.

4.6 Summary

In this chapter, the concept of measuring interference fringe period with a beamsplitter is proposed, and rigorously quantified. The findings from Section 4.1 prove that despite possible manufacturing and installation flaws, the beamsplitter can measure the nominal grating period as seen by the substrate with a theoretical accuracy that is on the part-per-billion level.

With the SBIL prototype now housed inside an environmental chamber, equipped with updated metrology frame and heterodyne fringe locking, the period measurement repeatability of the system has improved by more than two orders of magnitude to 2.8 ppm, three-sigma. This meets the current SBIL period measurement requirement.

It is critically important that no accumulating nonlinear phase error exists in the resist grating because of a ppm-level period measurement error. Through a combination of theoretical analysis and numerical modeling, Section 4.5 demonstrates quantitatively that this is indeed the case. Thanks to overlapping scans, any phase nonlinearity is cyclic and easily subnanometer in magnitude. The period of the resist grating is not the actual grating image period but the measured period from which the stage step size is calculated. As a result, the period of the resist grating can be modified at the picometer level.

There is room for future improvements. Continuing to upgrade the stage and fringe locking performance may enable further improvements on measurement accuracy. A large chunk of the work lies with one's ability to obtain a uniform air index, an assumption that Section 4.1 has operated under, but is extremely difficult to attain in reality. The tiny air column just below the beam pickoff window (Fig. 4-30), and prior to the top surface of the rectangular beamsplitter is not fringe locked, so it must be controlled with exquisite care.

Chapter 5

Wavefront metrology

For SBIL to work, errors from various sources must be brought under control. Thus far, I have described how the SBIL beam alignment system and the period measurement system have been designed, constructed, and tested to meet the part-per-million (ppm) period control requirement.

Another important error that must be thoroughly understood and controlled is the nonlinear phase distortions in the grating image. To remind the reader, by "grating image" or "image grating", I am referring to the millimeter-sized standing wave pattern made by the interference of two coherent Gaussian beams. For SBIL to succeed, phase errors written into the photoresist, which originate from phase nonlinearities in the grating image, must be brought down to the 1 nm level.

Ideally, one would like to produce the image grating by interfering two plane waves. Since they are rare commodities in reality, I have settled for the next best thing: collimated Gaussian beams with their waists located at the substrate plane. Recall that the wavefront at the Gaussian beam waist is planar[1].

The goal of SBIL wavefront metrology is in short to design and implement a system that exploits moiré-based interferometry to accurately measure the nonlinear phase distortions in the grating image, so that the Gaussian beam waists can be located to the substrate and the grating image nonlinearities minimized.

5.1 Introduction

During SBIL wavefront metrology, the lithography interferometer is configured to the grating mode (Sec. 2.2.5). A metrology grating, which has a close-to-ideal linear spatial phase, is placed on the vacuum chuck. The grating is used under the so-called Littrow condition, where the 0-order reflected beam from the left arm coincides

[1]Strictly speaking, this is true only for an idealized Gaussian beam (Sec. 5.2.2).

with the -1-order back-diffracted beam from the right arm [Fig. 5-1(a)]. The beams interfere and produce an interferogram that gets recorded by a charge-coupled device (CCD) camera.

Physically, the interferogram reflects the difference in phase between the reflected and back-diffracted beams. It is also equivalent to the substrate-plane moiré pattern that arises due to a difference in phase between the metrology grating and the grating image. Since the metrology grating has a linear phase, any phase distortion away from linearity observed in the moiré pattern can only be due to the distortion in the grating image. One can then adjust the SBIL optics to minimize the nonlinear phase component. Since the grating image is generated by interfering two collimated Gaussian beams, a minimum nonlinear phase is obtained when the two beams interfere at their waists, where the wavefronts are planar [Fig. 5-1(b)]. The goal of SBIL wavefront metrology is to design and implement a system that exploits moiré-based interferometry to accurately locate the Gaussian beam waists at the substrate, so that the nonlinear phase component in the grating image can be minimized to the nanometer level.

Section 5.2 discusses the physics behind SBIL wavefront metrology. Numerical simulations show that among all the system parameters, only one needs to be adjusted with care—the relative offset between the distances of the two collimating lenses to their respective pinholes, z_{1L} and z_{1R} in Figure 5-1(b). For the simulated SBIL setup, which yields a grating period of 400 nm and a substrate beam spot of 1.4 mm in diameter, a nonlinear phase distortion of 3 nm across the spot requires a relative offset of around 80 μm. Using a simplified analytical model, Sections 5.2.9 and 5.2.10 demonstrate the equivalence between the interferogram recorded by the CCD camera and the substrate-plane moiré pattern. Section 5.3 briefly describes the technique—phase shifting interferometry (PSI)—used to retrieve the moiré phase map from a series of phase-stepped interferograms. In particular, it discusses the Hariharan five-step algorithm currently in use. Section 5.4 describes the wavefront metrology system setup. Section 5.5 presents the experimental results. The demonstrated measurement repeatability is eight thousandth of a period, or 3.2 nm. At present time, the poor quality of the metrology grating and the lack of system automation limit the lowest detected nonlinear phase to around 12 nm. Ultimately, one cares only about the phase error written into the photoresist, the so-called printed error. In Section 5.6, I apply the theory of Gaussian amplitude-weighted moving average to describe the printed error. For example, for an image nonlinearity of 12 nm, I show that by overlapping scans, SBIL can achieve a printed error of less than 1 nm easily.

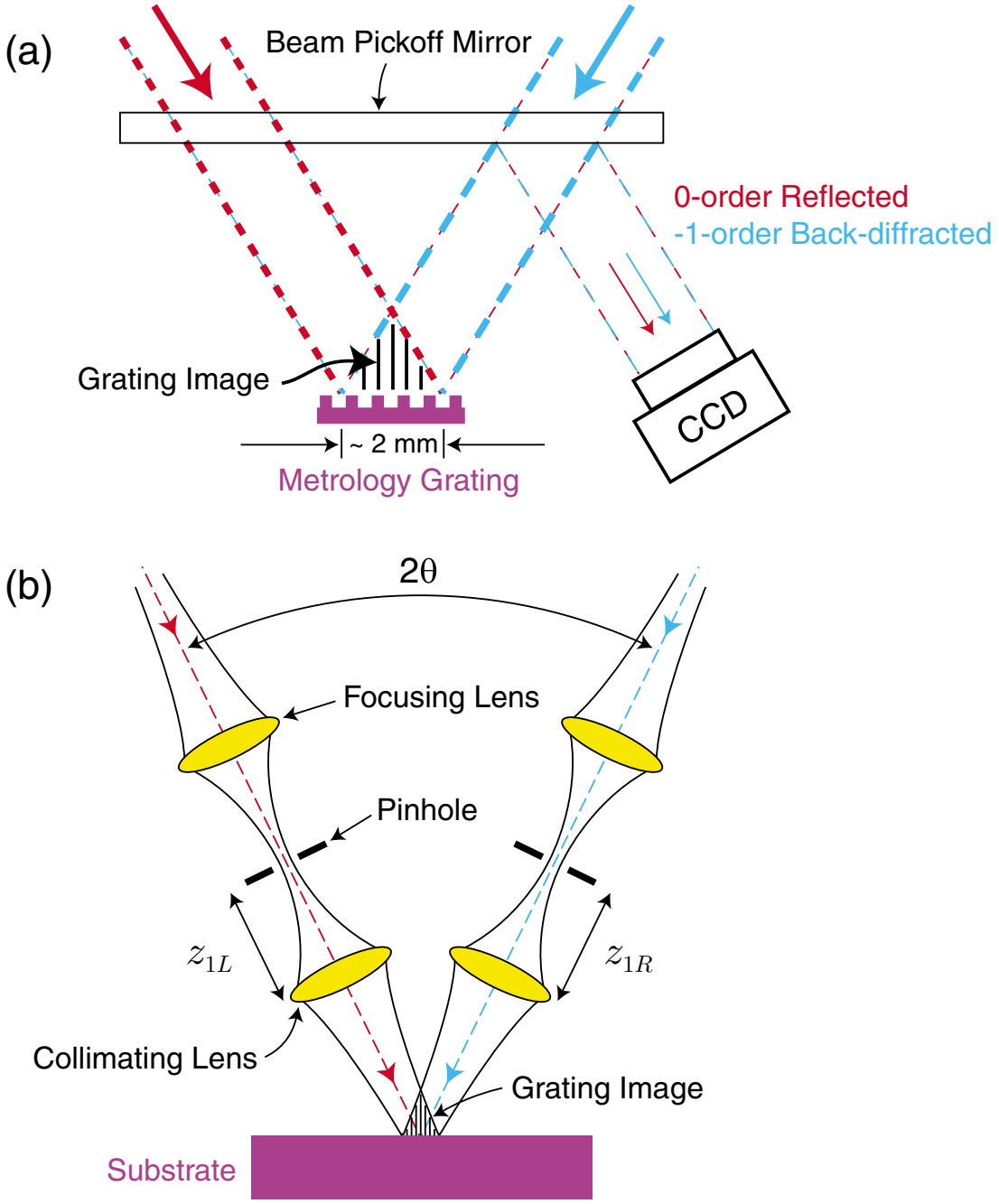

Figure 5-1: SBIL wavefront metrology concept. (a) A metrology grating with an ideal linear spatial phase is used under the Littrow condition. The reflected and back-diffracted beams interfere at a CCD camera. (b) Two collimated Gaussian beams interfere at their waists and produce the grating image. Beam size is exaggerated.

5.2 Theory

By completing this theoretical exercise, I hope to gain a quantitative understanding of the physical parameters that are the most essential to the implementation of SBIL wavefront metrology. The main goal is to construct a mathematical model to simulate the moiré pattern in the substrate plane. By varying the optical setup and studying the resulting changes in the moiré phase, I can deduce which set of parameters is the most critical and come up with the most effective design to position the Gaussian beam waists.

To quantitatively discuss the moiré interferometry-based SBIL wavefront metrology, I must first choose an appropriate model to describe the small beams used by SBIL, which are intrinsically Gaussian in nature. The action of the collimating lenses, which place the beam waists at the substrate, must be taken into account. Dependences on the beam waist size and location prior to the collimating lens, on the distance from the lens to the substrate and on the beam angle must also be considered. Finally, to generate the moiré pattern, I must be able to model the interference of two Gaussian beams and calculate the spatial phase of the resulting interference image.

5.2.1 Moiré phase

Moiré interferometry has been investigated by many authors [73, 74, 75, 76, 77]. Moiré fringes demonstrate the "beating" between two periodic patterns when they are laid on top of each other. The fringes are defined by the phase difference between the two patterns. As a simple example, Figure 5-2 shows the moiré fringes when two linear gratings with slightly different periods, p_1 and p_2, are superimposed. Phases of the two gratings can be written as

$$\phi_1(y) = 2\pi \frac{y}{p_1} \quad , \tag{5.1}$$

$$\phi_2(y) = 2\pi \frac{y}{p_2} \quad . \tag{5.2}$$

The spatial phase of the resulting moiré grating is defined by

$$\Delta\phi = \phi_1 - \phi 2 = 2\pi y \left(\frac{1}{p_1} - \frac{1}{p_2} \right) \quad , \tag{5.3}$$

from which, one can deduce its period

$$p_{\text{moiré}} = \frac{p_1\, p_2}{|p_1 - p_2|} \quad . \tag{5.4}$$

During SBIL wavefront metrology, the grating image lays on top of a linear metrology grating. The phase difference between the two gives rise to a moiré pattern. If the metrology grating has an ideal linear phase, the moiré pattern is then a direct

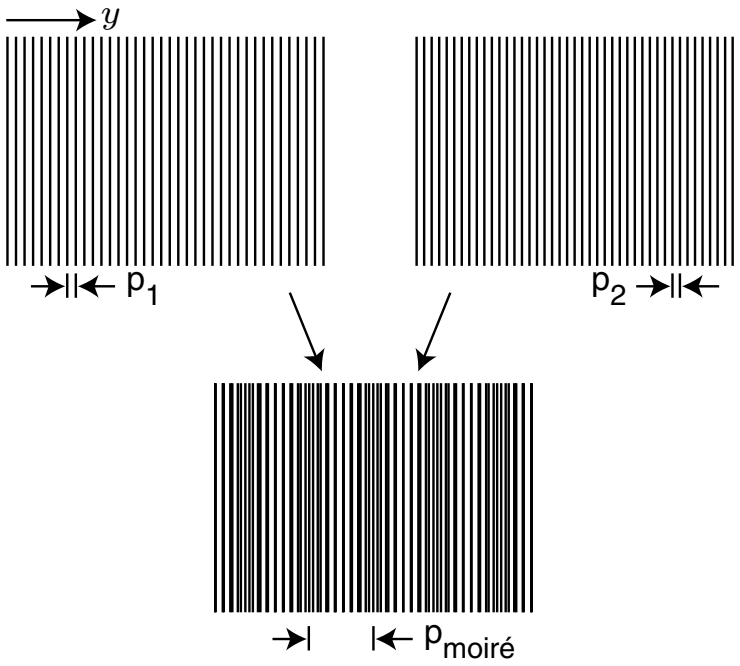

Figure 5-2: The superimposition of two linear gratings gives rise to Moiré fringes.

representation of the phase nonlinearity in the grating image. The goal of wavefront metrology is to measure how large this nonlinear component is, and then adjust the lithography optics to minimize it.

5.2.2 Scalar Gaussian beam

In my Master's thesis [45], I demonstrated the equivalence among three interference models—spherical, scalar Gaussian and vector Gaussian models—to generate a low-distortion grating image for use by SBIL. I assumed that the interference takes place in the "far field", a region that is sufficiently beyond the pinhole spatial filters, and no beam collimation is present.

In the current SBIL setup, to restrict the nonlinear phase in the interference image to a minimum, collimating lenses are used such that the waists of two collimated Gaussian beams interfere at the substrate. Reasons for adopting beam collimation will be discussed in detail in Section 5.2.11. Since the wavefront at the waist of a Gaussian beam is planar, it renders invalid any interference model based on spherical waves. The vector Gaussian model is complicated and unnecessary. Compared to the leading paraxial term, the next higher-order term in a full vector Gaussian expansion is weaker in magnitude by a factor $\mathcal{F}^2$ [78], where $\mathcal{F} = (\frac{1}{\sqrt{2}} k w_0)^{-1}$ is a unitless expansion parameter, $k = 2\pi/\lambda$ is the wave number and w_0 is the $1/e^2$ beam waist radius. For SBIL, the laser wavelength is 351.1 nm and beam waist radius at the substrate is approximately 1 mm. Together, they give $\mathcal{F}^2 \approx 6 \times 10^{-9}$, a tiny number

indeed. By default, to describe the small beams used in SBIL, a scalar Gaussian beam model is the most appropriate.

The solution u to the paraxial wave equation

$$\left(\frac{\partial^2}{\partial x^2}+\frac{\partial^2}{\partial y^2}\right)u-2jk\frac{\partial u}{\partial z}=0 \tag{5.5}$$

is known in the literature as the paraxial solution or the paraxial term. I call it the scalar Gaussian term to distinguish it as the leading term in the solution to the full vector wave equation [78]. Eq. (5.3) from Reference [58] presents the solution as,

$$u(x,y,z)=\frac{\sqrt{2}}{\sqrt{\pi}w(z)}\exp[j\phi(z)]\exp\left(-\frac{x^2+y^2}{w(z)^2}\right)\exp\left[-\frac{jk}{2R(z)}(x^2+y^2)\right] \quad , \tag{5.6}$$

where

$$w(z)^2=\frac{2b}{k}\left(1+\frac{z^2}{b^2}\right) \quad , \tag{5.7}$$

$$\frac{1}{R(z)}=\frac{z}{z^2+b^2} \quad , \tag{5.8}$$

$$\tan\phi(z)=\frac{z}{b} \quad . \tag{5.9}$$

The physical electric field ($\mathbf{E}$) is related to u via Eq. (4.50) from the same reference,

$$\mathbf{E}=-j\omega u\exp(-jkz)\,\hat{\mathbf{n}} \quad , \tag{5.10}$$

where ω is the angular frequency and $\hat{\mathbf{n}}$ is the polarization vector. The field is a wave traveling in the $+z$ direction with curved phase fronts of radius $R(z)$ and a Gaussian profile defined by the $1/e^2$ beam intensity radius $w(z)$ (Fig. 2-2). The so-called confocal parameter or Rayleigh range b is related to the minimum beam intensity radius, i.e., the beam waist radius w_0 by

$$b=\frac{1}{2}kw_0^2=\frac{\pi w_0^2}{\lambda} \quad . \tag{5.11}$$

In terms of w_0, Eqs. (5.7)–(5.9) can be rewritten as

$$w(z)^2=w_0^2\left[1+\left(\frac{\lambda z}{\pi w_0^2}\right)^2\right] \quad , \tag{5.12}$$

$$\frac{1}{R(z)}=\frac{z}{z^2+\left(\frac{\pi w_0^2}{\lambda}\right)^2} \quad , \tag{5.13}$$

$$\tan\phi(z)=\frac{z}{\left(\frac{\pi w_0^2}{\lambda}\right)} \quad . \tag{5.14}$$

Note that at the beam waist ($z=0$), the radius of curvature becomes infinite, which means that the phase front is strictly planar.

By "scalar Gaussian beam", I mean a beam described by the electric field (5.10).

5.2.3 The q transforms

A scalar Gaussian beam is completely defined by the so-called q-parameter,

$$\frac{1}{q} \equiv \frac{1}{z+jb} = \frac{1}{R(z)} - j\frac{\lambda}{\pi w(z)^2} \ , \tag{5.15}$$

where the real part is the phase front curvature and the imaginary part the Gaussian beam radius. The free space propagation of a Gaussian beam and its transformation by a thin lens are defined by their respective q transforms. From Eq. (5.61) in Reference [58], the q transform for a Gaussian beam traversing a free space of length D is

$$q' = q + D \ , \tag{5.16}$$

where q and q' are the initial and the transformed parameter, respectively. Eq. (5.65) from the same reference gives the q transform for a thin lens,

$$\frac{1}{q'} = \frac{1}{q} - \frac{1}{f} \ , \tag{5.17}$$

where f denotes the focal length of the lens. Eqs. (5.16) and (5.17) provide the physical tools with which I model SBIL wavefront metrology.

5.2.4 The model

In SBIL, the photoresist on a moving substrate records the grating image produced by two collimated Gaussian beams interfering with one another. The spatial phase of the grating image ϕ_{gi} is given by

$$\phi_{gi} = \phi_{\mathbf{E}_L} - \phi_{\mathbf{E}_R} \ , \tag{5.18}$$

where $\phi_{\mathbf{E}_L}$ and $\phi_{\mathbf{E}_R}$ are the wavefront phases for the left and the right beam, respectively. If one can find expressions for $\phi_{\mathbf{E}_L}$ and $\phi_{\mathbf{E}_R}$, ϕ_{gi} can be modeled. Physically, Eq. (5.18) originates from the fact that only the field interaction term in the irradiance (i.e., the intensity $I \propto |\mathbf{E}_L + \mathbf{E}_R|^2$) gives rise to interference. Assuming perfect phase linearity for the underlying metrology grating, the phase of the moiré pattern is simply ϕ_{gi} with its linear component removed. The nonlinear component results from non-planar wavefronts. Its magnitude is measured by the SBIL wavefront metrology system. Locations of the beam waists are then adjusted accordingly to minimize the phase nonlinearity.

Figure 5-3 shows the setup geometry for one of the lithography interferometer arms. The z-axis origin is chosen at the pinhole plane, where the initial focused beam waist lies. Prior to the pinhole, there is a focusing lens [not shown in Fig. 5-3 but can be seen in Fig. 5-1(b)], whose action on the placement and the size of the initial beam waist is studied in Section 5.2.7. The collimating lens has a focal length f and is at

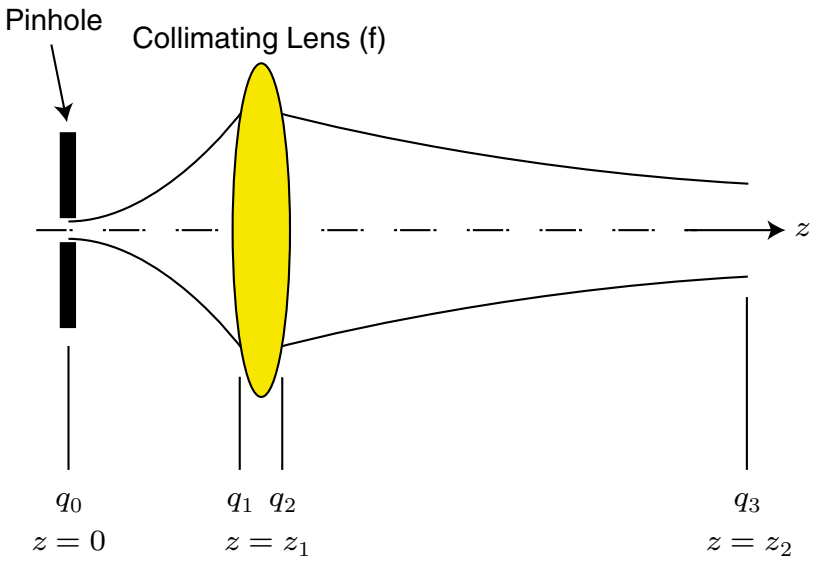

Figure 5-3: Setup geometry for one of the lithography arms. The collimating lens is by assumption a thin lens. Beam size is exaggerated.

a distance z_1 from the origin. The thickness of the lens is by assumption negligible, i.e., it is considered thin. I am interested in knowing the beam properties such as the curvature R at some output plane $z = z_2$. The parameters q_0 through q_3 describe the beam at the indicated locations. In particular, q_1 and q_2 label the input and the output plane of the lens, respectively. Note that due to the thin lens assumption, both planes are located at $z = z_1$.

When Eqs. (5.16) and (5.17) are applied appropriately, four equations appear in the end,

$$q_0 = jb_0 \ , \tag{5.19}$$

$$q_1 = q_0 + z_1 \ , \tag{5.20}$$

$$\frac{1}{q_2} = \frac{1}{q_1} - \frac{1}{f} \ , \tag{5.21}$$

$$q_3 = q_2 + (z_2 - z_1) \ , \tag{5.22}$$

where b_0 is the initial confocal parameter and is related to the initial beam waist radius w_0 by $b_0 = \frac{1}{2}kw_0^2$. Solve for q_3 in terms of the known variables b_0, f, z_1 and z_2, and arrange the final result into its real and imaginary parts,

$$q_3 = A + jB \ , \tag{5.23}$$

where

$$A = \frac{-fz_1^2 + f^2 z_1 - b_0^2 f}{z_1^2 - 2fz_1 + f^2 + b_0^2} + (z_2 - z_1) \ , \tag{5.24}$$

$$B = \frac{b_0 f^2}{z_1^2 - 2fz_1 + f^2 + b_0^2} \quad . \tag{5.25}$$

An inversion of Eq. (5.23) leads to

$$\frac{1}{q_3} = C + jD \quad , \tag{5.26}$$

where

$$C = \frac{(z_1^2 - 2fz_1 + f^2 + b_0^2)z_2 - z_1^3 + fz_1^2 - b_0^2 z_1 - b_0^2 f}{(z_1^2 - z_1 z_2 + fz_2)^2 + (b_0 z_1 - b_0 z_2 + b_0 f)^2} \quad , \tag{5.27}$$

$$D = \frac{-b_0 f^2}{(z_1^2 - z_1 z_2 + fz_2)^2 + (b_0 z_1 - b_0 z_2 + b_0 f)^2} \quad . \tag{5.28}$$

From q_3 and its inverse, values of ϕ [Eq. (5.9)] and $1/R$ [Eq. (5.15)] can be derived for the plane $z = z_2$,

$$\phi(z_2) = \tan^{-1}\left(\frac{A}{B}\right) \quad , \tag{5.29}$$

$$\frac{1}{R(z_2)} = C \quad . \tag{5.30}$$

The phase of the left beam, given by the Gaussian electric field [Eq. (5.10)], is

$$\phi_{\mathbf{E}_L} = -kz_L + \phi_L(z_L) - k\frac{(x_L^2 + y_L^2)}{2R_L(z_L)} \quad , \tag{5.31}$$

where I have changed the subscript in z_2 to "L" to denote the left arm. Similarly, for the right arm, I have

$$\phi_{\mathbf{E}_R} = -kz_R + \phi_R(z_R) - k\frac{(x_R^2 + y_R^2)}{2R_R(z_R)} \quad . \tag{5.32}$$

5.2.5 Coordinate transformations

Even though expressions for the phases $\phi_{\mathbf{E}_L}$ and $\phi_{\mathbf{E}_R}$ have been found, they are written in the beams' coordinate frames—$x_L y_L z_L$ and $x_R y_R z_R$ in Figure 5-4, respectively. To study the interference in the laboratory frame xyz, coordinate transformations are required.

The angles of incidence are θ_L and θ_R, for the left and the right arm, respectively. The distance from the left collimating lens to the origin O is d_L, and the right d_R. Those from the lenses to their respective pinholes where the initial beam waists lie are z_{1L} and z_{1R}. Once everything is labeled, coordinate transformations are straightforward. Taking note that the beams interfere in the plane $z = 0$ where the substrate is located, one gets for the left beam,

$$\begin{bmatrix} x_L \\ y_L \\ z_L \end{bmatrix} = \left.\begin{pmatrix} -\cos\theta_L\, x \\ y \\ -\sin\theta_L\, x + z_{1L} + d_L \end{pmatrix}\right|_{z=0} \quad , \tag{5.33}$$

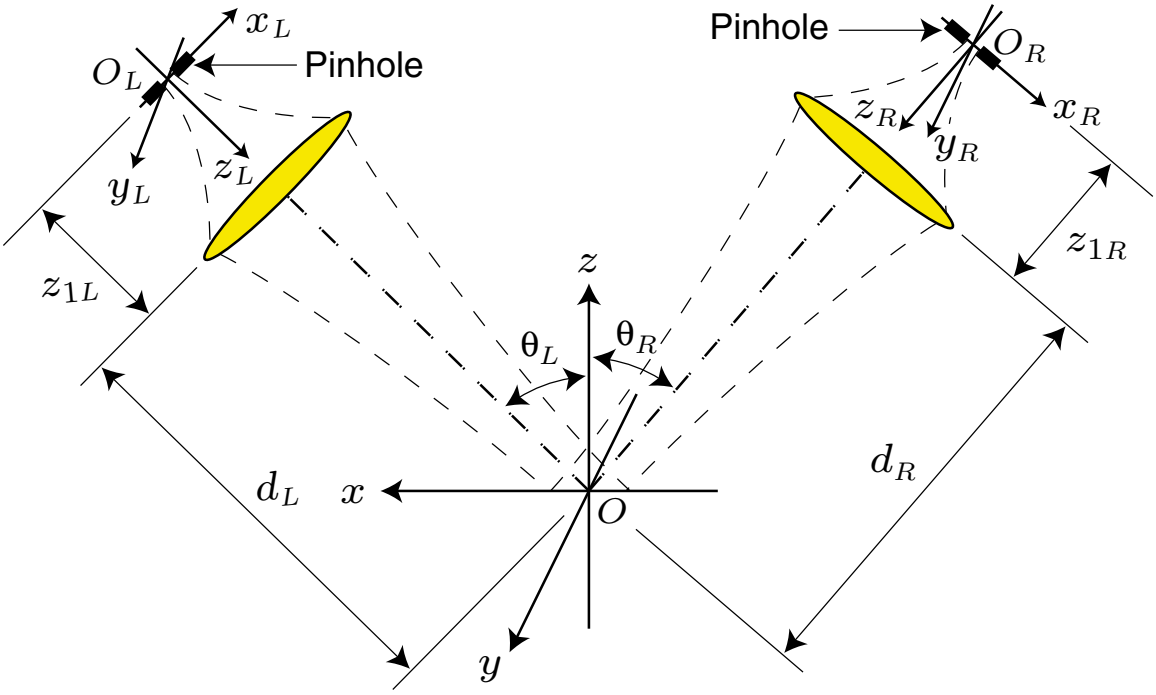

Figure 5-4: Coordinate frames describing the interference of collimated Gaussian beams. Beam size is exaggerated.

and for the right,

$$\begin{bmatrix} x_R \\ y_R \\ z_R \end{bmatrix} = \begin{pmatrix} -\cos\theta_R\, x \\ y \\ \sin\theta_R\, x + z_{1R} + d_R \end{pmatrix} \Bigg|_{z=0} \quad . \tag{5.34}$$

Note that $y_L = y_R = y$, i.e., the optical axes of the beams are assumed to lie within the $y = 0$ plane. The factors $(z_{1L} + d_L)$ and $(z_{1R} + d_R)$ are due to the displacements of the beam origins O_L and O_R from the lab system origin O.

5.2.6 Simulated moiré phase maps

By substituting the appropriate coordinate transformations into phase expressions $\phi_{\mathbf{E}_L}$ and $\phi_{\mathbf{E}_R}$ [Eqs. (5.31) and (5.32)], one calculates the spatial phase of the grating image ϕ_{gi} by applying Eq. (5.18). Exploiting the fact that a phase is only known up to some arbitrary constant, an offset is chosen such that ϕ_{gi} is normalized to zero at the coordinate origin O,

$$\phi_{\text{offset}} = k(z_R - z_L) - (\phi_R - \phi_L)|_{x=y=0} \quad . \tag{5.35}$$

The phase of the moiré is the difference between the normalized grating image phase and the phase of the linear metrology grating

$$\phi_{\text{lin}} = 2\pi \frac{x}{p} \quad , \tag{5.36}$$

Parameter	Value (units)
λ = laser wavelength	351.1 (nm)
$\rho = 1/e^2$ beam intensity radius at the substrate	0.7 (mm)
f = focal length of the collimating lens	108.2 (mm)
p = metrology grating period	400 (nm)
z_1 = distance from the initial beam waist to the collimating lens	108.33 (mm)
d = distance from the collimating lens to the substrate	328 (mm)
w_0 = initial beam waist radius at the pinhole	17.25 (μm)
θ = incident angle for writing a 400 nm nominal period grating	0.45 (rad) or 26°

Table 5.1: Parameters for simulating SBIL moiré patterns. The base values for z_1, d, w_0 and θ are listed. Ideally, the interference optics in both arms should be set to these values, which is the reason why the subscripts "L" and "R" have been dropped.

which is an ideal linear phase also normalized to zero at the origin. The period of the metrology grating is p.

The problem is now ready for numerical modeling. The MATLAB code for generating simulated moiré patterns, Moiré.m, is included in Appendix G. Values for the $1/e^2$ beam spot radius at the substrate, the focal length of the collimating lens, and its distance from the substrate are taken from Section 2.2.1, which discusses the layout of SBIL lithography optics. The routine WaistLoc.m, also documented in Appendix G, takes these three values and back-calculates the precise beam waist size at the pinhole and the distance from the pinhole to the collimating lens, such that the collimated beam waist is situated exactly at the substrate plane. The angle of incidence is calculated for a nominal grating period of 400 nm. Table 5.1 lists the values for z_1, d, w_0 and θ obtained in this fashion. Ideally, both arms should operate at these so-called base values, which is why the subscripts "L" and "R" have been dropped. During the simulation however, for either arm, the parameters defining Gaussian beam interference can be individually varied around the base operating values. The reader may notice that the 34.5 μm-diam. beam waist calculated here is different from the 37.9 μm estimate in Section 2.2.1. The difference is due to a harmless modeling inconsistency already explained in that same section.

A detailed examination of the substrate-plane phase distortion through computer modeling follows from here on. I explore the dependences of the nonlinear phase on various parameters that define the SBIL interference. Numerous simulated moiré phase maps are generated. Table 5.2 summarizes the findings. Figure 5-4 serves as a graphical reference on the various physical parameters involved.

Figure 5-5 shows the moiré phase contours when both arms are set exactly at the

Figure no.	Parameter(s) varied	Nonlinear phase distortion
Figure 5-5	–	< 0.04 nm
Figure 5-6	z_{1L}: $+80$ μm	1.98 nm
Figure 5-7	z_{1L}, z_{1R}: $+5$ mm	< 0.1 nm
Figure 5-8	z_{1L}: $+5.08$ mm, z_{1R}: $+5$ mm	2.45 nm
Figure 5-12	w_{0L}: -3 nm, w_{0R}: $+3$ nm	< 0.04 nm
Figure 5-13 (worst case)	z_{1L}: $+5$ mm, z_{1R}: $+4.92$ mm d_R: -10 mm w_{0L}: -3 nm, w_{0R}: $+3$ nm	2.84 nm
Figure 5-15	same as in Figure 5-13, plus θ_L: $+238.6$ μrad, θ_R: -238.6 μrad	2.82 nm
Figure 5-16	same as in Figure 5-13, plus θ_L: $+244.6$ μrad, θ_R: -238.6 μrad	$\sim$2.8 nm

Table 5.2: Result summary for the moiré phase simulations. Various physical parameters are varied to reveal their effects on substrate plane-phase distortions. Parameter changes occur around their respective base values (Table 5.1).

base values. The phase is normalized to the grating period of 400 nm. As expected, because the collimated beam waists are located at the substrate, phase nonlinearity is at its minimum. The oblique incidence gives rise to the elliptical shape of the beam spot. Clearly, the distortion across the spot is negligible, at less than 0.04 nm. One must wonder why there is any distortion at all? Figure 5-4 shows that only the origin O is truly located at the beam waist; elsewhere, because of the nonzero incident angle, wavefront curvatures do exist which, when interfered, lead to small nonlinearities.

Figure 5-6 shows the moiré phase map when the distance z_{1L} is slightly larger than its base value by 80 μm. The nonlinear phase is at 2 nm across the spot. Unless otherwise noted, it is implied that all parameters take base values, except the one being varied. For example, in the current case, z_{1L} is the only variable. Simulations show that the polarity of the variation poses no concern. Also, had z_{1R} been the variable, the sign of the phase would switch but the magnitude would remain the same.

In reality, while mounting a collimating lens to the optical bench, I can be certain of its placement to within 5 mm of the desired location—a safe estimate. Figure 5-7 shows the phase map when both z_{1L} and z_{1R} are increased from their base value by $+5$ mm. Now the beams propagate symmetrically but interfere away from their waists. The nonlinear phase, at less than 0.1 nm across the spot, is slightly larger compared to the number found in Figure 5-5. Because a change of -5 mm shows even less phase distortion, I only consider the worse of the two polarities. If in

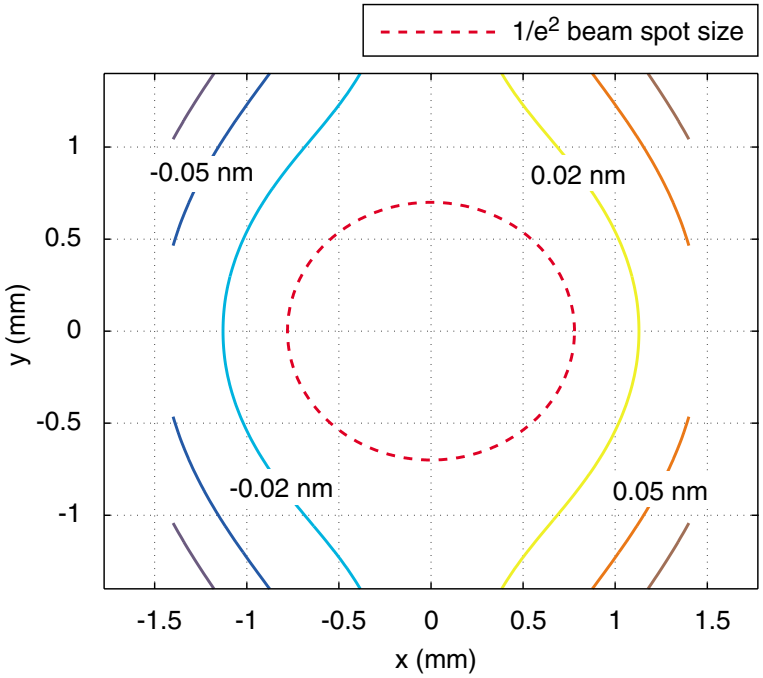

Figure 5-5: The moiré phase map when parameters in both arms are set to base values (Table 5.1).

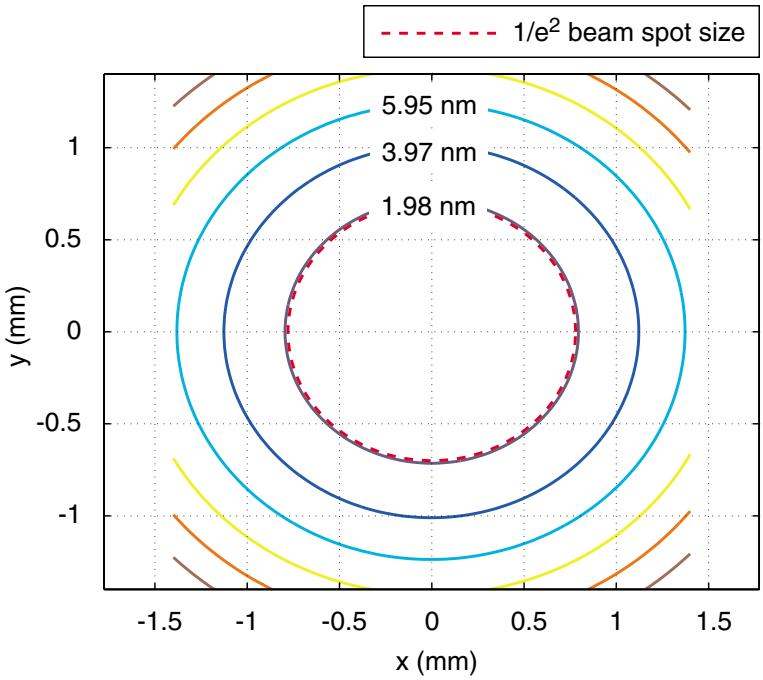

Figure 5-6: The moiré phase map when z_{1R} is at base value and z_{1L} is increased by 80 μm, i.e., the relative offset between the two collimating lenses is 80 μm. See Figure 5-4 for coordinate definitions.

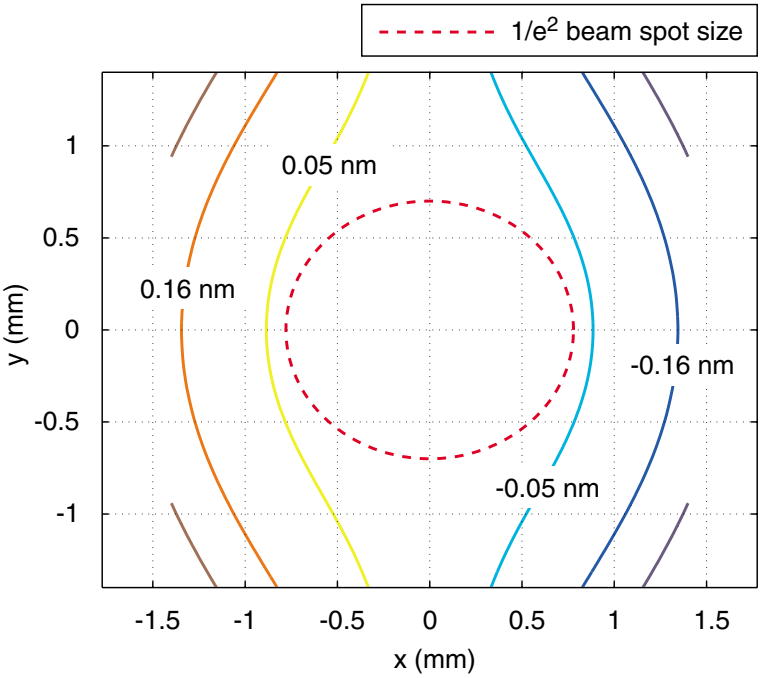

Figure 5-7: The moiré phase map when both z_{1L} and z_{1R} are increased from their base value by 5 mm.

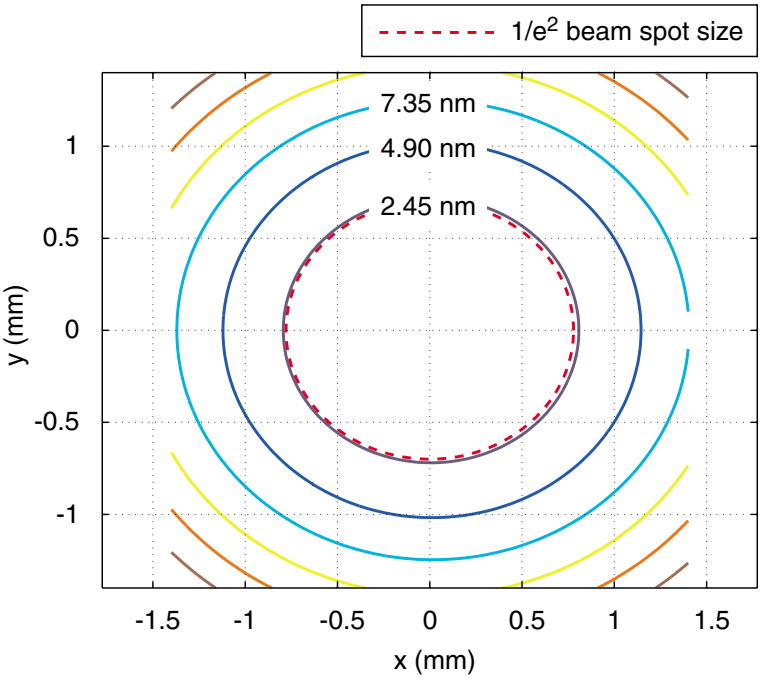

Figure 5-8: The moiré phase map when z_{1R} is increased by 5 mm and z_{1L} by 5.08 mm, i.e., the relative offset between the two collimating lenses is 80 μm.

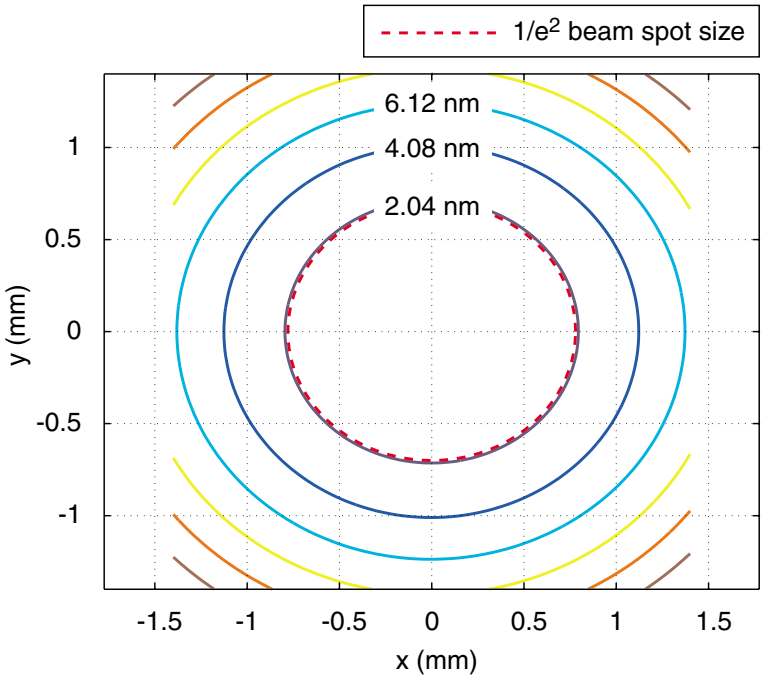

Figure 5-9: The moiré phase map when d_L is increased from its base value by 135 mm.

addition, a relative mismatch of 80 μm is introduced, the moiré phase contours become those shown in Figure 5-8. Again, without loss of generality, the distance z_{1L} is assumed slightly longer. Compared to Figure 5-6, although both lenses are now grossly misplaced from their ideal locations, the same 80 μm relative offset yields a nonlinear distortion of 2.45 nm, only slightly larger than the 2 nm figure from when the ideal location (with relative offset) is used. Therefore, it is inconsequential whether or not the collimating lenses are located precisely where they are supposed. A generous amount of error tolerance is built into the optical design. The nonlinear phase seems to depend only on the relative offset between the lenses.

Figure 5-4 graphically defines d_L and d_R as the distances from the left and right collimating lenses to the substrate plane. What if there is a mismatch between the two? Figure 5-9 plots the phase map when d_L is unrealistically increased from its base value by 135 mm. The resulting distortion is merely 2 nm. No amount of operator carelessness can result in this much asymmetry in the optical layout. By considering the absurdity, I only intend to demonstrate the parameter's "irrelevance".

Thus far through the discussion, the critical parameter which determines the substrate-plane phase nonlinearity seems to be the relative difference between z_{1L} and z_{1R}, the distances of the two collimating lenses to their respective pinholes. However, before a formal conclusion can be drawn, one needs to investigate the dependence on one more set of parameters, namely, w_{0L} and w_{0R}, the left and right beam waist radii

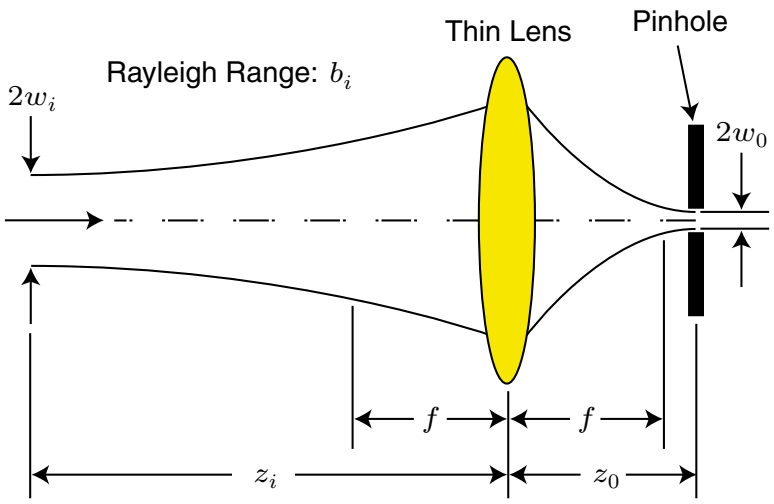

Figure 5-10: Spatial filter geometry. Beam size is exaggerated.

at the pinholes.

5.2.7 Action of the focusing lens

Prior to their collimation and interference, the beams pass through two spatial filters. Each filter assembly constitutes a converging lens and a pinhole. By focusing a beam through a pinhole, a spatial filter rids the beam of undesired high-spatial-frequency amplitude noise. Section 2.2.2 presents details on spatial filtering for SBIL. Figure 5-10 shows the geometry of the spatial filter. By choice, the lens in the spatial-filter assembly has the same focal length (f = 108.2 mm) as the collimating lens. The focused beam waist at the pinhole is approximately 38 μm in diameter.

Section 2.1.3 has already discussed how various parameters are related when a Gaussian beam propagates through a thin lens. Specializing those findings to the current set of symbols, one has

$$z_0 = f + \frac{f^2(z_i - f)}{(z_i - f)^2 + b_i^2} \quad , \tag{5.37}$$

$$w_0 = \frac{f}{\sqrt{(z_i - f)^2 + b_i^2}}\, w_i \quad , \tag{5.38}$$

where b_i is the Rayleigh range for the incoming beam; w_i and w_0 are the beam waist radii before and after the lens, respectively. Differentiating z_0 with respect to z_i yields an equation

$$\Delta z_0 = -\frac{f^2\left[(z_i - f)^2 - b_i^2\right]}{\left[(z_i - f)^2 + b_i^2\right]^2}\, \Delta z_i \quad , \tag{5.39}$$

which links Δz_i, a small displacement of the lens with respect to the waist of the incoming beam, to Δz_0, a displacement of the focused beam waist. Similarly, differentiating Eq. (5.38) gives a relation between Δz_i and Δw_0, the change in size of the

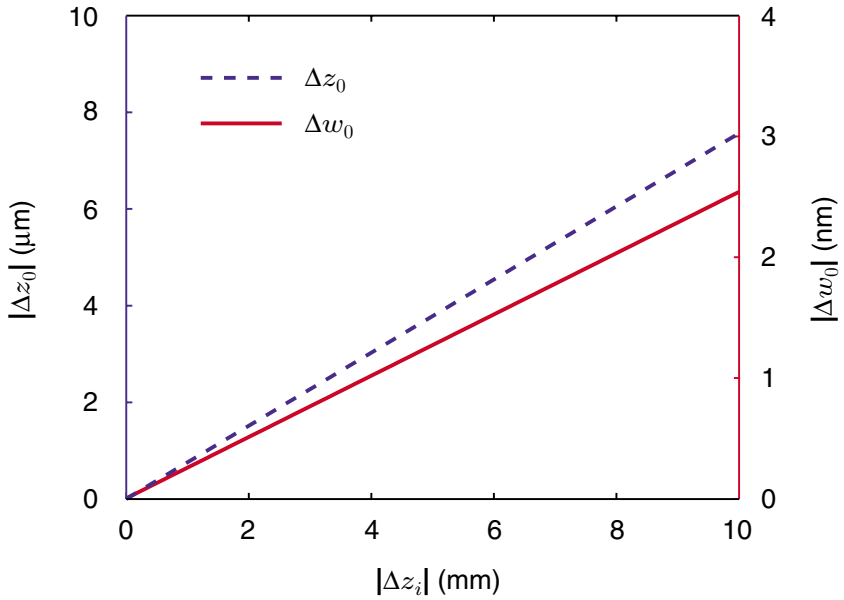

Figure 5-11: A plot of $|\Delta w_0|$ and $|\Delta z_0|$ vs. $|\Delta z_i|$. Displacement of the focusing lens affects the focused beam waist size and location.

focused beam waist,

$$\Delta w_0 = -\frac{f w_i (z_i - f)}{[(z_i - f)^2 + b_i^2]^{\frac{3}{2}}} \Delta z_i \quad . \tag{5.40}$$

Here is the concern. After passing through the grating beamsplitter, the laser splits and forms two lithography arms. There is no guarantee that the left and right focusing lenses are placed symmetrically about the beamsplitter. After all, there are quite a few intermediate optical components whose placement errors do accumulate. By the time one gets to the spatial filters, there may be a mismatch in the placements of the lenses by as much as ± 10 mm, erring on the safe side. What effect will this have on the substrate phase distortion?

Based on Eqs. (5.39) and (5.40), Figure 5-11 plots $|\Delta w_0|$ and $|\Delta z_0|$ vs. $|\Delta z_i|$, with the sign of Δz_i chosen to give the larger variations. It shows how the lens's displacement affects the focused beam waist size and location. The values for the waist radius, position and Rayleigh range of the incoming beam, $w_i = 0.7$ mm, $z_i = 0.32$ m and $b_i = 4.03$ m, respectively, are all ballpark figures taken from Section 2.2.1 (Table 2.3). I am only after an order of magnitude estimate. At a maximum displacement of 10 mm, the focused beam waist varies in radius by less than 3 nm and shifts in location by roughly 8 μm. The last figure is perhaps counter-intuitive. Can a lens movement of 10 mm only induce a focal spot shift of 8 μm? For a Gaussian beam, apparently it can, under the circumstance. Since the Rayleigh range b_i is much greater than both z_i and f, Eq. (5.39) simplifies to $\Delta z_0 \approx f^2/b_i^2 \, \Delta z_i \approx 7.2 \times 10^{-4} \, \Delta z_i$.

Physically, the lens is located well within the Rayleigh range of the incoming beam, where the wavefronts are least collimated. The classical ray-optics picture of the lens-and-focal-spot-movement does not apply.

The 8 μm shift in the waist location is of no concern. It means the optical design is so tolerant that once the two collimating lenses have been located with a relative offset of 80 μm, it is safe to move one of the focusing lenses blatantly by 10 mm and maintain roughly the same offset. Figure 5-12 shows the moiré phase map when the beam waists at the pinholes, w_{0L} and w_{0R}, change in size by -3 nm and $+3$ nm, respectively. These numbers correspond to a focusing-lens-placement asymmetry of 20 mm. While the contours exhibit an interesting twist in shape, the overall phase distortion is at less than 0.04 nm, the same as Figure 5-5.

Figure 5-13 is a worst case study specific to SBIL wavefront metrology where w_{0L}, w_{0R}, d_R, z_{1L} and z_{1R} are offset from their base values by -3 nm, $+3$ nm, -10 mm, $+5$ mm and $+4.92$ mm, respectively. In other words, I am assuming all focusing and collimating lenses have been misplaced from their ideal locations in such a fashion as to conspire the worst possible nonlinear distortion, provided of course, that the misplacements are within reasonable limits (Sec. 5.4.1). Given the same 80 μm difference between z_{1L} and z_{1R} as before, the distortion only amounts to 2.84 nm.

Without considering the effects of beam angle variations, one can now make the following statement: the single most critical parameter during SBIL wavefront metrology, which sets the level of nonlinear phase distortion at the substrate plane, is the relative difference between the distances from the collimating lenses to their respective pinholes.

5.2.8 Phase nonlinearity due to beam angle variations

During wavefront metrology, the ideal case [Fig. 5-14(a)] sees the specularly reflected ray from the left arm and the -1-order back-diffracted ray from the right arm coincide after the metrology grating. According to the grating equation [Eq. (1.3)], the diffracted angle θ_{-1} and the incident angle θ are related by

$$\sin\theta_{-1} - \sin\theta = -\frac{\lambda}{p} \quad , \tag{5.41}$$

where p is the period of the metrology grating. The beams can only coincide if

$$\theta_{-1} = -\theta = -\sin^{-1}\left(\frac{\lambda}{2p}\right) \quad . \tag{5.42}$$

The negative sign is an artifact due to the way θ_{-1} is defined in the grating equation. In terms of magnitude, θ_{-1} equals θ.

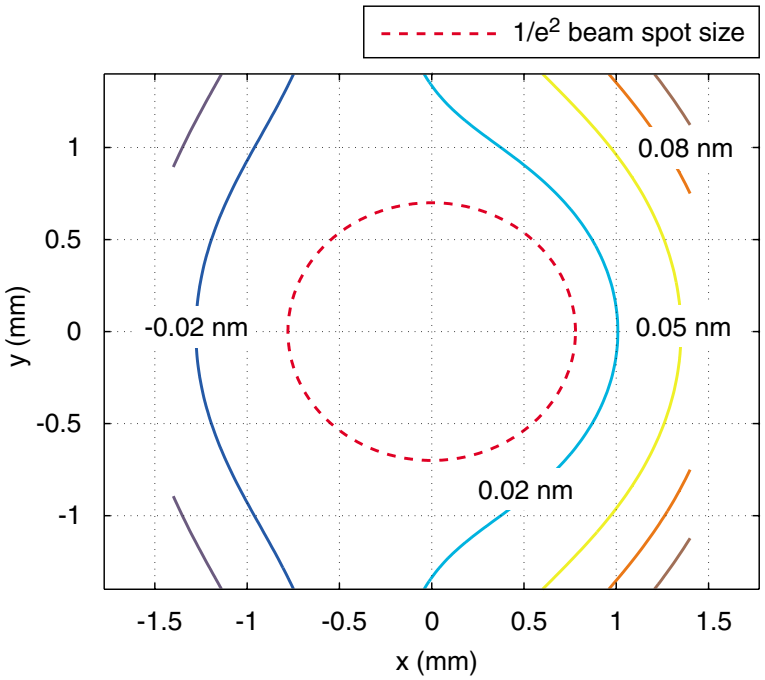

Figure 5-12: The moiré phase map when the initial beam waist radii at the pinholes, w_{0L} and w_{0R}, are changed by -3 nm and $+3$ nm, respectively.

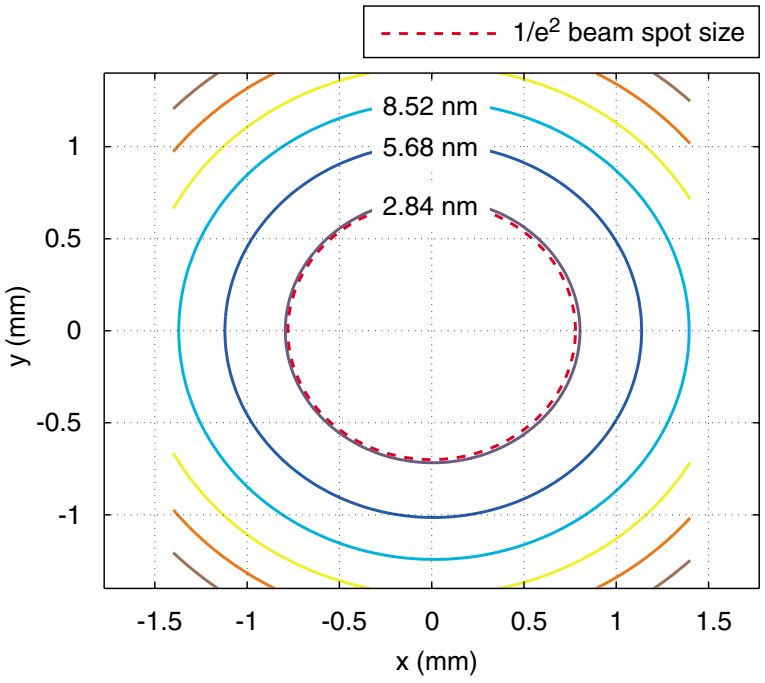

Figure 5-13: The moiré phase map for a worst case study where the parameters w_{0L}, w_{0R}, d_R, z_{1L} and z_{1R} are offset from their base values by -3 nm, $+3$ nm, -10 mm, $+5$ mm and $+4.92$ mm, respectively. Again, the relative offset between z_{1L} and z_{1R} is 80 μm.

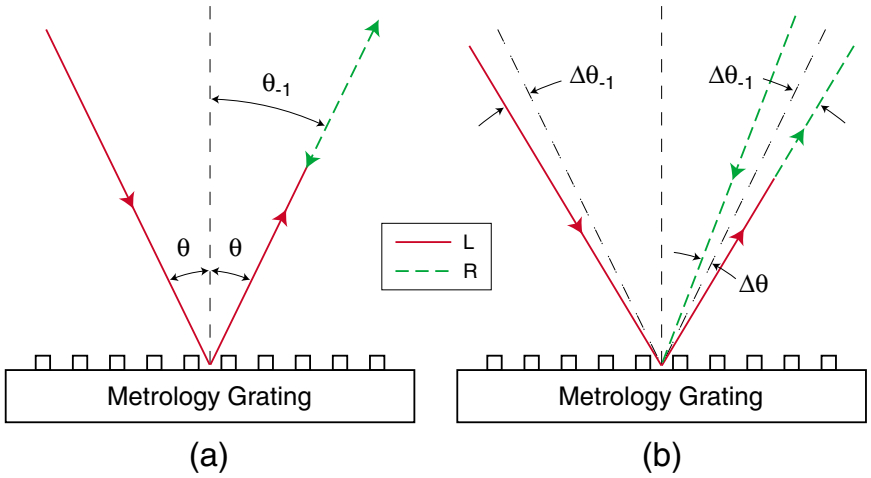

Figure 5-14: Beam angles during grating mode alignment. (a) Ideal case. (b) Non-ideal case.

As pointed out in Section 3.2.4, during grating mode alignment, one can not assure that both beams have equal angles of incidence with respect to the metrology grating. Schematically, the beam paths may look as shown in Figure 5-14(b). Note that in aligning the reflected and back-diffracted rays, the left beam sees a slight increase in its angle of incidence by $\Delta\theta_{-1}$ and the right a slight decrease by $\Delta\theta$. By differentiating Eq. (5.41) and making use of Eq. (5.42), one can show

$$\Delta\theta \approx \Delta\theta_{-1} \quad . \tag{5.43}$$

I use the approximation sign to allow the real-world possibility that θ_{-1} may not be equal to θ exactly, though any error in Eq. (5.43) is of second order and can be ignored.

To split the laser and form the lithography interferometer, SBIL uses a grating beamsplitter. The advantages are many (Sec. 2.1.1). As mentioned in Section 3.5.1, even with an active beam steering system, the SBIL laser has a small pointing instability. The measured angular noise is $\delta = 11.4$ μrad, three-sigma. After the grating, the laser splits into two. The angular variations in the two arms are antisymmetrically correlated (Sec. 3.4).

Mathematically, combining the $\Delta\theta$ effect [Eq. (5.43)] and the beams' angular noise correlation, one can write the incident angles as

$$\theta_L = \theta + \theta_{\text{err}} + \Delta\theta - \delta \quad , \tag{5.44}$$

$$\theta_R = \theta - \Delta\theta + \delta \quad . \tag{5.45}$$

Ignore the θ_{err} term for now. Notice that the angle changes are antisymmetrical, i.e., the changes are equal in magnitude but opposite in sign. A very crude ceiling estimate

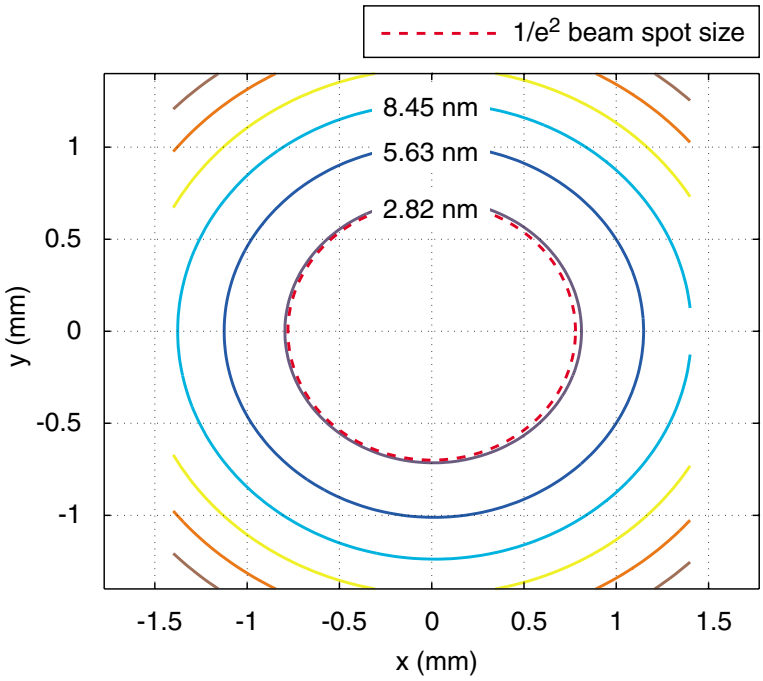

Figure 5-15: The moiré phase map produced with the same set of parameters as in Figure 5-13, except angle variations are now included, with $\theta_L = \theta + \Delta\theta - \delta$ and $\theta_R = \theta - \Delta\theta + \delta$, where θ is the base value (Table 5.1), $\Delta\theta = 250$ μrad and $\delta = 11.4$ μrad.

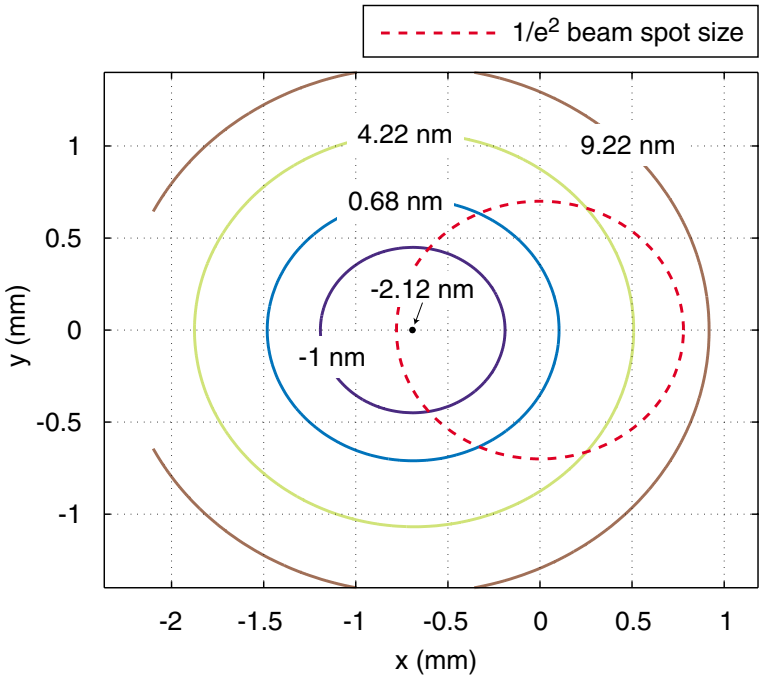

Figure 5-16: The moiré phase map produced with the same parameter values as in Figure 5-15, except now $\theta_L = \theta + \theta_{\text{err}} + \Delta\theta - \delta$, where $\theta_{\text{err}} = 6$ μrad.

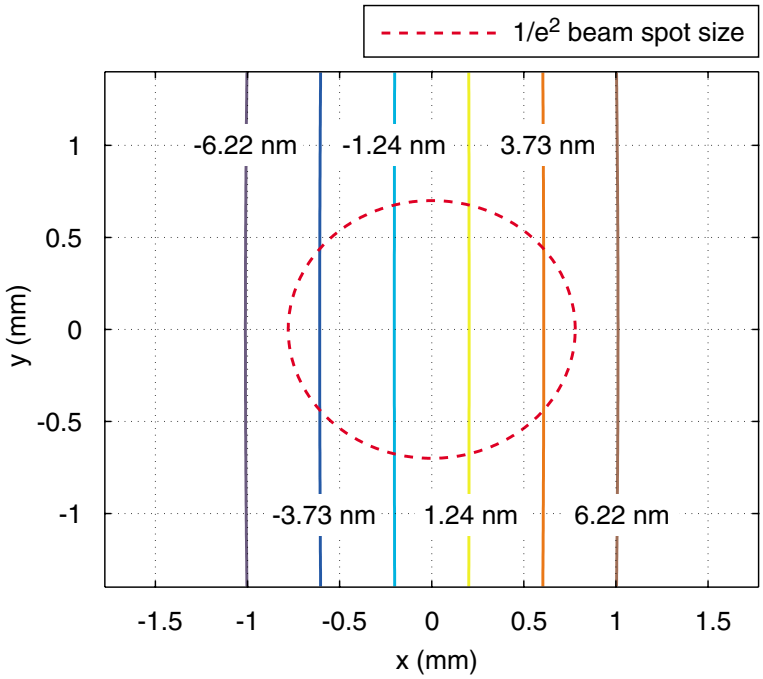

Figure 5-17: The moiré phase map produced with all parameters set at base values, except θ_L, which is increased by 6 μrad. The linear phase shown is due to the difference in period between the metrology grating and the grating image.

for $\Delta\theta$ is around 250 μrad. The estimate came from an empirical experiment. During beam alignment, one can hold a microscope slide in the beam path and examine the overlap between the right incident beam and the left reflected beam. The overlap of two ~ 0.5 mm-radius spots over a slide-to-substrate distance of ~ 1 m gives this upper limit. Figure 5-15 studies the worst case (Fig. 5-13) again, with angle variations included. The antisymmetry proves most beneficial as the nonlinear phase component is unchanged at 2.82 nm across the spot.

Figure 5-16 repeats the same simulation with $\theta_{\text{err}} = 6$ μrad to account for possible angle alignment errors. I should remind the reader that the SBIL beam alignment system can align the mean angle to around 2 μrad (Sec. 3.5.2), so the 6 μrad figure is again a generous overestimate. The center of the phase contours has shifted to the left. It may seem the distortion across the spot has gotten dramatically worse, but it is just an illusion. By "beating" the grating image, which has a certain nominal period, against an ideal linear metrology grating with the same period, the moiré contours reveal solely phase nonlinearities in the image. However, changing one of the incident angles by θ_{err} induces a fringe-tilt-related period shift (Appendix B). The resulting moiré contours are contaminated with some linear phase as well, i.e., phase due to the slight difference in period between the grating image and the metrology

grating (Sec. 5.2.1). Aside, the pure antisymmetrical angle variations also introduce a period shift, but it is of second-order and can be ignored [Eq. (B.2) in Appendix B]. In Figure 5-16, this can be suggestively identified by the positive contour values to the right of the origin, itself always remaining at zero phase by construction, and the negative ones to the left. One can see this linear phase most clearly in a simulation where all parameters but one angle are set to base values, so that the nonlinear phase in the grating image is at minimum (Fig. 5-17). Also, If one were to modify the metrology grating period and subtract out the linear component, one would regain Figure 5-15. In practice, the metrology grating can not be modified and the angle alignment errors do exist, how can one conclude the value for the pure nonlinear phase distortions by staring at an output such as Figure 5-16? Here is a "trick". First, figure out the value at the center of the phase contours, -2.12 nm in Figure 5-16. Then travel outwards and find the line whose shape corresponds to the $1/e^2$ beam spot size, ~ 0.68 nm in the current case. The difference between these two values yields the pure nonlinear phase across the spot—approximately 2.8 nm which again is in agreement with Figures 5-13 and 5-15. To appreciate the physics behind, all one has to realize is that the nonlinear phase is built into the circular shape of the contours. Whatever linear contamination there is only adds a DC offset, and shifts the center of the contours.

A long discussion it may have been, the conclusion is simple: Angle variations do not pose a problem to SBIL wavefront metrology.

The $1/e^2$ beam spot outlined in all moiré phase maps thus far serves as an indicator only. Could the asymmetry in the optical layout, under the worst case, produce two spots on the substrate that are substantially different in size? Fortunately, the answer is no. Under a worst-case scenario, the mismatch in spot size is only about six parts per thousand. For a spot radius of 0.7 mm, the mismatch translates into roughly 4 μm. Finally, it should be pointed out that these heavily tilted beams, by as much as 250 μrad, will never be used to write gratings. The metrology grating mode is used to conduct wavefront metrology and to adjust the collimating lenses so that minimum phase nonlinearity occurs at the substrate. Once the lenses are properly adjusted and the minimum distortion achieved, the beams must be realigned to the rectangular beamsplitter before writing can proceed.

5.2.9 Observation of the moiré pattern (I)

In his PhD thesis [23], Ferrera briefly discussed the traditional interference lithography (IL) system used as a holographic interferometer. He stated the equivalence between the interferogram recorded at the CCD, which reflects the difference in phase

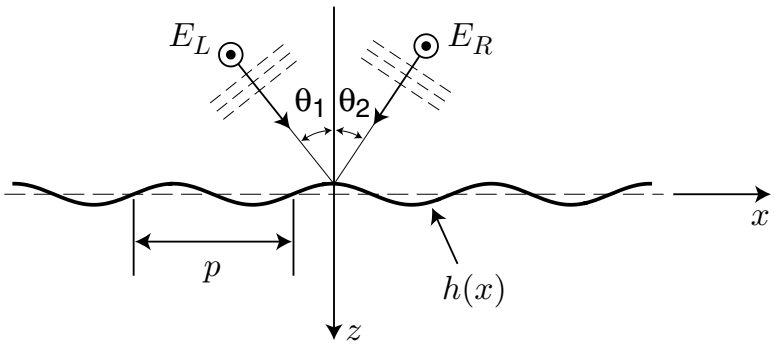

Figure 5-18: Light diffraction off a shallow sinusoidal reflection grating.

between the reflected and back-diffracted beams, and the substrate-plane moiré pattern, which arises from a phase difference between the metrology grating and the image grating. The same argument applies to the SBIL system, with the only difference being that SBIL employs small collimated Gaussian beams instead of IL's largely expanded spherical waves.

An alternative method to establish the equivalence, which does not rely on any reference to holography, is to model the interference of the reflected and back-diffracted beams, calculate the phase of the interferogram directly and compare it to the moiré phase. This approach of course requires detailed knowledge of both the reflected and back-diffracted beams. A rigorous analytical model is impossible to achieve because of some daunting difficulties: The beams, both of which are Gaussian in nature, diffract off a gold-plated metrology grating, which is not a perfect conductor and whose profile, despite its periodicity, is unknown. A numerical model is outside the scope of this thesis, and in any case, is only of limited value. I finally settled for a simplified analytical model, which shows suggestively the equivalence between the recorded interferogram and the substrate-plane moiré pattern. While not a rigorous proof, it is mathematically straightforward and conceptually easy to understand.

I start with three assumptions: (1) The metrology grating has a linear phase and has a shallow sinusoidal corrugation. (2) The grating is a perfect conductor, which enables an easy boundary condition of zero tangential electric field on the surface of the grating. (3) The incident, reflected and back-diffracted beams are all plane waves. The last assumption is perhaps controversial because if the waves are planar, there will not be any image phase nonlinearity to speak of. To that, my reply again is: With this analysis, I am only after a simple explanation, half-quantitative and half-qualitative. Once the equivalence is established for the easy case of plane waves, going to Gaussian beams just entails more complex mathematics and modeling.

Figure 5-18 shows a schematic of the grating surface, which can be defined math-

ematically by the function

$$h(x) = h_0 \cos \frac{2\pi}{p} x \quad \left(\frac{h_0}{p} \ll 1 \right) \quad . \tag{5.46}$$

By assumption, the amplitude h_0 of the sinusoidal grating is much smaller than its period p. Also shown are the incident electric fields E_L and E_R with angles of incidence θ_1 and θ_2, respectively. The solution of plane-wave diffraction off a shallow perfectly-reflecting sinusoidal grating has been studied elsewhere [58]. I quote the expressions for the reflected and back-diffracted fields here, modifying them slightly to describe SBIL wavefront metrology.

Given the coordinates defined in Figure 5-18, the reflected beam from the left arm is

$$E_{\text{refl}} = -E_{L0} \exp(-jk_{Lx}x) \exp(jk_{Lz}z) \quad , \tag{5.47}$$

where E_{L0} is some constant; k_{Lx} and k_{Lz} are the x and z components of the wave vector k_L describing the reflected beam: $k_{Lx} = k \sin\theta_1$, $k_{Lz} = k \cos\theta_1$. The -1-order back-diffracted beam from the right arm is

$$E_{\text{diff}} = R_{-1} \exp(jk_{Rx}x) \exp\left(-j\frac{2\pi}{p}x\right) \exp\left(jk_{Rz}^{(-1)}z\right) \quad , \tag{5.48}$$

where the amplitude R_{-1} is a constant and is related to the amplitude of the 0-order reflection E_{R0} by

$$R_{-1} = jk_{Rz}h_0E_{R0} \quad . \tag{5.49}$$

The quantity $k_{Rx} = k \sin\theta_2$ is the x component of the reflected wave vector, and $k_{Rz}^{(-1)} = k \cos\theta_{-1}$ is the z component of the back-diffracted wave vector. The angle θ_{-1} labels the direction of the back-diffracted beam. Grating diffraction in the -1 order gives rise to the phase $e^{-j2\pi x/p}$. The x component of the back-diffracted wave vector is given by

$$k_{Rx}^{(-1)} = k \sin\theta_{-1} = \frac{2\pi}{p} - k_{Rx} \quad . \tag{5.50}$$

All k_{**}'s are positive. Their signs have been embedded in the exponential phase factors. Interestingly, the assumption of a shallow sinusoidal grating means that diffracted orders beyond ± 1 are all suppressed, i.e., they vanish.

The interference of the reflected and back-diffracted beams leads to an intensity distribution

$$I = |E_{\text{refl}} + E_{\text{diff}}|^2 \quad . \tag{5.51}$$

If the beams are well aligned so as to coincide, one has $k_{Lz} = k_{Rz}^{(-1)}$, i.e., $\theta_1 = \theta_{-1}$. The phase of the interference is defined by the interaction between the fields E_{refl} and

E_{diff},

$$\phi(x) = (k_{Lx} + k_{Rx})x - \frac{2\pi}{p}x = k(\sin\theta_1 + \sin\theta_2)x - \frac{2\pi}{p}x \quad . \tag{5.52}$$

With $k = 2\pi/\lambda$, Eq. (5.52) can be rewritten in a more suggestive form

$$\phi(x) = 2\pi \frac{x}{\dfrac{\lambda}{\sin\theta_1 + \sin\theta_2}} - 2\pi \frac{x}{p} \quad . \tag{5.53}$$

The first term is simply the linear phase of the grating image due to the interference of two plane waves. For SBIL, this term would be replaced by the more complex 2D phase expressing the interference of two Gaussian beams. The second term corresponds to the phase of the linear metrology grating. In other words, the reflected and back-diffracted beams interfere, giving rise to a pattern characterized by the difference in phase between the grating image and the metrology grating, which is equivalent to the substrate-plane moiré pattern. Note how the metrology grating phase finds its way into Eq. (5.53). It arises only because the -1-order back-diffracted beam is used. Any other order would not have worked.

I made the shallow-sinusoidal-grating assumption to demonstrate a concrete example. The assumption is in fact unnecessary. The use of gratings with other types of profiles modifies the diffraction efficiency (i.e., the amplitudes E_{L0} and R_{-1} may change) and in general, may lead to other orders of diffraction. However, changing grating profiles will not modify the phases of E_{refl} and E_{diff}. Eq. (5.53) remains unchanged.

5.2.10 Observation of the moiré pattern (II)

There are a couple of issues that I did not consider in the last section. First, the back-diffracted and the reflected beams can be minutely misaligned, i.e., $\theta_{-1} \neq \theta_1$. Recall that the SBIL beam alignment system can only equalize the mean beam angles to within a few microradians. Secondly, observation of the moiré fringes takes place at a CCD camera. Detector orientation must be taken into account.

Intuition says that if the angles were misaligned, a linear phase component would be introduced into the observed moiré phase. This would generate a shift and a DC offset in the phase nonlinearity. The CCD orientation to the beams gives rise to a scale factor that will compress the x-axis distortions calculated earlier. For instance, if the beams fall normal to the detector, the elongation in phase contours along x seen in Figure 5-15 will be eliminated. Contours that appear elliptical before will come out as circles. I now verify these intuitions mathematically.

Figure 5-19 illustrates the coordinate setup of the problem. The distance from the CCD coordinate frame ($x'O'z'$) to the grating coordinate frame (xOz) is d. The

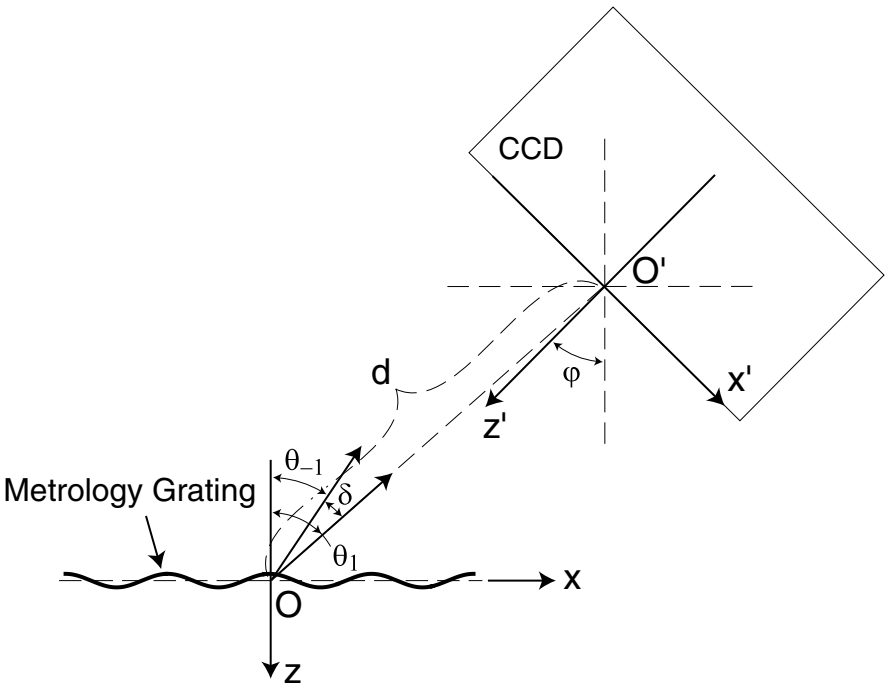

Figure 5-19: Observation of the moiré fringes. Coordinate setup.

angles of the reflected and the back-diffracted beams are θ_1 and θ_{-1}, respectively. Without loss of generality, I have chosen θ_1 greater than θ_{-1} by an amount δ. The rotation angle between the two coordinate frames is φ. Not shown are the mirrors used to redirect the beams. One can think of d as the mirror-unfolded beam path. For simplicity, I have ignored the alignment and orientation issues along y. Compared to those along x, they are quite negligible and can be treated in a similar fashion if necessary.

Eq. (5.54) presents the coordinate transformations,

$$\begin{pmatrix} x \\ z \end{pmatrix} = \begin{bmatrix} \cos\varphi & -\sin\varphi \\ \sin\varphi & \cos\varphi \end{bmatrix} \begin{pmatrix} x' \\ z' \end{pmatrix} + \begin{pmatrix} d\sin\theta_1 \\ -d\cos\theta_1 \end{pmatrix} \quad . \tag{5.54}$$

With notations already introduced in Section 5.2.9 and taking in account the beam misalignment, one can rewrite Eq. (5.52) in terms of x' at the face of the CCD where $z' = 0$,

$$\phi(x') = \left[\frac{2\pi}{\lambda}(\sin\theta_1 + \sin\theta_2) - \frac{2\pi}{p}\right]\cos\varphi\ x' + \left[\frac{2\pi}{\lambda}(\cos\theta_{-1} - \cos\theta_1)\right]\sin\varphi\ x' + \varphi_0 \quad , \tag{5.55}$$

where φ_0 is a constant given by

$$\varphi_0 = \left[\frac{2\pi}{\lambda}(\sin\theta_1 + \sin\theta_2) - \frac{2\pi}{p}\right] d\sin\theta_1 - \left[\frac{2\pi}{\lambda}(\cos\theta_{-1} - \cos\theta_1)\right] d\cos\theta_1 \quad . \tag{5.56}$$

The first term in Eq. (5.55) is the same moiré phase derived in the last section, the only difference being the presence of a scale factor $\cos\varphi$. Mathematically, it arises from the coordinate transformation, and is due physically to the camera orientation. If $\theta_{-1} \neq \theta_1$, the second term is nonzero. Small angle expansion about δ leads to

$$\cos\theta_{-1} - \cos\theta_1 = \cos(\theta_1 - \delta) - \cos\theta_1 \approx \sin\theta_1\,\delta \quad . \tag{5.57}$$

Physically, the term describes the linear fringes that appear when the two beams are misaligned. The period p_{lin} of the fringes is given by

$$p_{\text{lin}} = \frac{\lambda}{\delta \sin\theta_1 \sin\varphi} \quad . \tag{5.58}$$

For $\lambda = 351.1$ nm, $\delta = 6$ μrad, $\theta_1 = \varphi = 26°$, the period is $p_{\text{lin}} = 304.5$ mm, which is very large, not unexpected since the misalignment is so small.

Figure 5-20(a) presents what the substrate-plane moiré phase map already simulated in Figure 5-15 may look like at the CCD if there is no angle misalignment between the reflected and back-diffracted beams ($\delta = 0$). The beams are by assumption normal to the CCD. The previously elliptical phase contours are now circular due to scaling.

Figure 5-20(b) shows the map when a misalignment of $\delta = 6$ μrad exists. A linear phase—the second term in Eq. (5.55)—is introduced. It merely makes the circular contours shift to the left and adds a DC offset, -0.11 nm in this case. It does not impact the moiré phase measurement in any sense. For instance, if with perfect beam alignment, the observed nonlinear distortions across the $1/e^2$ intensity points is 5.63 nm. It will remain 5.63 nm after a misalignment of 6 μrad.

In the past two sections, I have argued both qualitatively and quantitatively that the moiré phase map observed at the camera duplicates that at the substrate plane faithfully.

5.2.11 The use of collimating optics

The use of collimating optics in SBIL is a matter of choice, not absolute necessity, as I shall explain in this section.

Figure 5-21 is a semi-log plot of the inverse radius of curvature of a Gaussian wavefront $(1/R)$ [Eq. (5.8)] as a function of the propagation distance (z). Plot coordinates are normalized to the beam's Rayleigh range (b) [Eq. (5.11)]. Planar wavefront corresponds to zero inverse radius of curvature. To produce a good linear grating image, one can operate under two distinct regions: interfere near the beam waist ($z = 0$) or at the "far field" ($z \to \infty$). The border separating the two is the Rayleigh range ($z = b$), where the wavefront is the most curved.

The fact that the wavefront becomes increasingly planar the further one gets

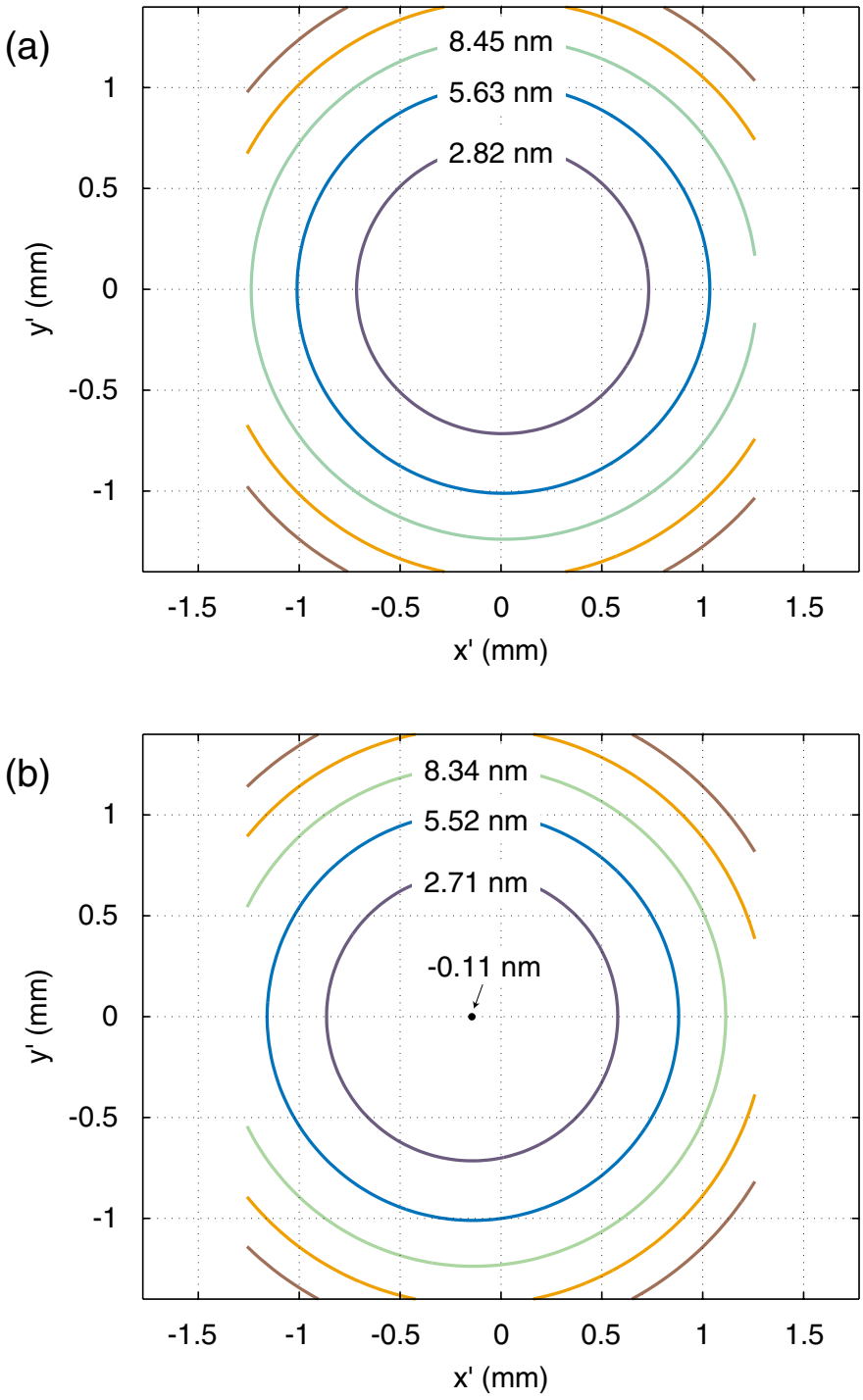

Figure 5-20: Moiré phase maps observed at the CCD. (a) When the system is used under the same condition that leads to Figure 5-15. (b) Under the same condition but with 6 μrad angle misalignment between the reflected and back-diffracted beams.

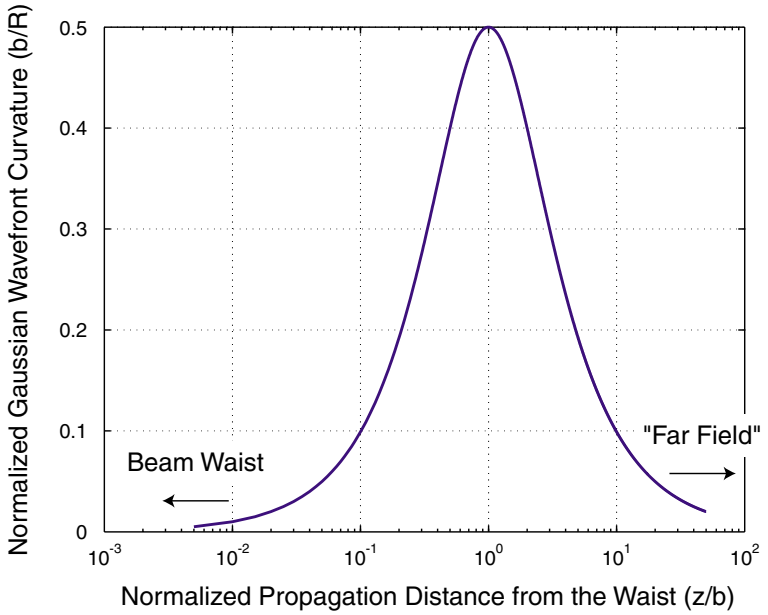

Figure 5-21: The inverse radius of curvature of a Gaussian wavefront as a function of the propagation distance.

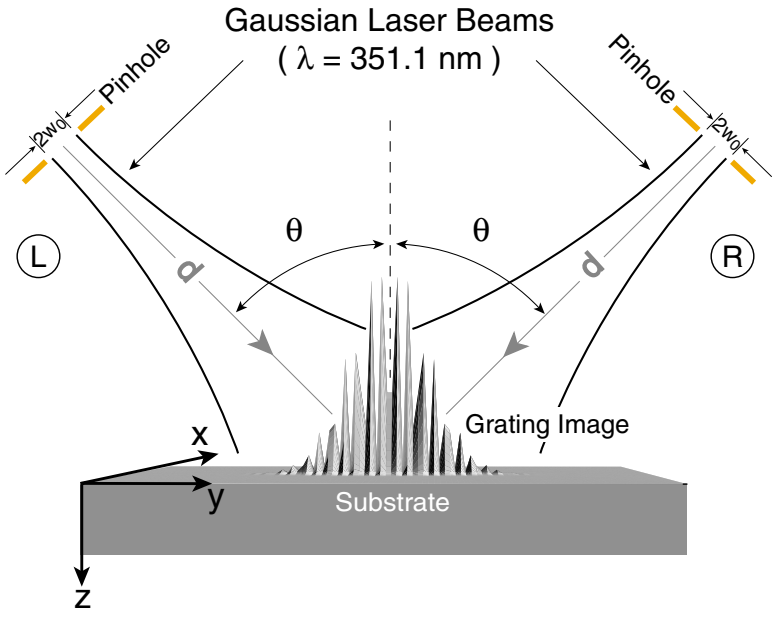

Figure 5-22: Geometric layout for Gaussian beam interference in the far field. The focused beam waist radius at the pinhole is w_0. The propagation distance from the waist to the substrate is d. Schematic only.

Interference at	Pros	Cons
Beam waist	Easy packaging Shorter optical column Easy to adjust waist location Allow aggressive spatial filtering	Lens aberrations Sensitivity to lens position
Far field	No collimating lens Good wavefront fidelity	Difficult packaging Longer optical column Limited spatial filtering

Table 5.3: Pros and cons of two different Gaussian beam interference setups.

away from the waist is not surprising. In traditional IL for instance (Sec. 1.4.1), the recorded grating nonlinearity decreases as the distance to the pinholes increases, because of reduced spherical wavefront curvature. The concern is not whether one can attain a sufficiently planar wavefront in the far field, but whether one can do that while keeping the beam diameter small. I have studied the problem in detail in my Master's thesis [45]. Figure 5-22 shows two Gaussian beams interfering at the far field. Figure 5-23(a) is a plot of the simulated maximum grating image phase discrepancy from an ideal linear grating as a function of the waist-to-substrate distance. The simulation is done for a nominal grating image period of 200 nm and $1/e^2$ diameter of 2 mm. Figure 5-23(b) is a corresponding plot of the initial beam waist radius as a function of the propagation distance. At a distance of 80 cm for example, the maximum phase nonlinearity inside a 2 mm-diam. grating image is less than 1 nm. The image size at the substrate is directly linked to the initial beam waist diameter. To produce a 2 mm-diam. grating image, one needs an initial beam waist radius of around 63 μm.

The simulation is a convincing proof that without the aid of collimating optics, two Gaussian beams can interfere at the far field and produce a proper sized grating image with subnanometer nonlinear phase. Table 5.3 lists the pros and cons of the different setups. Mainly because of optics packaging and spatial-filtering reasons, I chose to collimate the beams and interfere them at the waists. The real estate on the SBIL optical bench is extremely tight, as is clear from Figures 2-5–2-8. If one were to do a far-field interference, some 50 cm of extra beam path in each arm would be very difficult to allocate. Interfering at the waists also ensures that the beams can be more aggressively filtered. It is observed that the quality of the beams after the acousto-optic modulators (AOMs) is poor. Spatial-filtering is required to remove significant beam defects. While filtering is possible for far-field interference, because the size of the focused beam waist also sets the grating image size at the substrate,

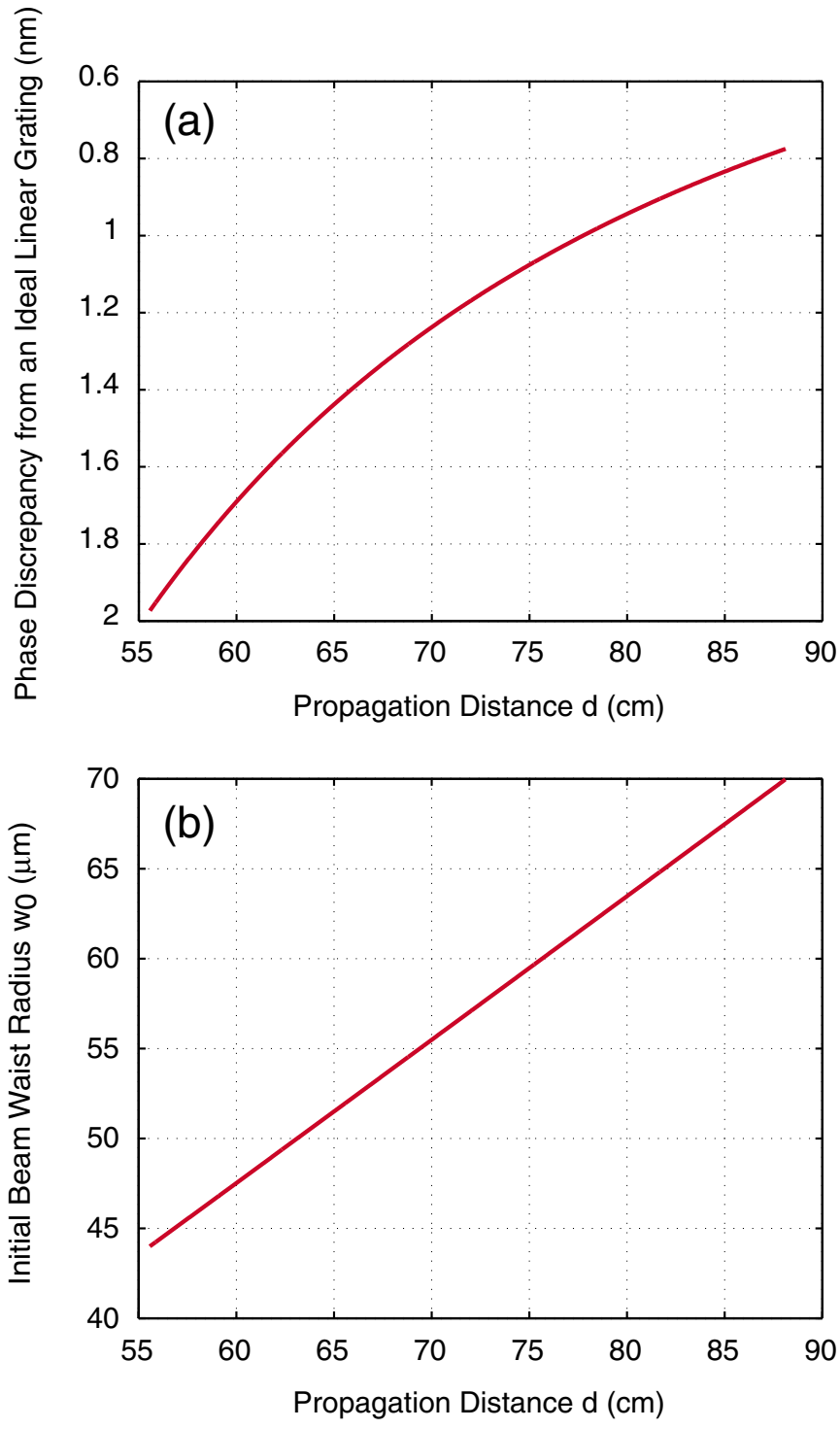

Figure 5-23: (a) The maximum grating image phase discrepancy from an ideal linear grating as a function of the waist-to-substrate distance d. The wavelength of the laser is 351.1 nm. The nominal grating period is 200 nm. The $1/e^2$ grating image diameter is 2 mm. (b) The corresponding initial beam waist radius w_0 as a function of the waist-to-substrate distance. See Figure 5-22 for parameter definitions.

filtering cannot be too aggressive. For instance, the far-field example considered in Figure 5-23 requires pinholes of approximately 125 μm in diameter, v.s. 50 μm in the current setup that uses collimating optics.

Gaussian beam collimation and interference deviate in many respects from classical ray optics. One must understand these differences before a correct physical intuition can be established.

5.2.12 The metrology grating

I have assumed throughout the section that the metrology grating is a perfect linear grating. In practice, such gratings do not exist, which is why the SBIL tool is being invented in the first place. The experimental results that I will show shortly in Section 5.5 are obtained using a grating made by traditional IL. Even if produced with perfectly aligned beams and spherical wavefront radii as large as 1 m, the so-called "sweet spot" for an IL grating—the region with less than 1 nm of nonlinear phase distortion, is less than 2.8 mm in diameter [Fig. 1-7(b)]. In reality, IL's incredible sensitivity to beam alignment introduces additional phase distortions.

In an ideal world, theory says that the nonlinear phase component in the grating image can be minimized to around 3 nm easily. In the everyday world, the lack of a good metrology grating and the presence of imperfect collimating optics make it difficult to observe distortions on the few nanometer level. I will elaborate more on this when I present the experimental results in Section 5.5.

It is questionable whether or not IL can ever be used to generate the metrology grating, because of its small sweet spot and extreme alignment sensitivity (Sec. 1.4.1). One may be able to pattern the grating with SBIL itself, by overlapping many scans tightly, effectively averaging out the grating image distortions. Details on overlapping scans to rid phase nonlinearity will be discussed in Section 5.6.

In addition to lithography-related phase errors, process-induced errors exist as well. Resist development, plating, particles may all impact the phase accuracy of the metrology grating. Process-induced errors are outside the scope of this thesis.

5.2.13 Summary

I have developed a Gaussian beam interference model specifically for the description of SBIL wavefront metrology. By simulating the moiré patterns produced by the "beating" of the grating image against the underlying metrology grating, I was able to study how various optical parameters determine the nonlinear phase distortions in the grating image. Provided that certain extremely lenient optics-placement tolerances are met, the single most critical parameter that sets the magnitude of the nonlinear phase is the relative offset between the two collimating lenses, i.e., the difference in

distances from the two lenses to their respective pinholes. To incur a distortion of 3 nm, the offset must be controlled to around 80 μm.

In practice, once the SBIL optics have been laid out according to design, one only needs to optimize the collimating-lens-pinhole distances in order to achieve nanometer-level phase nonlinearities.

5.3 Phase shifting interferometry

During SBIL wavefront metrology, a technique known as phase shifting interferometry (PSI) is used to map the moiré phase experimentally. In this section, I introduce the basic concept behind PSI, point out its many advantages over traditional single-interferogram analysis, and discuss the algorithm currently in use by the wavefront metrology system.

5.3.1 PSI vs. single-interferogram analysis

The so-called single-interferogram analysis precedes the arrival of PSI. The analysis starts by recording a static interferogram and proceeds to locate the centers of the fringes. Two fringes that are next to each other represent a surface height difference of $\lambda/2$, where λ is the wavelength of the laser in use. Single-interferogram analysis has several major drawbacks: (1) A trade-off between precision and sampling exists. Data is collected only along the fringe centers. For the best fringe-centering precision, the interferogram should contain only a few widely separated fringes, which limits the number of sampled data points. On the other hand, although a dense fringe pattern increases the sampling, it decreases the fringe-centering precision. (2) While filtering can remove the spurious phase extrema caused by high-frequency noise, low spatial-frequency phase ambiguities may still exist, because the wavefront phase may contain some local extrema. To rid the ambiguities, a wavefront tilt, i.e., a spatial-carrier frequency is usually introduced to guarantee a monotonic phase. (3) In single-interferogram analysis, intensity variations across the interferogram, spatial sensitivity variations and fixed pattern noise of the detector may all induce unwanted shifts in fringe locations. (4) The polarity of the part under test—concave or convex—can not be determined from a single interferogram. A further piece of information is required, for instance, the direction of the fringe movement when the reference object is pushed.

The concept of PSI has been well established since the 1960s [79, 80, 81, 82], but it was not until the emergence of good-quality CCDs and powerful PCs in the 1980s that the technique became really popular. As is common to all interferometric metrology techniques, two fields are made to interfere during PSI. One of them, carrying information from the part under test, is known as the test field. The other,

serving as a phase reference, is known as the reference field. In general, the test and the reference fields can be written, respectively, as

$$E_t(x,y) = A_t(x,y)\,\exp\{-j\phi_t(x,y)\} \quad , \tag{5.59}$$

$$E_r(x,y,t) = A_r(x,y)\,\exp\{-j[\phi_r(x,y) - \delta(t)]\} \quad , \tag{5.60}$$

where the coordinates x and y define the detector plane, $A_t(x,y)$ and $A_r(x,y)$ are the field amplitudes, $\phi_t(x,y)$ and $\phi_r(x,y)$ are the phases, and $\delta(t)$ is a time-dependent phase shift. The resulting irradiance or intensity at the detector (up to a proportionality constant) is

$$I(x,y,t) = |E_t(x,y) + E_r(x,y,t)|^2 \quad , \tag{5.61}$$

or

$$I(x,y,t) = I_a(x,y) + I_b(x,y)\,\cos[\phi(x,y) + \delta(t)] \quad , \tag{5.62}$$

where $I_a(x,y) = A_t(x,y)^2 + A_r(x,y)^2$ is an intensity bias, $I_b(x,y) = 2A_t(x,y)A_r(x,y)$ is the amplitude of the intensity modulation, and $\phi(x,y) = \phi_t(x,y) - \phi_r(x,y)$ represents the difference in phase between the test and the reference wavefronts. Eq. (5.62) is the governing equation for PSI. By analyzing the irradiance point by point over a series of interferograms (three and up) as $\delta(t)$ is varied, PSI obtains the phase $\phi(x,y)$.

To understand the principle of PSI and to appreciate its many advantages over the traditional single-interferogram analysis, it is perhaps best to look over a simple example. In a four-step PSI algorithm, four interferograms are collected when the phase is stepped by $\delta = 0$, $\pi/2$, π, and $3\pi/2$. From Eq. (5.62), one can calculate the irradiance at each phase step:

$$I_1 = I_a + I_b\,\cos\phi = I_a + I_b\,\cos\phi \quad , \tag{5.63}$$

$$I_2 = I_a + I_b\,\cos\left(\phi + \frac{\pi}{2}\right) = I_a - I_b\,\sin\phi \quad , \tag{5.64}$$

$$I_3 = I_a + I_b\,\cos(\phi + \pi) = I_a - I_b\,\cos\phi \quad , \tag{5.65}$$

$$I_4 = I_a + I_b\,\cos\left(\phi + \frac{3\pi}{2}\right) = I_a + I_b\,\sin\phi \quad . \tag{5.66}$$

The phase $\phi(x,y)$ can be analytically extracted from Eqs. (5.63)–(5.66) as

$$\phi(x,y) = \tan^{-1}\left[\frac{I_4(x,y) - I_2(x,y)}{I_1(x,y) - I_3(x,y)}\right] \quad . \tag{5.67}$$

Point by point, $\phi(x,y)$ is calculated by first performing the appropriate intensity subtractions in both the numerator and the denominator, and then performing the division. Subtractions remove the bias I_a and the division rids the modulation term

I_b. These operations ensure that in general, PSI is immune to intensity variations across the beam, fixed pattern noise and spatial sensitivity variations of the detector. Since the method does not depend on tracing fringes and locating fringe centers, it can be used to analyze any fringe patterns, including those with closed contours. Sampling is no longer restricted to fringe centers but across the entire interferogram. Furthermore, in contrast to single-interferogram analysis, PSI does not require the introduction of a spatial-carrier frequency. The polarity of the part under test is unambiguously determined because the phase is varied in a known manner. PSI can achieve phase measurement repeatability of one-hundredth of a wavelength, which is demonstrated by the results from SBIL wavefront metrology (Sec. 5.5.2). With further care, repeatability on the order of one-thousandth of a wave can be achieved.

Since PSI data collection is a serial process, temporal noise added during the measurement interval may degrade the system performance. Mathematically, Eq. (5.62) assumes that the phase shift $\delta(t)$ is the only time-dependent term. Any deviation from this assumption can result in errors. Signal-to-noise considerations also limit the performance. The most common PSI error sources include:

- Phase shift errors, i.e., incorrect phase step between data frames;
- Errors due to mechanical vibrations and air turbulence;
- Stray reflections and other coherent effects;
- Interferometer source instability, i.e., frequency instability of the laser;
- Source intensity fluctuations;
- Detector nonlinearities;
- Quantization errors, i.e., errors occurring during digitization.

Readers can find detailed discussions of the above error categories in works by Creath [83] and Greivenkamp and Bruning [84].

5.3.2 Phase unwrapping

The wavefront phase ϕ is calculated from an inverse tangent [Eq. (5.67)], which has an output range of $[-\pi, +\pi]$. (Ordinarily, the inverse tangent has a range from $-\pi/2$ to $+\pi/2$. However, in PSI, the range is doubled because one knows which quadrant ϕ lies in.) If ϕ extends over 2π, phase discontinuities exist in the raw data and must be removed by performing a wavefront reconstruction process, the so-called phase unwrapping. By itself, phase unwrapping can be the subject of a PhD thesis. Interested readers are referred to an introduction of the topic by Robinson [85].

Fortunately, phase unwrapping is not required for SBIL wavefront metrology. When the system is turned on for the first time, the observed moiré phase is al-

ready well within 2π radians (Sec. 5.5.2), thanks to the fact that the optics have been carefully laid out according to design (Ch. 2).

5.3.3 The Hariharan five-step algorithm

During SBIL wavefront metrology, the interferogram recorded by the CCD camera is, according to Section 5.2.9, a direct representation of the substrate-plane moiré pattern, which compares the grating-image phase to the phase of a reference metrology grating. In Figure 5-1(a), the back-diffracted beam can be thought of as the reference beam, since it incorporates the phase of the metrology grating [Eq. (5.48)]. The reflected beam is the test beam. Whether the phase shifting is commanded in the reference arm or the test arm is immaterial. SBIL wavefront metrology uses an acousto-optic modulator—AOM2 in Figure 2-8—to generate the necessary phase steps in the reflected beam. Presently, the Hariharan five-step phase-shifting algorithm is used [86], the mathematical formalism of which is discussed in this section. The algorithm is chosen for its robustness and simplicity.

The five-step algorithm is quite similar to the four-step algorithm discussed in Section 5.3.1, differing only in the sense that a fifth data frame, at $\delta = 2\pi$ is added. To a novice, adding this fifth interferogram may seem strange for it serves no apparent purpose—nominally, it contains the same information as the first interferogram, obtained at $\delta = 0$. However, as I shall point out shortly, the addition makes the algorithm much more error-tolerant than its four-step cousin.

First, I consider a generalized form of the five-step algorithm, in which, the relative phase step between two adjacent interferograms is α radians; α may or may not be $\pi/2$. The intensity at each step $\delta = [-2\alpha,\ -\alpha,\ 0,\ \alpha,\ 2\alpha]$ can be calculated from Eq. (5.62), respectively:

$$I_1 = I_a + I_b\,\cos(\phi - 2\alpha) = I_a + I_b\,(\cos\phi\,\cos 2\alpha + \sin\phi\,\sin 2\alpha)\ , \tag{5.68}$$

$$I_2 = I_a + I_b\,\cos(\phi - \alpha) = I_a + I_b\,(\cos\phi\,\cos\alpha + \sin\phi\,\sin\alpha)\ , \tag{5.69}$$

$$I_3 = I_a + I_b\,\cos\phi = I_a + I_b\,\cos\phi\ , \tag{5.70}$$

$$I_4 = I_a + I_b\,\cos(\phi + \alpha) = I_a + I_b\,(\cos\phi\,\cos\alpha - \sin\phi\,\sin\alpha)\ , \tag{5.71}$$

$$I_5 = I_a + I_b\,\cos(\phi + 2\alpha) = I_a + I_b\,(\cos\phi\,\cos 2\alpha - \sin\phi\,\sin 2\alpha)\ . \tag{5.72}$$

The phase map ϕ can be extracted from the above five intensity patterns I_1 through I_5,

$$\frac{\tan\phi(x,y)}{2\,\sin\alpha} = \frac{I_4 - I_2}{I_1 - 2I_3 + I_5}\ , \tag{5.73}$$

where intensities' dependence on (x,y) is implied. After differentiating Eq. (5.73) and minimizing the derivative with respect to α, one finds that when $\alpha = \pi/2$, ϕ is the

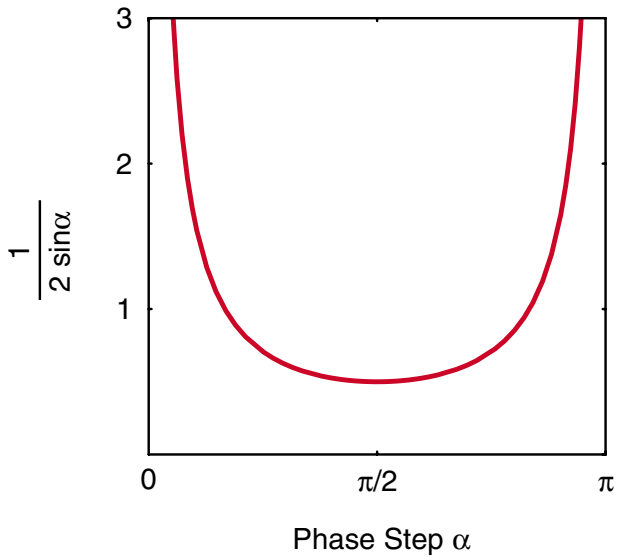

Figure 5-24: Phase insensitivity as a function of the phase step. Least sensitivity occurs at a phase step of $\pi/2$.

least sensitive to errors in α. Therefore, the optimal phase steps are

$$\delta = \left[0, \ \frac{\pi}{2}, \ \pi, \ \frac{3\pi}{2}, \ 2\pi\right] \quad . \tag{5.74}$$

The first and last interferograms are nominally the same. For $\alpha = \pi/2$, Eq. (5.73) reduces to

$$\phi(x,y) = \tan^{-1}\left[\frac{2\left(I_4 - I_2\right)}{I_1 - 2I_3 + I_5}\right] \quad . \tag{5.75}$$

Eq. (5.75) is used to calculate the observed moiré phase map, and is the key to doing SBIL wavefront metrology.

Furthermore, a data modulation function can also be evaluated from the series of interferograms:

$$\gamma(x,y) \equiv \frac{I_b}{I_a} = \frac{3\sqrt{4\left(I_4 - I_2\right)^2 + \left(I_1 - 2I_3 + I_5\right)^2}}{2\left(I_1 + I_2 + 2I_3 + I_4 + I_5\right)} \quad . \tag{5.76}$$

By definition, the function is the division of the intensity modulation term I_b by the bias term I_a, with I_b and I_a defined in Eq. (5.62). The function is useful for establishing the validity of the collected data—a γ-value near one means that the phase data is valid, whereas a value below a certain threshold indicates that the signal-to-noise is bad and the calculated phase is unreliable at that particular (x,y) location. A threshold of 5-10% is normal. Data below the threshold is ignored. As I will show in Section 5.5, I consistently achieve a γ-value of greater than 50% within the $1/e^2$ intensity diameter. Data with a γ of less than 50% is often masked to enable faster computation.

Figure 5-24 shows a plot of the left-hand-side of Eq. (5.73). For convenience, the numerator, $\tan\phi$, is assumed to be one; values other than one merely changes the vertical scale. A minimum of the function clearly occurs at $\alpha = \pi/2$ and has a broad range, where the phase is insensitive to changes in α. More quantitatively, assume that the phase step between adjacent frames is $\alpha = \pi/2 + \epsilon$ for $\epsilon \ll 1$, i.e., α is slightly "off-target" from the ideal value of $\pi/2$ by a small amount ϵ. One has from Eq. (5.73),

$$\frac{\tan\phi'(x,y)}{2\,\sin\alpha} = \frac{\tan\left[\phi(x,y) + \Delta\phi(x,y)\right]}{2\,\sin(\pi/2+\epsilon)} \quad , \tag{5.77}$$

where ϕ', the phase corresponding to the now off-target α, is related to ϕ, the phase at $\pi/2$, via the relation $\phi' = \phi + \Delta\phi$. The term $\Delta\phi$ is the so-called phase shift error, caused by an error ϵ in phase step. Expanding both the numerator and the denominator and keeping only the leading-order term, one finds

$$\tan\phi' \approx \tan\phi\left(1 + \frac{\epsilon^2}{2}\right) \quad , \tag{5.78}$$

from which, it follows that the dominant phase shift error is quadratic in ϵ,

$$\Delta\phi(x,y) \approx \frac{\epsilon^2}{4}\sin[2\phi(x,y)] \quad . \tag{5.79}$$

A similar analysis can be applied to the four-step PSI algorithm outlined in Section 5.3.1. In that case, the leading-order phase shift error is linear in ϵ,

$$\Delta\phi(x,y) \approx \frac{\epsilon}{2}\cos[2\phi(x,y)] \quad . \tag{5.80}$$

In collecting just one additional interferogram, the five-step algorithm has reduced the uncertainty of the phase recovery due to inaccurate phase stepping to second order. As an example, a 5% error in phase step leads to $\epsilon = 5\% \times \pi/2 = 0.0785$ rad. According to Eq. (5.79), the five-step algorithm yields a peak-to-valley error of $\Delta\phi = 0.0031$ rad, or roughly five-ten-thousandths of a wave. In comparison, the four-step algorithm gives $\Delta\phi = 0.0785$ rad, or only twelve-thousandth of a wave. The five-step algorithm has reduced the phase shift error by 25 times, a significant improvement.

Phase shift error is only one of the many error categories listed at the end of Section 5.3.1 that may impact the PSI measurement accuracy. The five-step algorithm has been shown to outperform the four-step algorithm in other categories as well [87], which is one of the reasons why it has been chosen for SBIL wavefront metrology. The other reason is its simplicity. In theory, the uncertainty in phase recovery may be further reduced by adding additional data frames, i.e., a N-step algorithm where $N > 5$. However, the success of a N-step algorithm hinges on the fact that temporal variations, i.e., random phase noise occurring during the measurement interval

can be minimized. This is done by maximally shortening the data acquisition time. Currently, because of a lack of system automation, the time that it takes to acquire and save five consecutive interferograms is a rather lengthy 20 s. Any benefit gained by having more data frames may be lost to noise added during the additional time required for data acquisition. Until an automated system gets built, more data does not necessarily yield better result—reason why I have chosen to use the simple yet robust Hariharan five-step algorithm.

As I will show in Section 5.5.2, the phase measurement repeatability of the present system is about 0.05 rad, three-sigma, achieved without an environmental enclosure. Normalizing to the period of the metrology grating, which is 401.23 nm, the repeatability is 3.2 nm, three-sigma, or about eight thousandth of a period.

5.3.4 Computer simulation of the interferograms

Having numerically simulated the moiré phase (Sec. 5.2), one can proceed further and simulate the series of interferograms observed at the CCD when the Hariharan five-step algorithm is applied. The MATLAB script for simulating the interferograms, MoiréCCD.m, is included in Appendix G.

5.4 System setup

The goal of SBIL wavefront metrology is to design and implement a system that exploits moiré-based interferometry to accurately locate the Gaussian beam waists at the substrate, so that nonlinear phase component in the grating image can be minimized to the nanometer level. Having described its theoretical foundations in the previous sections, I now describe the metrology system setup.

5.4.1 Optics placement requirements

The spatial filter assemblies together with the collimating lenses are key components among the SBIL wavefront metrology optics. Since they define the interference at the substrate, their placement accuracy must be assured. Based on findings from Section 5.2, Table 5.4 lists the requirements. The value for the distance from the focusing lens to the substrate is taken from Section 2.2.1. The distance from the collimating lens to the pinhole simply corresponds to the lens's focal length. In addition, the left and right interferometer arms, in going from the grating beamsplitter to the focusing lenses, must match in distance to ± 10 mm.

The placement requirements on all four lenses are so lax that the use of a tape measure is sufficient. Once they are in position, to achieve nanometer-level phase distortion, one needs to pay attention to one and only one parameter: the relative offset between the left and right collimating lenses. The distances from the lenses to

Optics	Required placement accuracy
Focusing lenses	Distance to substrate = 544 ± 5 mm
Pinholes	–
Collimating lenses	Distance to pinhole = 108 ± 5 mm
Relative offset between the collimating lenses: $\sim$**80 μm**	
Expected nonlinear phase distortion (worst case estimate): $\sim$**3 nm**	

Table 5.4: Required lens placement accuracy to achieve nanometer-level nonlinear phase distortions.

their respective pinholes must be matched to around 80 μm. With this match, Figure 5-20 shows that in the worst case, the expected nonlinear phase distortion across the grating image only amounts to about 3 nm. Of course, this assumes a perfect linear metrology grating.

For traditional IL, Ferrara has calculated the error budget for setting up the optics [23]. He showed that to achieve a 3 nm phase writing repeatability across a field of 2.5 cm, the pinhole-to-substrate distance must be controlled to within 200 nm, a most difficult proposition. In using collimated Gaussian beams to produce the grating image and shrinking the interference spot to millimeter-diameter, SBIL has relaxed the optics placement requirements significantly. Only a single parameter poses somewhat a challenge—the mismatch in distance between the two collimating lenses, but even it has a generous 80 μm tolerance, compared to the nanometer-level IL requirement.

5.4.2 System layout

During SBIL wavefront metrology, the lithography interferometer is used in the grating mode, whose optical layout is described in Section 2.2.5. Figure 5-25 is a photo of the system, with key components labeled. It should be studied in conjuction with earlier system drawings—Figures 2-6 and 2-8. Three large air ducts connect to thermal housings, which surround the acousto-optic modulators (AOMs). To prevent it from destabilizing refractive indices along critical beam paths, air heated by the AOMs is confined and continuously pumped away from the optical bench. The entire HeNe stage interferometer laser ($\lambda = 633$ nm), by far the largest local heat source (40 W), is also enclosed and air-pumped.

5.4.3 Experimental procedure

Currently, the SBIL system is set up to write gratings with a nominal period of 400 nm. Prior to wavefront metrology, a metrology grating, whose period matches that of the grating image, is placed on the vacuum chuck and used under the Littrow

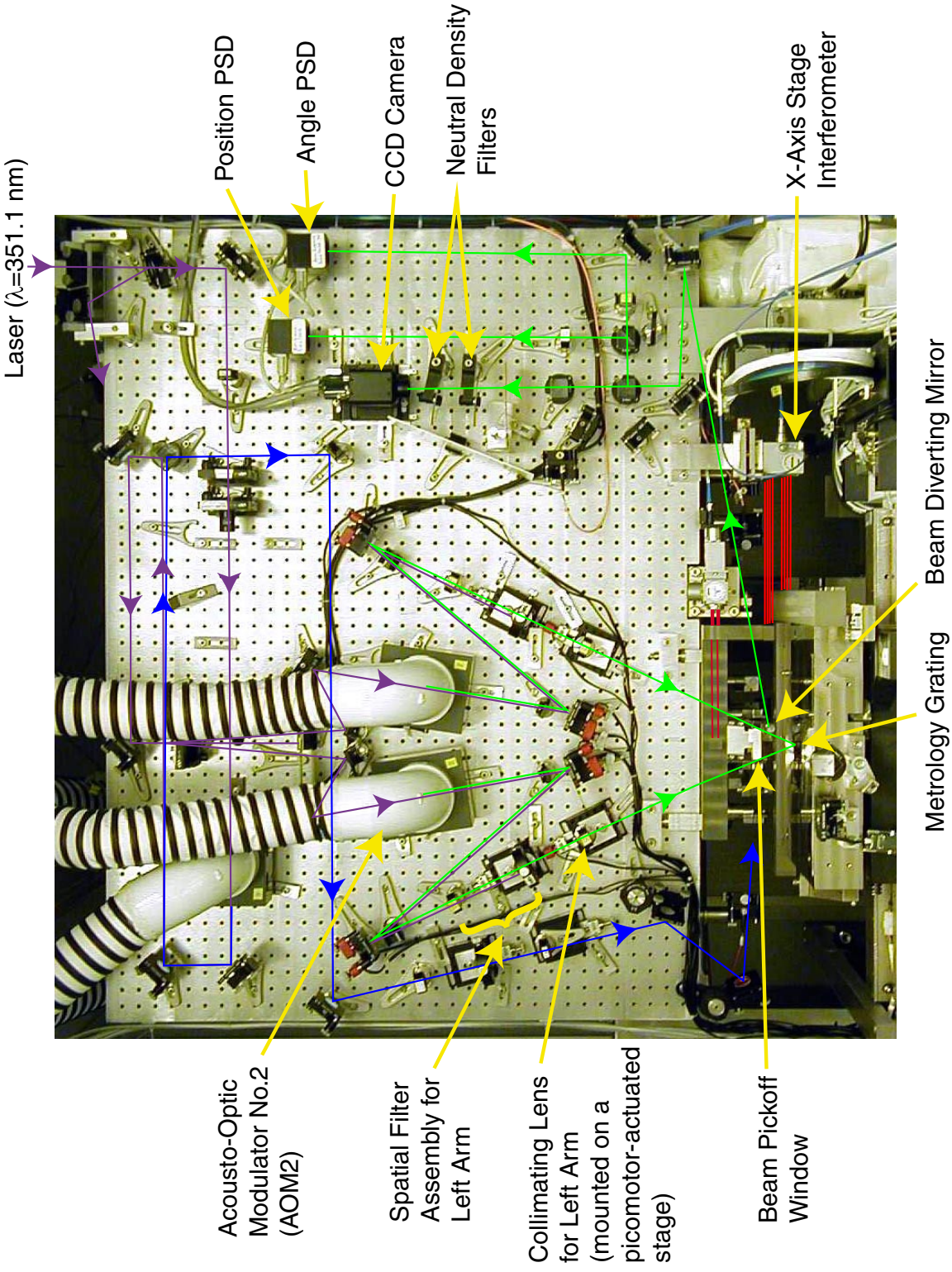

Figure 5-25: Photo of the SBIL wavefront metrology system. Study in conjunction with Figures 1-13, 2-6 and 2-8.

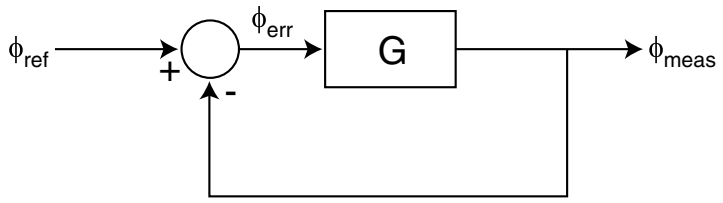

Figure 5-26: Control block diagram for generating phase steps.

condition. The SBIL beam alignment system aligns the reflected beam from the left arm and the back-diffracted beam from the right arm, so that they coincide and propagate to a CCD camera where they interfere. No beam magnification is necessary because of the fine resolution of the CCD.

During wavefront metrology, the grating image is stabilized, i.e., locked to the metrology grating by activating the stage control and the heterodyne fringe locking system. Phase steps are generated in the reflected beam by frequency-shifting AOM2. A simplified control diagram is shown in Figure 5-26. The plant G is a frequency synthesizer that drives AOM2. The measured phase ϕ_{meas} is compared to the reference phase ϕ_{ref}, giving rise to a phase error ϕ_{err}. By commanding a frequency shift $\Delta\nu$, the synthesizer changes the phase of the beam by an amount

$$\Delta\phi = 2\pi\,\Delta\nu\,t \tag{5.81}$$

till ϕ_{meas} and ϕ_{ref} are equal. This phase control loop is an integral part of the heterodyne fringe locking system.

Since camera control and image acquisition are implemented on a separate computer (Fig. 1-16), the five-step PSI sequence is carried out manually at present time. After acquiring an image frame, the operator must manually command the phase step before acquiring the next frame. Lack of automation between phase stepping and image acquisition limits the time for completing a PSI sequence to about 20 s.

5.4.4 Hardware

The CCD camera in use is a progressive scan black/white camera with 10-bit readout electronics, made by Cohu, Inc. (Model 7500). The image sensor is manufactured by Sony Corporation[2]. It has a total of 1296×1030 square pixels, each 6.7 μm $\times$ 6.7 μm in dimension. Sony does not specify the spacing between pixels as it is considered insignificant, particularly with the so-called Microlens technology [88]. This sets the camera's spatial sampling rate at 149.3 pixels/mm for both the horizontal and vertical dimensions. At $\lambda = 351$ nm, the Cohu-supplied estimate on the sensor's signal-to-noise ratio (SNR) is > 50 dB [88], which translates into a dynamic range that is

[2]Part number ICX085AL.

greater than 8 bits, justifying the use of 10-bit readout electronics. The glass window that protects the front of the CCD has been removed to prevent stray reflections.

Whether the CCD sensor would be sensitive enough at UV wavelength was initially a concern. The spectral response curve supplied by Sony does not have any data at 351 nm, but it does indicate a sharp drop in efficiency below 400 nm [89]. Fortunately, this turned out to be a null issue. The proper operation of the SBIL fringe locking system requires a certain minimum beam power, on the order of 1 mW, at the phase-meter fiber pickoffs, part of the phase measurement optics mounted on the Zerodur metrology block (Fig. 5-25). If the SBIL system is used under this minimum power configuration, the beams coming off the metrology grating still carry more than enough power to saturate the CCD, which is the reason why neutral density filters[3] have been installed to further attenuate the beams. Prior to the capture of a five-step sequence, the filters are adjusted such that the interferogram with the highest intensity does not saturate the CCD, i.e., all pixel values fall between 0 and 1023.

The camera is connected via a low voltage differential signaling (LVDS) interface to a National Instruments (NI) IMAQ PCI-1424 frame grabber board. The frame grabber controls the camera settings such as gain, offset and exposure time via a direct RS-232 link. All camera control and image acquisition software is written in LabVIEW.

Two collimating lenses are placed on top of stages that can be adjusted along the direction of the lenses' optic axes (Fig. 5-25). Picomotors are employed as actuators. The metrology grating used for the experiment is a gold-plated grating made by traditional IL. Section 1.4.1 made the point that IL is ill-suited for producing large gratings with extreme linear phase. Even with 1 m spherical-wavefront radii and perfectly aligned beams, Figure 1-7(b) shows that the "sweet spot" with subnanometer phase distortions is less than 2.8 mm in diameter. Moreover, when the alignment is imperfect, phase distortions increase dramatically. Figure 5-27 shows the nonlinear phase contours when the two arms of the IL interferometer are unbalanced in distance by 10 mm, in which case, phase nonlinearity has increased to over 5 nm across the sweet spot. To complicate matters even more, the exact location of the sweet spot is not known a priori.

Presently, the distorted metrology grating and the yet-to-be-automated measurement process conspire to limit the lowest detected nonlinear distortions to around 12 nm. Details of the system performance are discussed in Section 5.5. Section 5.6

[3]Reynard Corporation. Part number R04410-10.

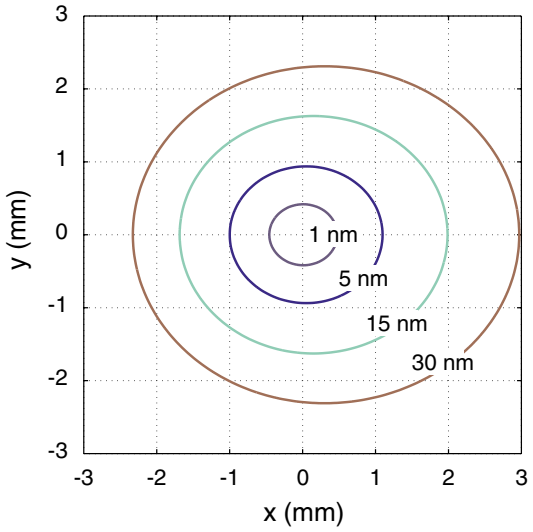

Figure 5-27: Plot of the phase discrepancy between an IL-exposed grating and a perfect linear grating. The nominal grating period is 400 nm. Compared to Figure 1-7(b), the only changed parameters are $d_R = 995$ mm, $d_L = 1005$ mm.

considers the phase errors that will be recorded in the resist, the so-called printed errors.

5.5 Results

Pinhole locations in the following experiments have been optimized by observing the power outputs from the PSDs. The camera is used in its low speed shutter mode, with an exposure time of 83.3 ms. The exposure is relatively long so that high-frequency errors can be averaged out. All phase data has been converted from radians to nanometers by multiplying by the measured metrology grating period of 401.23 nm. The period is obtained by using the lithography interferometer in the grating reading mode (Sec. 2.2.5). All phase maps have been DC-adjusted so that the minimum phase occurs at zero. Experiments are done inside a temperature-regulated cleanroom, but without the SBIL environmental control.

5.5.1 Beam diameter

Figure 5-28(a) shows the intensity pattern of the back-diffracted beam as recorded by the CCD. The beam is somewhat "dirty", which is not unexpected because after the spatial filter, it must traverse quite a few optics before arriving at the camera (Fig. 2-8). Figure 5-28(b) shows a cross section of the data at $y = 0$. The profile of the beam is Gaussian, with a fit showing the $1/e^2$ beam diameter to be approximately 1.92 mm, or 286 pixels. Due to the linear coordinate scales employed in Figure 5-28, the circular fringes around the bright central spot due to pinhole diffraction are not observed.

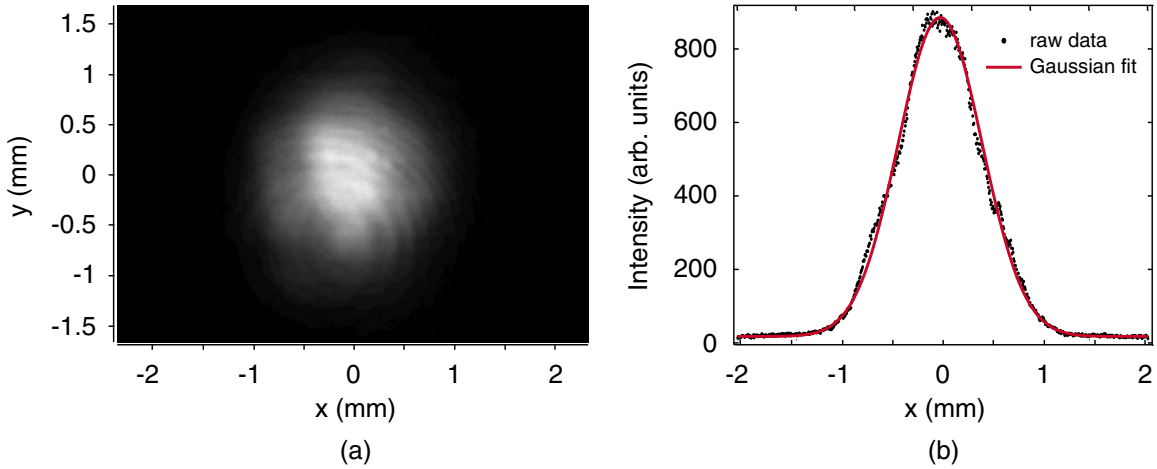

Figure 5-28: (a) Intensity distribution of the back-diffracted beam as recorded by the CCD. (b) Cross section of the intensity data in part (a) at $y = 0$, fitted with a Gaussian function. The fit shows that the $1/e^2$ beam diameter is approximately 1.92 mm, or 286 pixels.

Table 2.4 gives the modeled beam diameter of 1.4 mm at the substrate plane and its Rayleigh range of 4 m. Given the distance of 1.4 m from the wafer to the camera and Eq. (5.12), one can then estimate the beam diameter at the camera to be 1.5 mm, which is close to but different from the observed value. The discrepancy may be due to a couple of reasons: The model takes into account the Gaussian nature of the beams but does not account for pinhole diffraction. Diffraction makes the post-pinhole beam diameters larger than had there been no pinholes. Also, the model is grounded on beam specifications furnished by the laser manufacturer. Those specifications may very well have changed over time. Slight numerical differences however do not change any of the general conclusions that I have drawn based on modeling thus far.

5.5.2 Phase measurement repeatability

The results that I present in this section are obtained when SBIL wavefront metrology is conducted for the very first time. The stage is displaced such that the beams fall to the center of the metrology grating, where the phase is presumably close to being linear. No special effort is made to locate the so-called "sweet spot" of the metrology grating, where phase nonlinearity is at a minimum.

A total of 24 PSI sequences are obtained. Each contains five CCD intensity images corresponding to the Hariharan five-step algorithm (Fig. 5-29), from which a phase map can be calculated using Eq. (5.75). Figure 5-30(a) shows the average of the 24 moiré phase maps in a 3D plot, and (b) shows the corresponding phase contour plot. A circle is superimposed on top of the contours with its center at the minimum phase

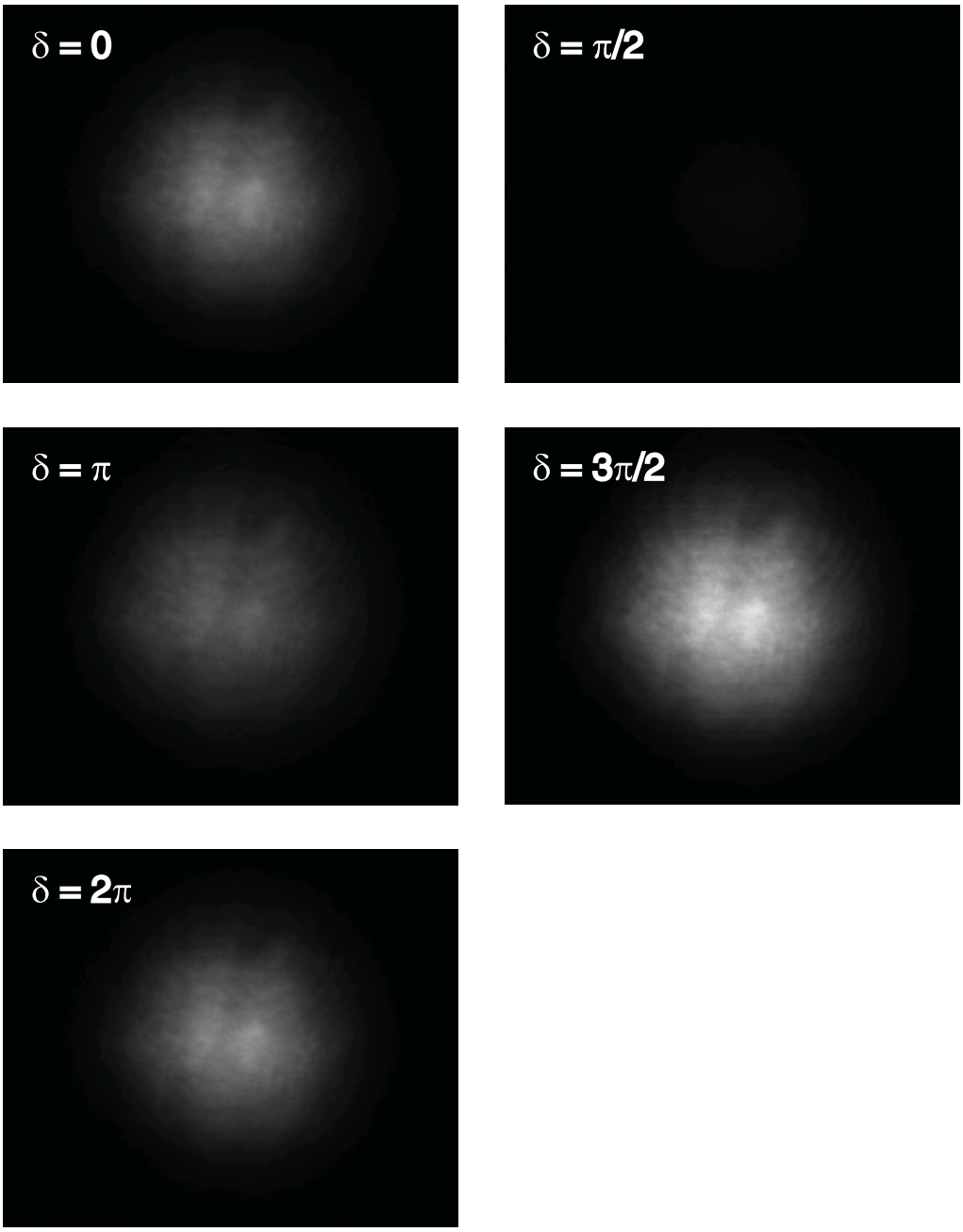

Figure 5-29: A sequence of five moiré intensity images, with $\pi/2$ rad phase shift between adjacent frames. The moiré phase across the image is much less than one period (Fig. 5-30), which explains the apparent lack of fringes.

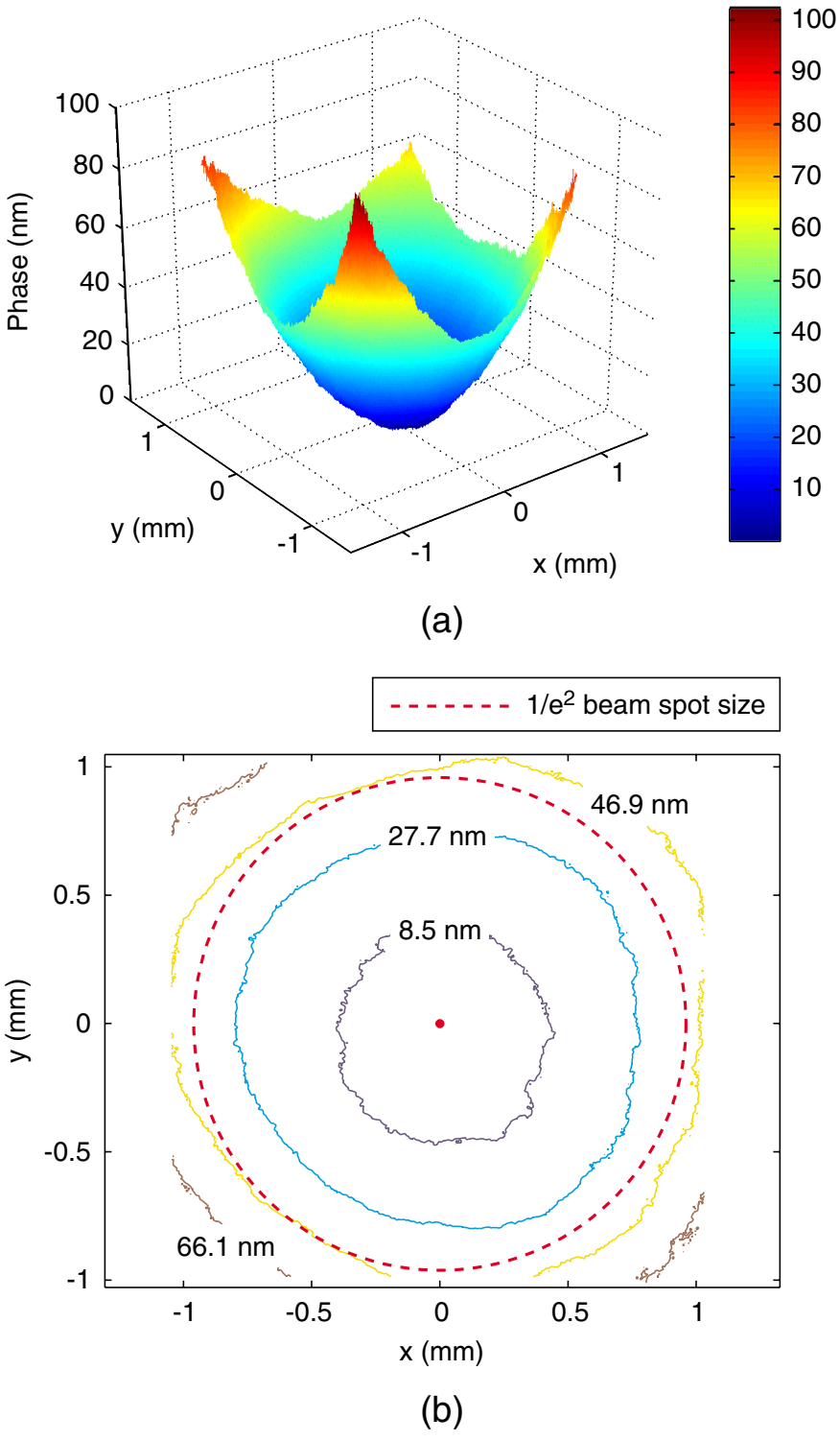

Figure 5-30: Moiré phase map, averaged from 24 data sets. (a) A 3D plot of the phase map. (b) 2D phase contours. A circle is superimposed with its center at the minimum phase point and its circumference outlining the 1.92 mm-diam. spot size.

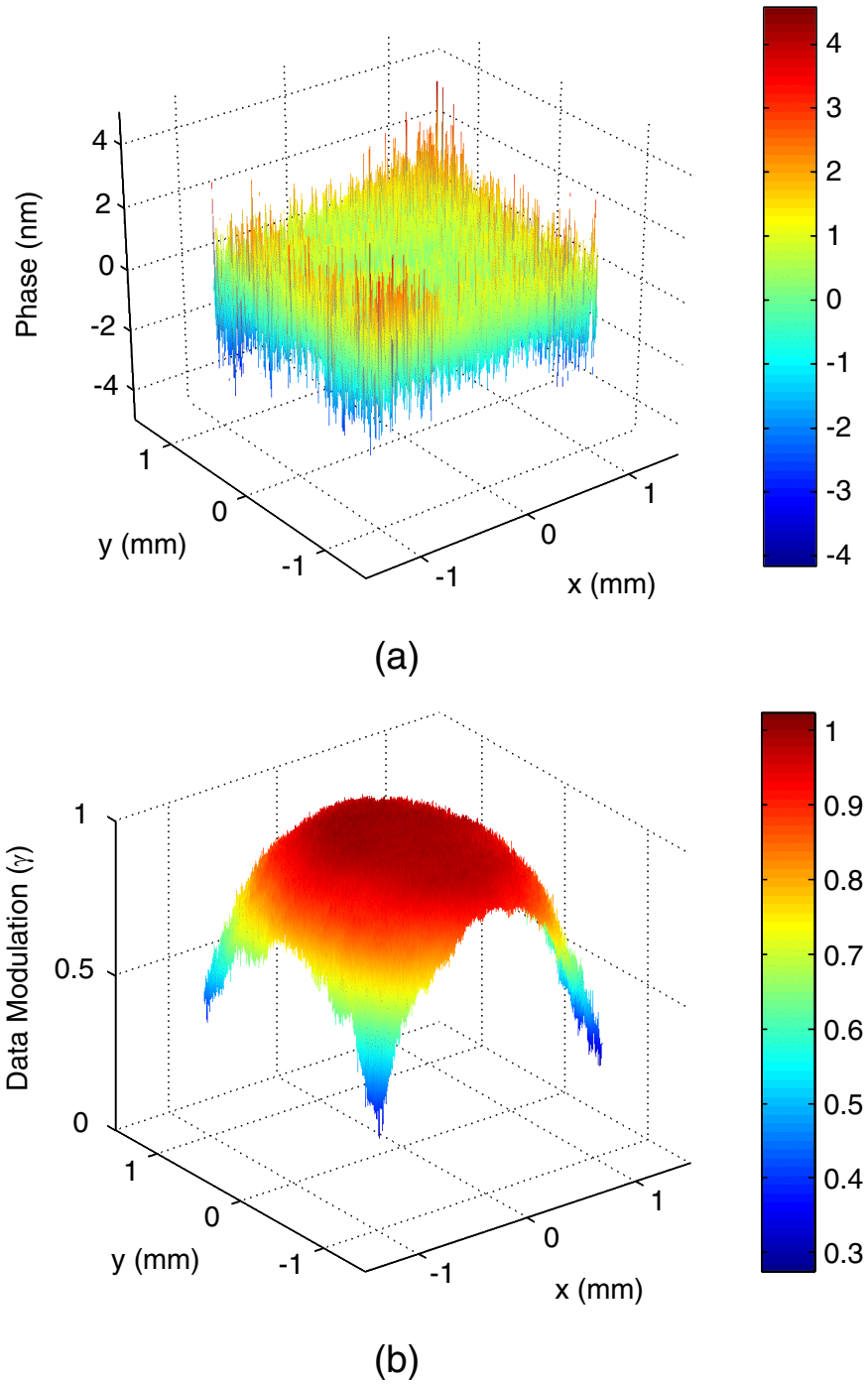

Figure 5-31: (a) Deviation of an individual phase map from the mean (Fig. 5-30). (b) Data modulation for a single data set as defined by Eq. (5.76).

point and its circumference outlining the 1.92 mm-diam. spot size. The measured nonlinear phase distortion across the spot is 0.73 rad, or 47 nm after normalizing to the metrology grating period ($p = 401.23$ nm). In other words, at the system's first light, the distortion is already below one eighth of a period. Phase unwrapping is unnecessary.

The system's repeatability is defined as the three-sigma deviation of the individual phase maps from the mean. Figure 5-31(a) plots one of the phase deviation maps. The measured repeatability is 0.05 ± 0.007 rad, or 3.2 ± 0.45 nm (about eight thousandth of a period).

Finally, Figure 5-31(b) plots γ, the data modulation of one of the data sets, calculated from Eq. (5.76). I consistently observe γ greater than 0.5 within the $1/e^2$ points, which proves that the signal-to-noise is excellent.

5.5.3 Minimization of the nonlinear phase

Several attempts have been made to minimize the nonlinear phase component in the grating image. The data in this section represents the best effort.

First, calipers are used to ensure that both collimating lenses are at the same distance from their respective pinholes. Error in lens placement is ± 1 mm, well within the error budget given in Section 5.4.1. The location of the collimating lens in the right arm is then adjusted by actuating the picomotor that drives the stage that the lens sits on. Systematically, various locations are tested. The observed phase distortion decreases initially, reaches a minimum and then increases. Figure 5-32 shows the result obtained at the minimum point. It is a plot of the mean of 8 data sets. The $1/e^2$ diameter is again outlined, centered at zero phase. The distortion across the beam is 12 nm, or roughly 1/33 of a period.

Based on simulation results from Section 5.2, for the grating image to have a distortion of 3 nm, the distances from the pinholes to the collimating lenses must be matched to 80 μm. This is a fairly large window of operation, especially for picomotors that can move in steps of 30 nm—80 μm translates into roughly 2700 picomotor steps. The fact that I see the distortions decreasing, reaching a plateau and then increasing again seems to suggest that the window has not been missed, though in the future, it would be most helpful to have a fully automated measurement process. So the question is: Why can't phase nonlinearities of only a few nanometers be observed at present time?

5.5.4 Lens aberrations

It is important to realize that the measured distortions represent not only curvatures in the Gaussian wavefronts, but also phase nonlinearities in the metrology grating

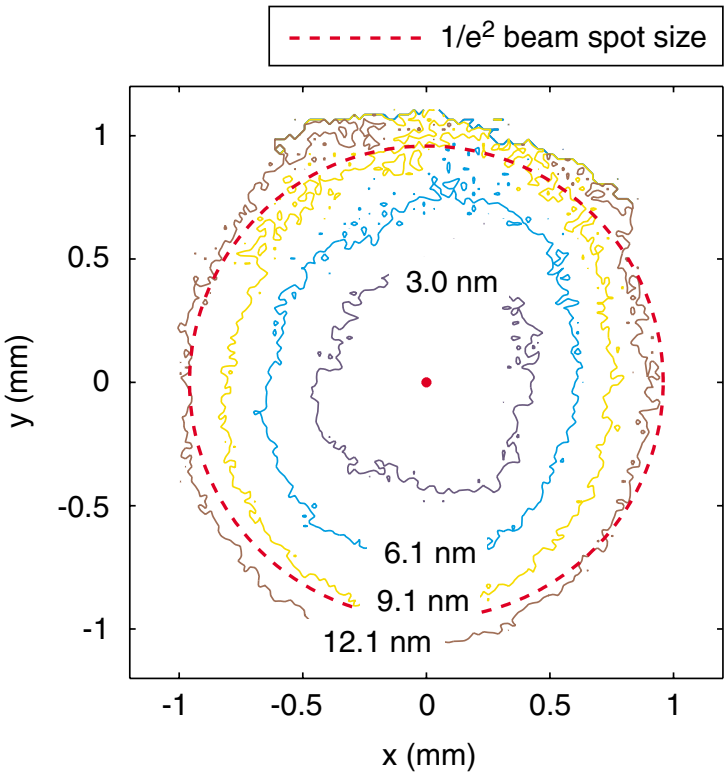

Figure 5-32: Moiré phase map, averaged from 8 data sets. The map represents current best effort in minimizing the nonlinear phase. A circle is superimposed with its center at the minimum phase point and its circumference outlining the 1.92 mm-diam. spot size.

and possible aberrations in the collimating optics.

The IL-produced metrology grating could easily contribute phase nonlinearities on the order of a few nanometers (Fig. 5-27). Circular moiré phase contours result as two rotationally symmetric wave fields interfere. Gaussian beams propagating under the thin-lens assumption generate these fields (Sec. 5.2). In reality however, thin lenses do not exist. The collimating lenses currently in use are commercial spherical singlet lenses purchased from CVI Laser Corporation. They have intrinsic aberrations, in particular, spherical aberration (SA), which happens to be rotationally symmetric as well—it can be characterized by a pupil function

$$\wp(\rho) = \exp\left(j\,\frac{2\pi}{\lambda}\,C_{sa}\,\rho^4\right) \quad , \tag{5.82}$$

where ρ is the radial vector defining the pass region of the lens (pupil of the lens), and C_{sa} is the spherical aberration coefficient [90]. Even though SBIL employs small-diameter beams that are significantly less sensitive to SA than beams that fill the entire lens aperture, residual aberrations may still exist. While moving the collimating lenses flattens out the part of the wavefronts that is Gaussian in nature, the overall

wavefronts may remain slightly curved due to intrinsic lens aberrations such as SA. These aberrant waves interfere and result in increased nonlinear phase in the grating image.

Exactly to what extent SA and the other third-order aberrations contribute to the moiré phase nonlinearity might be an interesting topic of future research.

5.5.5 Theory vs. experiment

I now investigate what remains of Figure 5-32 when the circular phase contours are removed by subtracting a best fit in the least-squares sense.

The theoretical model used for the fit is discussed in Section 5.2. The rotational symmetry of the model means that it would not be able to distinguish circular distortions due to the interference of two ideal Gaussian beams, or to circular distortions in the IL metrology grating (Fig. 5-27). In other words, when applied, the model tends to remove circular symmetries of all origins. What remains should be random phase noise and any patterns that arise from non-rotationally symmetric sources.

Figure 5-33 gives the fit result in a filled contour plot. The sigma between the experimental data and the model is 2.2 nm over the entire 2×2 mm square area. For clarity of illustration, areas outside the $1/e^2$ intensity diameter have been masked. The model is applied when all but one parameter describing the wavefront metrology setup are fixed at their base values (Table 5.1). The only parameter allowed to vary is the relative offset between the two collimating lenses. A best fit yields an offset of 200 μm.

At first glance, removing circular symmetry yields a map of random noise. However, closer examinations seem to reveal a pattern. To aid the eye, I have divided the map into seven regions based on their respective values: 0 nm (green in color) is in the middle, with increasing values—1 nm, 2 nm and 3 nm—lying to either side of it. Note that this residual phase is not linear. Had it been, it would have negative values off to one side and positive ones to the other. Two possible reasons may account for this type of phase symmetry: (1) wafer tilt when the IL grating was originally exposed, and/or (2) lens astigmatism.

Reference [23] studied wafer-orientation-induced IL grating phase nonlinearities in detail. The observed value in Figure 5-33 seems to suggest a substrate rotation about the y axis [Fig. 1-7(a)] by roughly 1 mrad, which is entirely possible.

The pupil function for a pure astigmatic lens can be written as

$$\wp(\rho) = \exp\left(j\,\frac{2\pi}{\lambda}\,C_a\,x_0^2\,\rho^2\cos^2\theta\right) \quad , \tag{5.83}$$

where ρ is the radial vector defining the exit pupil of the lens, θ is the polar angle,

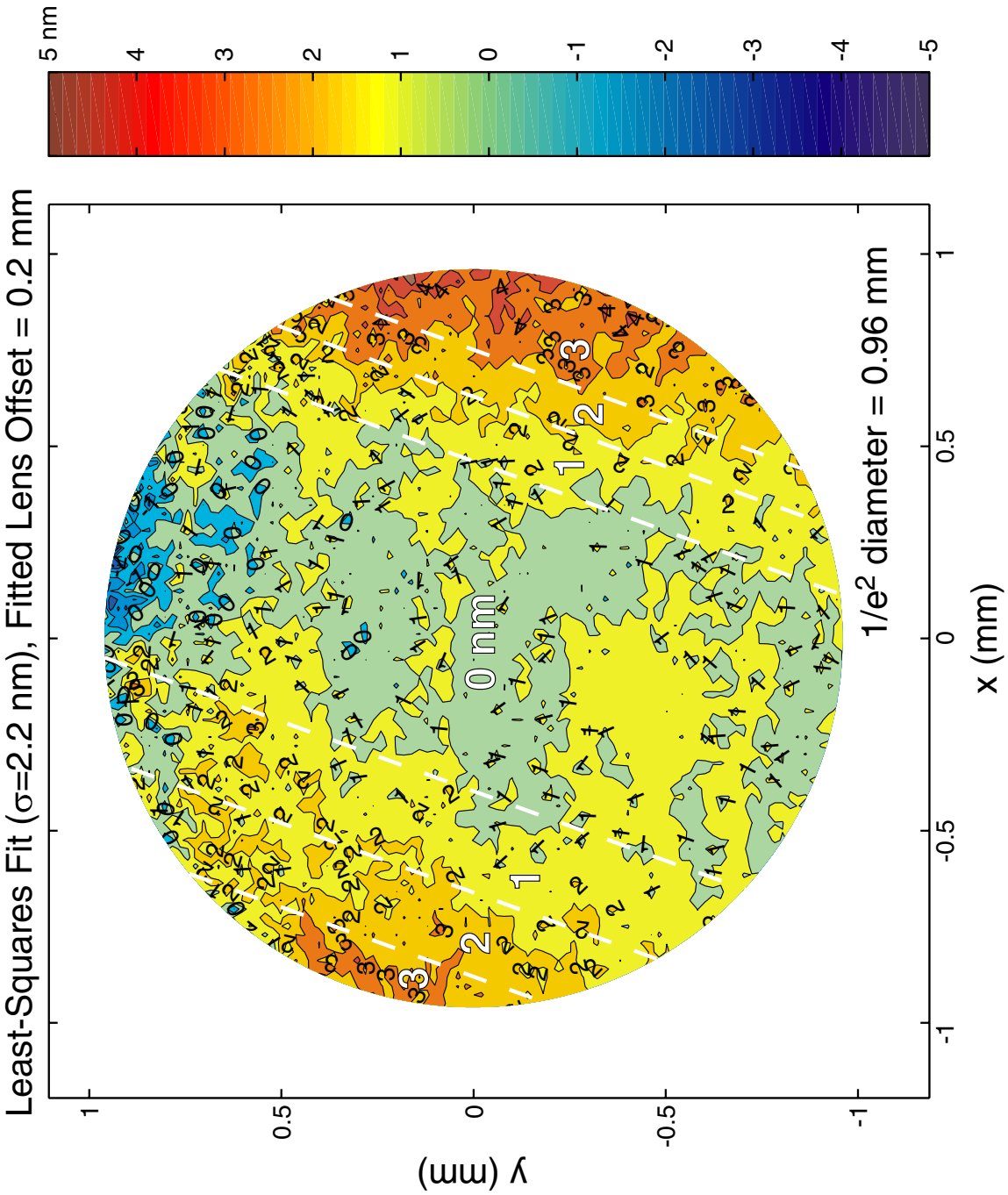

Figure 5-33: Least-squares fit of theory (Sec. 5.2) to the experimental data of Figure 5-32. The difference is plotted. The theoretical model is applied when all but one parameter describing the wavefront metrology setup are fixed at their base values (Table 5.1). The only parameter allowed to vary is the relative offset between the two collimating lenses. A best fit yields an offset of 200 μm.

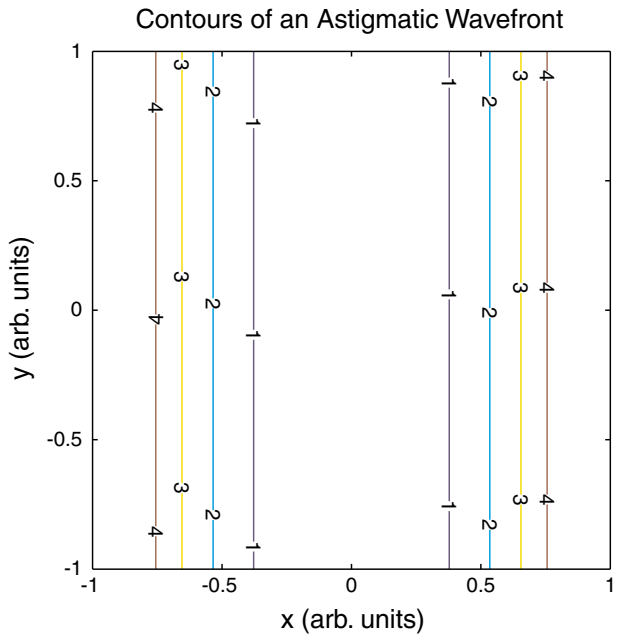

Figure 5-34: Contours of an astigmatic wavefront.

(x_0, y_0) is the image point and C_a is some coefficient [90]. The contours of an astigmatic wavefront is shown in Figure 5-34. Physically, astigmatism arises if the surface of a lens is slightly cylindrical, a common error in optics manufacturing, instead of being perfectly spherical. The wavefront emanating from an astigmatic lens will have different radii of curvatures in two orthogonal directions.

Of course, one should keep in mind that even though Figure 5-32 is obtained by averaging 8 moiré maps whereby the error on the mean has been reduced by a factor of $\sqrt{8}$, the error is still high at approximately 1.1 nm given the 3.2 nm three-sigma phase measurement repeatability. At this sensitivity, the symmetry observed in Figure 5-33 may well be fictitious, nevertheless, it is very suggestive. Here is a word on spherical aberration. As shown in Eq. (5.82), SA is indeed rotationally symmetric, but its wavefront has a ρ^4 dependence whereas the Gaussian wavefront has a ρ^2 dependence. So SA, if it exists by any significant amount, should remain after the removal of ρ^2 symmetries. The fact that Figure 5-33 does not show any apparent rotational symmetry seems to suggest that SA is minute. If SA is small, it is not a far stretch to say that astigmatism is small as well. The apparent pattern observed in Figure 5-33 is more likely due to phase nonlinearities in the metrology grating.

At this point, I am convinced that the poor quality of the IL metrology grating and the lack of a fast, fully automated measurement process, prevent phase nonlinearities at the few nanometer level from being achieved. However, this is not to say that the SBIL grating thus produced will have gross distortions at the dozen nanometer level.

5.6 Printed phase error

The grating image will be used to expose lines in the photoresist. Ultimately, the concern is not how distorted the image is, but how much nonlinear error the exposed grating has. I explore the so-called printed error in this section.

The dose required for an lithographic exposure can be mathematically modeled as

$$D(x,y) = \int_{-\infty}^{\infty} I(x,y,t)\,dt \quad , \tag{5.84}$$

where D is the dose, I is the irradiance or intensity of the grating image, and the coordinates (x,y) label a particular point over the resist. The scanning motion of the light spot is implied by the functional dependence on time t. More specifically, the intensity can be expressed as

$$\begin{aligned} I(x,y,t) &= B(x,y,t) + A(x,y,t)\,\sin\left[\phi_{gi}(x,y,t)\right] \\ &= B(x,y,t) + A(x,y,t)\,\sin\left[\frac{2\pi x}{p} + \phi_{\text{moiré}}(x,y,t)\right] \quad , \end{aligned} \tag{5.85}$$

where ϕ_{gi} is the phase of the grating image, which has been rewritten as the sum of the linear phase along x and the nonlinear moiré phase $\phi_{\text{moiré}}$. The nominal period of the image grating is p. The functions B and A represent the background intensity and the intensity amplitude of the grating image, respectively. Eq. (5.85) can be substituted into Eq. (5.84) to yield

$$D(x,y) = B_D(x,y) + A_D(x,y)\,\sin\left[\frac{2\pi x}{p} + \Phi_e(x,y)\right] \quad , \tag{5.86}$$

where B_D and A_D are the dose background and amplitude, respectively. The function Φ_e defines the printed error and is given by

$$\begin{aligned} \Phi_e(x,y) &= \tan^{-1}\frac{\displaystyle\int_{-\infty}^{\infty} A(x,y,t)\,\sin\left[\phi_{\text{moiré}}(x,y,t)\right]\,dt}{\displaystyle\int_{-\infty}^{\infty} A(x,y,t)\,\cos\left[\phi_{\text{moiré}}(x,y,t)\right]\,dt} \\ &\approx \frac{\displaystyle\int_{-\infty}^{\infty} A(x,y,t)\,\phi_{\text{moiré}}(x,y,t)\,dt}{\displaystyle\int_{-\infty}^{\infty} A(x,y,t)\,dt} \quad \text{for } \phi_{\text{moiré}} \ll 1 \quad . \end{aligned} \tag{5.87}$$

Physically, Eq. (5.87) says that the printed error in the photoresist is the amplitude-weighted moving average of the moiré phase, which makes intuitive sense. During SBIL, a particular location on the photoresist sees a time-varying Gaussian amplitude over it. The written phase error at the location should be determined primarily by the error of the point in the grating image that has contributed the highest amplitude

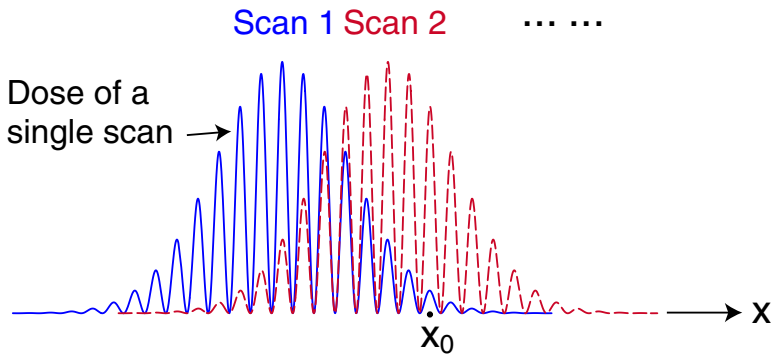

Figure 5-35: Nonlinear phase error at the location x_0 is determined more by Scan 2 than Scan 1, because the former contributes a much larger intensity amplitude.

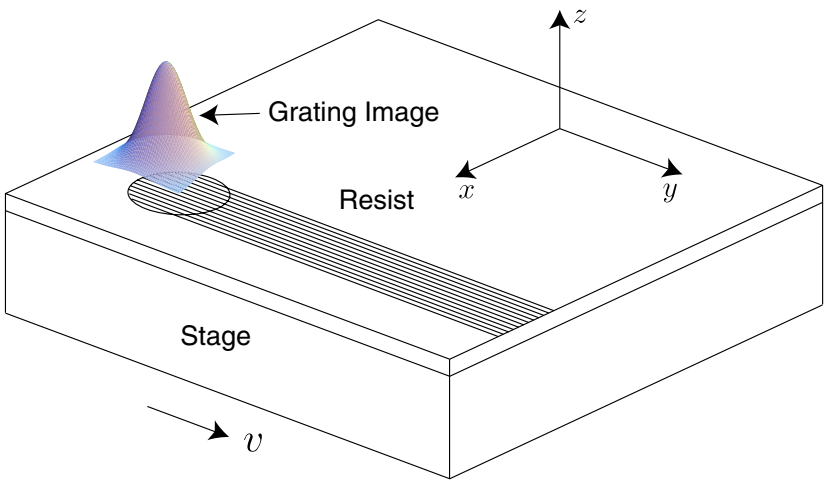

Figure 5-36: Cartoon of a single stage scan during SBIL.

(Fig. 5-35). In other words, the printed error should be weighted by the Gaussian amplitude profile over time.

Konkola has originally derived the above mathematical formalism to study the sensitivity of the printed error to stage-scan and frequency-locking induced image phase jitters [48]. The formalism is equally applicable for gaining a quantitative understanding of how sensitive the printed errors are to phase nonlinearities in the grating image.

While my goal is to come up with an estimate of the printed errors in a resist grating produced with multiple scans, it is an important first step to figure out the error associated with a single scan. For simplicity, I shall assume that both the stage and the fringe locking perform perfectly, i.e., no other printed errors are introduced except ones due to grating image nonlinearities. Figure 5-36 shows a cartoon. The grating image, whose Gaussian intensity profile is shown, remains stationary while

the resist-coated substrate moves underneath and gets exposed. Before Eq. (5.87) can be applied, one must know both $\phi_{\text{moiré}}$ and A. The former has been experimentally measured. The latter is numerically simulated:

$$A(x,y,t) = \exp\left[-2\,\frac{(x-x_0(t))^2 + (y-y_0(t))^2}{R^2}\right] \quad , \tag{5.88}$$

where (x_0, y_0) marks the center of the moving 2D Gaussian amplitude and R is the $1/e^2$ intensity radius. While a measured amplitude is more preferable, the intensity observed by the CCD is not a good representation of the intensity at the substrate, because of artifacts added by intervening optics (Sec. 5.5.1). The Gaussian intensity envelope at the substrate should be relatively free of contaminants since the beams have just gone through spatial-filtering, which is why I belive Eq. (5.88) is a good approximation.

Take the case where the distortion across the spot is around 12 nm (Sec. 5.5.3). Figure 5-32 shows the moiré phase map superimposed with the Gaussian radius. Center of the Gaussian corresponds to the phase minimum, despite possible beam alignment errors—recall arguments from Section 5.2.6. Eq. (5.87) can be implemented algorithmically as follows: The moiré phase matrix is multiplied by the Gaussian amplitude matrix, and the result is summed along y, the stage scan direction. This yields the numerator. The denominator is obtained in a similar fashion. I have ignored any error due to possible misalignment of the grating image from the scan direction. Any such misalignment should be small—on the microradian level—so that the model simulates reality with confidence.

Figure 5-37 is a plot of the resulting amplitude-weighted phase error. To mirror reality, the moiré phase data used for weighting is from a single PSI measurement, not the averaged phase of Figure 5-32. Two dots mark the locations of the $1/e^2$ intensity points, $R = 0.96$ mm as measured by the camera (Sec. 5.5.1). Strictly speaking, R at the substrate should be smaller than 0.96 mm, but not by much because of the large post-collimation beam Rayleigh range. In plotting Figure 5-37, I have assumed that the observed moiré data is entirely due to distortions in the grating image. That is of course an overestimate because nonlinearities in the metrology grating are also represented. So the actual printed error should be lower than what Figure 5-37 shows. The shape of the curve is roughly parabolic and symmetric about the center of the scan. Beyond the $1/e^2$ intensity points, the phase is noticeably noisier, caused most likely by the phase noise in the measured moiré. As expected, the nonlinear phase increases as one moves towards the edge of the scan. The error at the right edge is about 3 nm larger than that at the left. Physically, one would not expect the phase

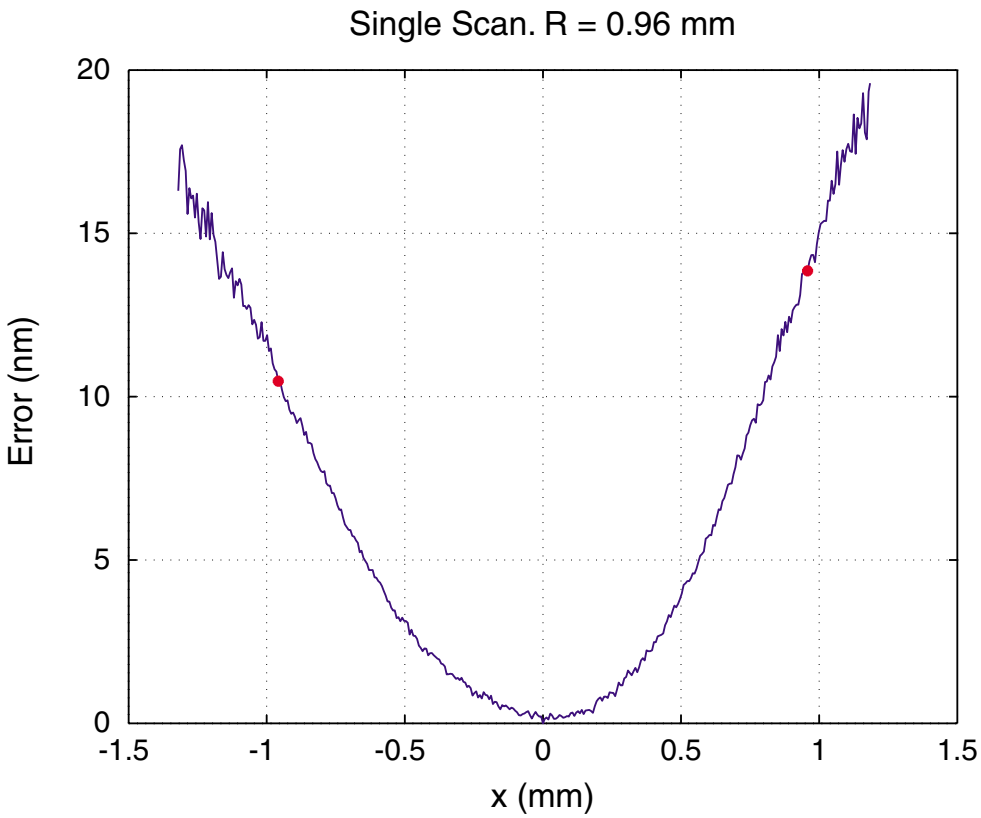

Figure 5-37: Printed phase error of a single scan. The moiré phase used for weighting has a maximum of about 12 nm at the $1/e^2$ diameter.

of the scan to have this type of asymmetry. It may be a telltale sign of the distortion in the underlying metrology grating.

Now that the printed error for a single scan has been established, I move on to model the error in multiple scans. Intuition says that in overlapping adjacent scans, one can greatly reduce the printed error. Again, Eq. (5.87) is applied. The function $\phi_{\text{moiré}}$ is now the error from a single scan (Fig. 5-37). Note that it is now a 1D function defined along x, the direction perpendicular to the scan. I call x the step direction for it is the direction that I will step over by an integer number of nominal fringe periods and start up another scan. The amplitude A is given by

$$A(x,t) = \exp\left[-2\,\frac{(x-s(t))^2}{R^2}\right] \quad , \tag{5.89}$$

where s is a discrete function defining the centers of the individual scans.

Figure 5-38 shows the amplitude-weighted phase error for 15 scans at a step size of $1R = 0.96$ mm. Except the $\sim$1 mm regions at the beginning and the end of the scan where no beam overlap has taken place, the printed error amounts to 0.95 nm peak-to-valley in the overlapped region. Note that numerical artifacts exist in the plot as

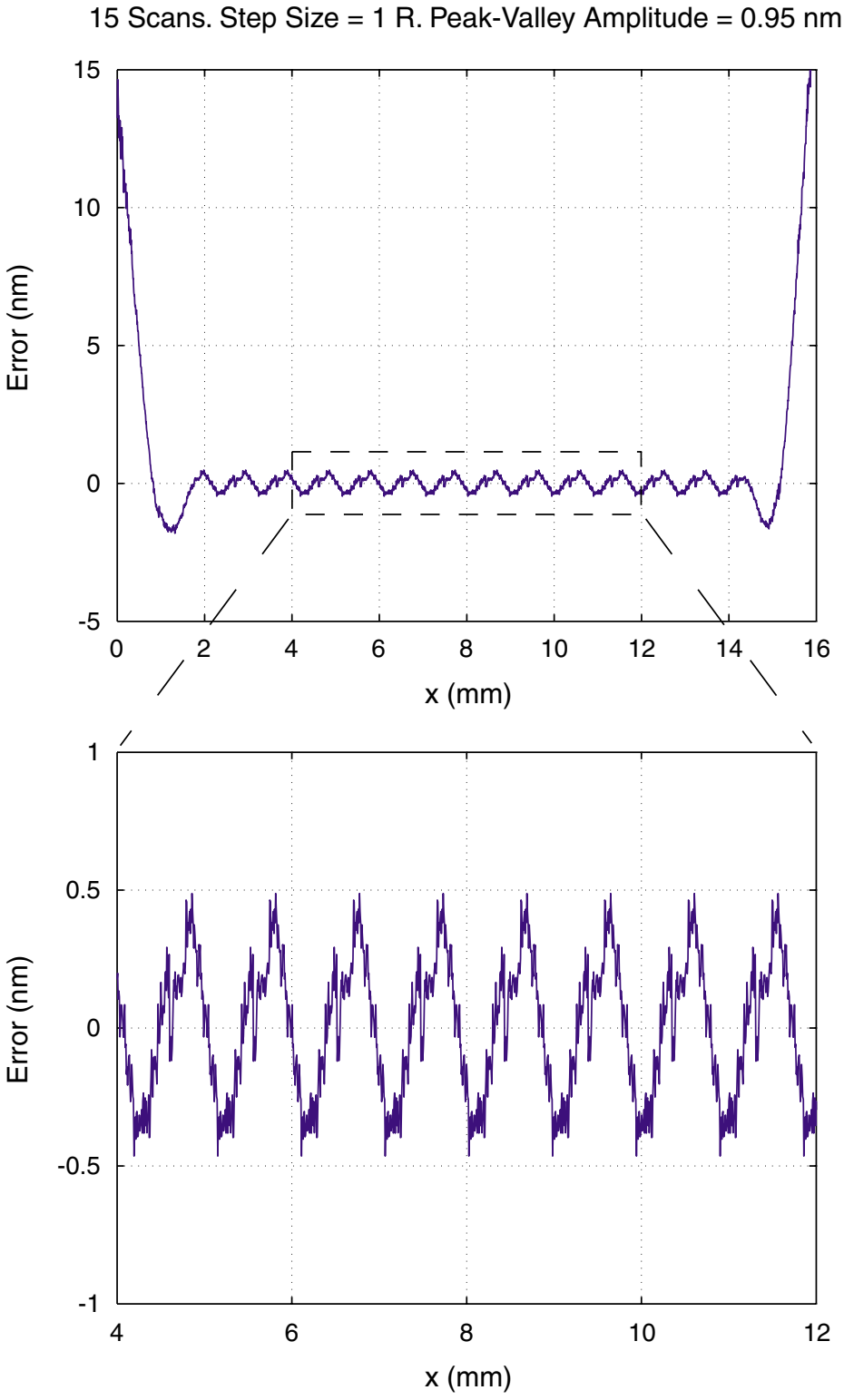

Figure 5-38: Printed error for 15 scans at a step size of 0.96 mm. Continued from Figure 5-37.

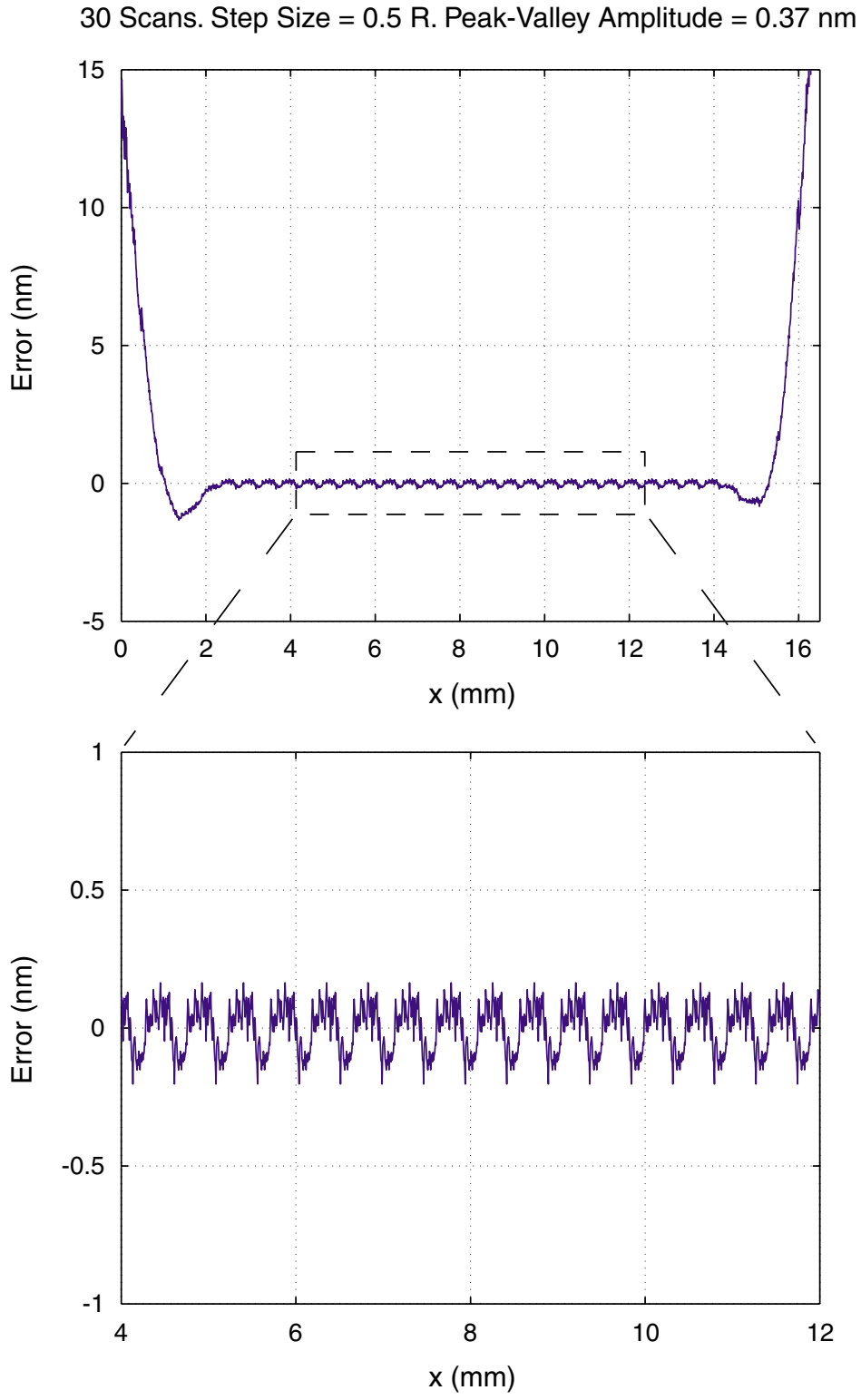

Figure 5-39: Printed error for 30 scans at a step size of $0.5\,R = 0.48$ mm. Continued from Figure 5-37.

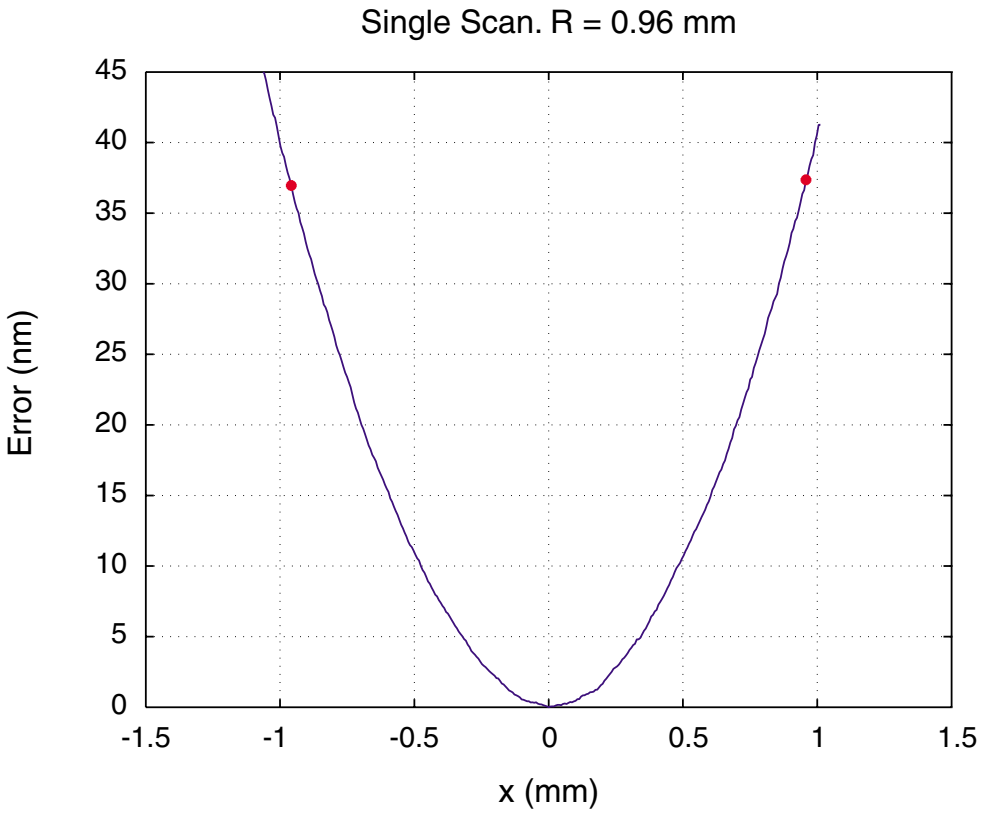

Figure 5-40: Printed phase error of a single scan. The moiré phase used for weighting has a maximum of about 47 nm at the $1/e^2$ diameter.

both the amplitude and the phase used in calculating the weighted average are limited in data length. The actual value, if one could have obtained longer data records, may be even smaller. This is an exciting result! Even if the grating image is distorted by a dozen nanometers, in step-and-scanning, SBIL manages to achieve a net error, which is 10 times smaller than that present in the image, all at a very reasonable step size. (Step size can not be arbitrarily large for dose control reasons—a $0.9\,R$ step size gives a dose uniformity of about 1%.) The beauty of SBIL is quantitatively demonstrated. Figure 5-39 is a repeat of the exercise at a step size of $0.5\,R = 0.48$ mm. More averaging has knocked down the peak-to-valley error to 0.37 nm. This should enable writing to the subnanometer level.

Figure 5-40 is a plot of the single scan error when the observed moire phase has not been minimized and is around 47 nm [Fig. 5-30(b)]. Again, the phase map from a single PSI measurement is used to generate the weighted average. The printed error is around 37 nm near the edge of the scan, already 10 nm smaller than the error in the moiré. Unlike in Figure 5-37, the errors at the edge of the scan are almost symmetric here. The symmetry can be explained if during the experiment, the grating

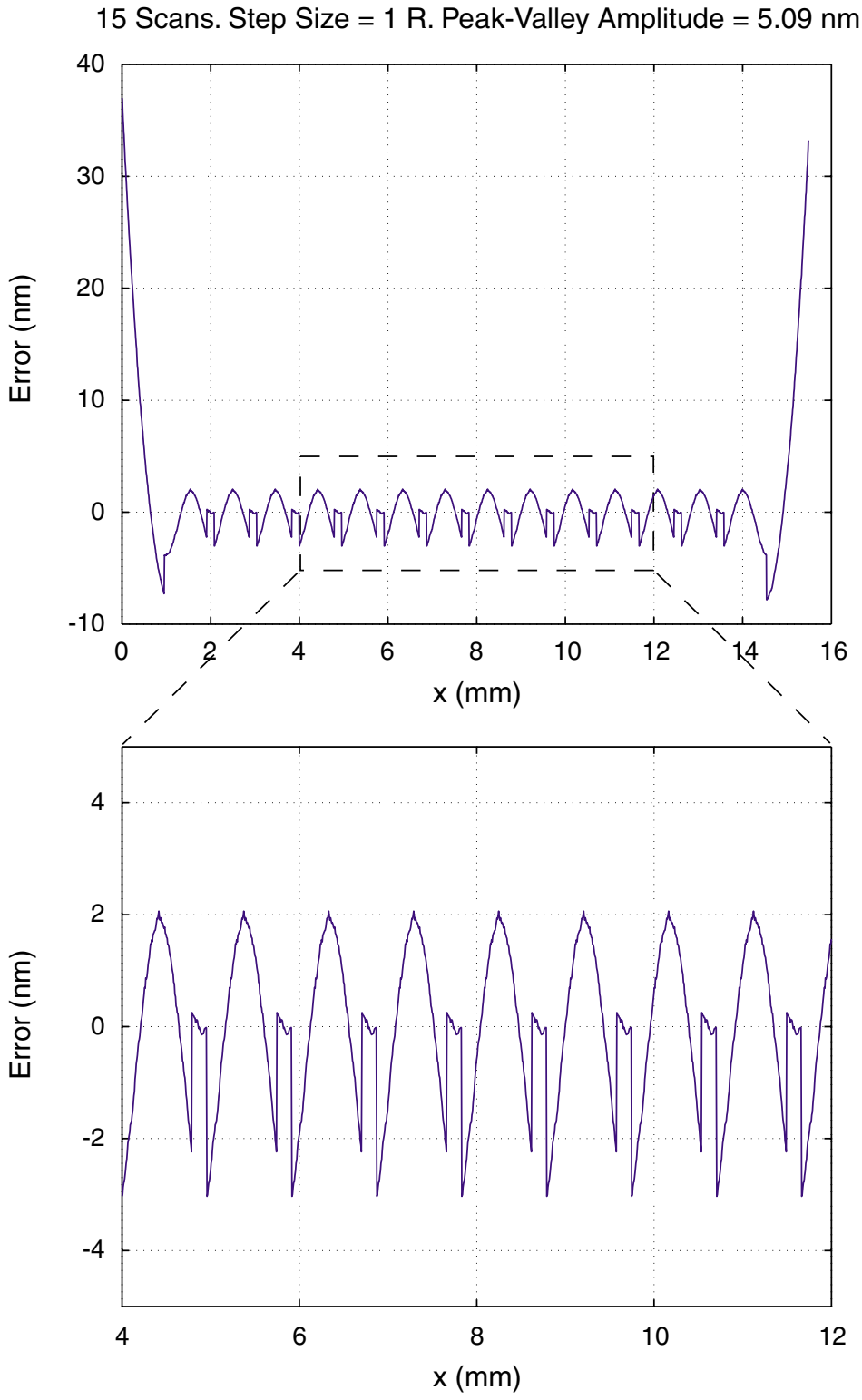

Figure 5-41: Printed error for 15 scans at a step size of 0.96 mm. Continued from Figure 5-40.

image happened to be placed on top of a patch of IL grating whose phase is roughly symmetric about the image. Figure 5-41 shows the amplitude-weighted phase errors when 15 scans are performed at a step size of $1R = 0.96$ mm. The peak-to-valley error is 5.09 nm. All of the very sharp, unnatural-looking features are not real—artifacts due to a finite data length, as I will explain in the next section.

Based on the findings of this section, it is desirable to use carefully overlapped SBIL gratings as linear metrology gratings. This should improve the accuracy of the wavefront metrology since phase nonlinearities associated with the metrology grating can be minimized.

5.7 Numerical artifacts and dose contrast

Figure 5-42(a) simulates the single-scan printed error shown in Figure 5-40 with a pure quadratic phase, and with the same data length: $N = 311$. Each data point corresponds to one CCD pixel. The simulated printed error, when 15 scans are performed at a step size of $1R = 0.96$ mm, is plotted in Figure 5-42(b). It bears a striking resemblance to its real world counterpart, Figure 5-41, and inherits all of the odd-looking features, the only difference being the peak-to-valley error: 3.91 nm simulated v.s. 5.09 nm actual. The slight difference may be explained by the lack of perfect quadratic symmetry in Figure 5-40.

Figure 5-43 repeats the simulation with the same exact quadratic phase, but with a longer data record: $N = 500$. The printed error for 15 scans has a reduced peak-to-valley error of 2.68 nm. The sharp features seen earlier for the shorter data record have all disappeared, proof that they are purely numerical artifacts and are not physical. From the error reduction, one can roughly estimate the actual peak-to-valley error for the data in Figure 5-41 to be approximately 3.5 nm.

A word of caution is now in order. The Gaussian amplitude assumption is after all only an approximation to reality. The beam amplitude at the substrate is really a collimated diffraction pattern of the laser through a pinhole. Only the bright central spot of the diffraction pattern can be reasonably approximated by a Gaussian profile. Both the stage scan and the fringe locking are imperfect and introduce considerable phase jitters. The jitters give rise to seemingly random printed errors, at around 2 nm at present time, in addition to any systematic ones due to the grating image distortions.

How would the nonlinear distortions impact the exposure dose contrast? Similar to the discussion in Section 4.5, the normalized dose amplitude error is defined by

$$e_A \equiv \frac{A_D(x,y)}{A_{D,0}(x,y)} - 1 \ , \tag{5.90}$$

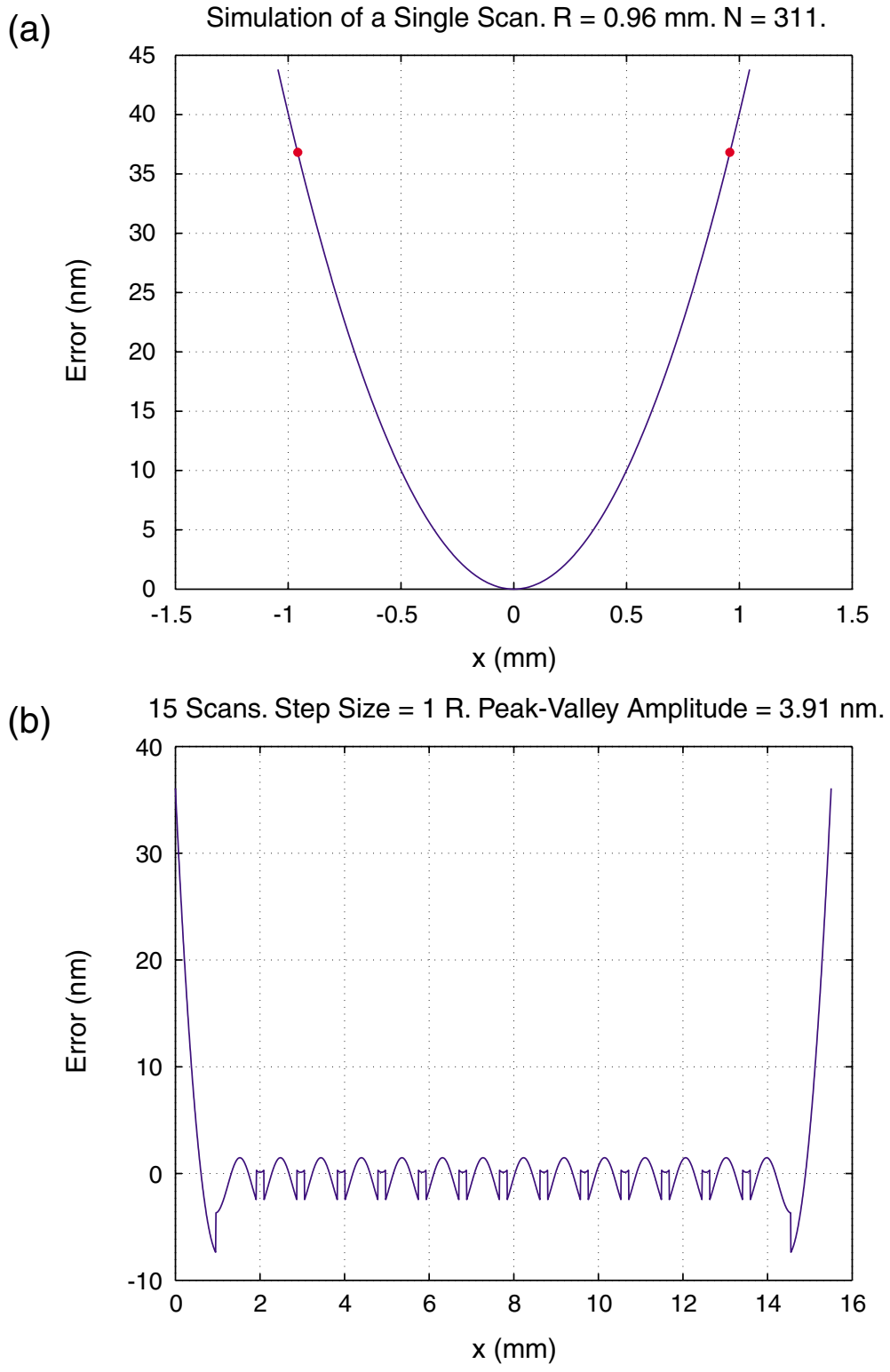

Figure 5-42: Simulated printed errors. (a) For a single scan. Figure 5-40 is simulated with a pure quadratic phase, and with the same amount of data points: $N = 311$. (b) For 15 scans at a step size of 0.96 mm.

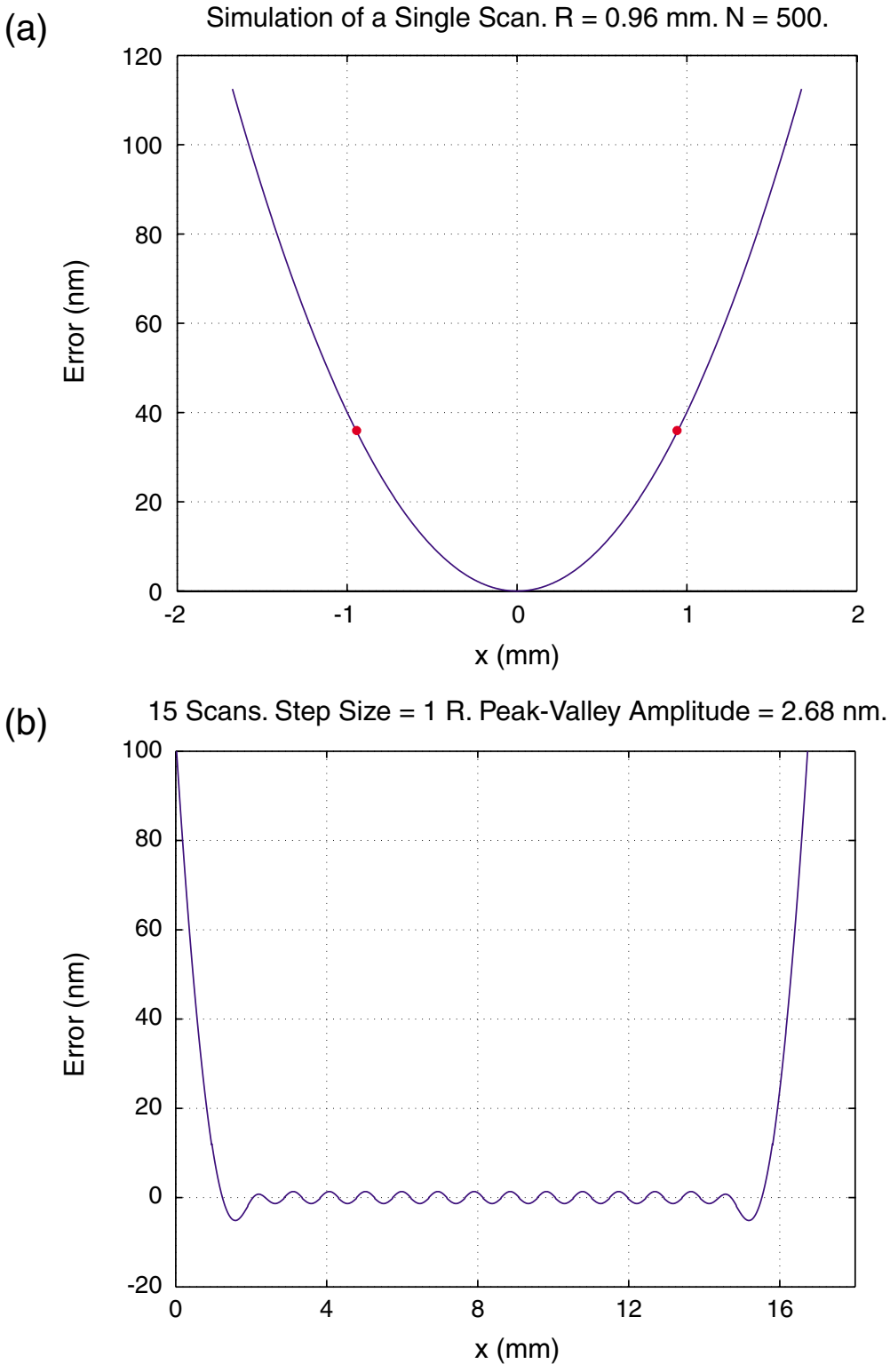

Figure 5-43: Simulated printed errors. (a) For a single scan. Same quadratic phase as in Figure 5-42(a), but with a longer data record: $N = 500$. (b) For 15 scans at a step size of 0.96 mm.

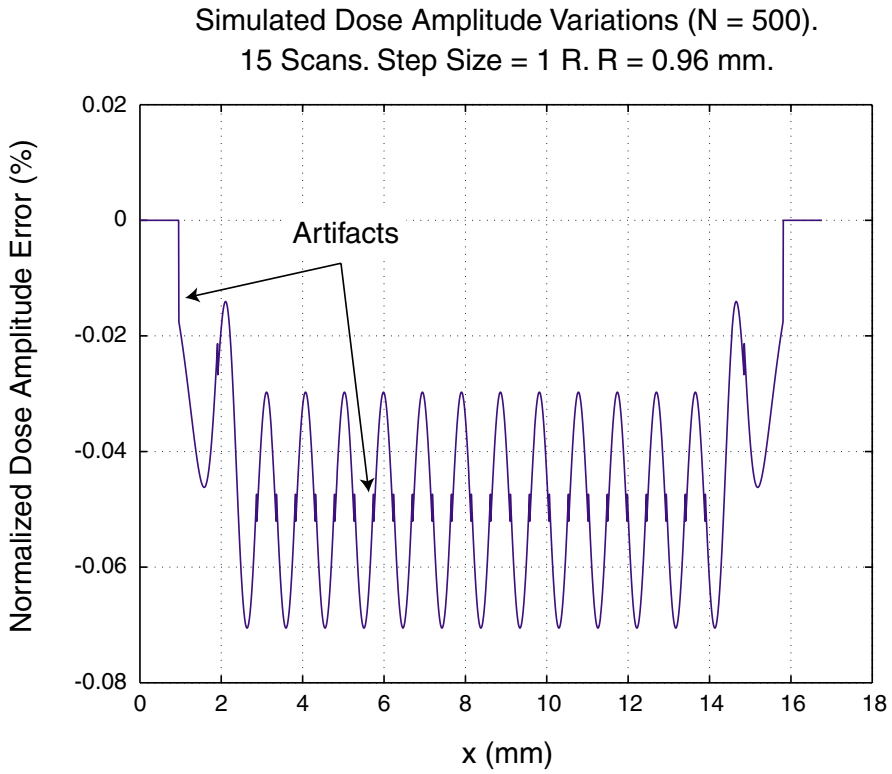

Figure 5-44: Simulated dose amplitude error for 15 scans at a step size of 0.96 mm. Continued from Figure 5-43.

where A_D is the dose amplitude [Eq. (5.86)] and $A_{D,0}$ is the nominal dose amplitude when phase nonlinearities do not exist

$$A_{D,0}(x,y) = \int_{-\infty}^{\infty} A(x,y,t)\, dt \quad . \tag{5.91}$$

Simple mathematical manipulations and the assumption of a small moiré phase lead to

$$e_A \approx \frac{1}{2}\left[\Phi_e(x,y)^2 - \Phi_{e,rsq}(x,y)^2\right] \quad \text{for } \phi_{\text{moiré}} \ll 1 \quad , \tag{5.92}$$

where Φ_e is the dose phase error, which is the topic of discussion for the previous section, and $\Phi_{e,rsq}$ is the amplitude-weighted root square phase error defined by

$$\Phi_{e,rsq}(x,y) = \sqrt{\frac{\displaystyle\int_{-\infty}^{\infty} A(x,y,t)\, \phi_{\text{moiré}}(x,y,t)^2\, dt}{\displaystyle\int_{-\infty}^{\infty} A(x,y,t)\, dt}} \quad . \tag{5.93}$$

For a grating image that is not optimized by wavefront metrology, nonlinear distortions can be tens of nanometers across the $1/e^2$ beam diameter. For concreteness, I go back to the experiment where the measured moiré phase is 47 nm. Since I want only a rough estimate of e_A, a simulated model suffices. There is the benefit of

adjustable data length so that any numerical artifacts can be minimized.

Figure 5-44 shows the simulation result. As in Figure 5-43, the length of the data is $N = 500$. Small artifacts remain but hardly influence the general shape of the result. The dose amplitude oscillates from one scan to the next and the overall change is below 0.08%, whose effect on SBIL is negligible. The negative sign symbolizes the fact that phase nonlinearities always cause the dose amplitude to decrease. For an optimized grating image, an even smaller e_A is expected.

5.8 Summary

I developed a Gaussian beam interference model specifically for the description of the SBIL wavefront metrology system. By simulating moiré patterns produced by the "beating" of the grating image against an ideal linear grating, I was able to determine how various system setup parameters influence phase nonlinearities in the image. Provided that certain extremely lenient optics-placement tolerances are met, the single most critical parameter that sets the magnitude of the nonlinear phase is the relative offset between the two collimating lenses. The offset is defined as the difference in distances from those two lenses to their respective pinholes. Theoretically, to incur a distortion of 3 nm, the offset must be controlled to around 80 μm.

SBIL wavefront metrology is based on phase shifting interferometry. The current lack of system automation dictates the use of the simple Hariharan five-step algorithm. Without the use of an environmental enclosure, phase measurement repeatability is established at eight thousandth of a period, or 3.2 nm, three-sigma. Further improvements are expected with the enclosure. By adjusting the location of a collimating lens, I was able to minimize the image phase nonlinearity to 12 nm across the 1.92 mm-diam. image. Sub-10 nm phase minimization is difficult to attain at this point because the PSI process is not yet automated and the metrology grating itself is nonlinear.

I applied the theory of Gaussian amplitude-weighted moving average to study the printed phase error in a resist grating. With 12 nm of image distortion, I showed that a 0.95 nm peak-to-valley printed error can be achieved by SBIL at a step size of one beam radius, or 0.96 mm, assuming ideal stage scan and fringe locking. At a step size of 0.48 mm, the printed error reduces to 0.37 nm, which should enable subnanometer-level SBIL writing. Even if the image distortion is as much as 47 nm, I showed that in overlapping scans, SBIL is able to achieve dramatically reduced printed errors, on the order of 3.5 nm peak-to-valley for a step size of 0.96 mm. Finer step size should decrease the error even more. Also, I studied the effect of phase nonlinearities on the exposure dose. The change is negligible as far as SBIL is concerned.

Future research efforts may focus on the following areas: System should be further enhanced to enable automatic phase shifting and image acquisition. Once the automation is in place, one can use a more complex PSI routine that is more error-tolerant than the Hariharan five-step. Better algorithm combined with a good environmental control should enable even better phase measurement repeatability. If an IL grating is to be used as the metrology grating, its phase should be mapped and sweet spot identified. Alternatively, carefully overlapped SBIL gratings can be used as linear metrology gratings. High-quality aspherical collimating optics should reduce any lens aberration related errors. Further effort should be made to reduce the spurious-reflection-related artifacts at the camera.

Chapter 6

Conclusions

The work documented in this thesis is about how to build a novel lithography tool based on the concept of scanning beam interference lithography (SBIL). By interfering two small diameter Gaussian beams and step-and-scanning the resulting interference image, SBIL can pattern large-area linear diffraction gratings in photoresist that are phase-accurate to the nanometer level.

SBIL engineering can be roughly classified into two areas: mechanical and optical engineering. The former focuses on solving the problem of locking the interference image to a fast-moving substrate with nanometer phase accuracy, while the latter on producing an interference image with minimum phase nonlinearity, while controlling its period to the part-per-million (ppm) level. Optical engineering is the theme of this thesis. It is a fusion of many different topics of research: optical design, modeling and analysis, interferometry, data acquisition, signal processing, and system integration, to name a few.

SBIL offers significant advantages over mechanical ruling and conventional interference lithography (IL). The biggest advantage, in my view, comes from the fact that the phase of the patterned resist grating is not determined by any one individual scan, but by the amplitude-weighted average of many scans. This averaging process, highly efficient due to the use of Gaussian beams, means that SBIL is rather immune to the grating image period measurement inaccuracy (Sec. 4.5) and the image phase nonlinearity (Sec. 5.6), as well as high-frequency phase jitters caused by imperfections in fringe locking.

Chapter 2 discusses the design and layout of SBIL optics. Instead of putting together the components via trial and error without any prior planning, I first built the lithography interferometer in virtual space, with the help of Pro/Engineer. Besides saving time and allowing precise part placement, the approach made possible

system-level modeling of the optics performance. For example, Tables 2.1–2.4 list the modeling results of Gaussian beam modification (waist size, Rayleigh range, etc.) by the various lenses in the system, which could not have been done without knowing the precise lens locations. Such modeling also enabled the numerical simulation of the SBIL wavefront metrology system.

The beam alignment system (Ch. 3) and the period measurement system (Ch. 4) essentially share the same hardware, among which, the rectangular beamsplitter is perhaps the most important piece. The beamsplitter is used both in aligning the beams and in measuring the grating image period. Its design and installation are described in Section 3.2.2. The alignment uses a so-called iterative beam alignment scheme (Sec. 3.1.3), which yields guaranteed convergence in both position and angle. The decoupling topologies that I used are not unique, and can be easily modified to accommodate different convergence speed or packaging needs.

Period control concerns SBIL's ability to set, stabilize and measure the grating image period. The goal is to achieve and maintain control at the ppm level, or at around one picometer (10^{-12} m) given that SBIL gratings can range in period from 200 nm to 2 μm. A grating beamsplitter stabilizes the period. In theory, given the measured beam angular noise of 11.4 μrad three-sigma and a nominal grating period of 400 nm, the grating can suppress angle-noise induced period variations six-order-of-magnitude better than a conventional cube beamsplitter. In Section 3.4.3, I demonstrated experimental results where period stabilization is measured at 1 ppm, which is an overestimate since high-frequency period variations do not get written into the resist due to averaging. The automated beam alignment system can reliably overlap the two beam centroids to around 10 μm and equalize the mean beam angles to better than 2 μrad (0.4 arcsec), which translates into a period adjustability of 4 ppm at 400 nm. Considerable effort is spent studying the physics of *in-situ* period measurement with a beamsplitter (Sec. 4.1). It is found that neither misalignment nor beamsplitter non-ideality causes any significant measurement error. At a period of 400 nm, the measurement repeatability is demonstrated at 2.8 ppm, three-sigma.

Modeling shows that period measurement error at ppm level does not accumulate as growing phase nonlinearities in the patterned resist grating; rather, the resist grating has an averaged period that equals to the measured period. Any residual phase nonlinearity is periodic and small. For instance, for a 2 mm-diam. grating image and at a between-scan step size of 0.9 mm, a 2.8 ppm measurement error at 400 nm period leads to a cyclic phase error of less than 0.05 nm peak-to-valley. Finer step size reduces the error even further. The fact that the resist grating period is

the measured period, not the actual grating image period, means that one can set the period of the resist grating to picometers simply for stepping the stage by an appropriate amount.

SBIL wavefront metrology refers to the process of mapping the phase of a grating image and adjusting the collimating optics so that image phase nonlinearity can be minimized. The use of collimating lenses in the current optical setup is a matter of choice, not absolute necessity, as I explained in Section 5.2.11. It leads to a configuration where the Gaussian beams interfere at their waists. The wavefront metrology system employs phase shifting interferometry (PSI) and determines phase nonlinearity through a moiré technique. The system is used in the grating reading mode, where a linear metrology grating, whose period is nominally equal to that of the grating image, is inserted. The resulting 0-order reflection and -1-order back-diffraction coincide and interfere to produce moiré fringes. I developed a Gaussian beam interference model to quantitatively describe the moiré scheme. The model takes into account the effect of collimating optics and is in good agreement with experiment. The single most critical parameter which sets the magnitude of the nonlinear phase in the grating image turns out to be the relative offset between the two collimating lenses, defined as the difference in distances from the lenses to their respective pinholes.

The wavefront metrology system has a phase measurement repeatability of 3.2 nm[1], three-sigma, established without any environmental enclosure. By adjusting the location of a collimating lens, I was able to minimize phase nonlinearity to 12 nm across a 2 mm-diam. grating image. Sub-10 nm phase minimization is difficult to attain at this point because the PSI process is not yet automated and the IL-produced metrology grating itself is nonlinear. Future work is required to rid these shortcomings. Carefully overlapped SBIL gratings may be used as linear metrology gratings. Modeling based on the theory of Gaussian-amplitude moving average shows that the printed phase error in the resist grating, due to a 12 nm distorted grating image, is better than 0.37 nm peak-to-valley at a step size of 0.5 mm. In other words, by overlapping scans, SBIL is able to pattern gratings with subnanometer phase distortion using a grating image that is distorted at the dozen nanometer level.

In reality, the resist-grating phase will have to incorporate errors due to stage scan and fringe locking. However, strictly from the point of view of period control and wavefront metrology, I conclude, based on the findings from this thesis, that SBIL is capable of producing gratings with subnanometer phase nonlinearities. These super-accurate gratings should enable important advances in fields such as semiconductor

[1]Normalized to the period of the metrology grating, which is measured at 401.23 nm.

pattern placement metrology and grating-based displacement measuring interferometry.

Appendix A

Recipe for writing 300 mm wafers

Prior to any SBIL exposure, one must conduct wavefront metrology (Ch. 5), align the beams (Ch. 3) and measure the period of the grating image (Ch. 4). The following recipe is optimized for a nominal photoresist thickness of 200 nm (Sumitomo PFI-34 i-line resist) and a nominal antireflection coating (ARC) thickness of 520 nm (Brewer ARC-XL). The UV laser is used at an output power of 300 mW. The measured beam power in each arm, prior to the beam pickoff window (Fig. 1-13), is approximately 7.5 mW.

1. Disengage beam steering. Shutter the UV laser at the source.

2. Move the stage to a convenient location, e.g., $(x, y) = (0.3\,\text{m}, 0.3\,\text{m})$. Load the wafer. Turn on the vacuum.

3. Center the stage to $(x, y) = (0.16\,\text{m}, 0.24\,\text{m})$. Allow approximately 30 minutes for the system to thermally equilibrate.

4. Cycle the vacuum to release any substrate stress.

5. Move the stage to the starting position at $(x, y) = (0.005\,\text{m}, 0.045\,\text{m})$. Engage beam steering. Engage fringe locking. Start the SBIL routine with the following operating parameters:

   scan velocity = 46 mm/s;
   number of scans = 388;
   scan length = 0.385 m;
   step length = 800 μm;
   measured grating image period, e.g., 401.221 nm ; and
   measured fringe orientation (in μrad) relative to the stage y axis.

6. Disengage fringe locking. Disengage beam steering. Shutter the UV laser. Move the stage to a convenient location. Turn off the vacuum. Unload the wafer.

7. Develop the wafer (Arch Chemicals OPD 262 positive resist developer) for 60 s. Rinse the wafer in DI water for 60 s. Blow dry.

Appendix B

Fringe period stabilization via a grating beamsplitter

According to Eq. (1.5), the fringe period in the wafer plane due to the interference of two plane waves with angles of incidence θ_1 and θ_2 is

$$p = \frac{\lambda}{\sin\theta_1 + \sin\theta_2} \quad . \tag{B.1}$$

Because a grating beamsplitter is used in SBIL to split the laser and form the lithography interferometer, the angular noise in the two arms is antisymmetrically correlated [Fig. 2-1(a)], i.e., if the angle change in one arm is $+\delta$, the other is $-\delta$.

For simplicity, assume $\theta_1 = \theta_2 = \theta$. Taking into account the angle correlation, one has

$$\begin{aligned} p_{\text{grat}} &= \frac{\lambda}{\sin(\theta+\delta) + \sin(\theta-\delta)} \\ &= p\left(1 + \frac{1}{2}\delta^2 + \mathcal{O}[\delta]^4\right) \quad , \end{aligned} \tag{B.2}$$

where $p = \frac{\lambda}{2\sin\theta}$ is the fringe period if there is no noise, and $\mathcal{O}[\delta]^4$ symbolizes all terms with orders δ^4 and higher. The leading error term is of second order. For small δ, the change in period is negligible.

Had SBIL employed a cube beamsplitter to split the laser, the angular noise would be symmetrically correlated [Fig. 2-1(b)]. If the change in one arm is $+\delta$, it is $+\delta$ for the other as well. The period becomes

$$\begin{aligned} p_{\text{cube}} &= \frac{\lambda}{\sin(\theta+\delta) + \sin(\theta+\delta)} \\ &= p\left(1 - \cot\theta\,\delta + \mathcal{O}[\delta]^2\right) \quad , \end{aligned} \tag{B.3}$$

where the leading term now is of first order in δ. In comparison to a cube beamsplitter,

a grating is more tolerant to laser angle noise-induced period variations.

Can the grating beamsplitter maintain its advantage if $\theta_1 \neq \theta_2$? Yes. Suppose that the difference in the two angles is Δ. Instead of Eq. (B.2), one has for the period expansion

$$\begin{aligned} p_{\text{grat}} &= \frac{\lambda}{\sin(\theta+\delta)+\sin(\theta+\Delta-\delta)} \\ &= p' \left[1+\frac{1}{2}(\delta^2-\delta\,\Delta)+\mathcal{O}[\Delta,\delta]^4\right] \quad , \end{aligned} \tag{B.4}$$

where the nominal fringe period is

$$p' = \frac{\lambda}{\sin\theta+\sin(\theta+\Delta)} \quad . \tag{B.5}$$

For small Δ and δ, the error is again of second order. Compared to Eq. (B.2), the nominal period has changed however, due to the tilting of the fringes with respect to the wafer. A similar expansion for the cube beamsplitter shows the leading percentage error remains first order at $(-\cot\theta\,\delta)$.

Appendix C

Drawings for installing and aligning the rectangular beamsplitter

The beamsplitter interface must be aligned perpendicular to the vacuum chuck surface. To facilitate the alignment, one face of the beamsplitter (Datum C in Fig. 3-10) has an enhanced aluminum coating. The alignment is done with the help of a Newport autocollimator that has a 0.1 μrad angle resolution and outputs a 1 in-diam. collimated beam at $\lambda = 670$ nm. First, the beamsplitter is mounted on the side of the vacuum chuck (Fig. C-1). Commercial optical mounts from New Focus, Inc. (NF) are used whenever possible. Chuck attachments are machined out of Super Invar, a low coefficient-of-thermal-expansion (CTE) material. Alignment Mirror Assembly No.1 is then attached, its mirror aligned to the x-axis interferometer stage mirror. Mirror Assembly No.2 is attached to direct the autocollimator beam to the beamsplitter and to Assembly No.1. The beamsplitter, with its coated surface facing the beam, is aligned to No.1's mirror. When the alignment is complete, both mirror assemblies are removed. Figure C-2 shows the engineering drawing of the rectangular beamsplitter assembly. The estimated alignment error is around 10 μrad in both pitch and yaw—angles defined with respect to the x-axis stage mirror.

The vacuum chuck design is by P. T. Konkola [48].

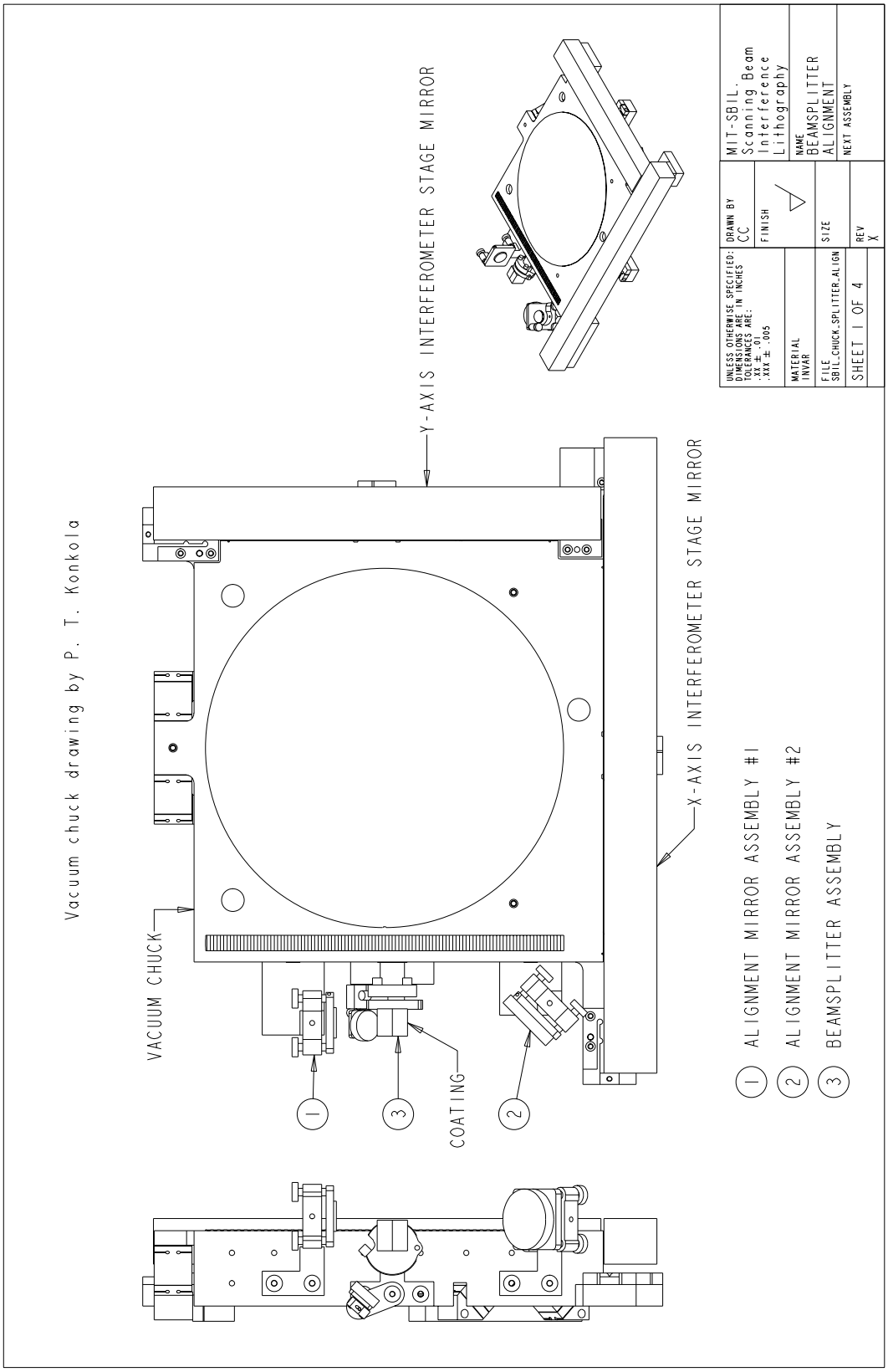

Figure C-1: Drawing of the rectangular beamsplitter alignment assembly attached to the vacuum chuck.

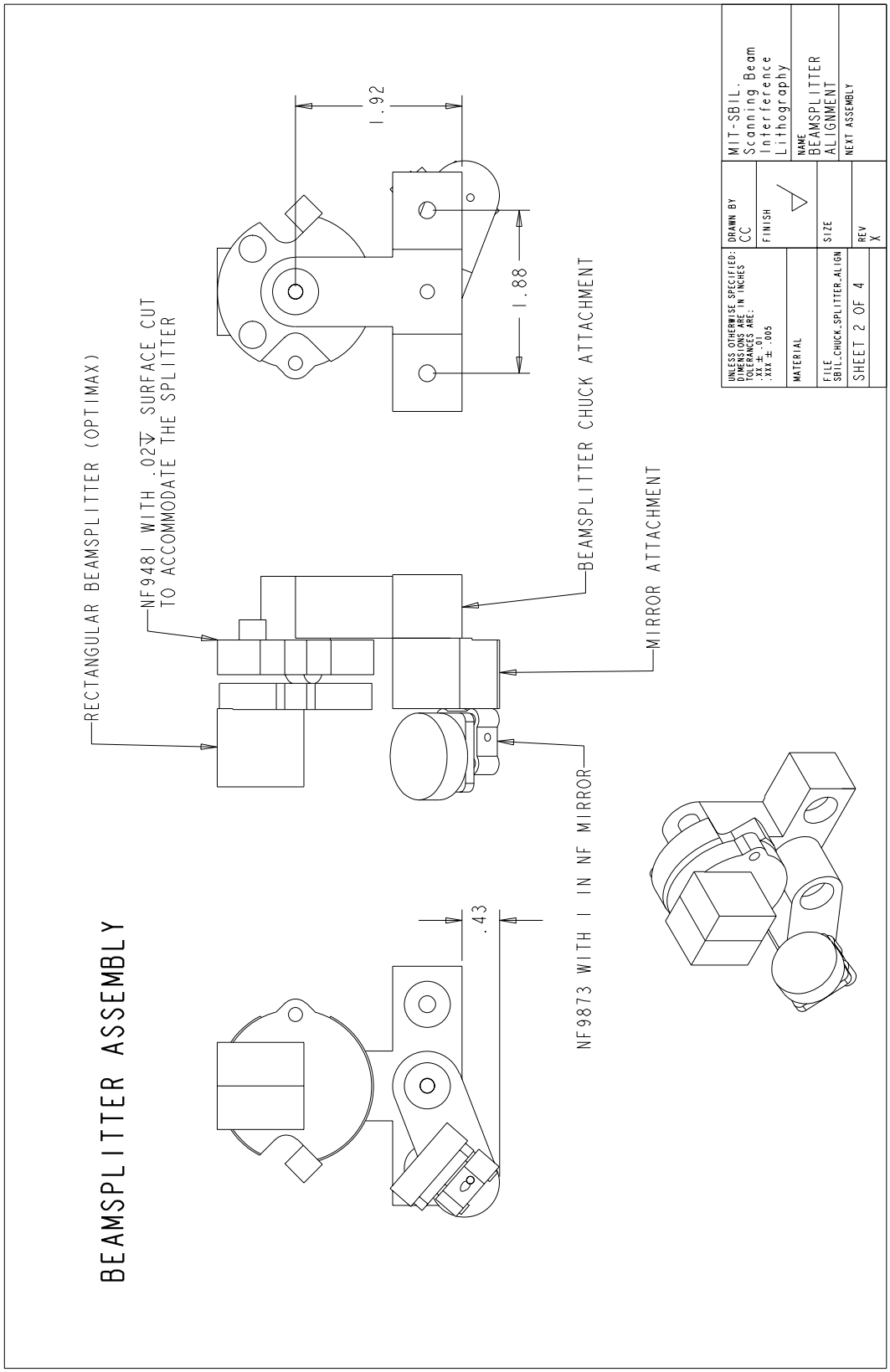

Figure C-2: Drawing of the rectangular beamsplitter assembly.

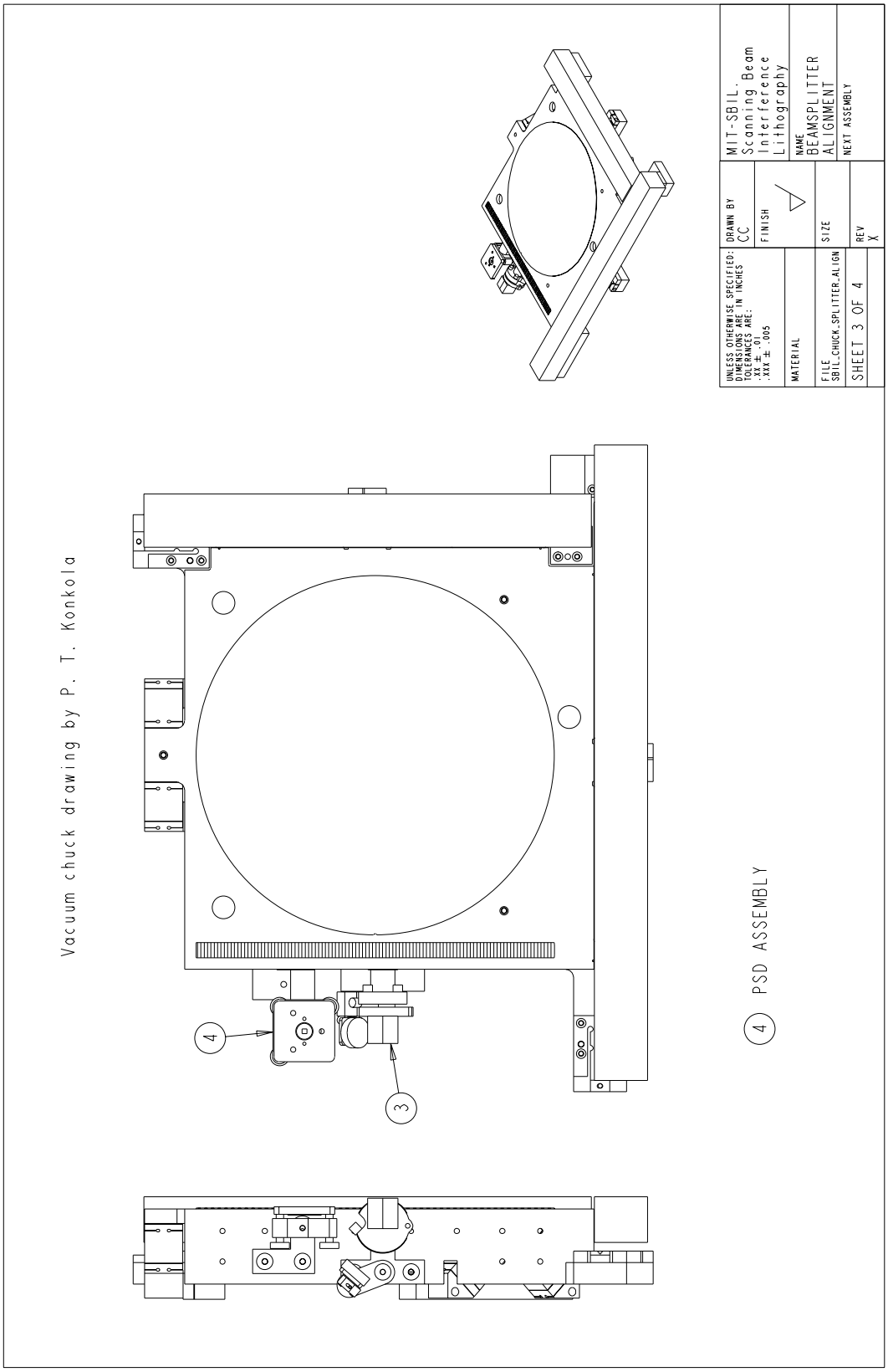

Figure C-3: Drawing of the rectangular beamsplitter and the beam overlapping PSD assembled to the vacuum chuck.

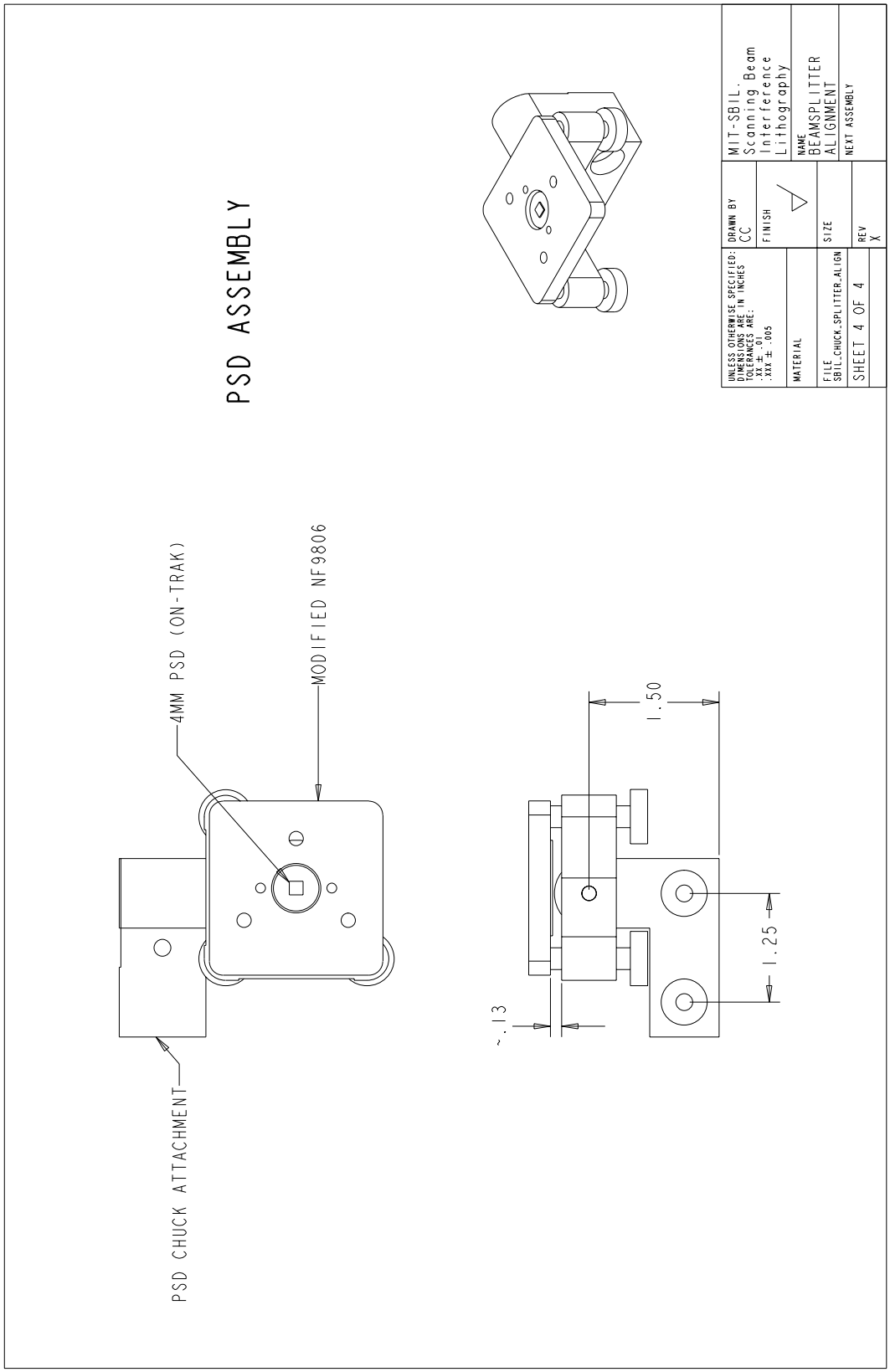

Figure C-4: Drawing of the beam overlapping PSD assembly.

Appendix D

Period measurement with a conventional cube beamsplitter

Figures D-1–D-3 show the overall measurement topology together with closeups of certain critical areas of the ray trace. The point detector is assumed fixed with respect to the moving beamsplitter. Symmetry suggests that the right arm sees no optical path length (OPL) change during the displacement,

$$\Delta R = 0 \ . \tag{D.1}$$

For the left arm, the change in OPL is

$$\Delta L = \Delta L_1 + \Delta L_2 \ , \tag{D.2}$$

where

$$\Delta L_1 = (\Gamma_1 + \Gamma_2) - n\,(\vartheta_1 + \vartheta_2) \ , \tag{D.3}$$

$$\Delta L_2 = n\,(\Gamma_3 + \Gamma_4 - \vartheta_3) \ , \tag{D.4}$$

and n is the beamsplitter's refractive index. The ray segments Γ_1 through Γ_4 and ϑ_1 through ϑ_3 are all graphically defined in Figures D-2 and D-3, so are all the intermediate variables.

One prevails over some heavy mathematics to obtain

$$\Delta L = \Delta L_1 + \Delta L_2 = 2\ D\ \sin\theta_1 \ . \tag{D.5}$$

The terms in ΔL which depend on the index n cancel out perfectly. In the end, the net change in OPL before and after the displacement is

$$\delta \mathrm{L} = \Delta L - \Delta R = 2\ D\ \sin\theta_1 \ . \tag{D.6}$$

This is the same expression as Eq. (4.10) and gives a measured period

$$p_{\mathrm{m}} = \frac{\lambda}{2\ \sin\theta_1}\ , \tag{D.7}$$

which is not the actual fringe period seen by the substrate.

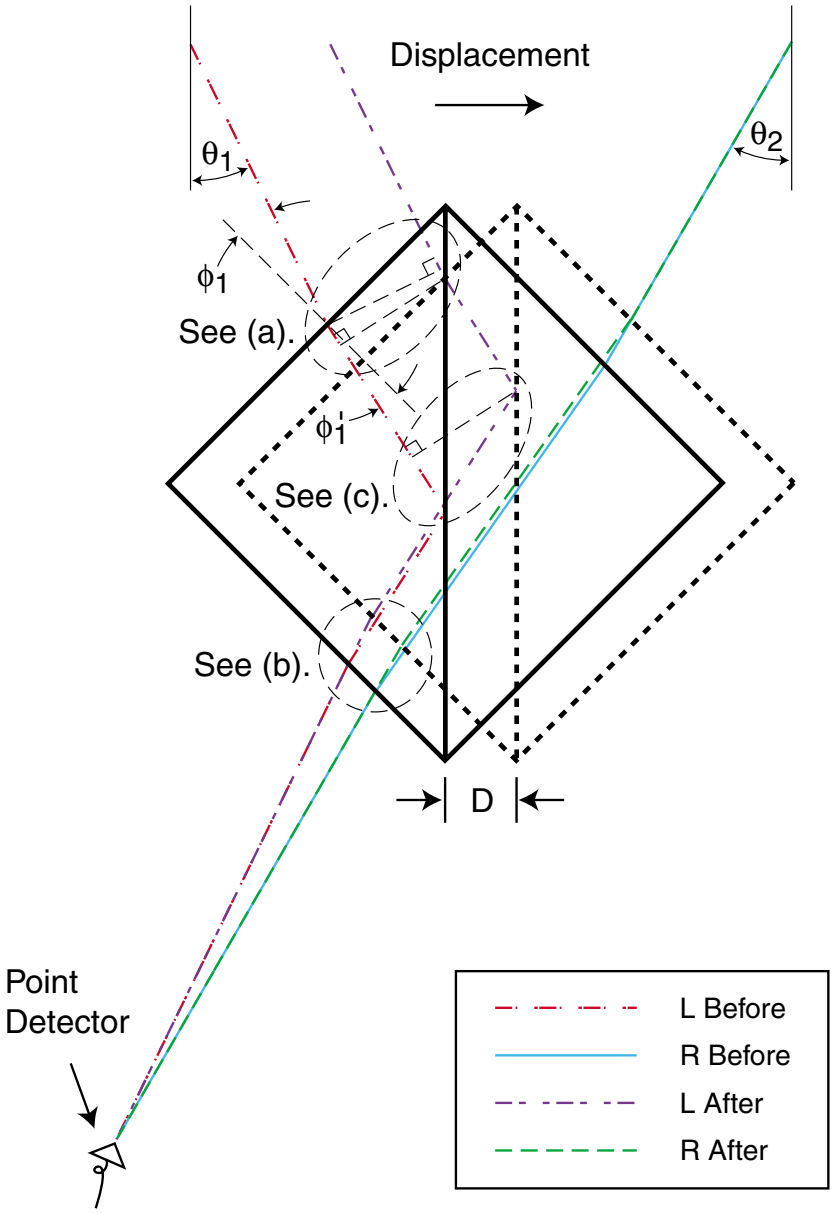

Figure D-1: Ray trace for period measurement where a point detector is fixed while a conventional cube beamsplitter moves by a distance D. To be continued in Figures D-2 and D-3.

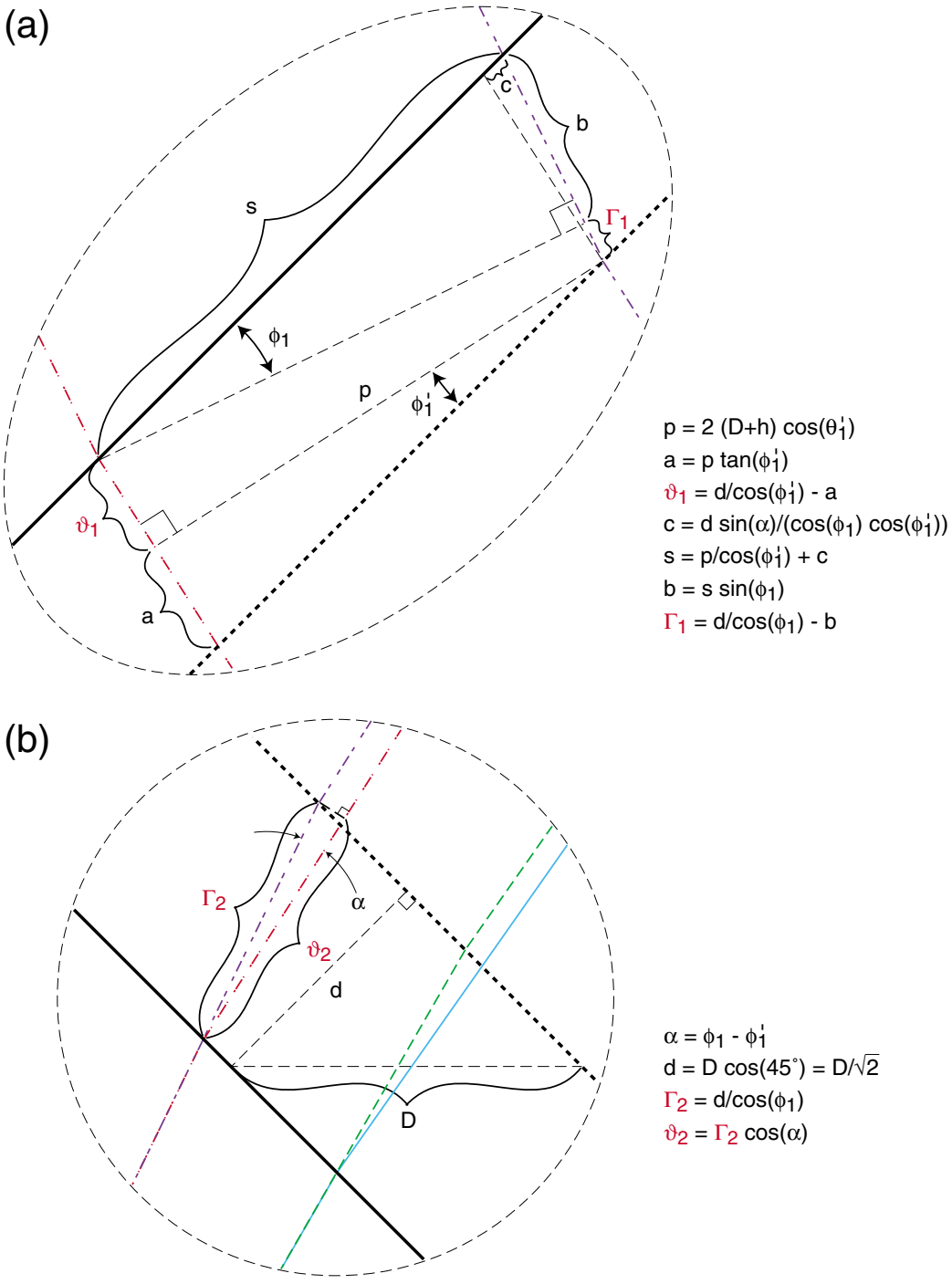

Figure D-2: Ray trace for period measurement where a point detector is fixed while a conventional cube beamsplitter moves by a distance D. Continued from Figure D-1.

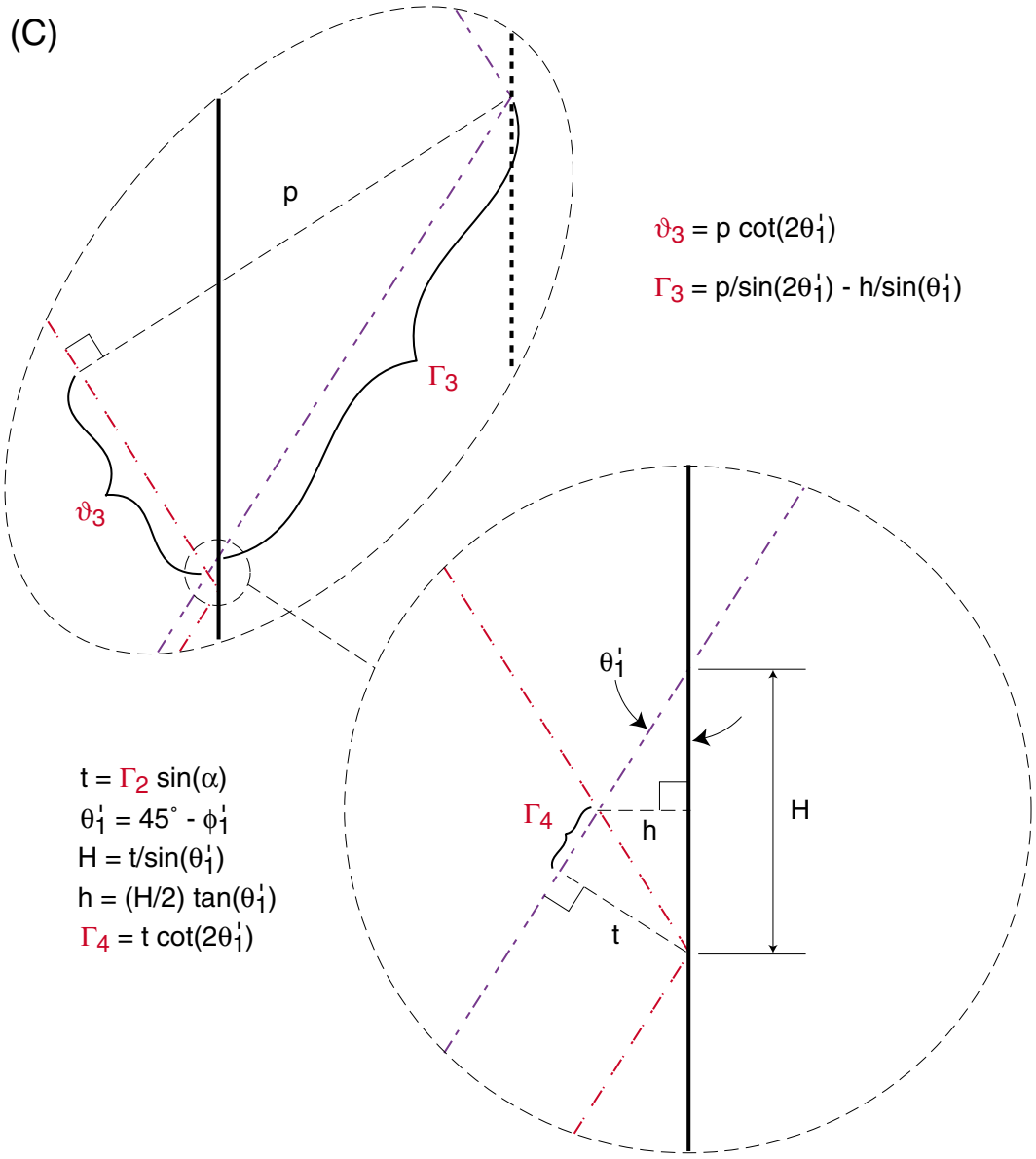

Figure D-3: Ray trace for period measurement where a point detector is fixed while a conventional cube beamsplitter moves by a distance D. Continued from Figure D-1.

Appendix E

Mathematics on intensity integration during period measurement

The AC power is

$$P_1(D) = \int_{-\infty}^{+\infty}\int_{\infty}^{+\infty} I_1(x,y,D)\,dx\,dy \quad , \tag{E.1}$$

where the intensity I_1 is given by Eq. (4.47),

$$\begin{aligned} I_1(x,y,D) = 2A_LA_R\, e^{-\frac{[x-X_L(D)]^2+y^2}{w_0^2}} e^{-\frac{[x-X_R(D)]^2+y^2}{w_0^2}} \cos\{k(\sin\gamma_2-\sin\gamma_1)x \\ +k[\Delta L(D)-\Delta R(D)]+(\phi_L-\phi_R)\} \quad . \end{aligned} \tag{E.2}$$

After integrating over y and pulling out terms that do not involve x, one gets

$$\begin{aligned} P_1 = A_LA_R\sqrt{2\pi}\,w_0\,\exp\left(-\frac{X_L^2+X_R^2}{w_0^2}\right)\int_{-\infty}^{+\infty}\exp\left(-\frac{2\left[x^2-(X_L+X_R)x\right]}{w_0^2}\right) \\ \cos\left[k(\sin\gamma_2-\sin\gamma_1)x+k(\Delta L-\Delta R)+(\phi_L-\phi_R)\right]\,dx \quad . \end{aligned} \tag{E.3}$$

Integration over x can be handled by the following identity [91],

$$\int_{-\infty}^{+\infty}\exp\left(-ax^2\right)\cos[bx+b_0]\,dx = \sqrt{\frac{\pi}{a}}\exp\left(-\frac{b^2}{4a}\right)\cos b_0 \quad , \tag{E.4}$$

but first, one must complete the square inside the integral,

$$\begin{aligned} P_1 = \sqrt{2\pi}\,A_LA_R\,w_0\,\exp\left[-\frac{(X_L-X_R)^2}{2w_0^2}\right]\int_{-\infty}^{+\infty}dx\,\exp\left(-\frac{2\left[x-\frac{1}{2}(X_L+X_R)\right]^2}{w_0^2}\right) \\ \cdot\,\cos\left[k(\sin\gamma_2-\sin\gamma_1)x+k(\Delta L-\Delta R)+(\phi_L-\phi_R)\right] \quad . \end{aligned} \tag{E.5}$$

After a change of variable to

$$\rho = x - \frac{1}{2}(X_L + X_R) \quad , \tag{E.6}$$

Eq. (E.5) becomes

$$P_1 = \sqrt{2\pi}\, A_L A_R\, w_0 \, \exp\left[-\frac{(X_L - X_R)^2}{2w_0^2}\right] \int_{-\infty}^{+\infty} d\rho \exp\left(-\frac{2\rho^2}{w_0^2}\right) \cos\left[k(\sin\gamma_2 - \sin\gamma_1)\rho + \Delta\phi + (\phi_L - \phi_R)\right] \quad , \tag{E.7}$$

where

$$\Delta\phi = k\left[\frac{1}{2}(\sin\gamma_2 - \sin\gamma_1)(X_L + X_R) + (\Delta L - \Delta R)\right] \quad . \tag{E.8}$$

After applying the identity Eq. (E.4) to finish the integration over ρ, one obtains Eq. (4.49).

Appendix F

MATLAB scripts for resist-grating phase simulations

F.1 RGP.m

Based on physics described in Section 4.5, the following program calculates and plots the phase error in the resist grating [Eq. (4.131)], as well as the normalized dose amplitude error [Eq. (4.132)], the quantities E and F which make up the total dose amplitude A_D^{tot} [Eq. (4.127)], and the nominal dose amplitude $A_{D,0}^{\text{tot}}$ [Eq. (4.133)].

```
clear all;

%Define the number of data points used to calculate A_D(x).
q = 1000;

%Define the x vector in data points.
x1 = [-round(q/2):1:round(q/2)];

%Unit for converting to distance, in mm.
u = 1e-2;

%Define input parameters.
Rho = 1; %1/e^2 beam intensity radius in mm
rho = round(Rho/u); %1/e^2 beam radius in number of data points
SS = 0.9; %step length between adjacent scans, in mm
stepsize = round(SS/u); %convert step length from mm to number of data points
period = 400e-6; %grating image period in mm
NN = round(SS/period); %number of periods in one step length
DD = 2.8e-6; %percentage period measurement error
```

```
delta = 2*pi*NN*DD; %define δ
n = 20; %number of scans

p = length(x1);
for i = 1: p,
    %Calculate A_D(x), single-scan Gaussian dose amplitude.
    A(i) = exp(-2*x1(i)^2/rho^2);
end
E = A; %For the initial scan, no step, E is A_D(x), F is 0.
F = zeros(1, p); %build a zero F vector
Anorm = A; %normalized dose amplitude A_{D,0}^{tot}

%Calculate E, F, A_{D,0} if more than one scan.
if (n > 1)
    for m = 2: n,
        temp = shiftadd(E, A*cos((m-1)*delta), stepsize);
        E = temp;
        temp = shiftadd(F, -A*sin((m-1)*delta), stepsize);
        F = temp;
        temp = shiftadd(Anorm, A, stepsize);
        Anorm = temp;
    end
end

%Dose amplitude A_D^{tot}(x) of the resist grating.
Gd = sqrt(E.^2 + F.^2);
%Phase deviation Φ_e(x) of the resist grating due to inability to
%measure the exact grating image period.
Phie = atan2(F,E);
%Dose amplitude error, normalized to A_{D,0}^{tot}.
dGd = (Gd - Anorm)./Anorm;
Phie = unwrap(Phie); %unwrap Φ_e(x)
x2 = [0:1:length(Gd)-1]*u; %build the length of the resist grating in mm
Phia = 2*pi*x2/(period); %linear phase Φ_a built from the actual image period
Phim = 2*pi*x2/(period*(1+DD)); %linear phase Φ_m built from the measured period
%Deviation of the resist grating phase from Φ_m.
dphi = Phia + Phie - Phim; %(Φ_a + Φ_e) gives the phase of the resist grating
dphi = dphi-mean(dphi); %remove the constant offset
dphi = dphi/(2*pi)*period*1e6; %convert to nm

%Plot the results.
figure(1)
plot(x2, dphi);
title(['grating image period=' num2str(period*1e6) 'nm, measured period=' num2str(period*(1+DD)*1e6) ...
```

```
        'nm, measurement error \Delta=' num2str(DD*1e6) 'ppm, 1/e^2 radius=' num2str(Rho) ...
        'mm, step size=' num2str(SS) 'mm']);
xlabel('x (mm)');
ylabel('Resist grating phase minus phase calculated from measured period (nm)');
grid on;

figure(2)
plot(x2, dGd*100);
title(['grating image period=' num2str(period*1e6) 'nm, measured period=' num2str(period*(1+DD)*1e6) ...
        'nm, measurement error \Delta=' num2str(DD*1e6) 'ppm, 1/e^2 radius=' num2str(Rho) ...
        'mm, step size=' num2str(SS) 'mm']);
xlabel('x (mm)');
ylabel('Normalized dose amplitude error (%)');
grid on;

figure(3)
subplot(4,1,1);
plot(x2, E);
xlabel('x (mm)');
ylabel('E (arb. units)');
title(['grating image period=' num2str(period*1e6) 'nm, measurement error \Delta=' num2str(DD*1e6) ...
        'ppm, 1/e^2 radius=' num2str(Rho) 'mm, step size=' num2str(SS) 'mm']);
grid on;
subplot(4,1,2);
plot(x2, F);
xlabel('x (mm)');
ylabel('F (arb. units)');
grid on;
subplot(4,1,3);
plot(x2, Gd);
xlabel('x (mm)');
ylabel('Gd (arb. units)');
grid on;
subplot(4,1,4);
plot(x2, Anorm);
xlabel('x (mm)');
ylabel('Anorm (arb. units)');
grid on;
```

F.2 ShiftAdd.m

ShiftAdd.m is a subroutine for the program RGP.m (Sec. F.1), performing a shift-and-add function.

```
function C = shiftadd(A, B, stepsize)
%Usage: The function shifts the vector B by stepsize, adds the shifted data to A to create C.
%For example, if stepsize = 1,
%A = [1, 2, 3, 4, 5, 6]
%B =          [1, 2, 3, 4]
%C = [1, 2, 3, 5, 7, 9, 4]

error(nargchk(3, 3, nargin)); %check for correct number of input arguments

La = length(A);
Lb = length(B);
overlap = Lb - stepsize; %calculate number of elements that overlap between A and B
C = zeros(1, La + stepsize);

C(1 : La - overlap) = A(1 : La - overlap);
C(La - overlap + 1 : length(A)) = A(La - overlap + 1 : length(A)) + B(1 : overlap);
C(length(A) + 1 : length(C)) = B(overlap + 1 : length(B));

%end
```

Appendix G

MATLAB scripts for wavefront metrology simulations

G.1 WaistLoc.m

The program calculates the location and the beam waist prior to the collimating lens, and plots the radius of curvature as the distance from the lens to the $z = z_2$ plane varies. See Figure 5-3 for reference.

```
%Program****************************************
clear all;

lambda = 351.1e-6; %laser wavelength in mm
k = 2*pi/lambda; %wave number in mm^-1

%See the chapter on SBIL optics for origins of the numerical values below.
% w3 = 1/e^2 beam intensity radius at the z = z_2 plane in mm
% f = focal length of the collimating lens in mm at 351.1 nm
% d = distance from the collimating lens to the z_2 plane in mm
% b3 = confocal parameter (i.e., Rayleigh range) after the collimating lens in mm
w3 = 0.7;
f = 108.2;
d = 328;
b3 = pi*w3^2/lambda;

%Calculate the distance from the lens to pre-lens beam waist (z_1) and the
%pre-lens confocal parameter (b0).
den = b3^2 + d^2 - 2*d*f + f^2; %denominator
z1 = (b3^2*f + d^2*f - d*f^2)/den %calculate z_1 (mm)
```

```
b0 = b3*f^2/den %calculate the initial confocal parameter b0 (mm)
w0 = sqrt(lambda*b0/pi) %the initial beam waist in mm

%****
%Plot the radius of curvature as the distance from the lens to the z2
%plane varies.
%****
% z2 = distance from the initial beam waist to the z2 plane.
dmin = 328; %d minimum in mm
dmax = 20000; %d maximum in mm
res = 1; %plot resolution in mm
dvec = [dmin: res: dmax];
z2 = z1 + dvec;

%Calculate the inverse radius of curvature normalized to the confocal
%parameter b3.
num = (z1^2 - 2*f*z1 + f^2 + b0^2).*z2 - z1^3 + f*z1^2 -b0^2*z1 - b0^2*f;
den = (z1^2 + f*z2 - z1*z2).^2 + (b0*f + b0*z1 - b0*z2).^2;
invR = b3*(num./den);

figure(1);
plot(dvec./1e3, invR, 'r');
axis tight;
grid on;
title(['Inv radius of curvature vs. distance for b3=' num2str(b3) ' mm.']);
xlabel('d (m)');
ylabel('b/R');

%end
%***********************************************
```

G.2 InvRphi.m

This function calculates the phase ϕ and the inverse radius of curvature $(1/R)$ based on Eqs. (5.29) and (5.30), respectively.

```
%Function*************************************
function [invR, phi] = invRphi(b0, z1, f, z2)

%The four inputs:
% b0 = the initial confocal parameter
% z1 = distance from the initial beam waist to the collimating lens
```

```
% f = focal length of the collimating lens at 351.1 nm
% z2 = distance from the initial beam waist to the z = z_2 plane

%The two outputs:
% invR = the inverse radius of curvature
% phi = the phase φ

error(nargchk(4, 4, nargin));

invR = ((z1^2 − 2∗f∗z1 + f^2 + b0^2)∗z2 − z1^3 + f∗z1^2 − b0^2∗z1 − ...
    b0^2∗f)/((z1^2 + f∗z2 − z1∗z2)^2 + (b0∗f + b0∗z1 − b0∗z2)^2);

phi = atan(((−f∗z1^2 + f^2∗z1 − b0^2∗f) + ...
    (z2 − z1)∗(z1^2 − 2∗f∗z1 + f^2 + b0^2))/(b0∗f^2));

error(nargchk(2, 2, nargout));

%end
%***********************************************
```

G.3 Moiré.m

The program allows variations in various physical parameters that define Gaussian beam interference. It generates a phase map for the resulting moiré pattern. The development of the algorithm follows Section 5.2 exactly.

```
%Program*************************************
clear all;

lambda = 351.1e−6; %laser wavelength in mm
k = 2∗pi/lambda; %wave number in mm^−1
period = 400e−6; %metrology grating period in mm
t = asin(lambda/(2∗period)); %nominal beam angle in radians
rho = 0.7; %1/e^2 beam intensity radius at the substrate in mm
f = 108.2; %collimating lens focal length (at 351.1 nm wavelength) in mm

xrange = 2∗rho; %in mm, plot range for the x-axis
xpts = 100; %number of plot points in x
yrange = xrange; %in mm, plot range for the y-axis
ypts = 100; %number of plot points in y

x = linspace(−xrange, xrange, xpts);
```

```
y = linspace(−yrange, yrange, ypts);

%Physical parameters for the right (R) arm. All base values are obtained
%from WaistLoc.m. To preserve numerical precision, long data format is used.
%Changes around the base values can be made by either addition or
%subtraction.
% w0R = R beam initial beam waist (mm)
% b0R = R beam initial confocal parameter (mm)
% z1R = distance from the initial beam waist to the R collimating lens (mm)
% dR = distance from the R collimating lens to the substrate plane (mm)
% tR = R beam incident angle (radians)
w0R = 17.25302017295e−3;
b0R = pi∗w0R^2/lambda;
z1R = 108.3335247791396;
dR = 328;
tR = t;
%Physical parameters for the left (L) arm. All base values are obtained
%from WaistLoc.m. To preserve numerical precision, long data format is used.
%Changes around the base values can be made by either addition or
%subtraction.
% w0L = L beam initial beam waist (mm)
% b0L = L beam initial confocal parameter (mm)
% z1L = distance from the initial beam waist to the L collimating lens (mm)
% dL = distance from the L collimating lens to the substrate plane (mm)
% tL = L beam incident angle (radians)
w0L = 17.25302017295e−3;
b0L = pi∗w0L^2/lambda;
z1L = 108.3335247791396;
dL = 328;
tL = t;

%Calculate the actual fringe period in the substrate plane (nm),
%period2 = period if and only if tR = tL = t.
period2 = lambda/(sin(tR) + sin(tL));

%Perform coordinate transformation for R arm in the substrate plane (z = 0).
x2R = −cos(tR)∗x;
y2R = y;
z2R = sin(tR)∗x + (z1R + dR);
%Perform coordinate transformation for L arm in the substrate plane (z = 0).
x2L = −cos(tL)∗x;
y2L = y;
z2L = −sin(tL)∗x + (z1L + dL);

```

```
%Compute the phase of the moiré pattern in the substrate plane.
%Call the invRphi function (see invRphi.m) to calculate the radii of
%curvature, the phases φ_R and φ_L.
% RR = inverse radius of curvature for the R arm in mm^-1
% phiR = the phase φ_R in radians
% pR = the overall phase in the R arm in radians
% RL = inverse radius of curvature for the L arm in mm^-1
% phiL = the phase φ_L in radians
% pL = the overall phase in the L arm in radians
% pdiff = the phase of the moiré pattern in radians
for m = 1: xpts, %x index
    for n = 1: ypts, %y index
        [RR, phiR] = invRphi(b0R, z1R, f, z2R(m));
        pR(n,m) = −k∗z2R(m) + phiR − 0.5∗k∗RR∗(x2R(m)^2 + y2R(n)^2);
        [RL, phiL] = invRphi(b0L, z1L, f, z2L(m));
        pL(n,m) = −k∗z2L(m) + phiL − 0.5∗k∗RL∗(x2L(m)^2 + y2L(n)^2);
        %Calculate the moiré phase by subtracting the linear
        %metrology grating phase from the Gaussian phase.
        pdiff(n,m) = pL(n,m) − pR(n,m) − 2∗pi∗(x(m)/period);
        %Note: Uncomment the following command line if one wants to study
        %the moiré phase when the two incident beam angles are no
        %longer equal. A metrology grating with a slightly different period
        %is required to properly study the pure nonlinear phase distortions.
        %pdiff(n,m) = pL(n,m) - pR(n,m) - 2∗pi∗(x(m)/period2);
    end
end

%Take care of the phase offset so that the grating image phase at the
%coordinate origin is zero, which implies that the moiré phase there
%is zero, too.
[RR, phiR] = invRphi(b0R, z1R, f, z1R + dR);
[RL, phiL] = invRphi(b0L, z1L, f, z1L + dL);
offset = k∗((z1R + dR) − (z1L + dL)) − (phiR − phiL);
pdiff = pdiff − offset;

%Convert the moiré phase from radians to nm. This is the final phase
%distortion map.
pdiff = pdiff/(2∗pi)∗period∗1e6;

%Generate a phase contour plot for this monkey to see.
figure(2);
[C, h] = contour(x, y, pdiff, 6);
clabel(C,h);
ylim([−yrange, yrange]);
```

```
xlim([−xrange, xrange]);
axis equal;
grid;
xlabel('x (mm)');
ylabel('y (mm)');
title(['d=' num2str(2∗rho) 'mm, p=' num2str(period∗1e6) 'nm, dL=' ...
   num2str(dL) 'mm, dR=' num2str(dR) 'mm, w0L=' num2str(w0L∗1e3) ...
   '“mum, w0R=' num2str(w0R∗1e3) '“mum, z1L=' num2str(z1L) ...
   'mm, z1R=' num2str(z1R) 'mm']);
hold on;

%For reference, also plot the perimeter of the 1/e^2 beam spot size,
%which takes into account the cos θ factor due to the beams'
%oblique incidence.
theta = 0:.01:2∗pi;
rhovec = rho./sqrt(cos(t)^2∗cos(theta).^2 + sin(theta).^2);
polar(theta,rhovec,'--r');
hold off;

%end
%**********************************************
```

G.4 MoiréCCD.m

The program simulates the series of interferograms observed at the CCD camera, when the Hariharan five-step algorithm is applied. The code could be easily adapted for other phase shifting algorithms. Similar to the routine Moiré.m, various optical parameters that define Gaussian beam interference can be varied here. Since interferograms are generated using a simulated moiré phase, the code makes no attempt to extract any phase information out of the interferograms, as the process can only reproduce the moiré phase.

```
%Program*****************************************
clear all;

lambda = 351.1e−6; %laser wavelength in mm
k = 2∗pi/lambda; %wave number in mm^−1
period = 400e−6; %metrology grating period in mm
t = asin(lambda/(2∗period)); %incident beam angle in radians
rho = 0.75; %1/e^2 beam intensity radius at the CCD in mm
f = 108.2; %collimating lens focal length (at 351.1 nm wavelength) in mm
```

```
10
xrange = 2*rho; %in mm, plot range for the x-axis
xpts = 100; %number of plot points in x
yrange = xrange; %in mm, plot range for the y-axis
ypts = 100; %number of plot points in y
15
x = linspace(-xrange, xrange, xpts);
y = linspace(-yrange, yrange, ypts);

%Physical parameters for the right (R) arm. All base values are obtained
20 %from WaistLoc.m. To preserve numerical precision, long data format is used.
%Changes around the base values can be made by either addition or
%subtraction. Angle variation is not allowed in this version of the code,
%though can be added with relatively little work.
% w0R = R beam initial beam waist (mm)
25 % b0R = R beam initial confocal parameter (mm)
% z1R = distance from the initial beam waist to the R collimating lens (mm)
% dR = distance from the R collimating lens to the substrate plane (mm)
w0R = 17.25302017295e-3;
b0R = pi*w0R^2/lambda;
30 z1R = 108.3335247791396;
dR = 328;
%Physical parameters for the left (L) arm. All base values are obtained
%from WaistLoc.m. To preserve numerical precision, long data format is used.
%Changes around the base values can be made by either addition or
35 %subtraction. Angle variation is not allowed in this version of the code,
%though can be added with relatively little work.
% w0L = L beam initial beam waist (mm)
% b0L = L beam initial confocal parameter (mm)
% z1L = distance from the initial beam waist to the L collimating lens (mm)
40 % dL = distance from the L collimating lens to the substrate plane (mm)
w0L = 17.25302017295e-3;
b0L = pi*w0L^2/lambda;
z1L = 108.3335247791396;
dL = 328;
45
%Perform coordinate transformation for R arm in the substrate plane (z = 0).
x2R = -cos(t)*x;
y2R = y;
z2R = sin(t)*x + (z1R + dR);
50 %Perform coordinate transformation for L arm in the substrate plane (z = 0).
x2L = -cos(t)*x;
y2L = y;
z2L = -sin(t)*x + (z1L + dL);
```

```
%Calculate the phase offset so that the grating image phase at the
%coordinate origin is zero.
[RR, phiR] = invRphi(b0R, z1R, f, z1R + dR);
[RL, phiL] = invRphi(b0L, z1L, f, z1L + dL);
offset = k*((z1R + dR) - (z1L + dL)) - (phiR - phiL);

%Assume the Hariharan five step algorithm. Define the phase-step values.
phaseshift = [0, pi/2, pi, 3*pi/2, 2*pi];
for q = 1:5,
    %Compute the phase of the moiré pattern in the substrate plane.
    %Call the invRphi function (see invRphi.m) to calculate the radii of
    %curvature, the phases φ_R and φ_L.
    % RR = inverse radius of curvature for the R arm in mm^-1
    % phiR = the phase φ_R in radians
    % pR = the overall phase in the R arm in radians
    % RL = inverse radius of curvature for the L arm in mm^-1
    % phiL = the phase φ_L in radians
    % pL = the overall phase in the L arm in radians
    % pdiff = the phase of the moiré pattern in radians
    for m = 1: xpts, %x index
        for n = 1: ypts, %y index
            [RR, phiR] = invRphi(b0R, z1R, f, z2R(m));
            pR(n,m) = -k*z2R(m) + phiR - 0.5*k*RR*(x2R(m)^2 + y2R(n)^2);
            [RL, phiL] = invRphi(b0L, z1L, f, z2L(m));
            %Incremental phase shift is added to the left arm during each of the five steps.
            pL(n,m) = -k*z2L(m) + phiL - 0.5*k*RL*(x2L(m)^2 + y2L(n)^2) + phaseshift(q);
            %Note that the incremental phase shift is also included in the
            %moiré phase.
            pdiff(n,m) = pL(n,m) - pR(n,m) - 2*pi*(x(m)/period) - offset;
            %Calculate the intensity of the interferogram observed at the
            %CCD with arbitrary magnitude. The phase of the interferogram is
            %the moiré phase.
            pdiffint(n,m) = exp(-2*((x(m)^2 + y(n)^2)/rho^2))*(1 + cos(pdiff(n,m)));
        end
    end
%Generate the intensity plot.
figure(q);
surf(x, y, pdiffint);
shading interp;
xlim([-xrange,xrange]);
ylim([-yrange,yrange]);
grid on;
axis equal;
```

```
xlabel('x (mm)');
ylabel('y (mm)');
title(['d=' num2str(2*rho) 'mm, p=' num2str(period*1e6) 'nm, dL=' ...
    num2str(dL) 'mm, dR=' num2str(dR) 'mm, w0L=' num2str(w0L*1e3) ...
    '“mum, w0R=' num2str(w0R*1e3) '“mum, z1L=' num2str(z1L) ...
    'mm, z1R=' num2str(z1R) 'mm']);
end

%end
%*********************************************
```

Bibliography

[1] M. L. Schattenburg, C. Chen, P. N. Everett, J. Ferrera, P. Konkola, and H. I. Smith. Sub-100nm metrology using interferometrically produced fiducials. *J. Vac. Sci. Technol. B*, 17(6):2692–2697, November-December 1999.

[2] Max Born and Emil Wolf. *Principles of Optics*. Cambridge, 7th edition, 2002.

[3] M. C. Hutley. *Diffraction Gratings*. Academic, 1982.

[4] E. Hecht. *Optics*. Addison-Wesley, third edition, 1998.

[5] Erwin G. Loewen and Evgeny Popov. *Diffraction Gratings and Applications*. Marcel Dekker, 1997.

[6] D. Rittenhouse. Explanation of an optical deception. *Trans. Amer. Phil. Soc.*, 2:37–42, 1786.

[7] J. Fraunhofer. Kurtzer bericht von the resultaten neuerer versuche über die gesetze des lichtes, und die theorie derselbem. *Ann. d. Physik*, 74:337–378, 1823.

[8] H. Rowland. Preliminary notice of results accomplished on the manufacture and theory of gratings for optical purposes. *Phil. Mag.*, 13:469–474, 1882.

[9] Albert A. Michelson. Recent advances in spectroscopy. Nobel Lecture. December 12, 1907.

[10] George R. Harrison and Erwin G. Loewen. Ruled gratings and wavelength tables. *Applied Optics*, 15(7):1744–1747, 1976.

[11] George R. Harrison. The production of diffraction gratings I. Development of the ruling art. *J. Opt. Soc. Am.*, 39(6):413–426, 1949.

[12] George R. Harrison and George W. Stroke. Interferometric control of grating ruling with continuous carriage advance. *J. Opt. Soc. Am.*, 45(2):112–121, 1955.

[13] Erwin G. Loewen. What's new in gratings? In L. B. Robinson, editor, *Instrumentation for Ground-Based Optical Astronomy, Present and Future*, pages 118–123. Springer-Verlag, 1987.

[14] C. Palmer. *Diffraction Grating Handbook*. Richardson Grating Laboratory, 4th edition, 2000.

[15] J. M. Lerner. Diffraction gratings ruled and holographic—a review. *Proc. SPIE*, 240:82–88, 1980.

[16] L. I. Bakh and G. N. Rassudova. Method of determining the ruling errors of diffraction gratings. *Sov. J. Opt. Technol.*, 54(4):195–198, April 1987.

[17] J. U. White and W. Frazer. Method of making optical elements. *U.S. Patent No. 2,464,738*, 1949.

[18] M. Seya and K. Goto. Production of replica gratings. *Science of Light*, 5:46–48, 1956.

[19] Albert A. Michelson. *Studies in Optics*. University of Chicago, 1927. Reprinted by Dover in 1995.

[20] Antoine Labeyrie and Jean Flamand. Spectrographic performance of holographically made diffraction gratings. *Opt. Comm.*, 1(1):5–8, April 1969.

[21] Von D. Rudolph and G. Schmahl. High precision gratings produced with laserlight and photoresist layers. *Optik*, 30:475–487, 1970.

[22] E. H. Anderson, H. I. Smith, and M. L. Schattenburg. Holographic lithography. *U.S. Patent No. 5,142,385*, 1992.

[23] Juan Ferrera. *Nanometer-Scale Placement in Electron-Beam Lithography*. PhD dissertation, Massachusetts Institute of Technology, Department of Electrical Engineering and Computer Science, June 2000.

[24] M. C. Hutley. Interference (holographic) diffraction gratings. *J. Phys. E*, 9:513–520, 1976.

[25] R. D. Boyd, J. A. Britten, D. E. Decker, B. W. Shore, B. C. Stuart, M. D. Perry, and Lifeng Li. High-efficiency metallic diffraction gratings for laser applications. *Applied Optics*, 34(10):1697–1706, April 1995.

[26] International Technology Roadmap for Semiconductors, http://public.itrs.net. *The International Technology Roadmap for Semiconductors: 2002 Update*, 2002.

[27] Norman Bobroff. Recent advances in displacement measuring interferometry. *Meas. Sci. Technol.*, 4:907–926, 1993.

[28] Frank C. Demarest. High-resolution, high-speed, low data age uncertainty, heterodyne displacement measuring interferometer electronics. *Meas. Sci. Technol.*, 9(7):1024–1030, 1998.

[29] Klaus-Dieter Röth and Carola Bläsing-Bangert. Performance data obtained on a next-generation mask metrology tool. *Proc. SPIE*, 2725:779–785, May 1996.

[30] Thomas Struck and Klaus-Dieter Röth. Matching of different pattern placement metrology systems: an example for practical use of different LMS systems in the inspection process for photomasks. *Proc. SPIE*, 3677:629–634, June 1999.

[31] Jun Ye, C. N. Berglund, R. F. W. Pease, G. Owen, Rolf Jaeger, Katie Alexander, and Judith Seeger. Field distortion characterization using linewidth or pitch measurement. *J. Vac. Sci. Technol. B*, 13(6):2904–2908, November-December 1995.

[32] Seong-Yong Moon, Won-Tai Ki, Seung-Hune Yang, Tae-Moon Jeong, Sung-Woon Choi, Woo-Sung Han, and Jung-Min Sohn. Analysis of photomask distortion caused by blank materials and open ratios. *Proc. SPIE*, 4186:227–232, 2001.

[33] Leica Microsystems Wetzlar GmbH, Germany. *Leica LMS IPRO fully automated mask and wafer metrology system*, 1999. Sales brochure.

[34] Klaus-Dieter Röth. Performance data on the new LMS IPRO2. Leica Microsystems Wetzlar GmbH. http://www.semiconation.com.

[35] H. I. Smith, S. D. Hector, M. L. Schattenburg, and E. H. Anderson. A new approach to high fidelity e-beam lithography based on an in-situ, global fiducial grid. *J. Vac. Sci. Technol. B*, 9:2992–2995, 1991.

[36] Per Liden. Cost-effective pattern generation for 64-Mb and 256-Mb photomasks. *Proc. SPIE*, 3236:55–63, 1997.

[37] F. M. Gerasimov. Use of diffraction gratings for controlling a ruling engine. *Applied Optics*, 6(11):1861–1865, 1967.

[38] L. Berger. Grating interferometry for positioning the X-Y stages of a wafer stepper. *Proc. SPIE*, 503:130–134, August 1984.

[39] Alfons Ernst. *Digital linear and angular metrology.* verlag moderne industrie, third edition, 1998.

[40] Dr. Johannes Heidendain GmbH, http://www.heidenhain.de, 83301 Traunreut, Deutschland. *General Catalog*, 2003.

[41] H. Kogelnik. On the propagation of Gaussian beams of light through lenslike media including those with a loss and gain variation. *Applied Optics*, 4:1562–1569, 1965.

[42] M. L. Schattenburg and H. I. Smith. The critical role of metrology in nanotechnology. *Proc. SPIE*, 4608:116–124, 2001.

[43] K. Hibinio and Z. S. Hegedus. Hyperbolic holographic gratings: analysis and interferometric tests. *Applied Optics*, 33(13):2553–2559, May 1994.

[44] J. Ferrera, M.L. Schattenburg, and H.I. Smith. Analysis of distortion in interferometric lithography. *J. Vac. Sci. Technol. B*, 14(6):4009–4013, November-December 1996.

[45] Carl Gang Chen. Microcomb fabrication for high accuracy foil x-ray telescope and vector Gaussian beam modeling. Master's thesis, Massachusetts Institute of Technology, Department of Electrical Engineering and Computer Science, June 2000.

[46] N. Bobroff. Residual errors in laser interferometry from air turbulence and nonlinearity. *Applied Optics*, 26:2676–2682, 1987.

[47] Carl G. Chen, Paul T. Konkola, Ralf K. Heilmann, G. S. Pati, and Mark L. Schattenburg. Image metrology and system controls for scanning beam interference lithography. *J. Vac. Sci. Technol. B*, 19(6):2335–2341, November-December 2001.

[48] Paul Thomas Konkola. *Design and analysis of a scanning beam interference lithography system for patterning gratings with nanometer-level distortions.* PhD dissertation, Massachusetts Institute of Technology, Department of Electrical Engineering and Computer Science, June 2003.

[49] P. T. Konkola, C. G. Chen, R. K. Heilmann, and M. L. Schattenburg. Beam steering system and spatial filtering applied to interference lithography. *J. Vac. Sci. Technol. B*, 18(6):3282–3286, November-December 2000.

[50] Robert R. Hershey and Emmett N. Leith. Grating interferometers for producing large holographic gratings. *Applied Optics*, 29(7):937–943, 1990.

[51] Emmett N. Leith and R. Hershey. Transfer functions and spatial filtering in grating interferometers. *Applied Optics*, 24(2):237–239, 1985.

[52] Paul T. Konkola. Analysis of a grating interferometer for interference lithography. White Paper. October 2000, Revised March 2001.

[53] Ralf K. Heilmann, Paul T. Konkola, Carl G. Chen, G. S. Pati, and Mark L. Schattenburg. Digital heterodyne interference fringe control system. *J. Vac. Sci. Technol. B*, 19:2342–2346, November-December 2001.

[54] Amnon Yariv. *Optical Electronics in Modern Communications.* Oxford, fifth edition, 1997.

[55] Chris J. Evans, Robert J. Hocken, and W. Tyler Estler. Self-calibration: reversal, redundancy, error separation, and "absolute testing". *CIRP Annals*, 45(2):617–634, 1996.

[56] Carl G. Chen, Ralf K. Heilmann, Chulmin Joo, Paul T. Konkola, G. S. Pati, and Mark L. Schattenburg. Beam alignment for scanning beam interference lithography. *J. Vac. Sci. Technol. B*, 20(6):3071–3074, November-December 2002.

[57] Donald C. O'Shea. *Elements of Modern Optical Design.* Wiley, 1985.

[58] H. A. Haus. *Waves and Fields in Optoelectronics.* Prentice Hall, 1984.

[59] Coherent, Inc. *Operator's Manual: The Coherent Innova Sabre Ion Laser*, 1995. Part Number 0167-697-00, Rev. B.

[60] Carl G. Chen, Ralf K. Heilmann, Paul T. Konkola, G. S. Pati, and Mark L. Schattenburg. A novel sub-microradian beam diagnostic and alignment system. *Proceedings of ASPE 16th annual meeting*, 25:216–219, November 2001.

[61] Paul Horowitz and Winfield Hill. *The Art of Electronics.* Cambridge, second edition, 1989.

[62] Samuel D. Stearns and Don R. Hush. *Digital Signal Analysis.* Prentice Hall, second edition, 1990.

[63] National Instruments Corporation. *NI 6034E/6035E/6036E User Manual*, May 2001. Part Number 322339B-01.

[64] Semyon Rabinnovich, editor. *Measurement Errors: Theory and Practice.* AIP Press, 1995.

[65] Louis Lyons. *A Practical Guide to Data Analysis for Physical Science Students.* Cambridge, 1991.

[66] William N. Partlo, Charles H. Fields, and William G. Oldham. Direct aerial image measurement as a method of testing high numerical aperture microlithographic lenses. *J. Vac. Sci. Technol. B*, 11(6):2686–2691, November-December 1993.

[67] Chulmin Joo, G. S. Pati, Carl G. Chen, Paul T. Konkola, Ralf K. Heilmann, Mark L. Schattenburg, Alexander Liddle, and Erik H. Anderson. Precision fringe metrology using a Fresnel zone plate. *J. Vac. Sci. Technol. B*, 20(6):3075–3079, November-December 2002.

[68] Carl G. Chen, Paul T. Konkola, Ralf K. Heilmann, Chulmin Joo, and Mark L. Schattenburg. Nanometer-accurate grating fabrication with scanning beam interference lithography. *Proc. SPIE*, 4936:126–134, 2002.

[69] Kenneth Alan Goldberg. *Extreme Ultraviolet Interferometry.* PhD dissertation, University of California, Berkeley, Department of Physics, 1997.

[70] John G. Proakis and Dimitris G. Manolakis. *Digital Signal Processing: Principles, Algorithms and Applications.* Prentice Hall, third edition, 1995.

[71] Alan V. Oppenheim, Alan S. Willsky, and S. Hamid Nawab. *Signals & Systems.* Prentice Hall, second edition, 1996.

[72] Alan V. Oppenheim, Ronald W. Schafer, and John R. Buck. *Discrete-Time Signal Processing.* Prentice Hall, second edition, 1999.

[73] G. T. Reid. Moiré fringes in metrology. *Optics and Lasers in Engineering*, 5(2):63–93, 1984.

[74] D. Post. Developments in moiré interferometry. *Optical Engineering*, 21(3):458–467, 1982.

[75] C. A. Sciammarella. The moiré method: a review. *Experimental Mechanics*, 22(11):418–433, 1982.

[76] M. Takeda. Fringe formula for projection type moiré topography. *Optics and Lasers in Engineering*, 3(1):45–52, 1982.

[77] K. Creath and J. C. Wyant. Moiré and fringe projection techniques. In D. Malacara, editor, *Optical Shop Testing*, pages 653–685. Wiley, second edition, 1992.

[78] Carl G. Chen, Paul T. Konkola, Juan Ferrera, Ralf K. Heilmann, and Mark L. Schattenburg. Analyses of vector gaussian beam propagation and the validity of paraxial and spherical approximations. *J. Opt. Soc. Am. A*, 19(2):404–412, 2002.

[79] P. Carré. Installation et utilisation du comparateur photoelectrique et interferentiel du bureau international des poids et mesures. *Metrologia*, 2:13–23, 1966.

[80] R. Crane. Interference phase measurement. *Applied Optics*, 8:538–542, 1969.

[81] J. H. Bruning, D. R. Herriott, J. E. Gallagher, D. P. Rosenfeld, A. D. White, and D. J. Brangaccio. Digital wavefront measuring interferometer for testing optical surfaces and lenses. *Applied Optics*, 13(11):2693–2703, 1974.

[82] J. C. Wyant. Use of an AC heterodyne lateral shear interferometer with real-time wavefront correction systems. *Applied Optics*, 14(11):2622–2626, 1975.

[83] K. Creath. Phase-measurement interferometry techniques. In E. Wolf, editor, *Progress in Optics*, volume XXVI, pages 349–393. North-Holland, 1988.

[84] J. E. Greivenkamp and J. H. Bruning. Phase shifting interferometry. In D. Malacara, editor, *Optical Shop Testing*, pages 501–598. Wiley, second edition, 1992.

[85] D. W. Robinson. Phase unwrapping methods. In D. W. Robinson and G. T. Reid, editors, *Interferogram Analysis: Digital Fringe Pattern Measurement Techniques*, pages 194–229. Institute of Physics Publishing, 1993.

[86] P. Hariharan, B. F. Oreb, and T. Eiju. Digital phase-shifting interferometry: A simple error-compensating phase calculation algorithm. *Applied Optics*, 26:2504, 1987.

[87] James C. Wyant. Phase-shifting interferometry. Lecture notes for Optics 513: Optical Testing at the University of Arizona.

[88] Lon Gray. Cohu, Inc., private communication.

[89] Sony Corporation. *ICX085AL: 2/3-inch Progressive Scan CCD Image Sensor with Square Pixel for B/W Cameras.* Specifications sheet.

[90] J. C. Wyant and K. Creath. Basic wavefront aberration theory for optical metrology. In J. C. Wyant and R. R. Shannon, editors, *Applied Optics and Optical Engineering*, volume XI, chapter 1. Academic, 1997.

[91] I. S. Gradshteyn and I. M. Ryzhik. *Table of Integrals, Series, and Products.* Academic, fifth edition, 1994.